

**NANOELECTRONIC DEVICES AND
MEASUREMENTS TOWARD
NANOCRYSTAL-BASED OPTOELECTRONICS
AND DNA SEQUENCING WITH SOLID-STATE
NANOPORES**

Lauren J. Willis

A DISSERTATION

in

Physics and Astronomy

Presented to the Faculties of the University of Pennsylvania in Partial Fulfillment of
the Requirements for the Degree of Doctor of Philosophy

2013

Marija Drndić, Associate Professor of Physics and Astronomy
Supervisor of Dissertation

Alan T. Johnson, Professor of Physics and Astronomy
Graduate Group Chairperson

Dissertation Committee:

Marija Drndić, Associate Professor of Physics and Astronomy
A. T. Charlie Johnson, Professor of Physics and Astronomy, Electrical and Systems
Engineering, and Materials Science and Engineering
Charles Kane, Professor of Physics and Astronomy
Christopher B. Murray, Professor of Chemistry and Materials Science and Engineering
Evelyn Thomson, Associate Professor of Physics and Astronomy

UMI Number: 3565283

All rights reserved

INFORMATION TO ALL USERS

The quality of this reproduction is dependent upon the quality of the copy submitted.

In the unlikely event that the author did not send a complete manuscript and there are missing pages, these will be noted. Also, if material had to be removed, a note will indicate the deletion.



UMI 3565283

Published by ProQuest LLC (2013). Copyright in the Dissertation held by the Author.

Microform Edition © ProQuest LLC.

All rights reserved. This work is protected against unauthorized copying under Title 17, United States Code



ProQuest LLC.
789 East Eisenhower Parkway
P.O. Box 1346
Ann Arbor, MI 48106 - 1346

NANO ELECTRONIC DEVICES AND MEASUREMENTS TOWARD NANOCRYSTAL-BASED OPTOELECTRONICS AND DNA SEQUENCING WITH SOLID-STATE NANOPORES

COPYRIGHT

2013

Lauren Ja Yung Willis

Acknowledgements

I would like to thank everyone that has been in the Drndić lab with me. Specifically, I want to thank Mike Fischbein, who taught me almost everything I know about fabrication and transport measurements; Claudia Querner, who taught me everything I know about chemistry; Ken Healy, who taught me about nanopores; Meni Wanunu, who had the best puns; Jessamyn Fairfield, who introduced me to a lot of great blogs; Matt Puster, who kept me informed about North Carolina; and Kim Venta, who introduced me to Jim Butcher novels. I would also like to give a shout out to all the other labmates I've worked with: Postdocs Yuanzhen Chen, Tali Dadosh, Vishva Ray, Chris Merchant, Gaby Shemer, Julio Rodriguez-Manzo, and Adrian Balan; graduate students Siying Wang, Matt Hickman, Alexandra Adegoke, and Will Parkin; and undergraduate students Greg Calusine, Robin Havener, Neil Peterman, John Bartel, Lee Burwasser, Bart Machielse, and Elizabeth Oppong. And of course, I'd like to thank my advisor Marija Drndić.

I would also like to thank all my professors, both here at Penn, and from Swarthmore College. My Swarthmore professors did an amazing job preparing me for graduate school, and my Penn professors taught me about the different specializations within physics.

I am very grateful for the fantastic facilities at Penn, including the Penn Regional Nanotechnology Facility and the Wolf Nanofabrication Facility. The staff, including Doug Yates, Iulian Codreanu, and Kyle Keenan were amazing and instrumental to much of my work. I would also like to thank the Johnson lab, which was like my second lab. I also owe a big thank you to the Nano-Bio Interface Center, especially

for my IGERT fellowship, and the staff members who organized everything, including Jim McGonigle, Holly Burnside, and Danielle Tadros.

I want to thank all my friends in graduate school who helped me get through this graduate school marathon. I really enjoyed my time in the Zoo with my yearmates, and I want to especially thank Elizabeth Libby for our lunches and general hijincks together.

Finally, I would like to thank my family. I certainly couldn't have gotten to where I am today without their support and love. Last, but certainly not least, I want to thank my husband, Ben Rhee, for his support and love through every trial and tribulation.

ABSTRACT

NANOELECTRONIC DEVICES AND MEASUREMENTS TOWARD
NANOCRYSTAL-BASED OPTOELECTRONICS AND DNA SEQUENCING
WITH SOLID-STATE NANOPORES

Lauren J. Willis

Dr. Marija Drndić

Nanoelectronics are critical to exploring nanoscale materials: including nanocrystals, which could revolutionize optoelectronics, and DNA, which could revolutionize medicine. Our suspended silicon nitride membranes combined with electron beam lithography and transmission electron microscopy have been essential to our device fabrication and measurements. Nanocyrstal-based optoelectronics have garnered much interest, and thus new ways of increasing their transport are constantly being researched. We used ligand exchanges to decrease the interparticle spacing of nanocrystal films, which is known to augment transport. Using gaps only a few nanoparticles-wide, we measured transport and found that current could be controlled with annealing, hydrazine treatment, and voltage-sweeping. Annealing destroyed the insulating ligand surrounding each nanocrystal and allowed the particles to move closer. This usually increased the photocurrent, without significantly increasing the dark current. However, this was ineffective on sub-monolayers. Hydrazine was similar, except it replaced the ligand, rather than destroying it, and it was effective on sub-monolayers; however, it caused a large increase in the dark current as well.

as the photocurrent. Sweeping the voltage overnight could increase or decrease the photocurrent of a sample depending on whether the sample was illuminated or in the dark, corresponding to traps being emptied or filled. In addition to nanocrystals, our devices were used in solution to sense DNA. We fabricated nanelectrodes and nanowires next to nanopores and showed DNA translocations ionically. We also developed methods to make the pores hydrophilic without the use of piranha; we instead used rapid thermal annealing, heated ozone treatments, and oxygen/hydrogen plasmas. While high rates of device failure was a challenge, recommendations for future experiments are presented, including grounding of all equipment and an extreme focus on sample cleanliness. We have shown that our nanoelectronics can be successfully integrated into nanocrystal optoelectronics and DNA nanopore sequencing devices. We hope that the exploration of both our successes and failures will advance nanoelectronics and their applications.

Contents

Acknowledgements	iii
ABSTRACT	v
LIST OF TABLES	xii
LIST OF ILLUSTRATIONS	xii
1 Introduction to Nanocrystals	1
1.1 What are nanocrystals?	1
1.2 Synthesis	3
1.3 Characterization	5
1.4 Quantum Confinement	8
1.5 Transport Measurements	20
1.5.1 Transport through Films	22
1.5.2 Carrier Generation	24
1.5.3 Multiple Excitons	24
1.5.4 Field Effect Transistors	26
1.6 Overview of Results	27
2 Introduction to DNA Sequencing and Sensing	29
2.1 DNA	29
2.2 DNA Sequencing Techniques	31
2.2.1 Sanger Sequencing	31
2.2.2 Polony Sequencing	34

2.2.3	Nanopore Sequencing	38
2.2.4	Transmission Electron Microscopy Sequencing	42
2.3	Nanopore Theory	43
2.3.1	Length Scales	43
2.3.2	Diffusion	48
2.4	Overview of Results	52
3	Fabrication	54
3.1	Typical Devices	54
3.2	Resist-Based Lithographies	54
3.2.1	Electron Beam Lithography	55
3.2.2	Photolithography	60
3.3	Evaporation	64
3.3.1	Liftoff	66
3.4	Transmission Electron Beam Ablation Lithography	68
3.5	Wafer Processing	71
4	Measurement Setup	72
4.1	Cryostats	72
4.1.1	Integration into Measurement Setups	76
4.2	Microfluidics Setup	78
5	Synthesis and TEM Analysis of PbSe	83
5.1	Introduction	83
5.2	Ligand Exchange	84
5.2.1	Ligand Calculation	85
5.2.2	Results	87
5.3	Clusters	88

5.3.1	Synthesis	88
5.3.2	Results	93
5.4	Conclusions	95
6	Lead Selenide Nanorod Measurements	97
6.1	Introduction	97
6.2	Synthesis	98
6.3	Device Fabrication	99
6.4	Measurement Setup and Background Measurements	100
6.5	Results	102
6.5.1	No Treatment	102
6.5.2	Annealing	104
6.5.3	Hydrazine	108
6.6	Conclusions	111
7	Nanocrystal Traps	113
7.1	Introduction	113
7.2	Devices	114
7.2.1	Nanocrystal Characterization	114
7.3	Measurement Setup and Control Measurements	117
7.3.1	Annealing	118
7.3.2	Background and Dark Current Measurements	120
7.4	Results and Discussion	123
7.5	Conclusions	135
8	Nanoelectrode Translocation Measurements	137
8.1	Introduction	137
8.2	Methods	140

8.2.1	Silicon Nitride Membrane Fabrication	140
8.2.2	Nanoelectrode Fabrication	141
8.2.3	Nanopore Drilling and Nanoelectrode Shaping	141
8.2.4	Measurements	142
8.3	Results and Discussion	143
8.4	Conclusions	155
9	Nanowires for DNA Sensing	156
9.1	Introduction	156
9.2	Methods	157
9.3	Results and Discussion	160
9.4	Conclusions	165
10	Conclusions	167
10.1	Nanocrystals	167
10.2	Nanopores	168
A	Recipes	169
A.1	Lithography	169
A.1.1	Electron Beam Lithography	169
A.1.2	Photolithography	171
A.2	Wafer Processing	172
A.3	Solutions for DNA Project	174
	BIBLIOGRAPHY	175

LIST OF TABLES

2.1	Debye screening length for different molarities.	45
3.1	Ways to increase EBL resolution and the sacrifices of each.	60
5.1	Variables used in the calculation for the number of oleic acid ligands on the surface of a PbSe nanocrystal.	86
5.2	Summary of interparticle spacing results for different ligands.	88
5.3	Summary of interparticle spacing results for different ligands.	93
7.1	Relative photocurrent ratios of the low- and room-temperature photo- currents for several nanogap devices on a single chip	128
A.1	Writing parameters for the Elionix.	170
A.2	Writing parameters for PMMA the Johnson lab SEM.	171

LIST OF ILLUSTRATIONS

1.1	Transmission electron micrograph (TEM) of gold nanocrystals.	2
1.2	Schematic of a core/shell nanocrystal.	2
1.3	Schematic of a nanocrystal synthesis.	4
1.4	Absorption spectra of different-sized nanocrystals.	6
1.5	Emission of different-sized nanocrystals when illuminated with a UV lamp.	7
1.6	Emission and absorption spectra from the same nanocrystal sample. .	7
1.7	(a) Zoom out of CdSe nanocrystals and a (b) zoom in on a few nanocrystals.	8
1.8	Models of (a) wurtzite and (b) rock salt lattices. Image courtesy of Wikipedia commons.	9
1.9	The spherical coordinate system used in this derivation will have ρ as the length of the vector, θ as the latitudinal angle, and ϕ as the azimuthal angle.	10
1.10	For one nanocrystal between a source and a drain, (a) the Fermi energies of all three align at zero voltage. (b) The source Fermi energy is lowered by negative voltage, and (c) raised by a positive voltage.	21
1.11	Multiple excitons are generated by a highly excited exciton relaxing into two lower energy excitons.	25
1.12	For one nanocrystal between a source and a drain, (a) a negative gate raises the nanocrystal energy levels. (b) A positive gate lowers the nanocrystal energy levels.	26

2.1	Chemical structure of DNA.	30
2.2	Restriction enzymes cut DNA leaving either (a) sticky ends or (b) blunt ends.	32
2.3	(a) The original Sanger method and (b) current method for DNA sequencing.	32
2.4	(a) Gel electrophoresis and (b) capillary electrophoresis for DNA fragment separation.	33
2.5	Results of a Sanger sequencing run.	35
2.6	Schematic of polony growth. (a) through (d) represent passing time as the polonies grow and fluoresce.	36
2.7	DNA being voltage-driven through a pore in a membrane.	39
2.8	In a polar solvent, such as water, the lipids arrange into a bilayer with their tails facing inward and their heads facing the solvent.	40
2.9	The bases in (a) a DNA sequence can have different high-Z markers attached to three different nucleotides, which can be identified in TEM. A schematic of this is shown in (b).	43
3.1	Sample chip with metal electrodes and contact pads on silicon nitride substrate.	55
3.2	Poly(methyl methacrylate), known as PMMA, is a long chain polymer that is used as an electron beam resist.	56
3.3	(a) Resist on a substrate is exposed, usually by electrons or photons. After developement, the exposed area (b) is washed away for positive resist or (c) is cross-linked for negative resist.	56
3.4	(a) Electrons can scatter off the substrate causing an undercut in the resist. (b) This can improve liftoff of evaporated metal.	58

3.5 Long and short chain polymer orientation for enhanced (a) liftoff or (b) resolution.	59
3.6 (a) A modified JEOL JSM-6400 SEM and (b) an Elionix ELS-7500EX.	61
3.7 For a negative photoresist, the pattern is black, so that the surrounding area is exposed and crosslinked. For a positive photoresist, the pattern is clear, so that the patterned area is exposed and crosslinked.	63
3.8 Photolithography can cause either an (a) overcut, (b) vertical cut, or (c) undercut.	64
3.9 (a) Dual-tone resist and (b) carefully aligned multiple exposures can increase resolution beyond the traditional limit.	65
3.10 Home-built thermal evaporator used for the work in this thesis.	67
3.11 5 mm x 5 mm chips can be viewed in a TEM using a modified holder.	69
3.12 A nanopore drilled in a silicon nitride membrane using a TEM beam.	69
3.13 (a) A JEOL 2010 TEM and (b) a JEOL 2010F TEM.	70
4.1 (a) A Janis VPF-700 and (b) a Janis ST-100H cryostat.	73
4.2 (a) The liquid nitrogen, chicken-feeder dewar and (b) the radiation shield for the Janis ST-100H cryostat.	74
4.3 Photograph of the removable insert of a cryostat. The top right inset is a close-up of the coldfinger and sample socket, and the bottom right inset is the chip carrier that plugs into the socket.	75
4.4 (a) The cryostat has a quartz window to allow the sample to be seen and exposed to light sources. (b) The optical transmission for the quartz windows of the cryostats.	75
4.5 The electronics used for the cryostats.	76

4.6	The temperature controller connects to the cryostat with a military connector and a two-prong plug. There is a port for a vacuum pump, and liquid nitrogen is added to the bath from the top.	77
4.7	(a) The outer acoustic enclosure for the DNA measurements and (b) the inner Faraday cage that covers the cell and accompanying measurement devices.	79
4.8	Inside the double enclosures, the apparatus includes three HEKA head stages, micromanipulators with probes, and AgCl electrodes. Inset: a close up of the AgCl electrodes.	79
4.9	The HEKA amplifier.	80
4.10	(a) A PDMS cell used for the DNA experiment. (b) A PDMS cell with a chip attached using QuickCast. A small well around the window has also been drawn with QuickCast for the top droplet.	81
4.11	A two-component elastomer is used to seal the chip to the PDMS cell. Once mixed, it solidifies within a minute.	82
5.1	(a) TEM of PbSe nanocrystals. (b) Combined histogram of PbSe diameters.	84
5.2	TEM images of PbSe assembly when the ligand was (a) oleic acid, (b) octylamine, (c) hexylamine, and (d) butylamine.	89
5.3	Histograms of interparticle spacing when the ligand was (a) oleic acid, (b) octylamine, (c) hexylamine, and (d) butylamine.	90
5.4	Combined histograms with the same binning of interparticle spacing when the ligand was oleic acid, octylamine, hexylamine, and butylamine.	91
5.5	TEM of PbSe nanocrystals with a ligand exchange of diaminoheptane and octylamine. The nanocrystals became irregular and aggregated, with no ordered assembly.	91

5.6	(a) TEM of synthesized gold nanocrystals. (b) Histogram of nanocrystal diameters. Each nanocrystal was measured twice, with the two measurements approximately perpendicular to each other.	92
5.7	Cluster of aggregated PbSe particles.	94
5.8	For a longer synthesis, the particles that compose the clusters are more well-defined ellipsoids.	95
6.1	(a) TEM image of the PbSe rods. (b) Absorbance spectrum for the PbSe rods. Images courtesy of Weon-kyu Koh.	99
6.2	CAD schematic of the EBL electrodes. Inset: Close-up of a gap. . . .	100
6.3	(a) TEM image of a gap before cleaning. Small metallic debris left after liftoff is indicated by arrows. (b) TEM image of the same gap after using the TEM beam to clean off the metal.	101
6.4	Background measurements of Gap 1, which has a low background current, at (a) room temperature and (b) 79K. Background measurements of Gap 2, which has a measurable background current, at (c) room temperature and (d) 79K.	103
6.5	Gap 1 IV sweeps of untreated PbSe rods in the dark and with the laser at (a) room temperature and (b) 79K. Gap 2 IV sweeps of untreated PbSe rods in the dark and with the laser at (c) room temperature and (d) 79K.	105
6.6	IV sweeps of Gap 1 with annealed PbSe rods in the dark and with the laser at (a) room temperature and (b) 79K. IV sweeps of Gap 2 with annealed PbSe rods in the dark and with the laser at (c) room temperature and (d) 79K.	106
6.7	Calculated room temperature photocurrent of the annealed PbSe rods.	107

6.8 Calculated (a) dark and (b) photocurrent of the PbSe rods, both untreated and annealed at room temperature.	107
6.9 TEM images of Gap 1 (a) before measurements, zoomed in, and (b) after measurement with PbSe rods, zoomed out.	108
6.10 (a) Electrodes spanned by a large network of PbSe nanorods that showed no current. (b) A gap connected by two nanorods that had no measurable current.	109
6.11 Dark and photocurrent of a flat background gap at (a) room temperature and (b) 79K after the hydrazine treatment. Dark and photocurrent of a nonzero background gap at (c) room temperature and (d) 79K after the hydrazine treatment.	110
6.12 (a) TEM image of Gap 4 after it has blown up after measurement. The red lines indicate the area shown in (b) the close-up of PbSe rod network that most likely contacted the electrodes.	112
 7.1 (a) Schematic of a photodetector nanogap device. (b) TEM of electrodes before nanocrystal deposition. (c) Optical image of a chip. (d) TEM image of the nanocrystals.	115
7.2 (a) Histogram of nanoparticle sizes. (b) Absorption and emission spectra for the nanocrystals studied.	117
7.3 Optical images of (a) an entire chip and (b) a close-up of the window after measurements with annealed nanocrystals.	119
7.4 TEM images of two different nanogaps on the same chip after measurements with nanocrystals annealed at 498K.	120
7.5 Representative IV dark current curves for a bare device and devices with nanocrystals annealed up to 573K, measured at 295K and 78K. .	121
7.6 IV curve for one of the few devices with measurable dark current. .	122

7.7	Arrhenius plot for one of the few devices with measurable dark current.	122
7.8	Photocurrent vs. voltage for CdSe/ZnS nanocrystals in devices where the low-temperature photocurrent is higher (a) or lower (b) than the room-temperature photocurrent.	124
7.9	Photocurrent from three different laser excitation wavelengths. Inset: Absorption and emission intensities vs. wavelength for CdSe/ZnS nanocrystals in solution.	125
7.10	Distribution of photocurrent magnitudes for nanogap devices illuminated with 532 nm light at 295K.	127
7.11	Histograms of R values for nanogap devices illuminated with (a) 532 nm and (b) 650 nm excitation.	127
7.12	Measurements of photocurrent vs. laser intensity (a) before and (b) after a dark voltage treatment of a single nanogap.	128
7.13	Histogram of change in R after different treatments.	129
7.14	Energy level schematic of a nanocrystal device at (a) steady state, (b) after a laser voltage treatment, and (c) after a dark voltage treatment.	131
7.15	Current vs. Intensity at (a) room temperature and (b) 78K.	134
8.1	(a) Transverse sensing concept. (b) Diagram showing a cross-section of a chip. (c) Photograph of an actual chip.	139
8.2	(a-c) Finite element simulations. (d) Diagram of how plots (a-c) are oriented. (e) TEM image of nanoelectrodes with TiO ₂ insulation. (f) Leakage current.	145
8.3	(a) Comparison of pore currents. Ionic data for (b) a SiN pore, (c) a pore with uninsulated electrodes, and (d) a pore with insulated electrodes. (e) Noise power spectral density plots.	148

8.4	Different electrodes shapes were used: (a) electrodes with thin finger-like extensions that had a sharp tip and (b) electrodes with a blunt tip.	149
8.5	(a-d) TEM images of a range of nanopore-nanoelectrode devices. (e) Optical image showing a silicon nitride membrane with twelve pairs of nanoelectrodes.	150
8.6	(a) Membrane rupture due to mechanical shock. (b, c) Ruptures due to electrostatic discharge. (d) Nanoelectrodes gone, even though there is no membrane rupture.	154
9.1	Optical images of (a) a chip with three wires and of (b) the window. TEM images of (c) a chrome oxide wire and (d) a nanopore.	158
9.2	(a) TEM and (b) AFM images of a nanowire and pore surrounded by a crystallized, circular mass of the ALD layer. Image (b) courtesy of Matthew Puster.	159
9.3	Resistance measurements of two wires (a) without treatment and (b) after rapid thermal annealing at 350°C for 10 minutes. The insets in (a) are TEM images of the wires and the scales bars are 50 nm.	161
9.4	(a) IV Sweep of the same nanopore. Inset: A TEM image of the nanopore with a scale bar of 2 nm. Ionic time traces of the same nanopore (b) before DNA is added and (c) after DNA is added.	163
9.5	(a) Histogram of the blocked current with a three gaussian fit. (b) The fit with the collision peak removed. Inset: Scatter plot of event length vs the median blocked current for each event.	164
9.6	(a) When measuring in solution, the gold wires tend to react with the solution and dissolve. (b) It is very common for the nanowires to blow up before it can be measured.	165

CHAPTER 1

Introduction to Nanocrystals

1.1 What are nanocrystals?

Nanocrystals are crystalline materials that are on the order of nanometers, which are billionths of a meter, see Figure 1.1 for an example. Due to their small size, their properties may differ significantly from bulk material. Some properties can be tuned by changing their shape and size, which is often easily achievable through controllable chemical synthesis. Other chemical treatments can be used to further tune their properties. Due to their great tunability and novel properties, nanocrystals are of great interest for a number of devices such as light emitting diodes, biological tags, solar cells, and even medical treatments.

Semiconductor nanocrystals are specifically of interest due to their device applications. Among their more useful properties, many fluoresce in a wide range of wavelengths, conduct current when illuminated, and assemble in an ordered manner. The most common nanocrystals are made of two materials: the first often being lead (Pb), cadmium (Cd), or zinc (Zn), and the second material often being sulfur (S), tellurium (Te), or selenium (Se). They can also be synthesized in many different shapes including spheres, rods, stars, and tetrapods, among others.^{1–5} In addition to the core material, nanoparticles can also have shells of other materials and various ligands covering the surface.^{6–8} These ligands can be exchanged, which can change solubility and interparticle spacing. The different parameters must be tuned to maximize their usefulness for different applications.

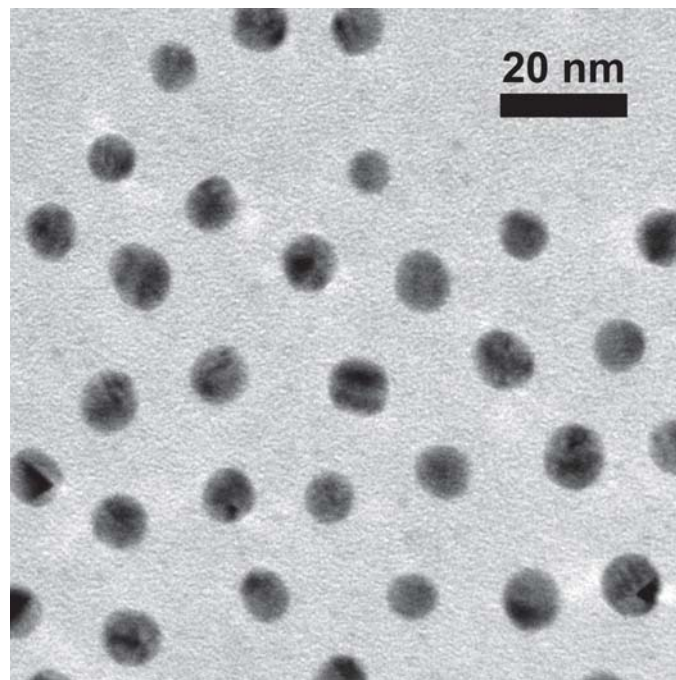


Figure 1.1: Transmission electron micrograph (TEM) of gold nanocrystals.

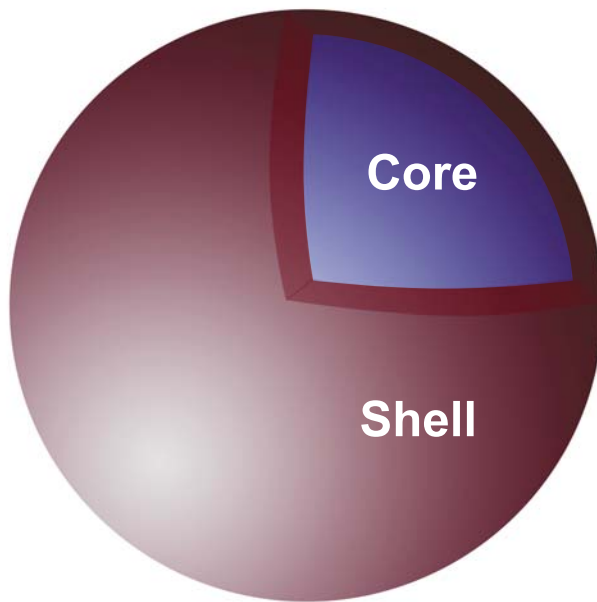


Figure 1.2: Schematic of a core/shell nanocrystal.

1.2 Synthesis

One important discovery was the process to fabricate semiconductor nanocrystals easily with high monodispersity, $\sigma \leq 5\%$, using inexpensive solution-based chemistry. One of the most popular and most versatile is the hot-injection method.⁹ A typical process for synthesizing semiconducting nanoparticles is to have a fast injection of precursors into a hot coordinating solvent, see Figure 1.3. Original methods used dimethyl cadmium, though greener, less flammable methods were later developed.¹⁰ For example, to synthesize CdSe particles, cadmium oxide (CdO), trioctylphosphine oxide (TOPO), and tetradecylphosphonic acid (TDPA) are combined in a three-neck flask, attached to a Schlenk line with inert gas. This is heated to 300°C while stirring, until the red CdO powder dissolves, and the solution becomes clear. This means that the Cd has formed a complex with the ligands. A room temperature solution of Se dissolved in trioctylphosphine (TOP) is quickly injected. To stop the reaction, the heat source is removed, and a solvent such as methanol may be added to further quench the reaction.

Size and shape can be controlled by changing the reaction time, temperature, concentration of precursors, ligands, and coordinating solvent. The fast injection into a hot solution begins a nucleation of homogenously sized crystals. When precursors are plentiful, smaller particles grow faster because their smaller surface area requires less atoms to increase the radius by a monolayer. This causes size focusing, which increases monodispersity. However, once the precursors become depleted, Ostwald ripening can occur as larger particles grow at the expense of smaller particles.¹¹ This occurs because a smaller volume to surface area ratio is less energetically favorable.

CdSe quantum dots can often have low quantum yields, or fluorescence, which was a challenge for most applications. However, the addition of a shell, such as ZnS, passivates surface traps, and if the material has a wider bandgap, excitons are

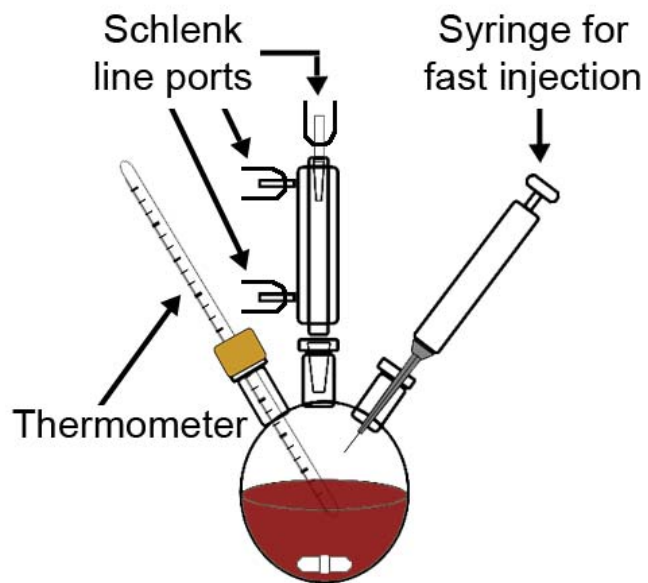


Figure 1.3: Schematic of a nanocrystal synthesis: Typically, a three-neck flask with a coordinating solvent is heated and stirred under inert gas and with the temperature carefully monitored. A fast injection of a precursor initiates the nanocrystal growth.

further confined, see Figure 1.2.^{8,12} Note that lattice mismatch may cause strain and create charge traps, which are areas where charge can be localized and prevented from moving freely.¹³ A sample synthesis uses CdSe nanocrystals, heated to 300°C, then slowly adding a solution of Zn and S in TOP. This injection can be added dropwise and with multiple injections.

The ligands that cap the nanocrystals provide passivation of surface traps, control the growth rate, prevent agglomeration in solution, and allow solubility in different solvents.¹⁴ The ligand-nanocrystal interaction is dynamic, with ligands adhering to the surface, and desorbing regularly. While ligands are necessary for the synthesis, they can be a hindrance to electrical measurements, since they are often insulating and long. However, ligand exchange, washing, and annealing can be used to mitigate their role as barriers to conduction.^{15–20}

1.3 Characterization

Spectroscopy is a widely-used method of nanocrystal characterization because the absorption and emission peak of nanocrystals are strongly size-dependent.^{21,22} The absorption, A , is given by

$$A = -\log_{10} \left(\frac{I}{I_0} \right) \quad (1.1)$$

where I is the intensity of the sample and I_0 is the intensity of the reference. The absorption can also be used to find the concentration, c , if the molar absorptivity, ε , and the path length, ℓ , that the light travels is known:

$$A = \varepsilon c \ell. \quad (1.2)$$

See Figure 1.4 for sample spectra of different sized nanocrystals. The absorp-

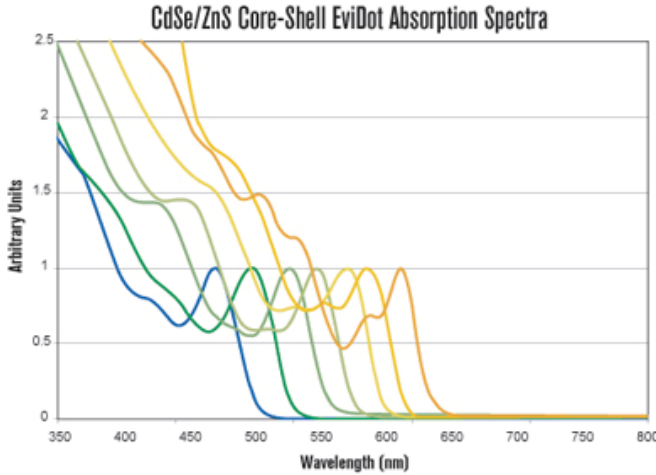


Figure 1.4: Absorption spectra of different-sized nanocrystals. The larger their diameter, the redder their absorption peak is. Image courtesy of EviDot.

tion redshifts as the nanocrystal diameter increases. Similarly, the emission of the nanocrystals is also dependent on size, see Figure 1.5. When light is absorbed by a nanocrystal, an exciton, or an electron-hole pair, can form, which can recombine radiatively. Note that due to the Stokes shift, the emission of a nanocrystal is redshifted from the absorption peak, see Figure 1.6, usually due to loss of heat energy. The highest energy absorption peak we see is from the “first exciton” state, which also gives rise to the emission peak, and is the $1S_{\frac{3}{2}}\text{-}1S_e$ transition.²² For high quality samples, other peaks may appear in the absorption spectra that represent other transitions, which can be observed in Figure 1.4. However, these do not cause a significant number of radiative recombinations. The width of the peaks is another measure of the quality, since poor monodispersity will broaden the peaks.

In addition to optical techniques, electron microscopy is often used to characterize nanocrystal size, since spectroscopy can be affected by other elements such as shape, air exposure, and traps. For example, in the TEM image in Figure 1.7a, one can see that nanocrystals are sometimes not perfectly round. You can also examine the



Figure 1.5: Emission of different-sized nanocrystals when illuminated with a UV lamp. The larger their diameter, the redder their emission is. Image courtesy of Claudia Querner.

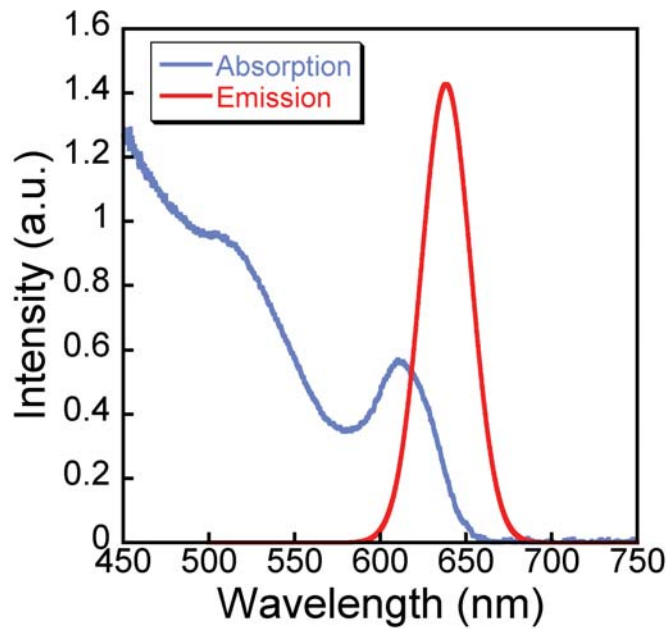


Figure 1.6: Emission and absorption spectra from the same nanocrystal sample. The emission peak is usually red-shifted from the absorption peak.

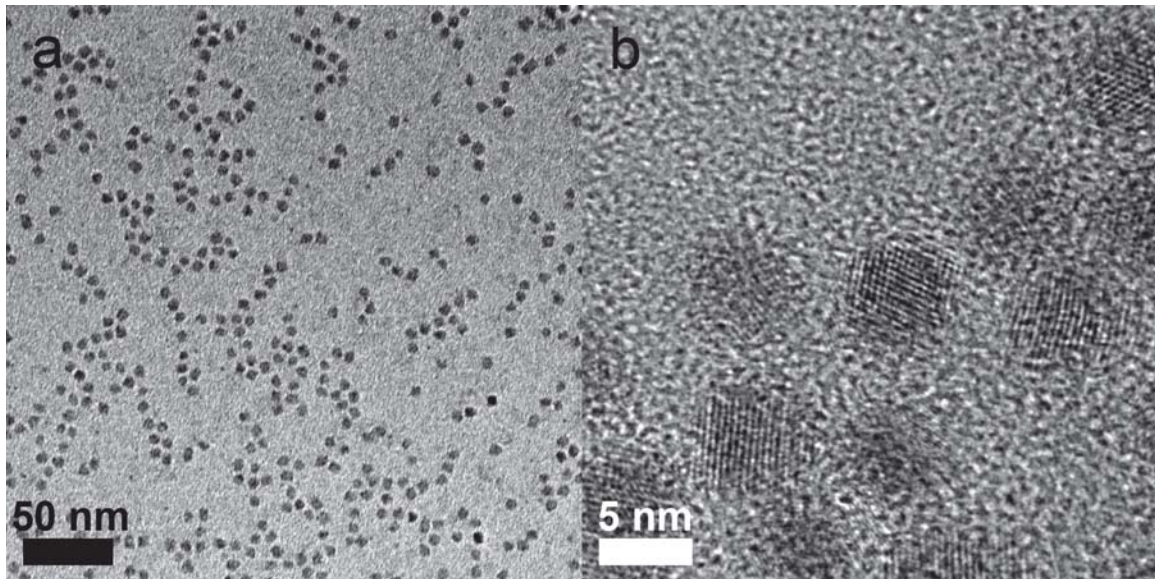


Figure 1.7: (a) Zoom out of CdSe nanocrystals and a (b) zoom in on a few nanocrystals.

crystallinity of the nanocrystals, as in Figure 1.7b. CdSe is usually a wurtzite lattice, and PbSe is usually rock salt, seen Figure 1.8.

1.4 Quantum Confinement

Nanocrystals have been referred to as “artificial atoms,” because just like atoms, they have discrete energy levels and have discrete numbers of electrons.²³ The energy required to add charge to a nanocrystal is inversely related to its size.²⁴ The energy level spacing for semiconducting nanoparticles is proportional to a^2 where a is the radius of the nanocrystal. This can be shown by approximating a charge in a nanocrystal as a particle in an spherical box surrounded by an infinite potential.

In the simplest case, the Hamiltonian for a nanocrystal approximated as a uniform

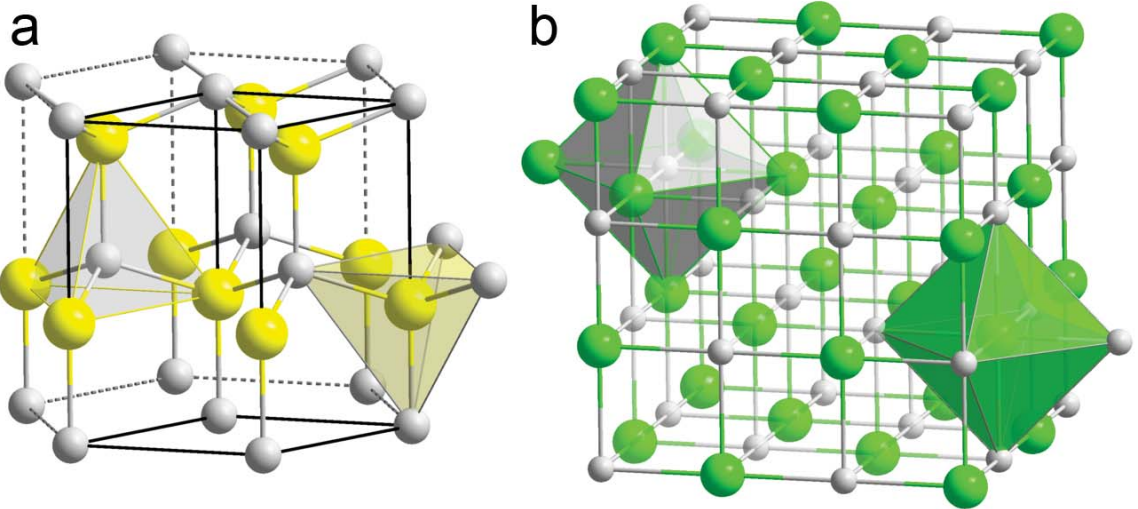


Figure 1.8: Models of (a) wurtzite and (b) rock salt lattices. Image courtesy of Wikipedia commons.

sphere with mass m and a radius of a is given by

$$\mathcal{H} = \frac{\mathcal{P}^2}{2m} + V(\rho) \quad (1.3)$$

where $V(\rho)$ is the potential

$$V(\rho) = \begin{cases} 0, & \rho < a \\ \infty, & \rho > a \end{cases} \quad (1.4)$$

using the coordinate system shown in Figure 1.9. The Schrodinger equation, $\mathcal{H}\Psi = E\Psi$, becomes

$$\left\{ -\frac{\hbar^2}{2m\rho^2} \frac{\partial}{\partial\rho} \left(\rho^2 \frac{\partial}{\partial\rho} \right) - \frac{\hbar^2}{2m\rho^2} \left[\frac{1}{\sin\phi} \frac{\partial}{\partial\phi} \left(\sin\phi \frac{\partial}{\partial\phi} \right) + \frac{1}{\sin^2\phi} \frac{\partial^2}{\partial\theta^2} \right] + V(\rho) \right\} \Psi(\rho, \theta, \phi) = E\Psi(\rho, \theta, \phi) \quad (1.5)$$

in spherical coordinates.

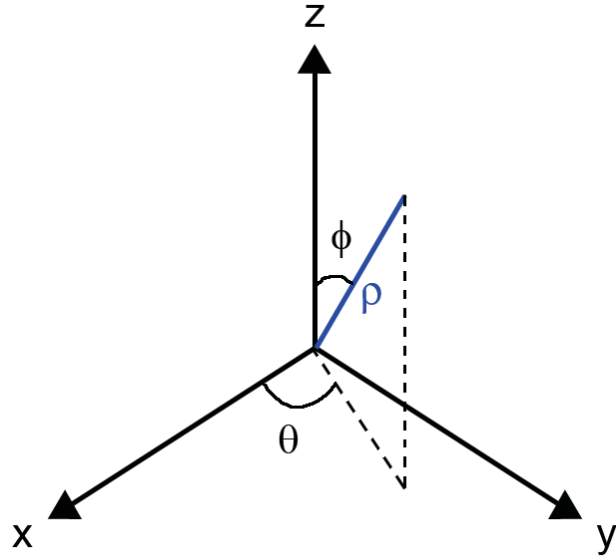


Figure 1.9: The spherical coordinate system used in this derivation will have ρ as the length of the vector, θ as the latitudinal angle, and ϕ as the azimuthal angle.

Using separation of variables, we guess that the solution to the Schrodinger equation is a radial part, $R(\rho)$, multiplied by a spherical part, $Y(\theta, \phi)$,

$$\Psi = R(\rho) Y(\theta, \phi). \quad (1.6)$$

This separates Equation 1.5 into

$$\frac{1}{R} \frac{d}{d\rho} \left(\rho^2 \frac{dR}{d\rho} \right) - \frac{2m\rho^2}{\hbar^2} [V(\rho) - E] = \lambda \quad (1.7)$$

and

$$\frac{1}{Y \sin \phi} \frac{\partial}{\partial \phi} \left(\sin \phi \frac{\partial Y}{\partial \phi} \right) + \frac{1}{Y \sin^2 \phi} \frac{\partial^2 Y}{\partial \theta^2} = -\lambda \quad (1.8)$$

$$\frac{1}{\sin \phi} \frac{\partial}{\partial \phi} \left(\sin \phi \frac{\partial Y}{\partial \phi} \right) + \frac{1}{\sin^2 \phi} \frac{\partial^2 Y}{\partial \theta^2} = -\lambda Y, \quad (1.9)$$

where λ is a constant. We see that 1.9 is equivalent to

$$L^2 Y = \ell(\ell + 1), \quad (1.10)$$

where L^2 is the square of the total angular momentum operator and ℓ is the quantum number associated with it. This means that

$$\lambda = \ell(\ell + 1). \quad (1.11)$$

We know that the solution to this equation will involve the associated Legendre polynomials, and since L^2 commutes with \mathcal{H} , these will be part of the final wavefunction. However, let us continue with the derivation. We can use separation of variables again on Equation 1.9 by assuming that the solution takes the form

$$Y(\theta, \phi) = \Theta(\theta) \Phi(\phi). \quad (1.12)$$

Equation 1.9 becomes

$$\frac{1}{\Theta(\theta)} \frac{d^2\Theta}{d\theta^2} = -m^2 \quad (1.13)$$

$$\frac{d^2\Theta}{d\theta^2} = -m^2 \Theta(\theta) \quad (1.14)$$

and

$$\lambda \sin^2 \phi + \frac{\sin \phi}{\Phi} \frac{d}{d\phi} \left(\sin \phi \frac{d\Phi}{d\phi} \right) = m^2 \quad (1.15)$$

$$\frac{1}{\sin \phi} \frac{d}{d\phi} \left(\sin \phi \frac{d\Phi}{d\phi} \right) + \left(\frac{m^2}{\sin^2 \theta} - \lambda \right) \Phi = 0, \quad (1.16)$$

where m is a constant. We notice that Equation 1.16 is equivalent to

$$L_z^2 \Theta(\theta) = m^2 \Theta(\theta), \quad (1.17)$$

where L_z is the operator for the angular momentum in the z -direction and m is its quantum number. Again, since L_z commutes with the Hamiltonian, \mathcal{H} , we can choose eigenfunctions such that they are eigenfunctions of both L_z and the Hamiltonian. Thus,

$$\Theta(\theta) = \frac{1}{\sqrt{2\pi}} e^{-im\theta}, \quad (1.18)$$

where m is an integer, given the periodic boundary conditions.

Rather than solving Equation 1.16, let us follow the derivation similar to that of Shankar²⁵ and Sakurai.²⁶ First, we examine the effect of the lowering operator, L_- , on the angular solution of the Schrodinger equation, Y_ℓ^m . We know that $-\ell \leq m \leq \ell$, thus, let us set $m = -\ell$:

$$0 = L_- Y_\ell^{-\ell} \quad (1.19)$$

$$= \left(i \frac{\partial}{\partial \phi} - \cot \phi \frac{\partial}{\partial \theta} \right) Y_\ell^{-\ell} \quad (1.20)$$

$$= \left(\frac{\partial}{\partial \phi} - \ell \cot \phi \right) \Phi(\phi) \quad (1.21)$$

$$\frac{d\Phi}{d\phi} = \ell \frac{d(\sin \phi)}{\sin \phi}. \quad (1.22)$$

We can integrate Equation 1.22 directly to get

$$\log \Phi = \ell \log \sin \phi + C \quad (1.23)$$

$$\Phi = C \sin^\ell \phi, \quad (1.24)$$

where C is a normalization constant. Combining Equations 1.18 and 1.24, we get

$$Y_\ell^{-\ell}(\theta, \phi) = C \sin^\ell \phi e^{-i\ell\theta}. \quad (1.25)$$

To find the normalization constant, we integrate $|Y_\ell^{-\ell}|^2$ over θ and ϕ , which must equal unity.

$$1 = \int_0^{2\pi} \int_{-1}^1 |Y_\ell^{-\ell}| d(\cos \phi) d\theta \quad (1.26)$$

$$= \int_0^{2\pi} \int_{-1}^1 |C|^2 \sin^{2\ell} \phi d(\cos \phi) d\theta \quad (1.27)$$

$$= 2\pi |C|^2 \int_{-1}^1 \sin^{2\ell} \phi d(\cos \phi). \quad (1.28)$$

Using the substitution

$$t = \cos^2 \phi \quad (1.29)$$

$$dt = 2 \cos \phi d(\cos \phi), \quad (1.30)$$

Equation 1.28 becomes

$$1 = \pi |C|^2 \int_1^1 t^{-\frac{1}{2}} (1-t)^\ell dt \quad (1.31)$$

$$= 2\pi |C|^2 \int_0^1 t^{-\frac{1}{2}} (1-t)^\ell dt. \quad (1.32)$$

Equation 1.32 is the Beta function,

$$B(x, y) = \int_0^1 t^{m-1} (1-t)^{n-1} dt \quad (1.33)$$

$$= \frac{\Gamma(m)\Gamma(n)}{\Gamma(m+n)}, \quad (1.34)$$

where $m = \frac{1}{2}$ and $n = \ell + 1$. Now, Equation 1.32 becomes

$$B\left(\frac{1}{2}, \ell + 1\right) = \frac{\Gamma\left(\frac{1}{2}\right)\Gamma(\ell + 1)}{\Gamma\left(\ell + \frac{3}{2}\right)}. \quad (1.35)$$

We recall that the Gamma function is defined as

$$\Gamma(n) = \begin{cases} (n-1)!, & n \in \mathbb{N} \\ \frac{1 \cdot 3 \cdot 5 \cdots (n-\frac{1}{2})\sqrt{\pi}}{2^{n-\frac{1}{2}}}, & n \in \frac{\mathbb{N}^+}{2}. \end{cases} \quad (1.36)$$

Then Equation 1.35 becomes

$$B = \frac{\sqrt{\pi}(\ell!)^2}{\left[\frac{1 \cdot 3 \cdot 5 \cdots (2\ell+1)\sqrt{\pi}}{2^{2\ell+1}}\right]} \quad (1.37)$$

$$= \frac{2^{2\ell+1}(\ell!)^2}{(2\ell+1)!}. \quad (1.38)$$

Substituting Equation 1.38 into Equation 1.32, we are left with

$$1 = 2\pi |C|^2 \frac{2^{2\ell+1}(\ell!)^2}{(2\ell+1)!} \quad (1.39)$$

$$|C|^2 = \frac{(2\ell+1)!}{4\pi [2^\ell (\ell!)^2]} \quad (1.40)$$

$$C = \frac{1}{2^\ell (\ell!)} \sqrt{\frac{(2\ell+1)}{4\pi}}. \quad (1.41)$$

Thus, $Y_\ell^{-\ell}(\theta, \phi)$ is given by

$$Y_\ell^{-\ell}(\theta, \phi) = \frac{1}{2^\ell (\ell!)} \sqrt{\frac{(2\ell+1)}{4\pi}} \sin^\ell \phi e^{-\ell\theta}. \quad (1.42)$$

Now, we can use the raising operator $\ell + m$ times on $Y_\ell^{-\ell}(\theta, \phi)$ to find $Y_\ell^m(\theta, \phi)$.

Given that

$$L_+ Y_\ell^m = \hbar \sqrt{(\ell - m)(\ell + m + 1)} Y_\ell^{m+1}, \quad (1.43)$$

we find that

$$Y_\ell^m(\theta, \phi) = \frac{1}{\hbar\sqrt{(\ell+m)[\ell-(m-1)]}} \frac{1}{\hbar\sqrt{(\ell+m-1)[\ell-(m-2)]}} \cdots \frac{1}{\hbar\sqrt{(2)[\ell-(-\ell+1)]}} \\ \times \frac{1}{\hbar\sqrt{(1)[\ell-(-\ell)]}} \left[\hbar e^{i\theta} \left(\frac{\partial}{\partial\phi} + i \cot\phi \frac{\partial}{\partial\theta} \right) \right]^{\ell+m} Y_\ell^{-\ell}(\theta, \phi) \quad (1.44)$$

$$= e^{i(\ell+m)\theta} \sqrt{\frac{(\ell-m)!}{(2\ell)!(\ell+m)!}} \left(\frac{\partial}{\partial\phi} + i \cot\phi \frac{\partial}{\partial\theta} \right)^{\ell+m} \left[\frac{1}{2^\ell (\ell!)} \sqrt{\frac{(2\ell+1)}{4\pi}} \sin^\ell \phi e^{-i\ell\theta} \right] \quad (1.45)$$

$$= \frac{e^{im\theta}}{2^\ell \ell!} \sqrt{\frac{(2\ell+1)(\ell-m)!}{4\pi(\ell+m)!}} \left[\frac{d}{d\phi} - (m-1) \cot\phi \right] \left[\frac{d}{d\phi} - (m-2) \cot\phi \right] \cdots \\ \times \left[\frac{d}{d\phi} - (\ell-1) \cot\phi \right] \left[\frac{d}{d\phi} - (\ell) \cot\phi \right] \sin^\ell \phi. \quad (1.46)$$

If we observe that

$$\left(\frac{d}{d\phi} + k \cot\phi \right) = \frac{1}{\sin^k \phi} \frac{d(\sin^k \phi)}{d\phi}, \quad (1.47)$$

Equation 1.46 becomes

$$Y_\ell^m(\theta, \phi) = \frac{e^{im\theta}}{2^\ell \ell!} \sqrt{\frac{(2\ell+1)(\ell-m)!}{4\pi(\ell+m)!}} \left[\frac{1}{\sin^{-(m-1)} \phi} \frac{d(\sin^{-(m-1)} \phi)}{d\phi} \right] \\ \times \left[\frac{1}{\sin^{-(m-2)} \phi} \frac{d(\sin^{-(m-2)} \phi)}{d\phi} \right] \cdots \left[\frac{1}{\sin^{-(\ell-1)} \phi} \frac{d(\sin^{-(\ell-1)} \phi)}{d\phi} \right] \\ \times \left(\frac{1}{\sin^{-\ell} \phi} \frac{d(\sin^{-\ell} \phi)}{d\phi} \right) \sin^\ell \phi \quad (1.48)$$

$$= \frac{\sin^m \phi e^{im\theta}}{2^\ell \ell!} \sqrt{\frac{(2\ell+1)(\ell-m)!}{4\pi(\ell+m)!}} \left(\frac{1}{\sin \phi} \frac{d}{d\phi} \right)^{\ell+m} \sin^{2\ell} \phi \quad (1.49)$$

$$= \frac{\sin^m \phi e^{im\theta}}{2^\ell \ell!} \sqrt{\frac{(2\ell+1)(\ell-m)!}{4\pi(\ell+m)!}} \left(-\frac{d}{d(\cos \phi)} \right)^{\ell+m} \sin^{2\ell} \phi. \quad (1.50)$$

If we use the substitution

$$x = \cos \phi \quad (1.51)$$

$$dx = d(\cos \phi), \quad (1.52)$$

we get

$$Y_\ell^m(\theta, \phi) = \frac{(-1)^{\ell+m} e^{im\theta}}{2^\ell \ell!} \sqrt{\frac{(2\ell+1)(\ell-m)!}{4\pi (\ell+m)!}} (1-x^2)^{\frac{m}{2}} \frac{d^{\ell+m}}{d^{\ell+m}} (1-x^2)^{2\ell} \quad (1.53)$$

$$= \frac{(-1)^m e^{im\theta}}{2^\ell \ell!} \sqrt{\frac{(2\ell+1)(\ell-m)!}{4\pi (\ell+m)!}} P_\ell^m(\cos \phi), \quad (1.54)$$

where $P_\ell^m(\cos \phi)$ is the associated Legendre polynomial. The functions $Y_\ell^m(\theta, \phi)$ are known as the spherical harmonics.

Now that the angular dependence of the Schrodinger equation has been solved, we will focus on the radial part. Using Equation 1.11 and rearranging variables, Equation 1.7 becomes

$$\rho^2 \frac{d^2 R}{d\rho^2} + 2\rho \frac{dR}{d\rho} - \left\{ \frac{2m\rho^2}{\hbar^2} [V(\rho) - E] - \ell(\ell+1) \right\} = 0. \quad (1.55)$$

Looking at the case $\rho < a$, we know $V = 0$, which gives

$$\rho^2 \frac{d^2 R}{d\rho^2} + 2\rho \frac{dR}{d\rho} + [\kappa^2 \rho^2 - \ell(\ell+1)] R = 0, \quad (1.56)$$

where

$$\kappa = \frac{\sqrt{2mE}}{\hbar}. \quad (1.57)$$

Using the substitution

$$x = \kappa\rho \quad (1.58)$$

$$x \frac{dR}{dx} = \rho \frac{dR}{d\rho}, \quad (1.59)$$

Equation 1.56 becomes

$$x^2 \frac{d^2 R}{dx^2} + 2x \frac{dR}{dx} + [x^2 - \ell(\ell + 1)] R = 0, \quad (1.60)$$

which we know has the solution of a linear combination of the ℓ th order spherical Bessel functions, j_ℓ and y_ℓ . Because the solution must be defined at $r = 0$, the solutions with y_ℓ are discarded. $\kappa\rho$ for $\rho = a$ must satisfy

$$\kappa a = \beta_{n\ell}, \quad (1.61)$$

where $\beta_{n\ell}$ is the n th zero of the ℓ th order spherical Bessel function.

Thus, the final form of Ψ is

$$\Psi_{n\ell m}(\rho, \theta, \phi) = C_{n\ell} j_\ell \left(\frac{\beta_{n\ell} \rho}{a} \right) Y_\ell^m(\theta, \phi), \quad (1.62)$$

where $C_{n\ell}$ is a normalization constant. From Equations 1.57 and 1.61 the energy of the particle is given by

$$E_{n\ell} = \frac{\hbar^2 \beta_{n\ell}^2}{2ma^2}. \quad (1.63)$$

The wavefunctions are atomic-like orbitals, and note that the quantum number ℓ may be represented by the orbital name, e.g., s , p , d , f , etc. The dependence on the size of the nanocrystal scales as $\frac{1}{a^2}$, suggesting that size plays an important part in determining nanocrystal properties.

However, this is not the whole picture because nanocrystals are crystalline rather than empty. Following the derivation by Norris,²⁷ we will now recall Bloch's theorem that the wavefunctions in a lattice can be written as

$$\Psi_{nk}(\vec{r}) = u_{nk}(\vec{r}) e^{i\vec{k}\cdot\vec{r}}, \quad (1.64)$$

where n is the band number, k is the wave number, and u_{nk} depends on the period of the lattice. Now, the potential must obey

$$V(x+a) = V(x). \quad (1.65)$$

For a direct gap semiconductor, such as the Cd and Pb salts, the band minimum/maximum occurs at $k = 0$. Using the effective mass approximation, the energy of a conduction band, c , is given by

$$E_{c,k} = \frac{\hbar^2 k^2}{2m_c^*} + E_g \quad (1.66)$$

and the energy of a valence band, v , is given by

$$E_{v,k} = -\frac{\hbar^2 k^2}{2m_v^*}, \quad (1.67)$$

where m^* is the effective mass and E_g is the bandgap. The effective mass is not an actual mass, but is instead a mathematical tool to approximate the complicated potentials felt by the particle in the lattice. The electrons and holes can be mathematically treated like free particles with a different mass. “Light” and “heavy” holes are sometimes used to describe holes that have high and low band curvature near the center of the Brillouin zone.²⁸ We will now use the envelope function approximation, which is acceptable if the lattice spacing of the nanocrystal is small compared to the scale of the variance of the non-periodic potential, in this case the nanocrystal size.²⁹

The wavefunction for a single particle can now be described by a linear combination of Bloch functions, $u_{nk}(\vec{r})$:

$$\Psi_{sp}(\vec{r}) = \sum_k C_{nk} u_{nk}(\vec{r}) e^{i\vec{k}\cdot\vec{r}}, \quad (1.68)$$

where C_{nk} are coefficients that force the sum to satisfy the nanocrystal boundary conditions. If we assume that the Bloch functions only weakly depend on k ,²⁷ they can be removed from the sum, and the wavefunction is now given by

$$\Psi_{sp}(\vec{r}) = u_n(\vec{r}) \sum_k C_{nk} e^{i\vec{k}\cdot\vec{r}}. \quad (1.69)$$

The form of this equation is now a periodic part, $u_n(\vec{r})$, and an envelope function. $u_n(\vec{r})$ can be solved using the tight-binding approximation

$$u_n(\vec{r}) \approx \sum_i C_{nk} \phi_n(\vec{r} - \vec{r}_i), \quad (1.70)$$

where i is the lattice site and n is the conduction band for electrons and the valence band for holes. The envelope function in Equation 1.69 is the spherical potential representing the spherical nanocrystal, and the wavefunctions are given by Equation 1.62.

Thus, the wave function for an electron-hole pair is

$$\Psi_{e-h} = C_{c,n_e,\ell_e,m_e}^{v,n_h,\ell_h,m_h} \left[u_c j_{\ell_e} \left(\frac{\beta_{n_e \ell_e} \rho_e}{a} \right) Y_{\ell_e}^{m_e}(\theta, \phi) \right] \left[u_v j_{\ell_h} \left(\frac{\beta_{n_h \ell_h} \rho_h}{a} \right) Y_{\ell_h}^{m_h}(\theta, \phi) \right] \quad (1.71)$$

with energies

$$E_{n_e, \ell_e, n_h, \ell_h} = E_g + \frac{\hbar^2}{2a^2} \left(\frac{\phi_{n_h \ell_h}^2}{m_v^*} + \frac{\phi_{n_e \ell_e}^2}{m_c^*} \right). \quad (1.72)$$

However, we have still ignored the Coulombic potential between the hole and the

electron. Since the confinement energy scales as $\frac{1}{a^2}$ and the Coulombic energy will scale as $\frac{1}{a}$, the confinement term will dominate. This occurs when the confinement is strong, so the radius of the nanocrystal is much smaller than the Bohr radii of the hole, electron, and exciton. The Bohr radius of a particle, a_p^B , is

$$a_p^B = \varepsilon \frac{m_e}{m_p} a_0, \quad (1.73)$$

where m_e is the rest mass of an electron, m_p is the mass of the particle, and a_0 is the Bohr radius of hydrogen, a_0^B , which is

$$a_0^B = \frac{4\pi\varepsilon_0\hbar^2}{m_e e^2}, \quad (1.74)$$

where ε_0 is the permittivity of free space, and e is the elementary charge.³⁰ The exciton Bohr radius for CdSe is 4.8 nm.³¹ The Bohr radius is 46 nm for PbSe, and the hole and electron Bohr radii for PbSe is 23 nm.³²

1.5 Transport Measurements

For measurements in this thesis, typically electrode pairs are fabricated as the source and drain, and nanoparticles are deposited between them. Dark current is then measured while applying a voltage in the dark, and photocurrent is measured while illuminating the sample. Semiconductors are usually either n-type or p-type, though some are both, called ambipolar. An n-type material transports electrons, and a p-type material transports holes. An example of an ambipolar material is graphene, or a single sheet of carbon atoms arranged in a hexagonal lattice. Some material can also change type due to a treatment; one such material is PbSe. Untreated PbSe nanocrystals with an oleic acid ligand are n-type. However, when treated with

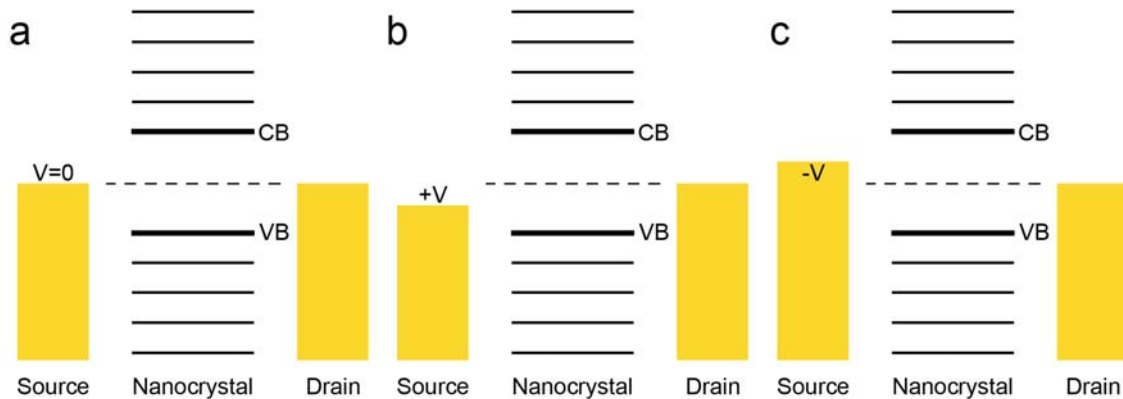


Figure 1.10: For one nanocrystal between a source and a drain, (a) the Fermi energies of all three align at zero voltage. (b) The source Fermi energy is lowered by negative voltage, and (c) raised by a positive voltage.

hydrazine, they become p-type.¹⁸ At zero voltage, the Fermi energies of the source, drain, and nanoparticle should be aligned, see Figure 1.10a for a schematic with one nanocrystal. A positive source drain bias lowers the Fermi energy, while a negative source drain bias raises the Fermi energy of the source, see Figure 1.10b and c.²⁸ Holes travel “up” and electrons fall “down” in energy diagrams.

Other factors can affect nanocrystal transport. The organic ligands that surround the nanocrystal can be extremely insulating. Not only are their ligands on the nanocrystals, but excess ligand from the solution they are dropcast from is also a factor. Several methods have been developed to mitigate this. Washing a sample, often with an alcohol, can suspend some of the ligands, and then the washing liquid can be soaked up or vacuumed away. Similarly, the current ligand can be exchanged with a shorter one.^{15,17,19,20} Annealing has also proven to be an effective method of breaking down ligands.^{16,18,33–35} Both of these methods have also been shown to decrease the interparticle spacing, which increases conduction. Other ways to increase conduction include the addition of chemical crosslinkers^{18,36,37} and using multiple materials to encourage exciton separation.

1.5.1 Transport through Films

Conduction in films of nanocrystals, sometimes called nanocrystal solids, are widely studied. Films can consist of sub-monolayers, monolayers, multilayers, or combinations thereof. Assuming the charge carriers within the nanocrystals are strongly confined, transport is limited by charge transfer between nanocrystals and not by transport within a nanocrystal.³⁸ However, traps, both in the core and on the surface of the nanocrystal, can affect transport by localizing the charge carriers. Previously, we had examined nanocrystals as an infinite potential well, though in practice, there is a finite barrier between nanocrystals that charge carriers may tunnel through. This barrier can be affected by interparticle spacing, chemical cross-linkers or ligands, and shells.

One important model for understanding nanocrystal film conduction is the percolation model. At $T = 0$, Middleton and Wingreen³⁹ found that the current, I , was a power law with voltage, V :

$$I \sim \left(\frac{V}{V_T} - 1 \right)^\zeta, \quad (1.75)$$

where V_T is the voltage threshold; for a 1D array, $\zeta = 1$, and for a 2D array, $\zeta = \frac{5}{3}$. For finite T , the system is modeled assuming some number of ohmic junctions that percolate across the array; Equation 1.75 holds until a crossover T^* , the temperature at which a continuous path of junctions is formed with only negligible Coulomb blockade.⁴⁰ However, V_T decreases linearly with T ,

$$V_T(T) = V_T(0) \left[1 - \frac{p(T)}{p_c} \right], \quad (1.76)$$

where $V_T(0)$ is the threshold voltage at $T = 0$, $p(T)$ is the fraction of junctions that act as linear resistors, and p_c is the percolation threshold for the lattice.⁴⁰ However, above T^* , the conductivity, σ , has an Arrhenius-like dependence on temperature,

T :^{41–43}

$$\sigma(T) = \sigma_0 e^{-\frac{E_A}{k_B T}}, \quad (1.77)$$

where σ_0 is a constant, E_A is the activation energy, and k_B is the Boltzmann constant. This activation energy can be approximated by low-field carrier generation in a granular metal film,

$$E_A = \frac{e^2}{8\pi\varepsilon\varepsilon_0} \left(\frac{1}{r} - \frac{1}{r+d} \right), \quad (1.78)$$

where e is the elementary charge, ε is the relative permittivity of the material the particles are in, r is the radius of the particles, and d is the interparticle spacing.⁴⁴ Note that for non-uniform particles, the dependence goes as $\sigma \sim T^{-\frac{1}{2}}$.⁴⁴

Another popular model for nanocrystal film conduction is variable range hopping (VRH), first proposed by Mott,⁴⁵ which states that electrons will try to find the lowest activation energy, E_A , and shortest hopping distance. The probability at zero bias is given by

$$P \sim e^{-\frac{2r}{d} - \frac{E_A}{k_B T}}, \quad (1.79)$$

where r is the optimal hopping distance and d is the diameter of the nanocrystals; Maximizing P , the conductance, σ , was found to scale as

$$\sigma \sim e^{-\left(\frac{T_M}{T}\right)^\nu}, \quad (1.80)$$

where T_M is the characteristic temperature, and $\nu = \frac{1}{D+1}$ where D is the dimensionality of the system.⁴⁵ This is known as Mott variable range hopping (M-VRH). However, this model failed to consider the long-range Coulomb interactions. Efros and Shklovskii⁴⁶ found that $\nu = \frac{1}{2}$ for both 2D and 3D systems, rather than $\nu = \frac{1}{3}$ and $\nu = \frac{1}{4}$ with only M-VRH; their model is known as ES-VRH. Above the critical

temperature,

$$T_C = \frac{e^4 d g_0}{k_B (4\pi\varepsilon\varepsilon_0)^2}, \quad (1.81)$$

where g_0 is the density of states, the Coulomb effect is negligible and M-VRH is observed; below T_C , ES-VRH is observed.⁴⁷

1.5.2 Carrier Generation

Dark current, current generated without photoexcitation, is a flow of electrons injected from electrodes into the nanocrystal film. Since the electrode-ligand-nanocrystal interface can be treated as a metal-insulator-semiconductor interface, injected electrons near or below the Fermi level of the metal must tunnel into the conduction band of the electrons.³⁸ Low work function metals are more efficient than high work function materials at injecting electrons into the film.⁴³ Photocurrent can be observed when light is applied to a nanocrystal film, and a drain-source bias is applied to discourage recombination of the photogenerated exciton. Current may be suppressed by charge localizations within the sample that cause free carriers to either be trapped or recombined with an opposite carrier; the latter process may be a source of luminescence.¹³

1.5.3 Multiple Excitons

Multiple excitons occur when a single photon can result in more than one exciton being generated and was first observed in PbSe by Schaller and Klimov.⁴⁸ Also known as carrier multiplication and impact ionization, the multiple exciton effect could greatly increase the power conversion efficiency of nanoparticle-based solar cells. A photon with energy many times the bandgap is absorbed by the material and excites an exciton high into the conduction band; the exciton loses energy, without recombining,

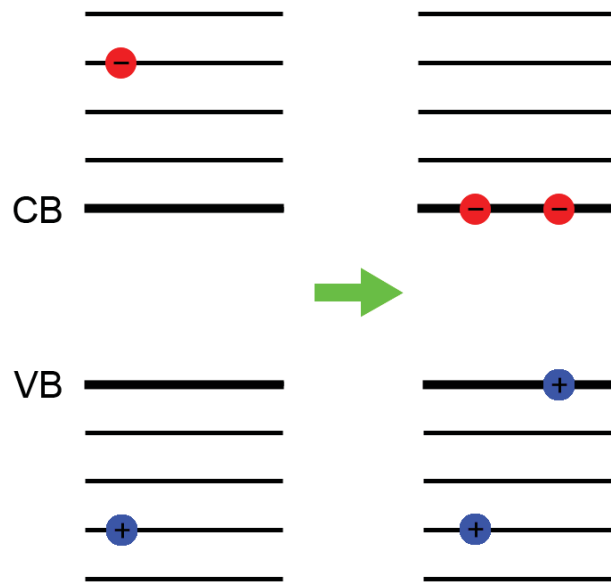


Figure 1.11: Multiple excitons are generated by a highly excited exciton relaxing into two lower energy excitons.

and that energy creates a second exciton, see Figure 1.11. This process can continue creating more excitons and is the opposite of Auger recombination.

Multiple exciton generation has been reported in the literature for various types of colloidal quantum dots.^{49–55} This generated a lot of interest in the solar cell community, since previous solar cells could usually harvest only one electron per photon, which led to energy from high-energy photons being wasted. Low bandgap materials, such as lead chalcogenides, could potentially harness much more energy through multiple exciton generation, to provide more current per photon. There are significant difficulties, such as separating the excitons and extracting the carriers before recombination, though work to address this is ongoing.

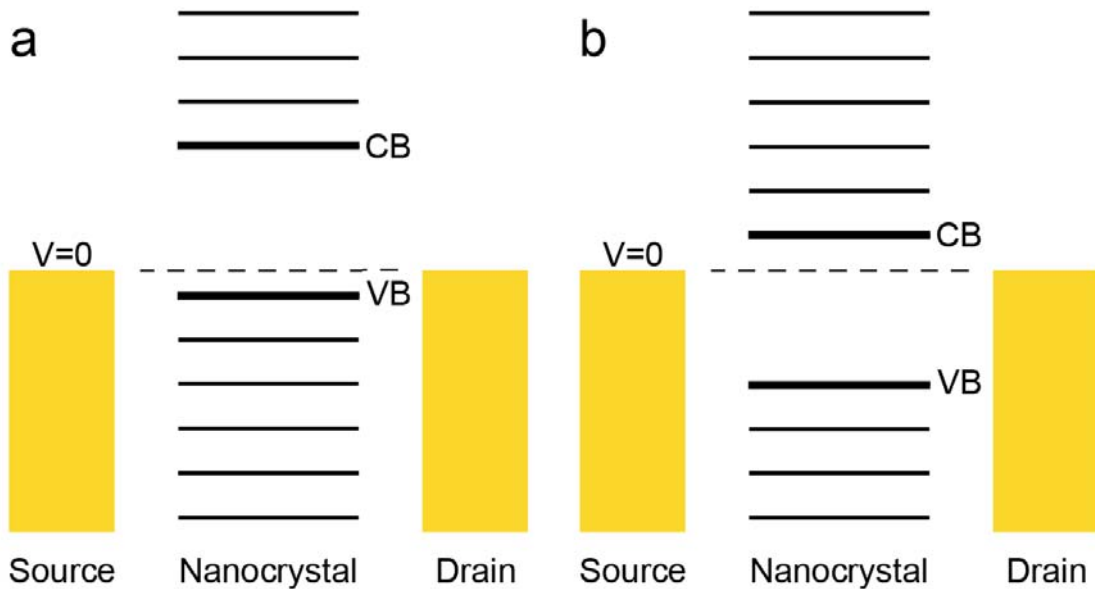


Figure 1.12: For one nanocrystal between a source and a drain, (a) a negative gate raises the nanocrystal energy levels. (b) A positive gate lowers the nanocrystal energy levels.

1.5.4 Field Effect Transistors

A field effect transistor (FET) uses the field of a gate electrode to modulate the current between the source and drain electrodes. A negative gate voltage moves the levels of the semiconductor up, bringing the valence band toward the Fermi energy and pushing the conduction band farther from the Fermi energy, see Figure 1.12a. A positive gate voltage moves the levels of the semiconductor down, see Figure 1.12b. Hole transport is enhanced by a negative gate voltage at negative drain source biases, whereas electron transport is enhanced by a positive gate voltage at positive drain source biases. Typically, for n-type materials, making the gate voltage more positive will result in larger currents at positive source-drain voltages. Conversely, for p-type materials, making the gate voltage more negative will result in larger currents for negative source-drain voltages.⁵⁶

When using a gate, the field creates a depletion region within a semiconductor,

where the mobile charge carriers have been forced away by an electric field. This can control the width of the conduction channel, and can stop the flow of electrons if the depletion region becomes too large. This is what gives field effect transistors their “on” and “off” states. For a metal-insulator-semiconductor, the width of this region, W is given by

$$W = \frac{\varepsilon_s}{C_i} \left(\sqrt{1 + \frac{2C_i^2 \Delta V}{qN\varepsilon_s}} - 1 \right), \quad (1.82)$$

where ε_s is the permittivity of the semiconductor, C_i is the capacitance per area of the insulator, ΔV is the voltage difference between the gate and the drain, and N is the number density of donors.⁵⁷ The capacitance per area can also be written as

$$C_i = \frac{\varepsilon_i}{d}, \quad (1.83)$$

where ε_i is the permittivity of the insulator and d is the thickness of the insulator.

Now, Equation 1.82 becomes

$$W = \frac{\varepsilon_s d}{\varepsilon_i} \left(\sqrt{1 + \frac{2\varepsilon_i^2 \Delta V}{qN\varepsilon_s d^2}} - 1 \right). \quad (1.84)$$

1.6 Overview of Results

While this thesis is about transport measurements and materials, it can be split into two main themes: Nanoparticles and nanopores. An introduction to DNA and various sequencing and sensing techniques is presented in Chapter 2, including an overview of results for nanopores. Fabrication techniques for devices used in this thesis are discussed in Chapter 3, with the measurement setup for nanocrystal experiments discussed in Chapter 4, Section 4.1. A description and analysis of ligand exchanges for PbSe nanocrystals, as well as a synthesis for gold-seeded PbSe agglomerations

is presented in Chapter 5. Chapter 6 summarizes transport measurements on PbSe rods synthesized by Weon-kyu Koh.⁵⁸ A discussion of how nanocrystal traps can be manipulated to change the photocurrent of CdSe/ZnS core/shell nanocrystals is presented in Chapter 7. Conclusions are presented in Chaper 10, Section 10.1

CHAPTER 2

Introduction to DNA Sequencing and Sensing

2.1 DNA

Deoxyribonucleic acid (DNA) is the building block of all life, and contains the essential code for our development and function. DNA is a double helix made of nucleotides, adenine (A), cytosine (C), guanine (G), and thymine (T). Each nucleotide is made up of a nucleoside plus a phosphate and sugar backbone, weighing, on average, 660 Daltons, which is approximately 1.0959×10^{-21} kg. Each nucleotide, or base, has a complement; A is paired with T, and C is paired with G. Each pair form a hydrogen bond, making each side of the DNA complementary to the other, see Figure 2.1. Double-stranded DNA (dsDNA) refers to the double helix, whereas single-stranded DNA (ssDNA) refers to only half the helix.

The human genome contains approximately three billion base pairs. Genes are sections of DNA that code for proteins, which are responsible for the physical expression of our DNA. To understand the link between DNA and gene expression, it is useful to know the sequence of base pairs that make up the gene. However, that is difficult since DNA is often folded, with a persistence length of approximately 44 nm,⁵⁹ and the base pairs are small, approximately 0.33 nm.

Current DNA sequencing techniques generally use fluorescent tagging of molecules that bind to the DNA, and with electrophoresis, the base associated with the tag can be identified. Newer methods have focused on using amplified DNA “colonies,” microscopy techniques, and nanopore sensing, both biological and solid state.

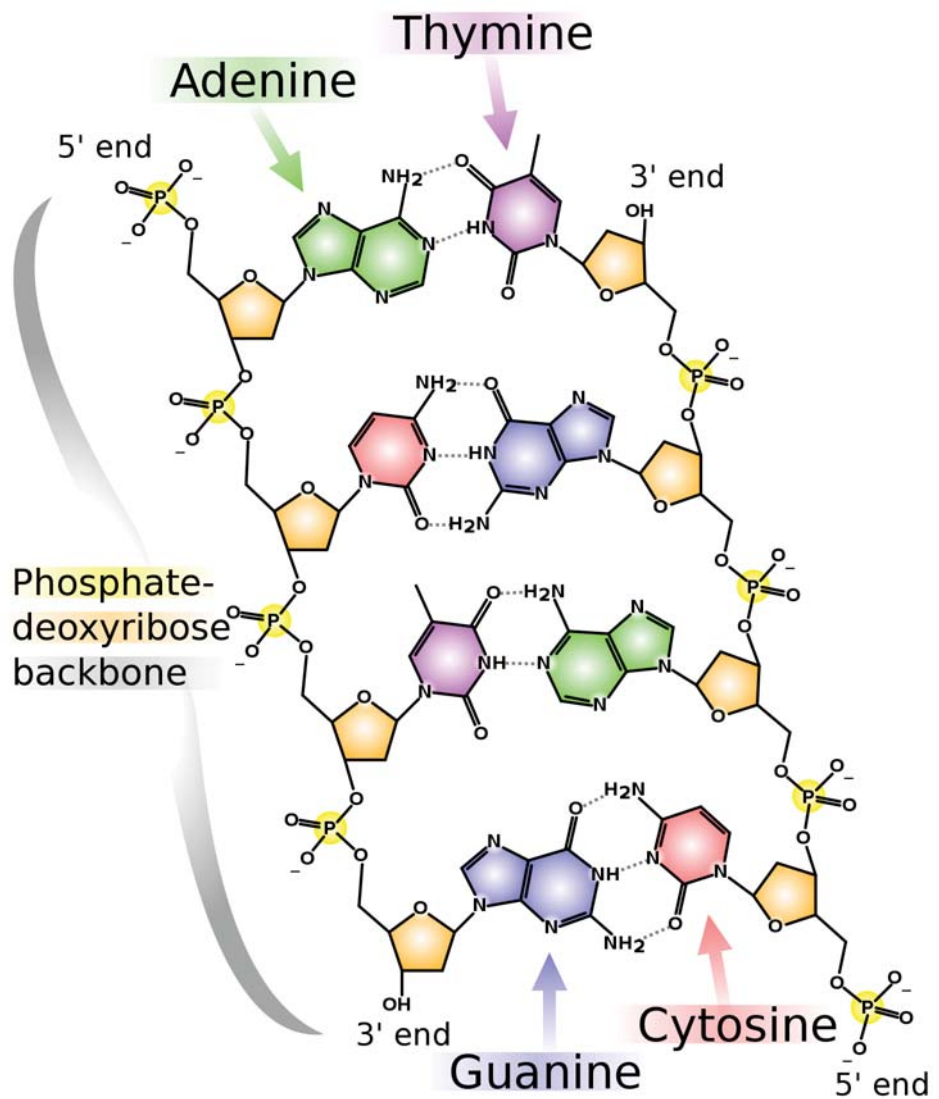


Figure 2.1: Chemical structure of DNA. Image courtesy of Madeleine Price Ball.

2.2 DNA Sequencing Techniques

2.2.1 Sanger Sequencing

The Sanger method⁶⁰ was first published in 1977, and with a few modifications, is still the gold standard for sequencing. The DNA to be sequenced must first be cloned into a vector, which are small pieces of DNA that can be transferred to an organism for cloning. Plasmids are commonly used as cloning vectors in bacterial cells. A restriction enzyme is added to the vector DNA and the target DNA, which cuts both at a specific nucleotide sequence, usually creating “sticky ends,” which are ends that have single-stranded overhangs, see Figure 2.2. The target DNA is then ligated, or chemically attached, into the cloning vector. The bacterial colonies are then grown, and the colonies with the target DNA are selected. Thus, millions of copies of the target DNA are produced. An enzyme known as primase is added to the DNA to create primers, which are short sequences that complement the beginning of the target DNA. Primers are necessary because DNA polymerase can only add nucleotides to the 3' end of a DNA strand, see Figure 2.1 that already exists.

In the original Sanger method, the amplified DNA was then separated into four reactions. Each of the four reactions contained the DNA to be sequenced, DNA polymerase, the primes, all four 2'-deoxyribonucleotide triphosphates (dNTPs), and one 2', 3'-dideoxynucleoside triphosphate (ddNTP) that is tagged with a radioactive molecule, see Figure 2.3a. When a ddNTP is randomly incorporated into a strand being synthesized, the strand synthesis is terminated. This results in differently sized DNA strands that coincide with the different positions of the corresponding base in the target DNA strand. The DNA from each reaction is then run through a polyacrylamide gel that can be used to determine the mass, or length, of each strand by running a voltage across the gel. The smaller the DNA fragment is, the farther it



Figure 2.2: Restriction enzymes cut DNA leaving either (a) sticky ends or (b) blunt ends.

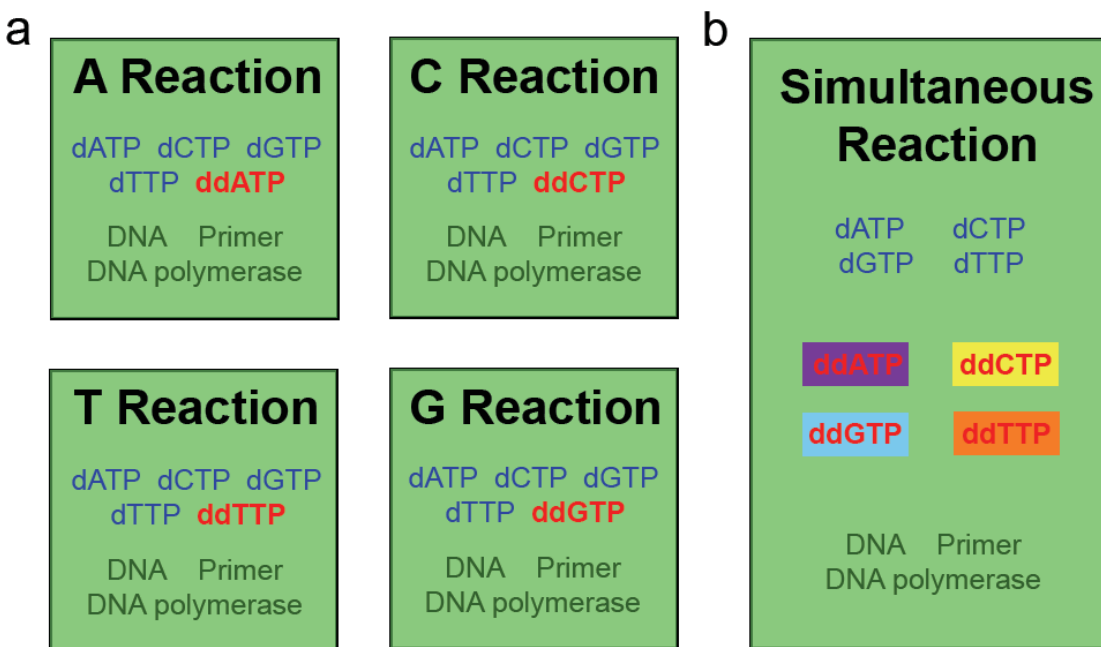


Figure 2.3: (a) The original Sanger method uses four reactions with each containing DNA, the primer, DNA polymerase, and one of the ddNTPs. (b) Current methods use four different fluorescent dyes to tag each of the ddNTPs so that only a single reaction is necessary.

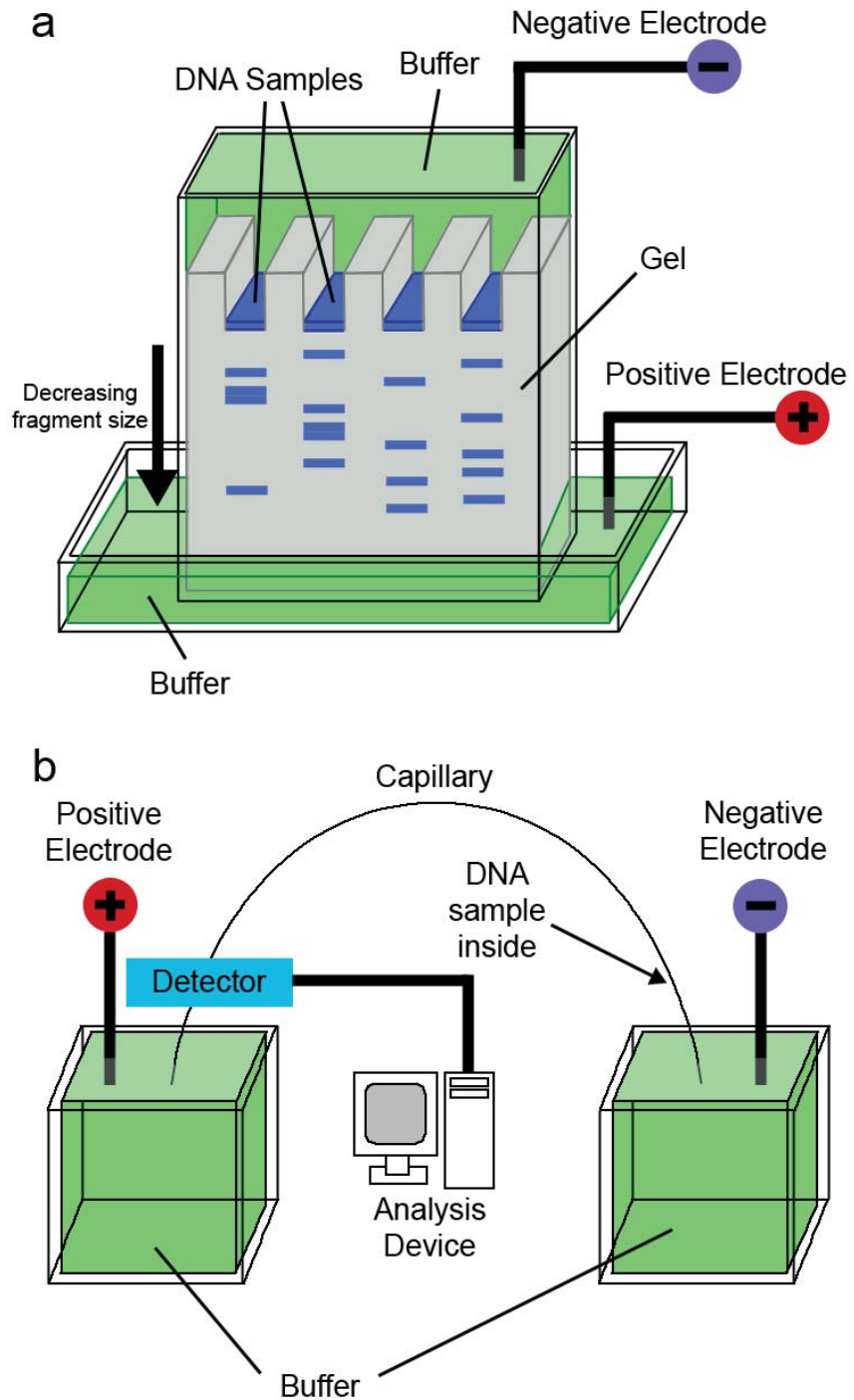


Figure 2.4: (a) Gel electrophoresis can be used to separate DNA fragments of different lengths by running a voltage through a gel with DNA samples. The shorter the DNA fragment, the farther it travels through the gel. (b) Capillary electrophoresis.

will travel toward the cathode, see Figure 2.4a. The gel can then be read with autoradiography to determine the sequence of the DNA, see Figure 2.5. Polyacrylamide gel is much more sensitive to small molecular weights than the more commonly used agarose, but it is also a powerful neurotoxin and must be handled with care.

Current applications of the Sanger method were greatly improved by the discovery of a one-pot reaction with automatic detection.⁶¹ Each ddNTPs was fluorescently labeled with a different color and added to a reaction with the four dNTPs, the DNA to be sequenced, the primer, and DNA polymerase, see Figure 2.3b. Another important improvement to the original Sanger sequencing was use of capillary gel electrophoresis, see Figure 2.4b, which increases the separation of the DNA fragments for increased sensitivity and speed of the reaction.⁶²

2.2.2 Polony Sequencing

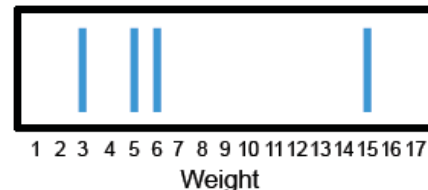
Historically, polymerase chain reaction (PCR) colonies, or polonies, were colonies of DNA that were grown to amplify a single nucleic acid molecule in situ within a gel matrix. PCR was performed in a gel, and each cycle would produce localized product, creating a “colony” that resembles the colonies used in bacterial cloning,⁶³ see Figure 2.6. The original concept of polonies as DNA attached to a gel evolved into DNA-coated beads. The method termed BEAMing,⁶⁴ short for beads, emulsion, amplification, and magnetics, was a significant advance due to increased density of polonies, increased DNA concentration for higher signal-to-noise, increased flexibility of reactions, and easier imaging due to identification of all the beads.⁶⁵

Briefly, from Dressman et al.,⁶⁴ BEAMing begins by preparing monodisperse, streptavidin-coated, magnetic beads. Biotinylated forward primers are added to the bead, with the biotin binding well to the streptavidin. These are then added to an aqueous solution containing the remaining ingredients for PCR amplification, though



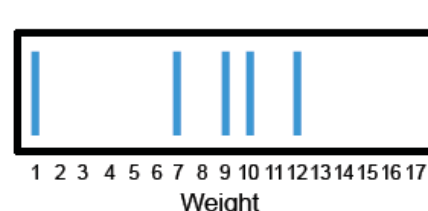
A Reaction with ddATP

TGA
TGACA
TGACAA
TGACAAATGTTCTGCA



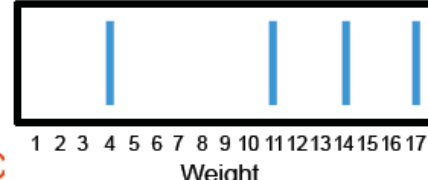
T Reaction with ddTTP

T
TGACAAT
TGACAATGT
TGACAATGTT
TGACAATGTTCT



C Reaction with ddCTP

TGAC
TGACAATGTTC
TGACAATGTTCTGC
TGACAATGTTCTGCAGC



G Reaction with ddGTP

TG
TGACAATG
TGACAATGTTCTG
TGACAATGTTCTGCAG

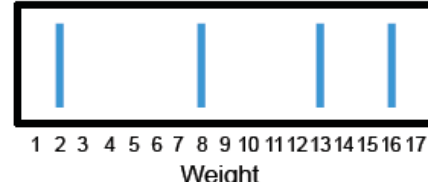


Figure 2.5: The results of the Sanger sequencing method are DNA strands of varying length depending on the ddNTP added to each reaction. Since the strand terminated when a ddNTP is added instead of a dNTP, the different lengths correspond to the positions of the complementary nucleotide in the original DNA strand. The lengths are then determined by running each reaction through a polyacrylamide gel.

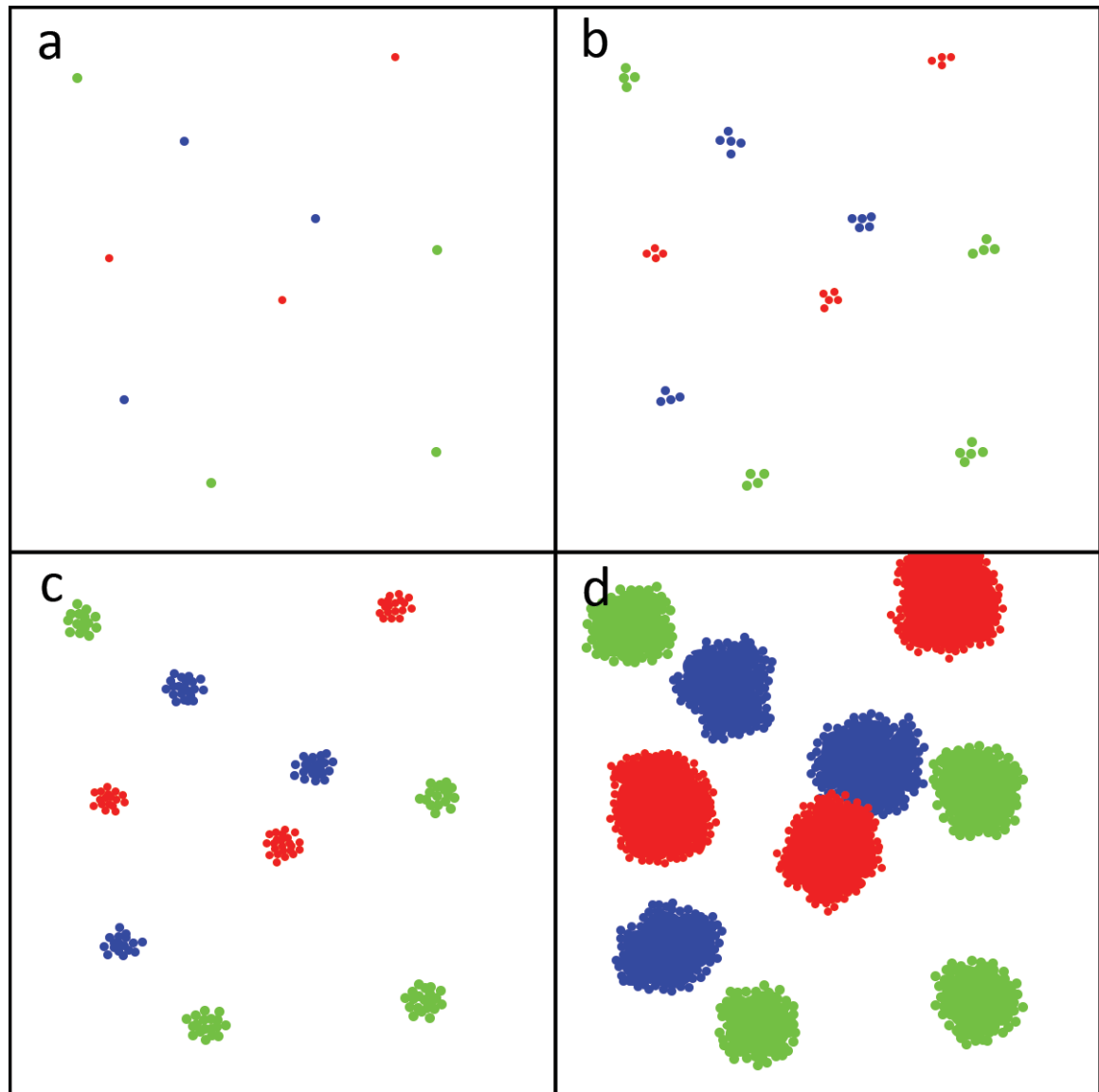


Figure 2.6: Schematic of polony growth. (a) through (d) represent passing time as the polonies grow and fluoresce.

additional forward and reverse primer is added due to inefficiency as compared with normal, in-solution primers. This aqueous solution is then mixed with an oil and surfactant to create tiny emulsions. The emulsions are temperature cycled, and the DNA is amplified if it lands in the same emulsion as a bead. After PCR, the emulsions are broken, and polystyrene beads with DNA complementary to the amplified DNA are added. The polystyrene beads attach to the magnetic beads that have amplified DNA attached, and the difference in mass can be used to separate the unamplified beads by centrifugation. The polystyrene-magnetic bead complex can be denatured chemically, and use of a magnetic field can separate the final product. This process, known as enrichment, can be repeated to maximize the percentage of successfully amplified DNA-coated beads. These beads are now attached to a glass coverslip.

The most popular polony sequencing method was originally the sequencing-by-synthesis approach.⁶⁶ Nucleotides with different fluorescent tags are added to the polonies, and a primer extension reaction takes place. The base can be read optically, and the fluorescent tag is cleaved from the base. The sample is washed, and fluorescently-tagged nucleotides can be added once more to determine the next base. However, this method has generally been replaced with sequencing-by-ligation, which is based on a technique known as massively parallel signature sequencing.⁶⁷ In short, rather than introduce fluorescently-tagged, individual nucleotides, four sets of tagged oligomers are introduced. Each set of oligomers have random bases for all but one position, and the query position, which corresponds to the base to be sequenced, is given a set nucleotide. Due to the specificity of the ligation reaction,⁶⁸⁻⁷⁰ the base being queried can be optically read and stored. The ligated oligomer can then be stripped off, and a new set of oligomers with a different query position is flowed in.

The commercially available sequencing technologies are based off of these ideas. Illumina's (Solexa's) Genome Analyzer IIx,^{71,72} Roche's (454 Life Sciences') GS FLX,⁷³

and Pacific Biosciences' PacBio RS⁷⁴ use variations of sequencing-by-synthesis, whereas Applied Biosystems' SOLiD^{75,76} and Complete Genomics' CGA platform⁷⁷ use variations of sequencing-by-ligation.

2.2.3 Nanopore Sequencing

Nanopores were first suggested as tools for DNA sequencing in a patent filed by Church et al. in 1995,⁷⁸ see Figure 2.7 for a schematic, with *Staphylococcal* α -hemolysin being the first nanopore to measure DNA.⁷⁹ This biological pore, with a 2.6 nm opening, was used to transport DNA through a lipid membrane, with chambers of buffer solution on either side. Electrodes inserted into the chambers were used to create an ionic current through the pore, and as DNA moved through the pore, the ionic current was decreased. By measuring the time of the DNA translocation, the length of the DNA strand can be found. This is similar to the patch clamp technique for studying ionic channels in cells.

Protein Pores

While *Mycobacterium smegmatis* porin A (MspA) has been studied,^{80,81} the most commonly used protein pore is *Staphylococcal* α -hemolysin, which is a mushroom-shaped protein pore. The cap is made of seven identical subunits and is approximately 10 nm across with a 2.6 nm opening in the center, this channel opens to a maximum of 4.6 nm and narrows to a minimum of 1.5 nm. The stem, or barrel, is 5.2 nm long, and the channel ranges between 1.4 nm and 2.4 nm.⁸² Due to the size of the barrel's narrowest constriction, α -hemolysin allows ssDNA to pass through but not dsDNA. α -hemolysin create a channel through a lipid bilayer. Lipids have a hydrophilic head and hydrophobic tails; in a polar solvent, such as water, a bilayer will form from two sheets of lipids arranged with their heads in contact with the solvent and their

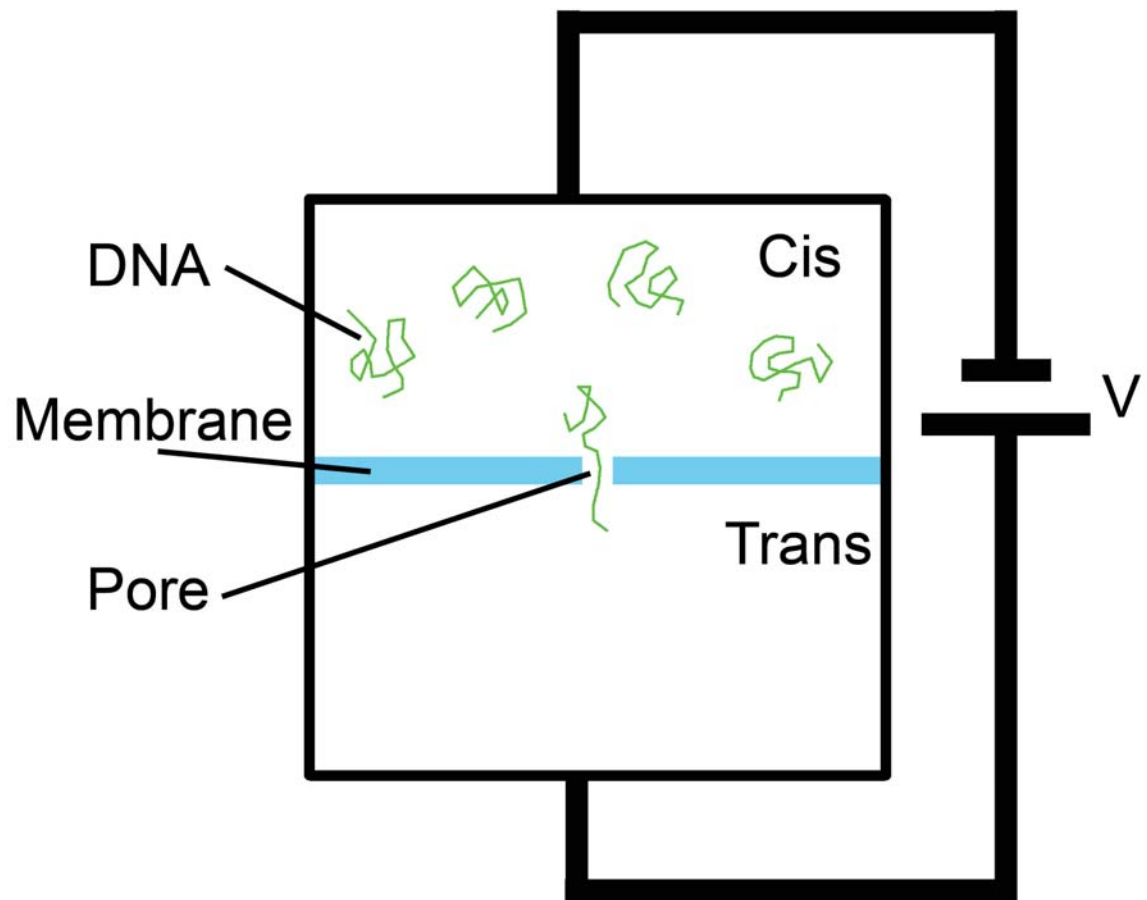


Figure 2.7: DNA can be voltage-driven through a pore in a membrane. The chambers on either side are sometimes referred to as the cis chamber, which initially has the DNA, and the trans chamber, into which the DNA translocates.

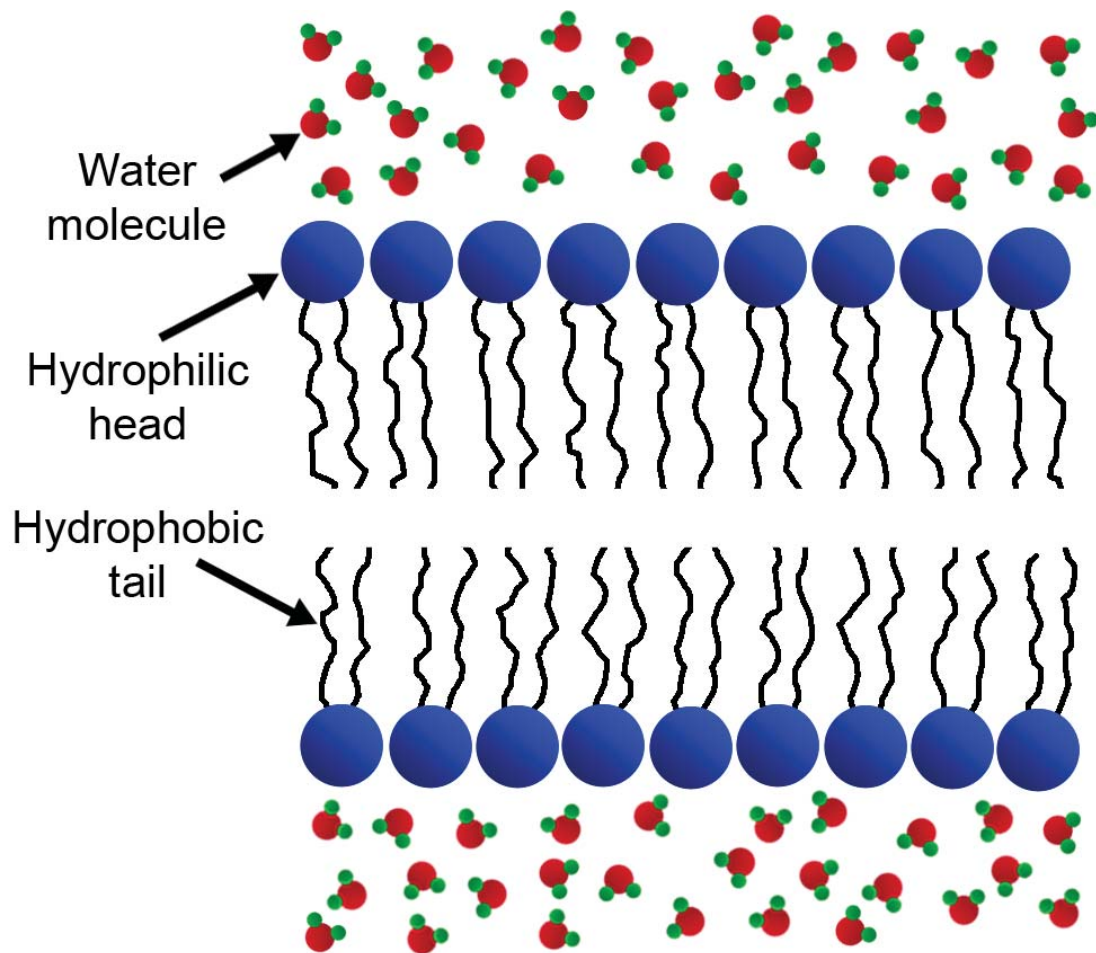


Figure 2.8: In a polar solvent, such as water, the lipids arrange into a bilayer with their tails facing inward and their heads facing the solvent.

tails protected within the bilayer, see Figure 2.8. The chambers on either side of the bilayer are filled with a buffered salt solution, and a molecule, such as DNA, is placed on one side, often known as the *cis* chamber. A voltage drop across the channel causes the DNA to travel through the α -hemolysin into the opposite channel, often known as the *trans* chamber. Careful measurement of the ionic current can provide information about the molecule that has been translocated.

Measuring ionic current through α -hemolysin has already been used to distinguish between different bases of DNA and RNA.⁸³⁻⁸⁵ However, sequencing DNA or RNA is

difficult due to the elongated barrel. Another problem is that the DNA translocates through the pore very rapidly, on the order of a couple microseconds, and with the barrel approximately 5 nm long, multiple bases are read at once. A common method to slow the DNA is to add molecules such as avidin⁸⁶ or DNA polymerase,⁸⁷ which binds to ssDNA. The DNA fragments that can be read by α -hemolysin must also be relatively short, which means that reconstructing an entire genome takes an enormous amount of computing power and storage space. Lastly, protein pores generally have short lifetimes and are very sensitive to conditions such as pH, high voltage, and salt concentration. One advantage of protein pores is that they are always identical, and they can be mutated to redesign features such as its charge to better capture and translocate DNA.⁸⁸

Currently, there are no commercially available devices to sequence DNA with this technique, though the company Oxford Nanopores is currently working to bring a product to market.⁸⁹

Solid State Nanopores

When issues with biological pores began to become more evident, other groups began to experiment with solid state pores. The same patch clamp measurements could be done, but factors such as pH, high voltage, salt concentration, and time were much less of an issue.⁸⁸ Pores are usually drilled by either a TEM or an ion beam.⁹⁰ The most common substrate is currently silicon nitride, though others, such as graphene,⁹¹⁻⁹³ are being explored. The pore sizes are widely variable, from a single nanometer to microns. Pore size can even be reduced by depositing material onto it, or if the pore is less than a certain critical size unique to the substrate, by a defocused electron beam through surface tension effects.⁹⁴ However, it is difficult to repeatedly get the same size and shape nanopore.

The speed of the DNA moving through the pore is still an issue, with two possible solutions: slow the DNA or speed up the electronics. Work on slowing DNA translocations has included adding glycerol,⁹⁵ use of optical tweezers,^{96,97} pore surface modification,^{98,99} and decreased temperature.⁸⁴ In addition to slowing down DNA, custom electronics that can raise signal bandwidths above 1 MHz have already been realized and successfully integrated with nanopore devices.¹⁰⁰

Currently, there are no commercially available devices to sequence DNA with this technique.

2.2.4 Transmission Electron Microscopy Sequencing

Transmission electron microscopy (TEM) has already been used to view single atoms. However, clear imaging with TEM depends on the atomic number (Z) of the sample, with low- Z materials being invisible in TEM and similar- Z materials having no contrast. Thus, DNA bases cannot currently be directly imaged with this method. The most common approach is to attach different high- Z markers to three of the nucleotides, and the fourth nucleotide is recognized if there is no marker, see Figure 2.9. The markers are attached to nucleotides, which are incorporated onto the original strand using DNA polymerase and a primer. The DNA is then flowed onto a substrate to elongate it.

To date, this technique has been realized with one nucleotide marker.¹⁰¹ The benefits of this technique are that it can produce extremely long read lengths, compared to chemical techniques that separate the DNA into smaller pieces, and it would have much higher throughput. This also reduces the number of times that the DNA must be amplified, which decreases the number of chances of introducing an error. However, there are still challenges in selecting the best high- Z molecules, successfully incorporating them onto a DNA strand at a very high rate, and making sure that the

a

DNA Sequence:

A G G C T A T C T G A A C T G

b

Corresponding TEM:



Figure 2.9: The bases in (a) a DNA sequence can have different high-Z markers attached to three different nucleotides, which can be identified in TEM. A schematic of this is shown in (b).

tags are spatially separated.

This method is not yet commercially available, though the company ZS Genetics is currently working on this technology.

2.3 Nanopore Theory

2.3.1 Length Scales

Nanopore transport measurements take place in solution, usually a buffered, aqueous solution. The ions in the fluid must be considered when thinking about interactions between DNA and the solution. It is often useful to consider the length scales at which these interactions become important.

Debye Screening Length

One important length scale is the Debye screening length in an electrolyte solution, κ^{-1} . For lengths greater than this distance, significant charge separation does not occur due to mobile charges screening the electric field. The Debye screening length is given by

$$\kappa^{-1} = \sqrt{\frac{\varepsilon_r \varepsilon_0 k_B T}{2 N_A e^2 I}}, \quad (2.1)$$

where ε_r is the dielectric constant of the medium, ε_0 is the permittivity of free space, k_B is the Boltzmann constant, T is the temperature, N_A is Avogadro's number, e is the charge of an electron, and I is the ionic strength.¹⁰²

The Bjerrum length, λ_B , is the length at which the electrostatic potential is equal to the thermal energy:

$$k_B T = \frac{e^2}{4\pi \varepsilon_r \varepsilon_0 \lambda_B} \quad (2.2)$$

$$\lambda_B = \frac{e^2}{4\pi \varepsilon_r \varepsilon_0 k_B T}. \quad (2.3)$$

For water at room temperature, $\lambda_B \approx 0.7$ nm.¹⁰² Equation 2.1 can be rewritten in terms of the Bjerrum length:

$$\kappa^{-1} = \sqrt{\frac{1}{8\pi \lambda_B N_A I}}. \quad (2.4)$$

The ionic concentration is given by

$$I = \frac{1}{2} \sum_{i=1}^n c_i z_i^2, \quad (2.5)$$

where c_i is the molar concentration of ion i and z_i is the ion's charge.¹⁰² For an ion like KCl with two equal, singly-charged ion concentrations, the ionic strength is equal

Molarity	Debye Length (nm)
1 mM	9.6702
10 mM	3.0580
30 mM	1.7656
100 mM	0.9670
300 mM	0.5583
1 M	0.3058
3 M	0.1766

Table 2.1: Debye screening length for different molarities.

to the molar concentration, C_0 . Note that a 1 M solution has a molar concentration of 1000 mol/m³. See Table 2.1 for the Debye screening lengths that correspond to various KCl in water molarities at 295K.

The Diffusion Limited Length Scale

For nanopore devices, the length scale, r^* , is such that for $r > r^*$, DNA diffuses freely, and for $r < r^*$, DNA is captured by the pore. An estimate of r^* is necessary, and the following derivations will follow from the work of Grosberg and Rabin.¹⁰³ The drift velocity of a negatively charged particle in an electric field is given by

$$\vec{v}_E = -\mu \vec{E}, \quad (2.6)$$

where μ is the mobility and \vec{E} is the electric field. Similarly, if there is another force, \vec{F} , the Einstein-Smoluchowski relation gives the mobility for that force, μ_F ,

$$D = \mu_F k_B T \quad (2.7)$$

$$\mu_F = \frac{D}{k_B T}, \quad (2.8)$$

where D is the diffusion constant, k_B is the Boltzmann constant, and T is the temperature.

The velocities add,¹⁰⁴ giving

$$\vec{v} = -\mu \vec{E} + \frac{D}{k_B T} \vec{F}. \quad (2.9)$$

Solving for \vec{F} , we can find the stall force:

$$\vec{F} = \frac{\mu k_B T}{D} \vec{E}. \quad (2.10)$$

Given that

$$\vec{F} = -\nabla W, \quad (2.11)$$

the work is given by

$$\vec{W} = \frac{\mu k_B T}{D} V. \quad (2.12)$$

At r^* , the work should be equal to $k_B T$, which from Equation 2.12 gives,

$$V(r^*) = \frac{D}{\mu}. \quad (2.13)$$

With the potential also given by

$$V = \frac{q_{eff}}{\epsilon r}, \quad (2.14)$$

we find that

$$r^* = \frac{q_{eff}\mu}{\epsilon D}. \quad (2.15)$$

The potential can be calculated another way: consider a current flowing from infinity to a spherical conductor of diameter, d . The medium has a conductivity of σ and the applied voltage is δV . Calculating the voltage drop across a spherical shell

from r to $r + dr$, we need the resistance,

$$R = \frac{\ell}{\sigma A}, \quad (2.16)$$

where ℓ is the length and A is the cross-sectional area. For our sphere,

$$R = \frac{dr}{\sigma 4\pi r^2}. \quad (2.17)$$

Using Ohm's law,

$$V = IR, \quad (2.18)$$

we find

$$dv = -\frac{I}{4\pi\sigma r^2} \quad (2.19)$$

$$V = \frac{I}{4\pi\sigma r} + V_\infty. \quad (2.20)$$

We know the voltage from infinity to $d = \frac{r}{s}$ is δV , so we find

$$\delta V = \frac{I}{2\pi\sigma d} \quad (2.21)$$

$$I = 2\pi\sigma d\delta V. \quad (2.22)$$

Substituting Equation 2.22 into Equation 2.20, and setting $V_\infty = 0$,

$$V = \frac{\delta V d}{2r}. \quad (2.23)$$

However, in the case of a nanopore, the current is actually across the membrane, which is double the space we were considering, which means that the current in

Equation 2.22 must be halved,

$$I = \pi\sigma d \delta V. \quad (2.24)$$

Given an applied voltage, ΔV , the voltage drop across the pore is $\Delta V - 2\delta V$. Thus using 2.18,

$$\Delta V - 2\delta V = \frac{4\ell I}{\pi\sigma d^2}. \quad (2.25)$$

Substituting Equation 2.24 into Equation 2.25, we find

$$\delta V = \Delta V \frac{\frac{d}{4\ell}}{1 + \frac{d}{2\ell}}. \quad (2.26)$$

Assuming $\ell \gg d$,

$$\delta V \approx \frac{d\Delta V}{4\ell} \quad (2.27)$$

Combining Equations 2.13 and 2.23, we find that the length scale for diffusion-limited capture is given by

$$r^* = \frac{d^2 \mu \Delta V}{8\ell D}. \quad (2.28)$$

The value of r^* is on the order of the persistence length of DNA,¹⁰³ which suggests that the DNA diffuses unperturbed until it is right next to the pore, and then it is captured by the voltage.

2.3.2 Diffusion

Diffusion can be modeled with Fick's first and second laws:

$$\phi = -D \nabla \rho \quad (2.29)$$

$$\frac{\partial \rho}{\partial t} = \nabla \cdot \phi_{ion} = -D \nabla^2 \rho, \quad (2.30)$$

where ρ is the number density of ions, ϕ is the flux, or number of ions moving across a boundary of unit area per second, and D is the diffusion constant. For a spherically symmetric system, Fick's second law becomes

$$\frac{\partial \rho}{\partial t} = \frac{D}{r} \frac{\partial^2}{\partial r^2} (r\rho). \quad (2.31)$$

Using the substitution $u = r\rho$, Equation 2.31 becomes

$$\frac{\partial u}{\partial t} = D \frac{\partial^2 u}{\partial r^2}. \quad (2.32)$$

To solve Equation 2.32, take the Laplace transform of both sides. If $\mathcal{L}\{u(r, t)\} = \hat{U}(r, s)$

$$s\hat{U}(r, s) - u(r, 0) = D \frac{\partial^2 \hat{U}}{\partial r^2}. \quad (2.33)$$

Given the boundary condition that the concentration is ρ_0 at all r when $t = 0$, $u(r, 0) = \rho_0 r$. Now Equation 2.33 can be written as follows:

$$D \frac{\partial^2 \hat{U}}{\partial r^2} - s\hat{U}(r, s) = \rho_0 r. \quad (2.34)$$

The complimentary solution to Equation 2.34 is given by

$$\hat{U}_c = A_1 e^{r\sqrt{\frac{s}{D}}} + A_2 e^{-r\sqrt{\frac{s}{D}}}. \quad (2.35)$$

The particular solution, by inspection, is given by

$$\hat{U}_p = \frac{\rho_0 r}{s}. \quad (2.36)$$

Given that the concentration is finite at infinity, $A_1 = 0$, which gives

$$\hat{U}(r, s) = A_2 e^{-r\sqrt{\frac{s}{D}}} + \frac{\rho_0 r}{s}. \quad (2.37)$$

Using the last boundary condition that the concentration is zero at $r = a$ for $t > 0$, we can solve for A_2 :

$$A_2 e^{-a\sqrt{\frac{s}{D}}} + \frac{\rho_0 a}{s} = 0 \quad (2.38)$$

$$A_2 = \frac{\rho_0 a}{s} e^{a\sqrt{\frac{s}{D}}}. \quad (2.39)$$

This gives

$$\hat{U}(r, s) = \frac{\rho_0 a}{s} e^{-(r-a)\sqrt{\frac{s}{D}}}. \quad (2.40)$$

We must now undo the Laplace transform; given that

$$\mathcal{L}\{\text{erfc}(x)\} = \frac{e^{-2x\sqrt{st}}}{s}, \quad (2.41)$$

where $\text{erfc}(x)$ is the complementary error function, the inverse Laplace transform of Equation 2.40 is

$$u(r, t) = -\rho_0 a \text{erfc}\left(\frac{r-a}{2\sqrt{Dt}}\right) + \rho_0 r. \quad (2.42)$$

Substituting ρr for u , we now have the solution

$$\rho(r, t) = \rho_0 \left(1 - \frac{a}{r} \text{erfc}\left(\frac{r-a}{2\sqrt{Dt}}\right)\right). \quad (2.43)$$

Note that $2\sqrt{Dt}$ is known as the diffusion length, which indicates how far the concentration has diffused in a time, t .

Using Fick's first law, Equation 2.29, we can calculate the flux at $r = a$:

$$\phi = \frac{D\rho_0}{a} \left(1 + \frac{a}{\sqrt{\pi Dt}} \right). \quad (2.44)$$

The second term of Equation 2.44 generally becomes small compared to the first term in a short amount of time.¹⁰⁵ The rate, R , of particles diffusing across a spherical boundary or radius a is given by

$$R = 4\pi a^2 \phi \quad (2.45)$$

$$= 4\pi a D \rho_0. \quad (2.46)$$

For a hemisphere, which describes DNA on one side of a membrane, the rate of diffusion, R_{diff} , is given by

$$R_{diff} = 2\pi a D \rho_0, \quad (2.47)$$

meaning that the rate constant, k_{diff} , is given by

$$k_{diff} = 2\pi a D N_A. \quad (2.48)$$

The capture rate of long DNA is limited by diffusion, whereas the capture rate for short DNA is limited by the free energy barrier of the pore.¹⁰⁶ In the case of a diffusion-limited capture rate, the flux of ions, ϕ_{ion} , is given by

$$\phi_{ion} = 2\pi a D c, \quad (2.49)$$

where a is the capture radius and c is the concentration of ions.¹⁰⁷ Since ϕ_{ion} can also

be written in terms of the diffusion-limited capture rate, R_{diff} , and concentration:

$$\phi_{ion} = R_{diff}C. \quad (2.50)$$

Combining Equations 2.49 and 2.50, we get

$$R_{diff} = 2\pi aD. \quad (2.51)$$

Now, substituting Equation 2.28 into Equation 2.51, such that $a = r^*$, the capture rate is given by

$$R_{diff} = \frac{\pi d^2 \mu \Delta V}{4\ell}. \quad (2.52)$$

This suggests that to increase the capture rate of DNA, larger pores, higher voltages, and thinner membranes are recommended. However, in regard to the pore size, it should be noted that larger pores clog far more frequently than smaller pores, possibly due to jamming.

While basic factors to enhance DNA translocations have been discussed, there are other methods that have been used. Rather than have the same salt concentrations on both sides of the membrane, a gradient can be established. Having a lower salt concentration in the cis chamber enhances the translocation rate, and increases the translocation time.¹⁰⁶ It has also been shown that modifying the charge of a biological nanopore can increase DNA translocations, usually by increasing its internal positive charge to attract the negatively charged DNA.¹⁰⁸

2.4 Overview of Results

While this thesis is about transport measurements and materials, it can be split into two main themes: Nanoparticles and nanopores. An introduction to nanoparticles and

various measurement techniques is presented in Chapter 1, including an overview of results for nanocrystals. Fabrication techniques for devices used in this thesis are discussed in Chapter 3, with the measurement setup for nanopore experiments discussed in Chapter 4, Section 4.2. A discussion of fabricating and using nanoelectrodes around a nanopore for DNA sensing is presented in Chapter 8. Chapter 9 shows work on fabricating and characterizing nanowires next to a nanopore for correlating transverse DNA measurements with ionic measurements. Conclusions are presented in Chapter 10, Section 10.2

CHAPTER 3

Fabrication

3.1 Typical Devices

Typically, metal electrodes are positioned over a suspended silicon nitride membrane, see Figure 3.1. This allows transmission electron microscopy (TEM), as well as decreased backscatter for electron beam lithography (EBL). These features allow closer inspection of devices and finer resolution of lithographic features. Silicon nitride has a dielectric constant of $6.5\text{--}7.2\epsilon_0$ and a breakdown field of 10^7 V/cm, i.e., 1 V/nm, making it compatible with electrical measurements.¹⁰⁹ It is also easy to etch without using dangerous chemicals such as hydrofluoric acid.¹¹⁰ However, not all silicon nitride wafers have had low leakage currents, and the membrane is fragile, requiring careful handling.

The electrodes are patterned using EBL, whereas larger features can be patterned with EBL or photolithography. Each electrode is connected to a large square, or contact pad, which can then be contacted through wirebonding or a probe station. Nanocrystals can then be dropcast onto the device for measurement, or a nanopore can be drilled for DNA sensing measurements.

3.2 Resist-Based Lithographies

Resists are long chain polymers, see Figure 3.2, that are sensitive to a process, usually electron or photon exposure. These processes either break or crosslink the chains, and then the smaller, broken parts are washed away during development. Resists are

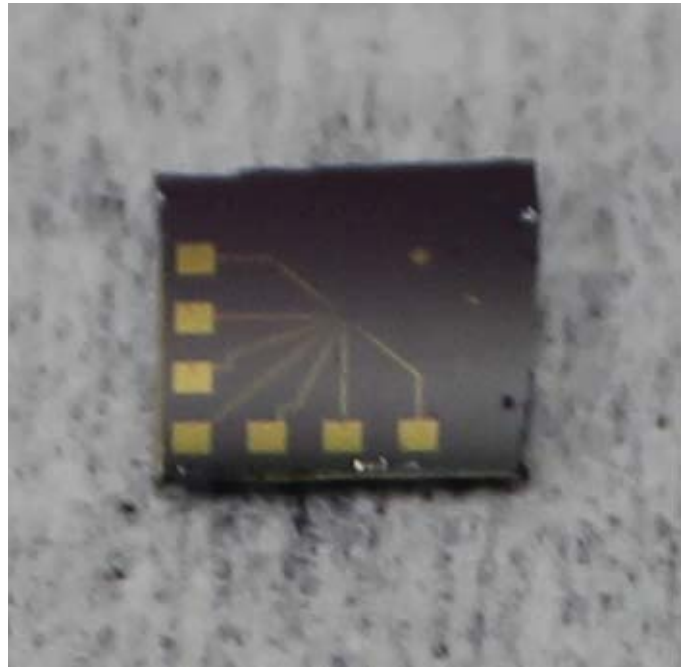


Figure 3.1: Sample chip with metal electrodes and contact pads on silicon nitride substrate.

usually either positive or negative, where positive means that the exposed polymer will be broken up, and negative means that the exposed polymer will be crosslinked, see Figure 3.3. It is sometimes possible to change the resist from positive to negative through severe overexposure, called a flood exposure; this is known as image reversal.

3.2.1 Electron Beam Lithography

EBL uses an electron beam to expose resist. EBL machines are usually modified scanning electron microscopes with software that condenses the beam and scans it over specific patterns, typically written in a computer-aided design (CAD) program. EBL resists tend to be on the order of hundreds of nanometers and may be light sensitive. While whole wafers may be written without human input during the writing, EBL is not considered a scalable technology for commercial purposes, though this technique can achieve very high resolution on the order of a nanometer.

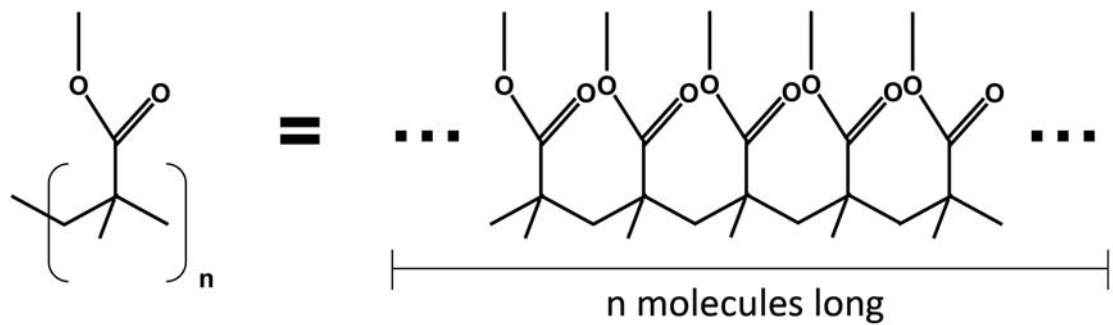


Figure 3.2: Poly(methyl methacrylate), known as PMMA, is a long chain polymer that is used as an electron beam resist.

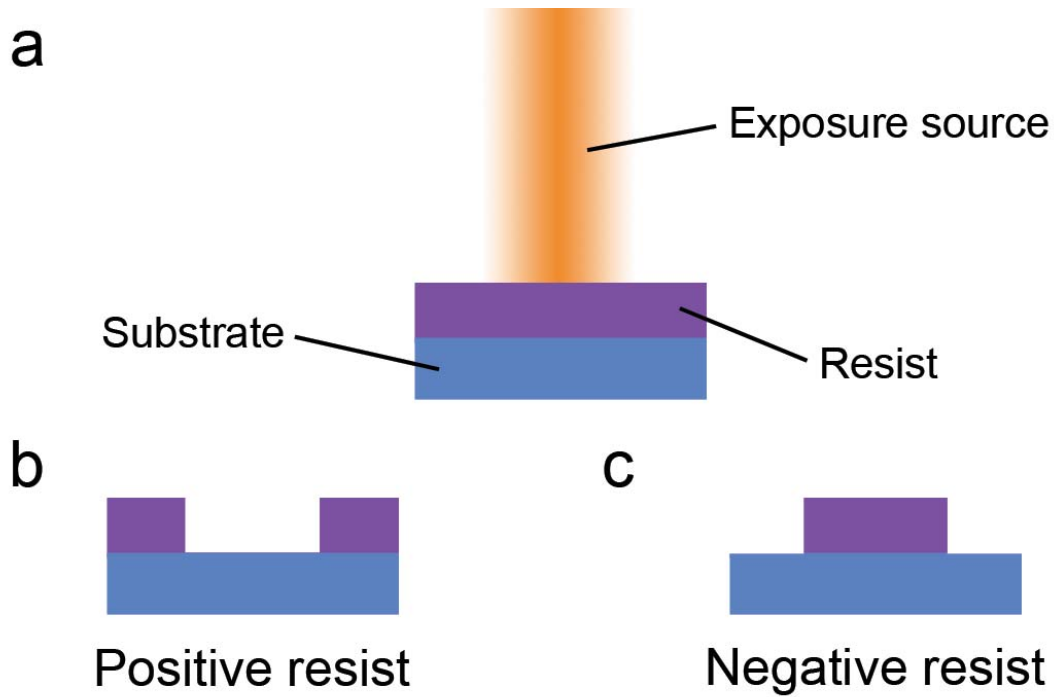


Figure 3.3: (a) Resist on a substrate is exposed, usually by electrons or photons. After developement, the exposed area (b) is washed away for positive resist or (c) is cross-linked for negative resist.

A commonly used resist for electron beam lithography is poly(methyl methacrylate) (PMMA), see Figure 3.2. Two commonly used types of PMMA are the A series and the C series, which use different solvents. The C series uses chlorobenzene as the solvent, and the A series uses anisole. Each series has different types that are denoted by a number after the C, which refers to the percentage of PMMA solids. A second number indicates the length of each chain, in units of thousands of molecules. For example, C2 950 means that the polymer is 950,000 molecules long and makes up 2% of the solution in the solvent chlorobenzene. The longer the polymer, the more difficult it is to completely destroy with electrons. Thus, for single layer resists, longer chains give better resolution. Less polymer in the solvent gives a thinner layer when spun. This can also increase resolution, though liftoff becomes less favorable.

Electrons in the beam can be scattered due to interactions with the sample. As electrons interact with the resist, they may scatter and cause broadening. This is called forward scattering, and the increase in beam diameter, d_{fs} , is given by

$$d_{fs} = 0.9 \left(\frac{R_t}{V_b} \right)^{1.5}, \quad (3.1)$$

where R_t is the resist thickness and V_b is the beam voltage in kilovolts.¹¹¹ Electrons penetrating the sample may also scatter off the substrate back toward the resist; these backscattered electrons can cause undercutting of the resist, see Figure 3.4a. This causes the proximity effect, where nearby patterns affect the current pattern, which causes broadening and uneven exposure.¹¹² Backscattering can also enhance liftoff, because after metal evaporation, the metal on the resist that will be removed is less attached to the metal on the substrate. However, this may also further increase the exposure area broadening. Decreasing backscattering significantly improves resolution, though higher doses and times may be needed. It is also possible to harness the

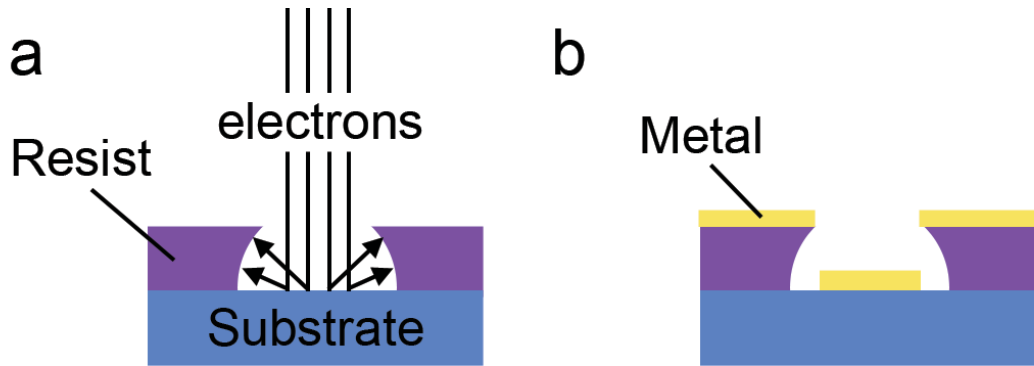


Figure 3.4: (a) Electrons can scatter off the substrate causing an undercut in the resist. (b) If metal is evaporated onto the sample, the undercut can aid liftoff since the metal attached to the substrate is more disconnected from the metal attached the resist, which will be removed.

undercut to improve liftoff by having a layer of thick, short chain resist covered by a tougher, long chain resist, see Figure 3.5a.¹¹¹ The beam can create a small opening in the short chain resist, but a very large undercut can prevent any contact between the metal deposited on the substrate and the resist that will be removed. Conversely, a long chain resist on the substrate covered by a short chain resist may enhance resolution because the bottom layer is less affected by the backscatter, and the top layer serves as a protection layer so that the bottom layer does not get too much exposure, see Figure 3.5b.¹¹³ In general, one must always balance resolution with liftoff. To ensure better liftoff of high resolution features, one solution is to perform the lithography in two steps. The smallest, finest features are fabricated first, and without larger features, the liftoff solution better infiltrates under the metal. This allows cleaner removal of the excess metal. The rest of the pattern can then be written with little regard to resolution.

The best resolution is achieved with a thin substrate and a thin layer of resist. In particular, we write on silicon nitride suspended membranes, which not only gives enhanced resolution over the more typical substrate, silicon oxide, but also serves

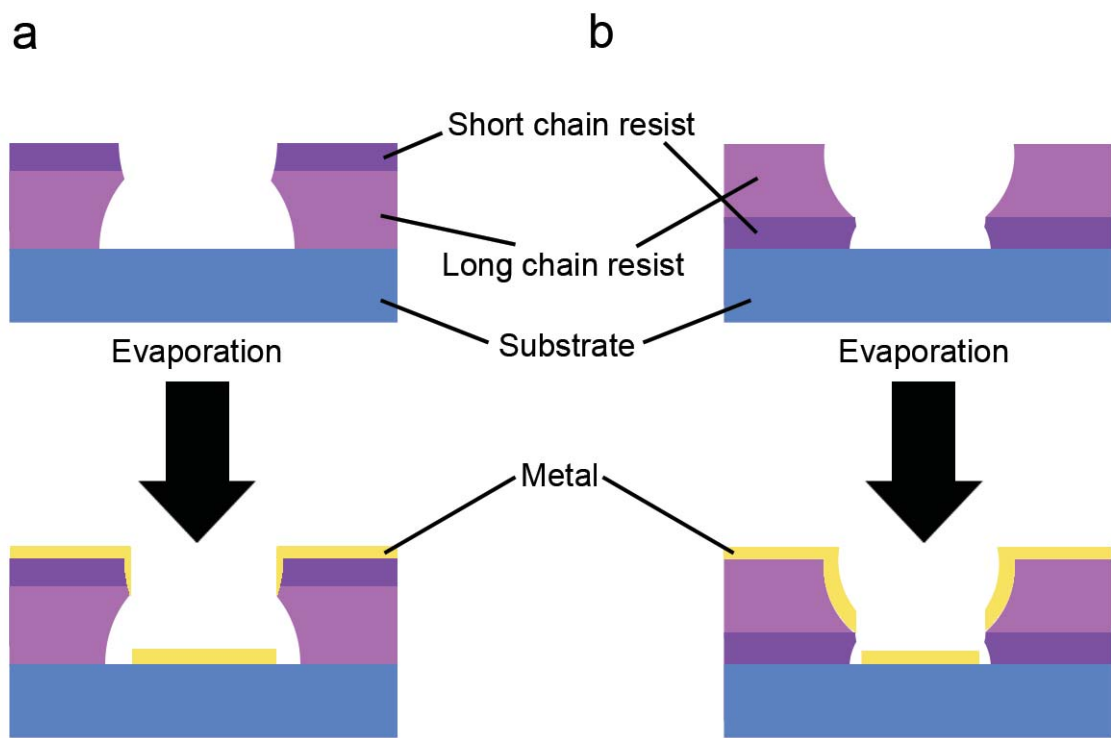


Figure 3.5: (a) With a long chain resist on the bottom and a short chain resist on the top, liftoff can be enhanced at the expense of resolution. (b) With a short chain resist on the bottom and a long chain resist on the top, resolution can be enhanced at the expense of liftoff.

Increased Resolution	Sacrifice
Thin resist	Liftoff
High-power beam	Cost
Long chain resist (on bottom if multilayer)	Liftoff
Multi-stage fabrications	Time
Thin substrate	Substrate stability
Low writing current	Time

Table 3.1: Ways to increase EBL resolution and the sacrifices of each.

a double purpose as it is TEM compatible. However, the membranes are easy to rupture because of their thinness. Resist and metal features can increase the physical stability of the membranes.

In terms of writing current, small currents provide better resolution. However, this will increase the write time. Resolution, in terms of beam current, must be balanced with write time. To maximize both, the smallest features are usually written with the smallest current, and larger features are written with larger currents in a different layer. To ensure that the layers align, some overlap should be added to the pattern, in case of beam or stage shifting.

See Table 3.1 for a summary of the most common ways to increase EBL resolution as well as the tradeoffs for each. The two EBL tools used for the work in this thesis were a JEOL JSM-6400 and an Elionix ELS-7500EX, see Figure 3.6. For specific EBL recipes, see Appendix Section A.1.1.

3.2.2 Photolithography

Photolithography uses light to expose resist, and different resists are made for use at specific wavelength ranges. The resist thickness tends to be on the order of hundreds of nanometers to microns. Since an entire wafer can easily be written in a single exposure, this technology is used for almost all commercial, large-scale device processing,



Figure 3.6: (a) A modified JEOL JSM-6400 SEM and (b) an Elionix ELS-7500EX.

including the electronics for computers, phones, and display screens.

Photolithography patterning is usually done with a mask. If your resist is positive, the pattern is clear and the background is black, whereas for negative or image reversal resist, the pattern is black and the background is clear, see Figure 3.7. Depending on the dose and the type of resist, exposure can cause overcutting, vertical cutting, or undercutting, see Figure 3.8. Positive resist is associated with overcutting, and negative or image reversal resists are associated with undercutting. Any resist may have vertical cutting, as the over and undercuts described previously are caused by low dosage. The opposite resist profiles are achievable by applying too large of a dose, due to backscattering. For the best results, if metal deposition and liftoff are going to be done, negative or image reversal resist is recommended, due to the formation of an undercut. However, for etching, a positive resist is recommended.

The resolution of traditional photolithography is on the order of microns. The minimum feature size is approximated by

$$CD = \frac{k_1 \lambda}{NA}, \quad (3.2)$$

where CD is the critical dimension, which is the minimum feature size, k_1 is a coefficient related to processing, λ is the wavelength of the exposure light, and NA is the numerical aperture of the lens from the wafer.¹¹⁴ This generally means that the wavelength of the exposure light limits the smallest feature size. To increase resolution, lasers with wavelengths down to 193 nm are used.¹¹⁵ The numerical aperture can also be increased to above one using liquid, typically ultra-pure water. This technique is known as immersion photolithography.¹¹⁶ Also, special resists such as dual-tone can be used to increase resolution. It is also possible to use various tricks to get features smaller than the critical dimension. Dual-tone resists can be developed once

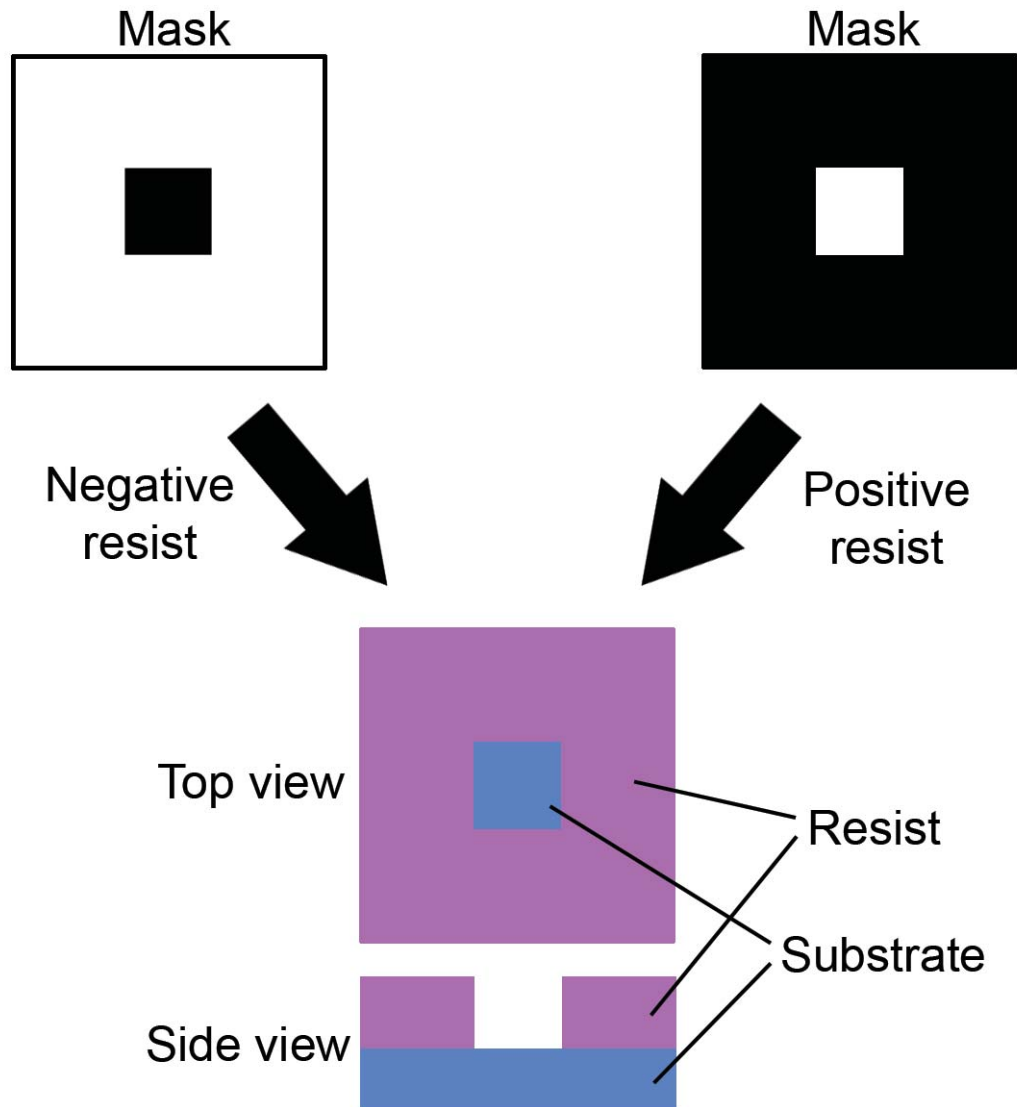


Figure 3.7: For a negative photoresist, the pattern is black, so that the surrounding area is exposed and crosslinked. For a positive photoresist, the pattern is clear, so that the patterned area is exposed and crosslinked.



Figure 3.8: Photolithography can cause either an (a) overcut, (b) vertical cut, or (c) undercut.

to remove the areas of highest exposure and then developed a second time to remove the areas of lowest exposure, see Figure 3.9a.¹¹⁷ Multiple exposures, when carefully aligned, can also increase resolution, see Figure 3.9b.¹¹⁸

The photolithography tool used for the work in this thesis was predominately a Karl Suss MA4 mask aligner, and on occasion, a Nanonex NX-2600 was used. For specific photolithography recipes, see Appendix Section A.1.2.

3.3 Evaporation

The two most commonly used evaporator types are electron beam and thermal. Electron beam evaporators use a focused beam of electrons to heat the evaporation material in a crucible. Thermal evaporators heat the evaporation material by running current through the boat holding the material. Samples are placed upside-down in the evaporator chamber above the material to be evaporated, usually with a shutter in place to shield the sample until ready. The chamber is vacuum pumped, first by a rough pump, and then by a cryo pump. The vacuum is necessary to ensure that the mean free path of the evaporation material is much greater than the distance to the sample. The mean free path, ℓ , is given by

$$\ell = \frac{k_B T}{\sqrt{2\pi d^2 P}}, \quad (3.3)$$

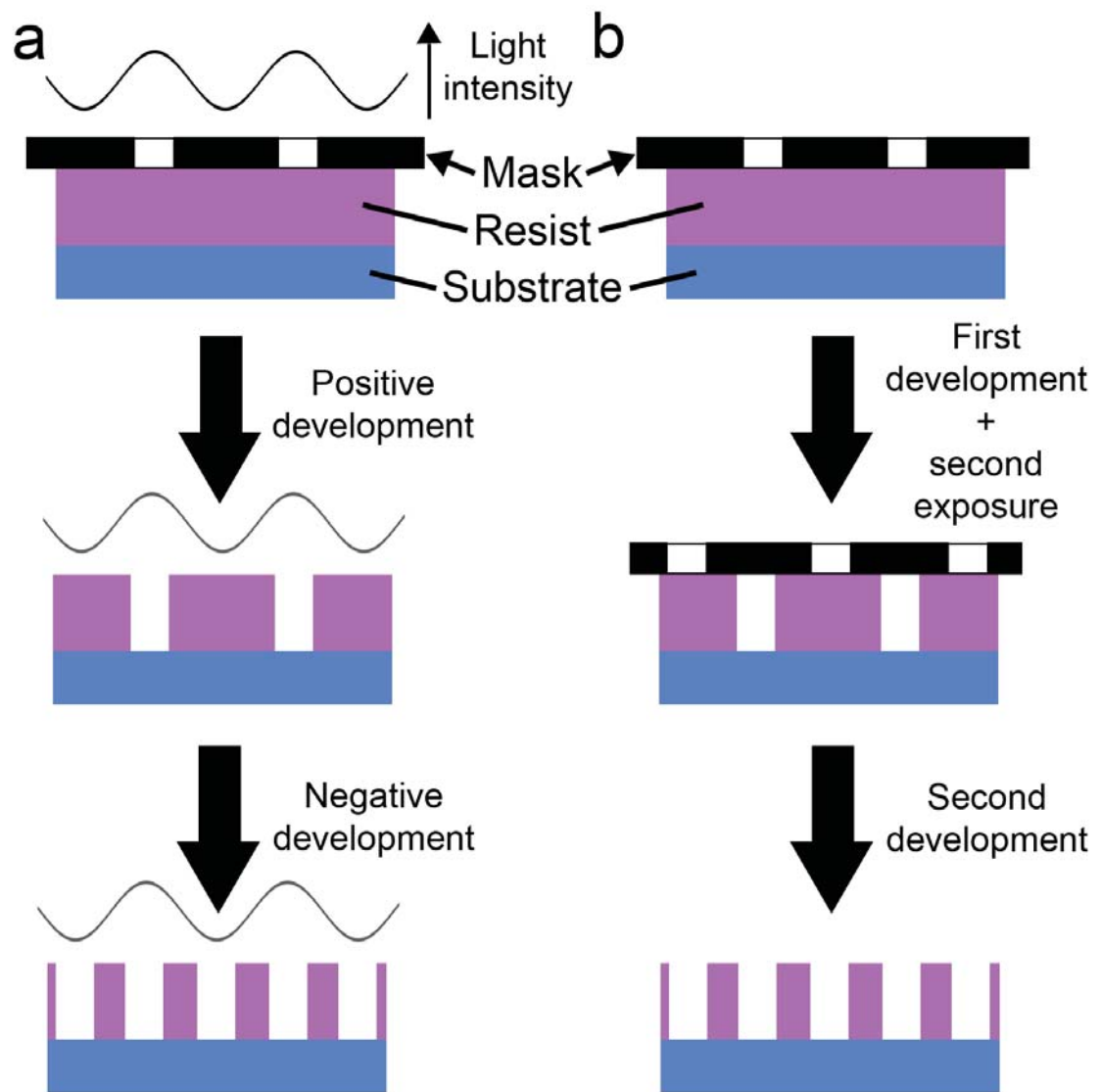


Figure 3.9: (a) A dual-tone resist is double developed, with one development washing away the most exposed areas and a second development washing away the least exposed areas. (b) Multiple exposures, with careful alignment of the masks for each exposure, can create patterns smaller than the critical dimension. Note that any undercuts or overcuts are not shown in this schematic due to their dependency on the resists and developer recipes used.

where k_B is the Boltzmann constant, T is the temperature, d is diameter of the evaporated particle, and P is the pressure.¹¹⁹ The evaporation material is heated and is usually monitored using an oscillating quartz crystal, whose oscillations depend on its mass. When the desired thickness is reached, the shutter is closed, and everything is allowed to cool.

The tool used for the work in this thesis was a home-built, thermal evaporator, see Figure 3.10. Samples were typically taped to the evaporation stage using double-sided conductive tape. It was important to make sure that the tape had minimal contact with the sample and that the sample was parallel to the stage. After pumping the chamber down to a vacuum of 10^{-6} Torr or less, an adhesion layer was evaporated first, due to many metals not having an affinity for silicon nitride. Chrome or nickel was the usual choice, with nickel being more ideal for small features due to the observation that it gives a cleaner liftoff. However, it required a higher temperature and the powder form evaporates very quickly. If the sample was to be used in a salt solution, Ti was used instead, which was also a high temperature metal. Next, the metal of interest was evaporated, which was usually gold. A typical evaporation rate for the adhesion layer was 0.15 nm/s for 3 nm, whereas for gold, the rate was approximately 0.2 nm/s for 30 nm, for small features, or 100 nm for large features.

3.3.1 Liftoff

After evaporation, samples were submerged in acetone overnight. If a faster liftoff was desired, the acetone may be carefully heated to 70°C though it must be watched to ensure it does not all evaporate. The metal should noticeably begin to crinkle in areas without features. Typically, using a pipette to aerate the sample was both harsh enough to remove the unwanted metal and gentle enough to keep the window intact. If a more vigorous liftoff was needed, the chip could be quickly transferred



Figure 3.10: Home-built thermal evaporator used for the work in this thesis.

to a petri dish with acetone, and a squirt bottle could be used to stream acetone onto the surface. Using a long working distance microscope, it was possible to do a rudimentary inspection of the chip while still in acetone, which can increase the yield. Once the chip had dried, it was nearly impossible to continue liftoff. If acetone was too slow or too dirty, dichloroethane (DCE) was used instead. If a sample were to sit in acetone overnight, less than an hour in DCE was necessary for approximately the same liftoff.

3.4 Transmission Electron Beam Ablation Lithography

The beam of a TEM can be used to ablate unwanted material in a process known as transmission electron beam ablation lithography (TEBAL).¹²⁰ If multiple chips have been fabricated in parallel, they are now broken into individual chips to fit into a custom-made holder, see Figure 3.11. They are examined with TEM, and if the desired pattern was a gap, it may have small pieces of metal around the edges or may be closed entirely. For debris around the edges, the beam can be focused directly on top of the particles, and they will either be ablated completely or, depending on the type of metal and the distance from the electrode, be absorbed onto the electrode. This ablation has been explained through two processes: elastic scattering that directly knocks out atoms and inelastic scattering that heats, ionizes, and excites the sample.¹²¹ TEBAL is commonly used to shape and drill holes in substrates such as graphene^{91–93,122} and silicon nitride membranes, see Figure 3.12.

The TEMs used in this thesis are a JEOL-2010 and a JEOL-2010F. However, only the JEOL-2010F can be used to perform TEBAL and drill pores. It uses a field emission gun, rather than a tungsten or LaB₆ source.



Figure 3.11: 5 mm x 5 mm chips can be viewed in a TEM using a modified holder.

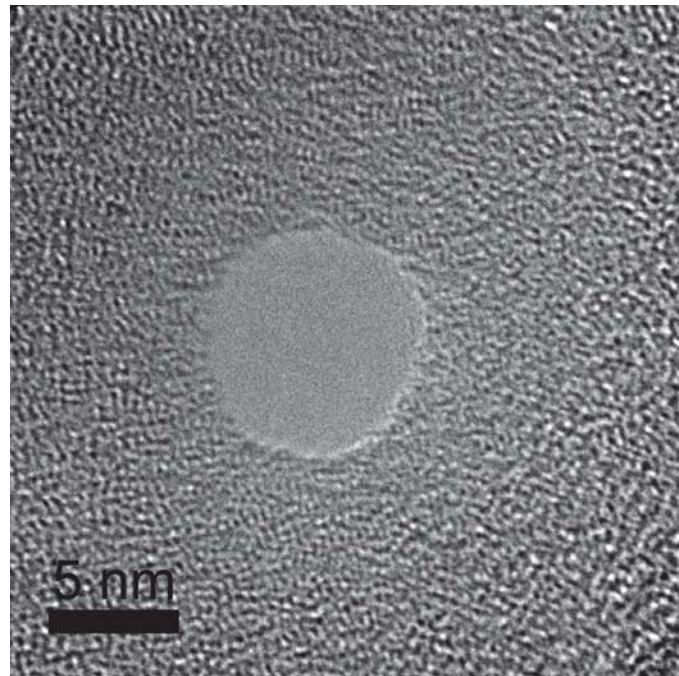


Figure 3.12: A nanopore drilled in a silicon nitride membrane using a TEM beam.

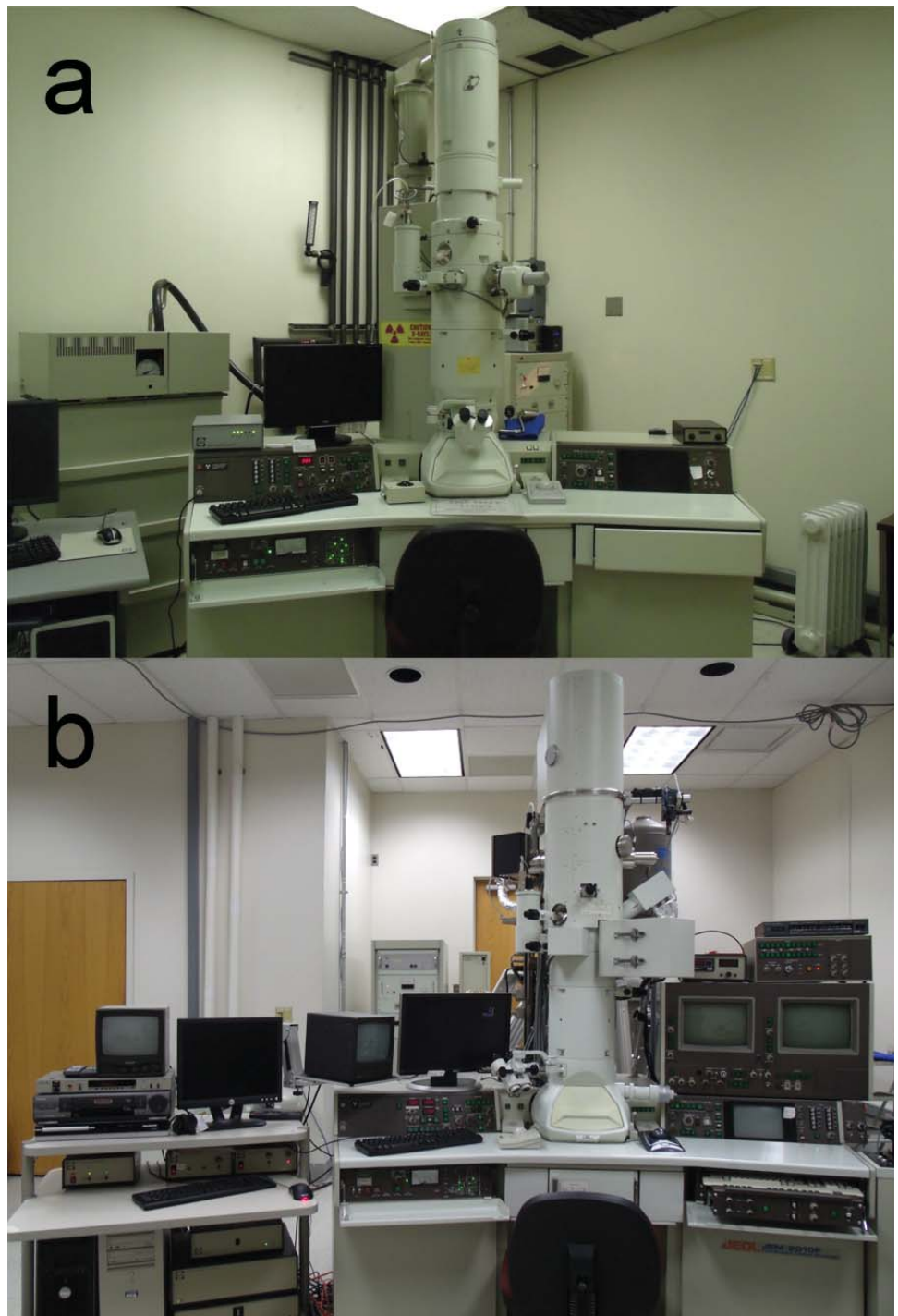


Figure 3.13: (a) A JEOL 2010 TEM and (b) a JEOL 2010F TEM.

3.5 Wafer Processing

The wafers used in this thesis are typically $500\ \mu\text{m}$ p-doped silicon sandwiched between low-stress silicon nitride with thicknesses varying from 25 to 100 nm. To fabricate suspended silicon nitride membranes, a mask with squares and perforated lines defining the windows and the edges of 5 mm by 5 mm chips is patterned using photolithography. The exposed silicon nitride is etched with a reactive ion etch using SF_6 . The resist is removed with a stripper and put into a potassium hydroxide (KOH) wet etch until the silicon is etched all the way to the opposite silicon nitride layer. The resulting silicon nitride membrane can be further etched with SF_6 , and it is recommended to etch from the back to prevent electrical shorts to the silicon during device fabrication. The wafers used for nanopore measurements also had a $5\ \mu\text{m}$ silicon oxide layer between the silicon and the silicon nitride, which lowers their noise and capacitance for nanopore measurements. See Appendix Section A.2 for a more detailed recipe.

CHAPTER 4

Measurement Setup

4.1 Cryostats

Measurements were performed in either a Janis ST-100H or Janis VPF-700 cryostat, see Figure 4.1, under vacuum down to the range of 10^{-7} Torr at room temperature. The Janis ST-100H cooling was achieved using a chicken feeder to keep the coldfinger in contact with liquid nitrogen, see Figure 4.2a, though liquid helium could also be continuously flowed through it. If liquid helium was being used, a radiation shield that covers most of the inner cylinder of the cryostat should be used, see Figure 4.2b. With the chicken feeder completely full, the Janis ST-100H would remain cool overnight. However, it took roughly an hour to cool completely. In contrast, the Janis VPF-700 was a bath cryostat with the mouth of the bath at the top and cooled in approximately 15 minutes, but it would begin to warm after about six hours. Both cryostats could withstand temperatures of up to 650K, though the sensor within the Janis ST-100H was unreliable at approximately 400K because it was designed for very low temperatures.

The insert for the Janis VPF-700 is shown in Figure 4.3 and is similar to that of the Janis ST-100H. Breakout boxes with BNC connectors were silver soldered to socket pins shown in the top right inset of Figure 4.3. Samples were connected with silver paste to a ceramic chip carrier, as seen in the bottom right inset of Figure 4.3, and wirebonded to the pads surrounding the square inset. Each pad was connected to a pin, where pin 1 was indicated by a gold square, and pad 1 was indicated by a missing corner close to the gold strip that runs to the edge of the carrier; the pins and

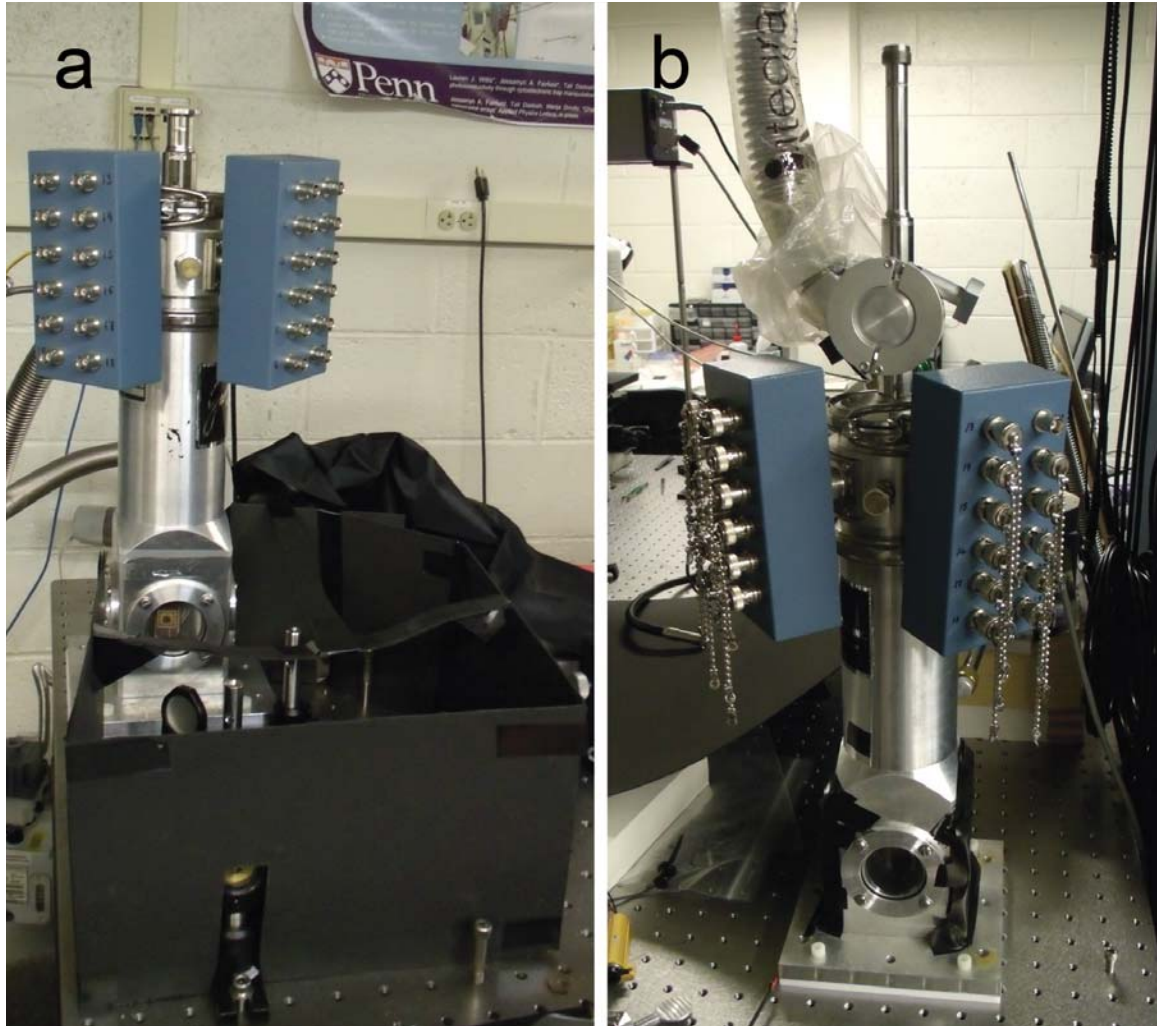


Figure 4.1: (a) A Janis VPF-700 and (b) a Janis ST-100H cryostat.



Figure 4.2: (a) The liquid nitrogen, chicken-feeder dewar and (b) the radiation shield for the Janis ST-100H cryostat.

pads incremented counterclockwise around the chip carrier. For the Janis VPF-700, the gold stripe should point away from the main cylinder, and for the Janis ST-100H, the stripe should point toward the main cylinder. Note that the chip carrier in Figure 4.3 still has the connector that prevents bending of the pins, which should be cut off before use. The pins should be trimmed to ensure the carrier can sit flat against the copper coldfinger.

A quartz window in front of the sample allowed visual inspection and irradiation by light sources, see Figure 4.4a. The optical transmission is shown in Figure 4.4b, showing approximately 94% transmission for wavelengths between 300 nm and 2000 nm. For photocurrent measurements, lasers were used to irradiate the sample. Typically laser pointers were used, powered by a Keithley voltage source.

Custom Labview software was used to control the equipment that applied voltage, heated the sample, and recorded data, see Figure 4.5. A programmable Yokogawa 7651 DC source was used to apply the voltage to samples. For historical reasons, the output was split to also go to an Agilent 34401A multimeter, which would then be read by the Labview software. Currents were input to a Keithley 428 current

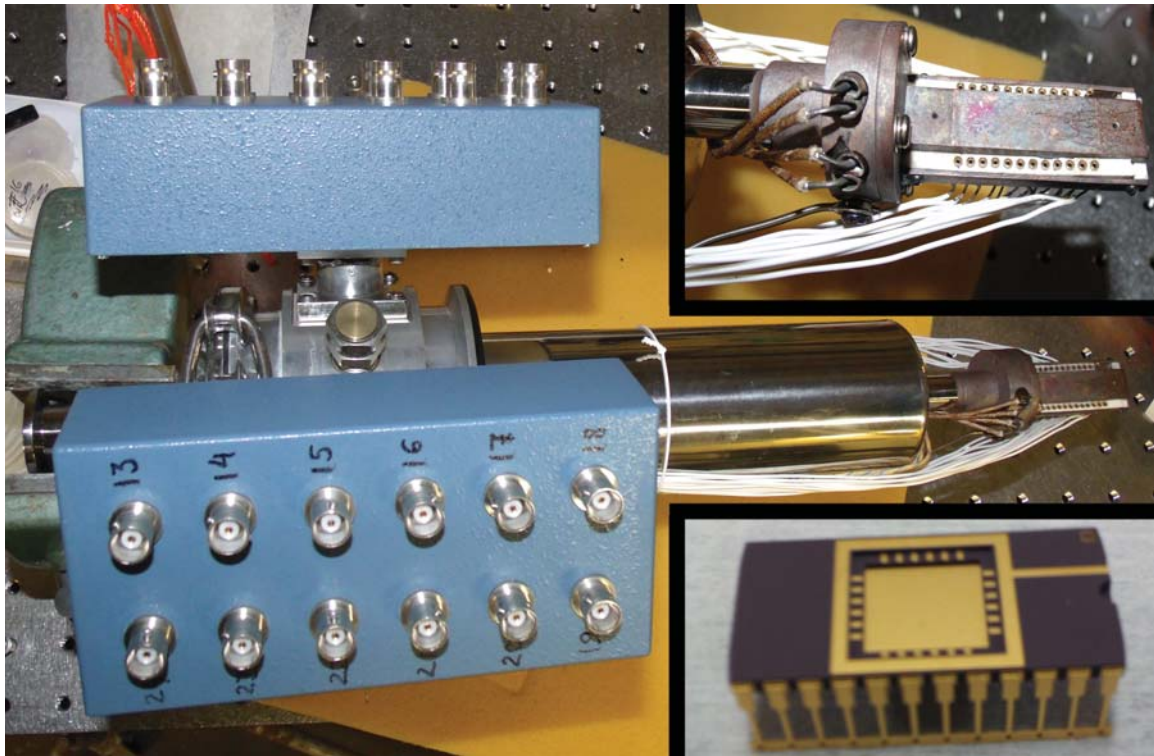


Figure 4.3: Photograph of the removable insert of a cryostat. The top right inset is a close-up of the coldfinger and sample socket, and the bottom right inset is the chip carrier that plugs into the socket.

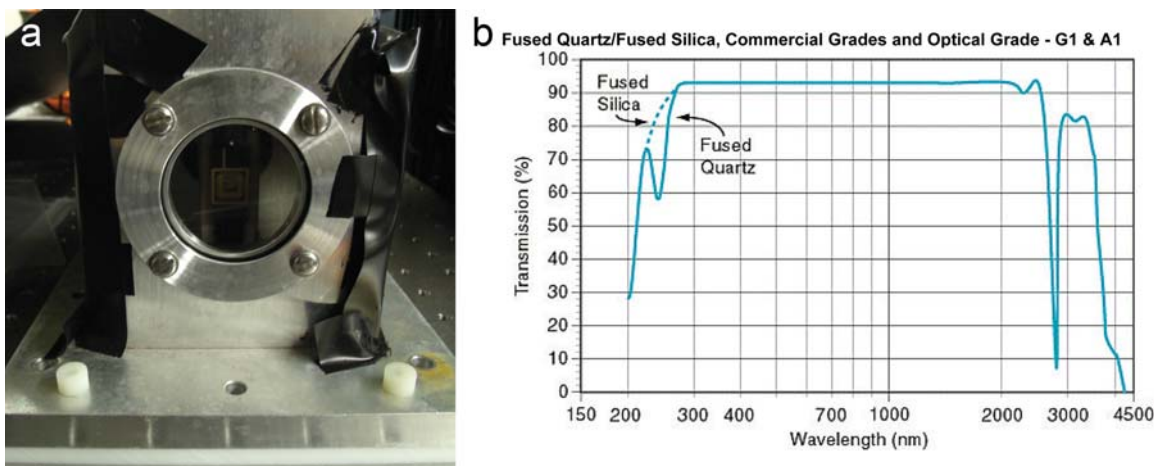


Figure 4.4: (a) The cryostat has a quartz window to allow the sample to be seen and exposed to light sources. (b) The optical transmission for the quartz windows of the cryostats. Image (b) courtesy of Janis Research Company, Inc.

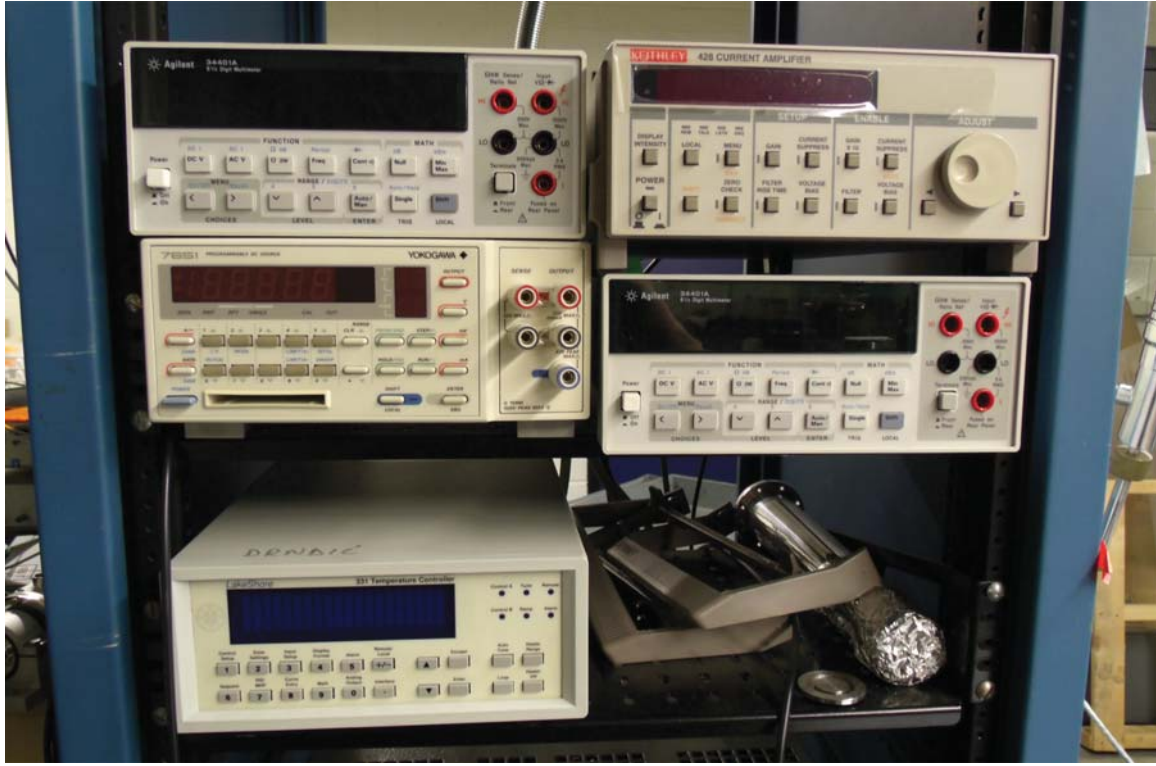


Figure 4.5: The electronics used were a programmable Yokogawa voltage source with an Agilent multimeter to communicate with Labview for historical reasons, a Keithley current amplifier, an Agilent multimeter to read the current, and a Lakeshore for temperature control.

amplifier and fed through another Agilent 34401A multimeter. Temperature was read and controlled by a Lakeshore 331 temperature controller. While the voltage and current were applied and read through BNC ports, the temperature controller was fed into the cryostat through a military connector and a two-prong plug, see Figure 4.6.

4.1.1 Integration into Measurement Setups

To measure chips in a cryostat, they were attached to a chip carrier using silver paste, DuPont's Conductive Composition 4929N, thinned with butoxyethyl acetate (EBA). The silver paste was applied only to the spot where the corner of the chip would rest

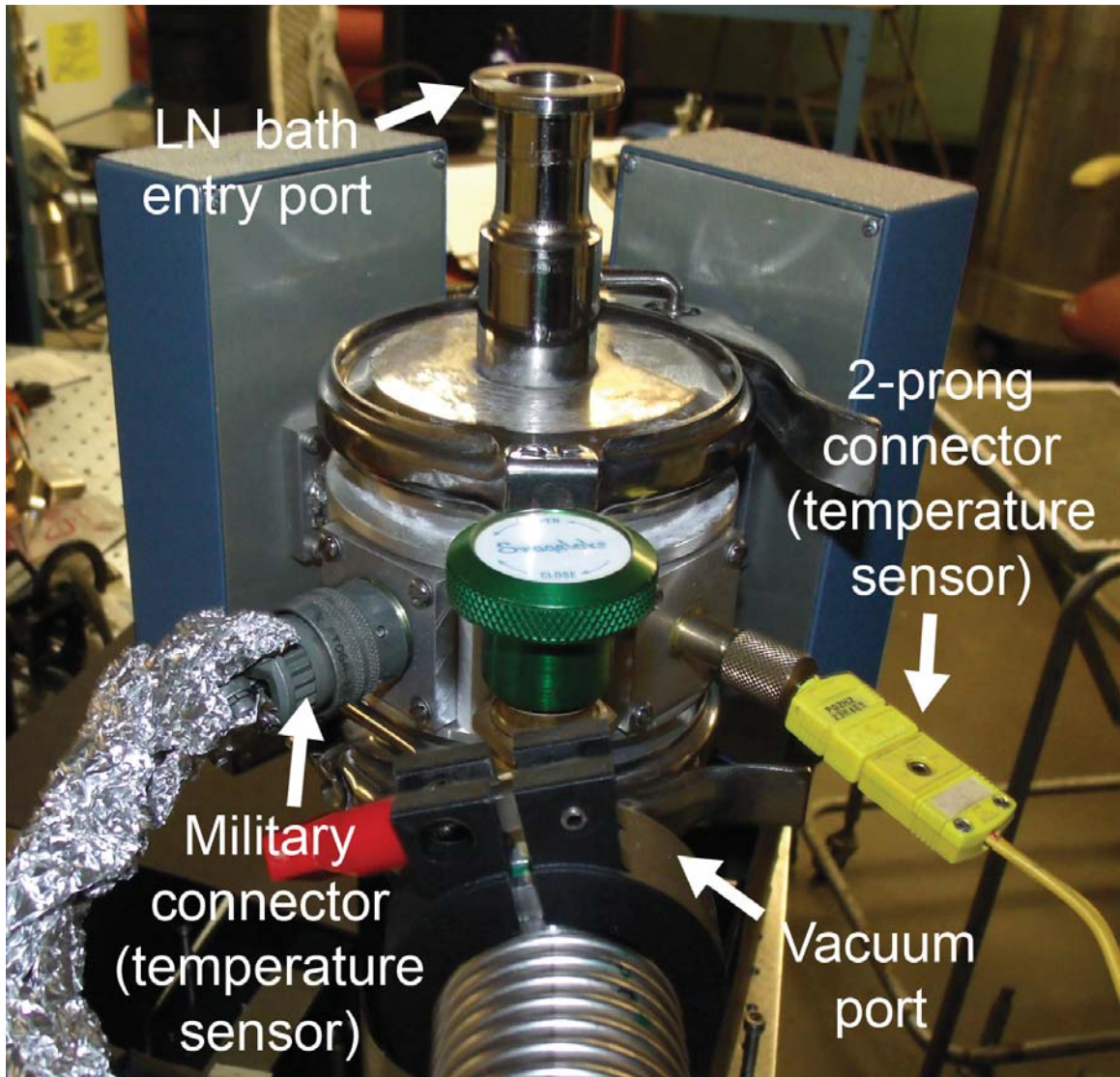


Figure 4.6: The temperature controller connects to the cryostat with a military connector and a two-prong plug. There is a port for a vacuum pump, and liquid nitrogen is added to the bath from the top.

so that the window would remain free of silver paste, and the chip could be easily removed when measurements are completed. The chip was then either wire bonded directly from the chip carrier to the contact pads or, if the sample was too fragile for bonding or the contact pads are not thick enough, the wire from the chip carrier could be carefully cut and silver pasted by hand to the contact pad. Getting the correct consistency of silver paste was key for this delicate procedure. If it was too runny, the paste would spread and possibly short to other wires, whereas if the paste was too thick, it would become stringy, and these strings could short to other wires. The paste was applied with a single, thin wire to ensure that the smallest drop of silver paste is achieved.

4.2 Microfluidics Setup

To reduce noise and the influence of outside signals, the microfluidics measurements were performed in an acoustic enclosure with the window covered, see Figure 4.7a. Inside, a second, smaller metal box served as a Faraday cage to further protect the measurement area, see Figure 4.7b, and there was microscope with a long working distance aperture. Note that the light for the microscope had to be unplugged during measurements to prevent extra noise. Inside the second box, there were three headstages that connect to a HEKA amplifier, micromanipulators that control small probes for contacting contact pads, and silver chloride (AgCl) electrodes for applying voltage to salt solutions, see Figure 4.8. The HEKA amplifier, see Figure 4.9, applied voltage and measured the current for our experiments, and it can do so on three channels, though this introduces crosstalk. A Keithley sourcemeter or battery was sometimes used instead, when a second channel measurement is needed.

To integrate our chips into our measurement setup, we created a polydimethyl-

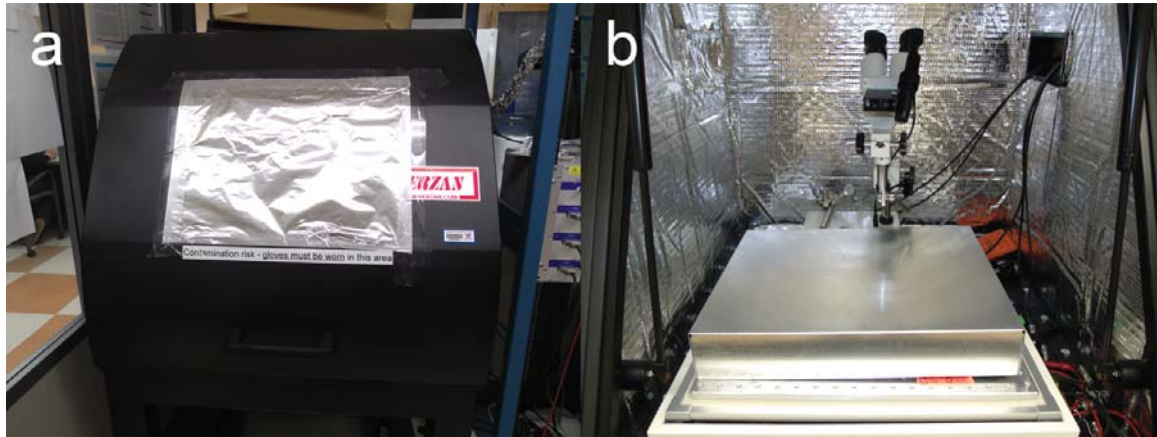


Figure 4.7: (a) The outer acoustic enclosure for the DNA measurements and (b) the inner Faraday cage that covers the cell and accompanying measurement devices.

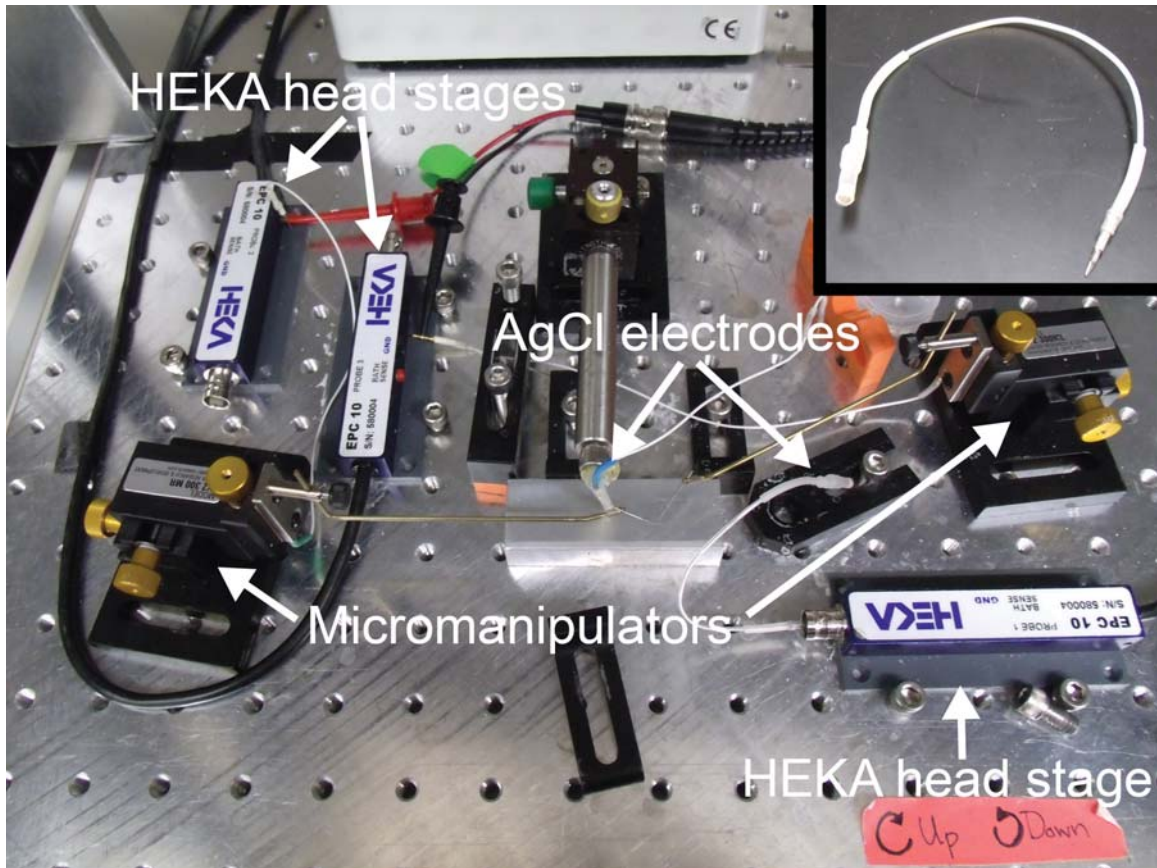


Figure 4.8: Inside the double enclosures, the apparatus includes three HEKA head stages, micromanipulators with probes, and AgCl electrodes. Inset: a close up of the AgCl electrodes.

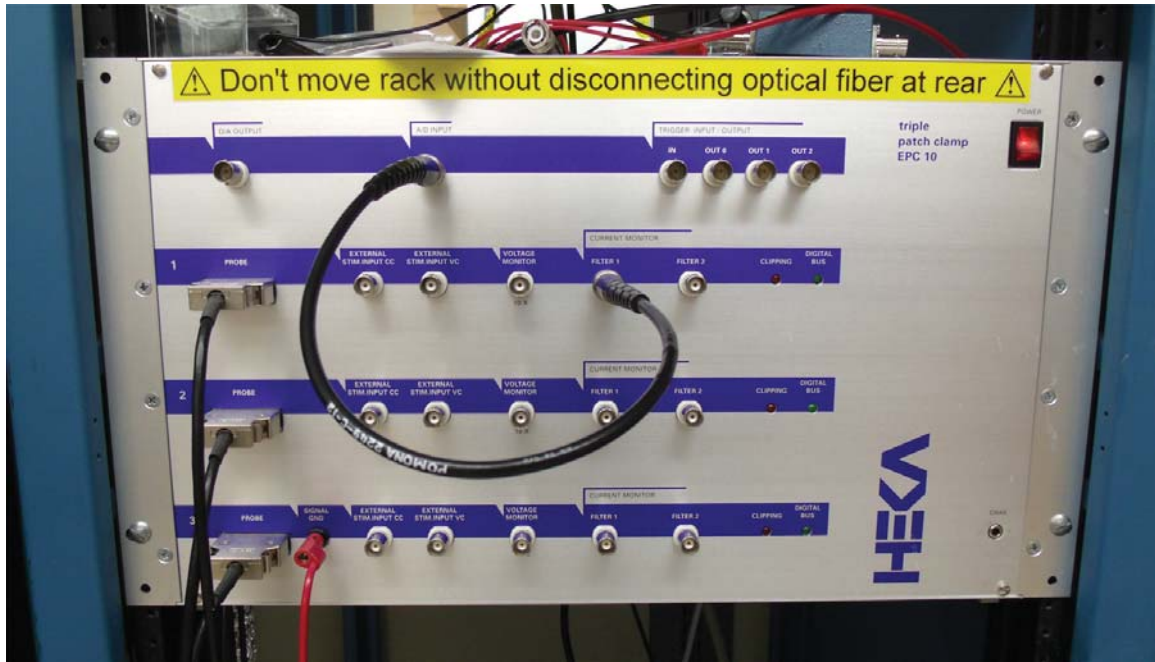


Figure 4.9: The HEKA amplifier.

siloxane (PDMS) fluidics cell. The PDMS cell was built using molds drawn in Auto-Cad 2009, then sent to Quickparts to be made from the Somos 18420 material using the stereolithography (SLA) process. The top and bottom pieces of the mold were put together and put in a small container with the channel on the bottom. This was to prevent bubbles getting trapped around the most crucial piece. The PDMS was degassed in a vacuum dessicator, and then poured into the container with the molds. This was placed in the vacuum desiccator and degassed until all bubbles are gone. The PDMS was then either be left to cure for a few days or put in an oven to speed the process. Once cured, a razor was used to free the mold from the excess PDMS, and then the cell was freed from the mold. Using oxygen plasma, the cell was bonded to a glass slide, creating microfluidic channels, see Figure 4.10a.

To attach our chips to the PDMS cell, we used a thinned, two-component elastomer, Ecoflex 5. Blue and yellow dyes were mixed with the components to discrim-

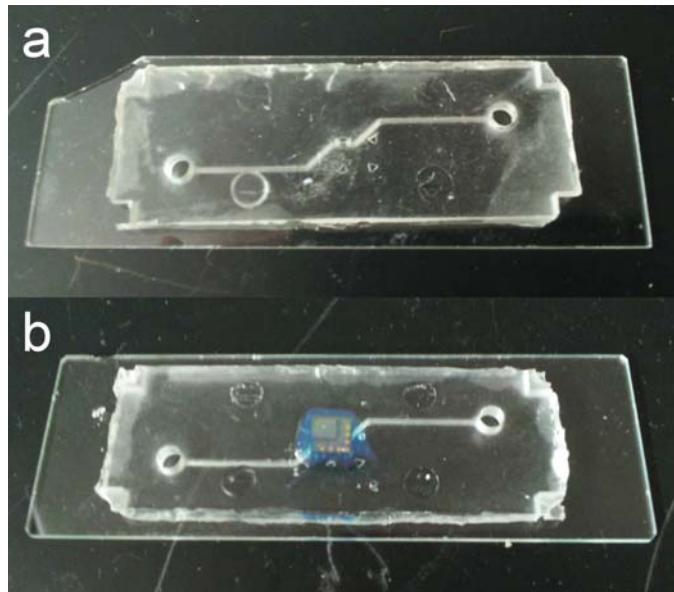


Figure 4.10: (a) A PDMS cell used for the DNA experiment. (b) A PDMS cell with a chip attached using QuickCast. A small well around the window has also been drawn with QuickCast for the top droplet.

inate between them, and the resulting green, once combined, ensured that they are well-mixed, see Figure 4.11. It would solidify within a minute, though the time varied due to other factors such as temperature and humidity. The chip was placed onto the center of the PDMS cell, where the two channels come to the surface close together. The positioning of the chip's well could be checked visually by holding the cell up to the light and viewing it from the bottom. Once the chip was properly positioned, the elastomer was mixed and then dripped onto the edges of the chip to seal it to the PDMS cell. A small amount of elastomer was carefully painted around the window area to create a well that sections off the window from the contact pads. This was usually applied with the tip of a small wire for more precision. See Figure 4.10b for an image of a chip attached to a cell. Solution can now be added to the channel through the large openings on either end of the PDMS cell and carefully added to the well on top of the chip.



Figure 4.11: A two-component elastomer is used to seal the chip to the PDMS cell. Once mixed, it solidifies within a minute.

CHAPTER 5

Synthesis and TEM Analysis of PbSe

5.1 Introduction

Lead selenide (PbSe) nanoparticles have been studied due to their semiconducting properties, small bandgaps,¹²³ and large Bohr radii.¹²⁴ However, the most common synthesis protocols^{125,126} use oleic acid as the ligand, which is long and insulating. They have previously been shown to not be conductive in a monolayer,¹²⁷ and even in multilayers, untreated films have low conduction.^{18,20} Decreasing the interparticle spacing can increase the electrical conduction of the particles, and this is traditionally done by performing a ligand exchange, adding a cross-linker, or annealing the sample.^{15–20}

It is possible that optoelectronic devices can be enhanced through the use of PbSe particles of various sizes and morphologies. The synthesis of PbSe nanoparticles has advanced, with reports on nanowires and nanorods,^{3,58,128} though the literature does not have quite the wide range as cadmium-based nanoparticles. Again, since transport strongly depends on how close particles are to each other, larger particles that retain some quantum confinement would be ideal.

Here we present work on exchanging the long oleic acid ligands with shorter amine chains, and examine the interparticle spacing with transmission electron microscopy (TEM). We also demonstrate a gold-seeded synthesis to make PbSe clusters that are clearly aggregates of smaller particles.

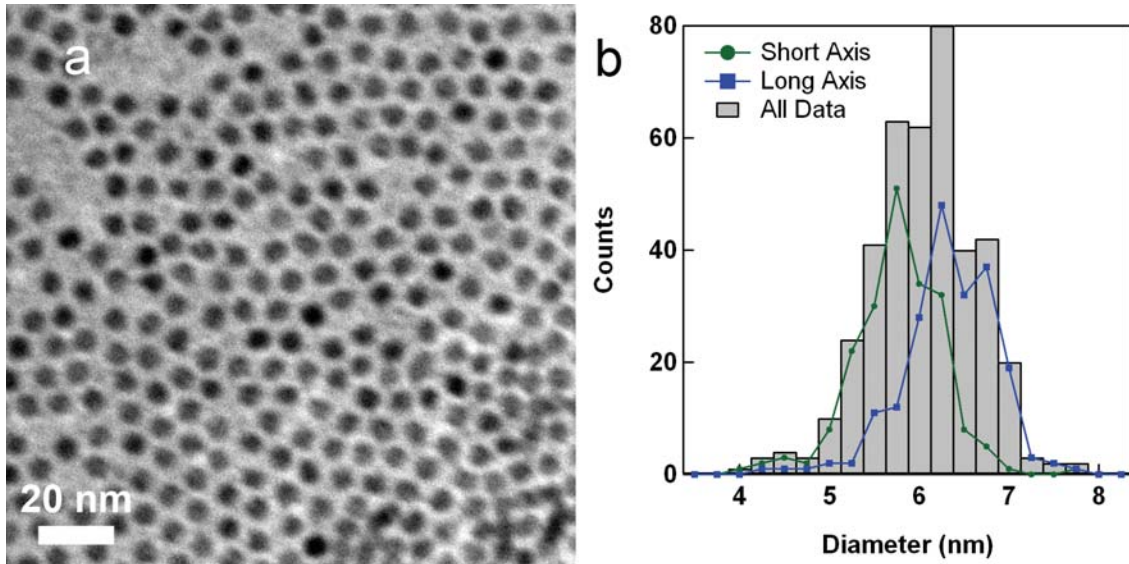


Figure 5.1: (a) Transmission electron micrograph (TEM) of PbSe nanocrystals. (b) Combined histogram of PbSe diameters. The green line with circles shows a histogram of only the short axis, and the blue line with squares shows a histogram of only the long axis.

5.2 Ligand Exchange

PbSe spheres suspended in hexane with an absorption peak at 1900 nm were purchased from Evident Technologies. TEM samples were prepared by dropcasting a solution of the PbSe nanocrystals onto a carbon grid and allowing it to dry in the hood or under vacuum, see Figure 5.1a. The average diameter of the nanocrystals was found to be 6.18 ± 0.56 nm, see Figure 5.1b for a histogram of diameters. Since visual inspection of the TEM images showed that the nanocrystals were not quite spherical, each particle was measured twice: once along its longest axis and once perpendicular to the first measurement.

5.2.1 Ligand Calculation

To exchange the oleic acid for another ligand, nanoparticles were added to a vial with approximately a 500 to 1000 times excess of the ligand. This required an estimate of the number of oleic acid molecules on each nanoparticle. Approximating the nanocrystals as spheres with radius, r_{NC} , the volume is given by

$$V = \frac{4}{3}\pi r_{NC}^3. \quad (5.1)$$

Given the density of the nanocrystal, ρ_{NC} , the mass, m_{NC} , is then given by

$$m_{NC} = \rho_{NC} V_{NC}. \quad (5.2)$$

Note that to change g/cm³ into g/nm³, multiply by 10⁻²¹. To change the mass of the nanocrystal from grams to moles, divide by the molecular weight, MW . The number of molecules, N , is

$$N = m_{NC} N_A, \quad (5.3)$$

where N_A is Avagadro's number, 6.022×10^{23} particles/mol. Given the nearest neighbor spacing, d_{NN} , find the number of molecules in a nanocrystal that has a radius, $r_2 = r_{NC} - d_{NN}$, which is

$$N_{r_2} = \frac{4}{3}\pi \rho_{NC} (r_{NC} - d_{NN})^3 N_A. \quad (5.4)$$

The number of molecules in the outermost layer of the nanocrystal is the difference between Equations 5.3 and 5.4. Combining Equations 5.1 to 5.4, the number of outer

Variable	Value
ρ_{NC}	$8.1 \times 10^{-21} \text{ g/nm}^3$
MW	286.16 g/mol
r_{NC}	3.09 nm
d_{NN}	0.264 nm

Table 5.1: Variables used in the calculation for the number of oleic acid ligands on the surface of a PbSe nanocrystal.

layer molecules, N_{outer} , is

$$N_{outer} = \frac{4\pi\rho_{NC}N_A}{3MW} [r_{NC}^3 - (r_{NC} - d_{NN})^3]. \quad (5.5)$$

Note that the lattice parameter of molecules may be difficult to find. It is possible to use the sum of the covalent radii of the atoms to estimate a lattice parameter. Using the parameters in Table 5.1, Equation 5.5 gives approximately 500 atoms on the outside of a PbSe nanocrystal. For PbSe, approximately 70% of the surface atoms are Se, and oxygen penetrates the surface, possibly substituting for the Se atoms.¹²⁹ This is the opposite of oxidized cadmium selenide (CdSe), for which approximately 70% of the surface atoms will be Cd, since Se oxidizes easily, and the resulting SeO_2 can be desorbed from the surface,¹² and oxygen does not quickly penetrate far into the nanocrystal.

The PbSe (Evidot, 1900 nm absorption) in hexane comes in a stock solution of $5 \times 10^{-9} \text{ mol/mL}$. For a typical ligand exchange, Vial 1 with 20 μL of the PbSe stock solution and 800 μL of hexane was prepared, which has diluted the PbSe nanocrystals to 10^{-10} mol in 820 μL of hexane. Vial 2 with 41 μL of octylamine (Aldrich, 99%) in 2 mL of hexane (Fisher Scientific, HPLC grade) was prepared. This has approximately $2.5 \times 10^{-4} \text{ mol}$ of octylamine. For actual ligand exchange, 82 μL of Vial 1, 20 μL of Vial 2, and 180 μL of hexane are combined. This has 10^{-11} moles of PbSe, which would have approximately $5 \times 10^{-9} \text{ moles}$ of surface atoms, and $2.5 \times 10^{-6} \text{ moles}$ of

octylamine, which gives a 500 times excess. After waiting at least an hour, a few microliters of solution was dropcast onto TEM grids and allowed to dry.

5.2.2 Results

TEM imaging found that the nanocrystals with oleic acid and hexylamine had assembled into well-ordered hexagonal films, see Figures 5.2a and c. However, when the ligand was octylamine or butylamine, the films was less ordered, see Figures 5.2b and d. Note that there are also some nanorods in Figure 5.2d, which suggest that some of the PbSe spheres have fused, possibly due to the ligand being very short, and therefore, less effective at steric hindrance. Interparticle spacing was measured in areas with good hexagonal packing. Samples were of different dilutions, but all dropcast from hexane only, rather than adding octane to enhance the superlattice.

The average interparticle spacing for untreated PbSe nanocrystals with oleic acid was 2.11 ± 0.64 nm, see Figure 5.3a. This was found from 3036 measurements from seven different dropcasts. When the oleic acid was replaced with octylamine, which has a length of 1.2 nm, the average interparticle spacing was 1.00 ± 0.43 nm, see Figure 5.3b. This was an average of 4351 measurements from three different ligand exchanges. The average interparticle spacing for the ligand hexylamine, which is 0.9 nm long, was 1.07 ± 0.48 nm, which was calculated from 2817 points from one ligand exchange, see Figure 5.3c. For the ligand butylamine, the average interparticle spacing was 1.22 ± 0.56 from 879 measurements of one ligand exchange, see Figure 5.3c. This data is summarized in Table 5.2.

The averages for the ligand exchanges all show a decrease in the interparticle spacing by at least 40%, see Figure 5.4 for histograms of all four ligands graphed together with the same binning. However, the standard deviation for all of the averages were very large. Another factor besides the size of the ligand that affected these

Ligand	Ligand Length (nm)	Average Spacing (nm)	# of Points	# of Dropcasts
Oleic Acid	2.5	2.11 ± 0.64	3036	7
Octylamine	1.2	1.00 ± 0.43	4351	4
Hexylamine	0.9	1.07 ± 0.48	2817	1
Butylamine	0.6	1.22 ± 0.56	879	1

Table 5.2: Summary of interparticle spacing results for different ligands.

measurements was the uniformity of the nanocrystal assembly.

A ligand exchange was attempted with diaminoheptane and octylamine, with the assumption that a bi-functionalized molecule would better attach to a nanocrystal on each end, decreasing the interparticle spacing even further. However, even when a small amount of diaminoheptane was added, the nanocrystals became irregularly shaped, with aggregation and no ordered assembly, see Figure 5.5.

5.3 Clusters

5.3.1 Synthesis

The following synthesis is a gold-seeded growth of PbSe clusters based on previous work by Yong et al.¹²⁸ The gold nanoparticles were synthesized with a two-phase approach.¹³⁰ A typical synthesis began with a preparation of 0.04 g of gold (III) chloride (HAuCl_4 , Sigma-Aldrich, 99.99%) in 23.5 mL of deionized water. A second solution of 0.15 g of tetraoctylammonium bromide (TOAB) (Sigma-Aldrich, 98%) in 10.5 mL of toluene (Fisher Scientific, HPLC grade) was made. In a flask, 5 mL of the aqueous gold solution was mixed with 2.5 mL of the organic TOAB solution. After stirring for 20 minutes, the clear aqueous phase was discarded and the red-orange organic phase was pipetted into a new flask. A solution of 0.07 g of dodecylamine (Sigma-Aldrich, 98%) in 2.50 mL of toluene was prepared, and 1.25 mL of the dodecylamine solution

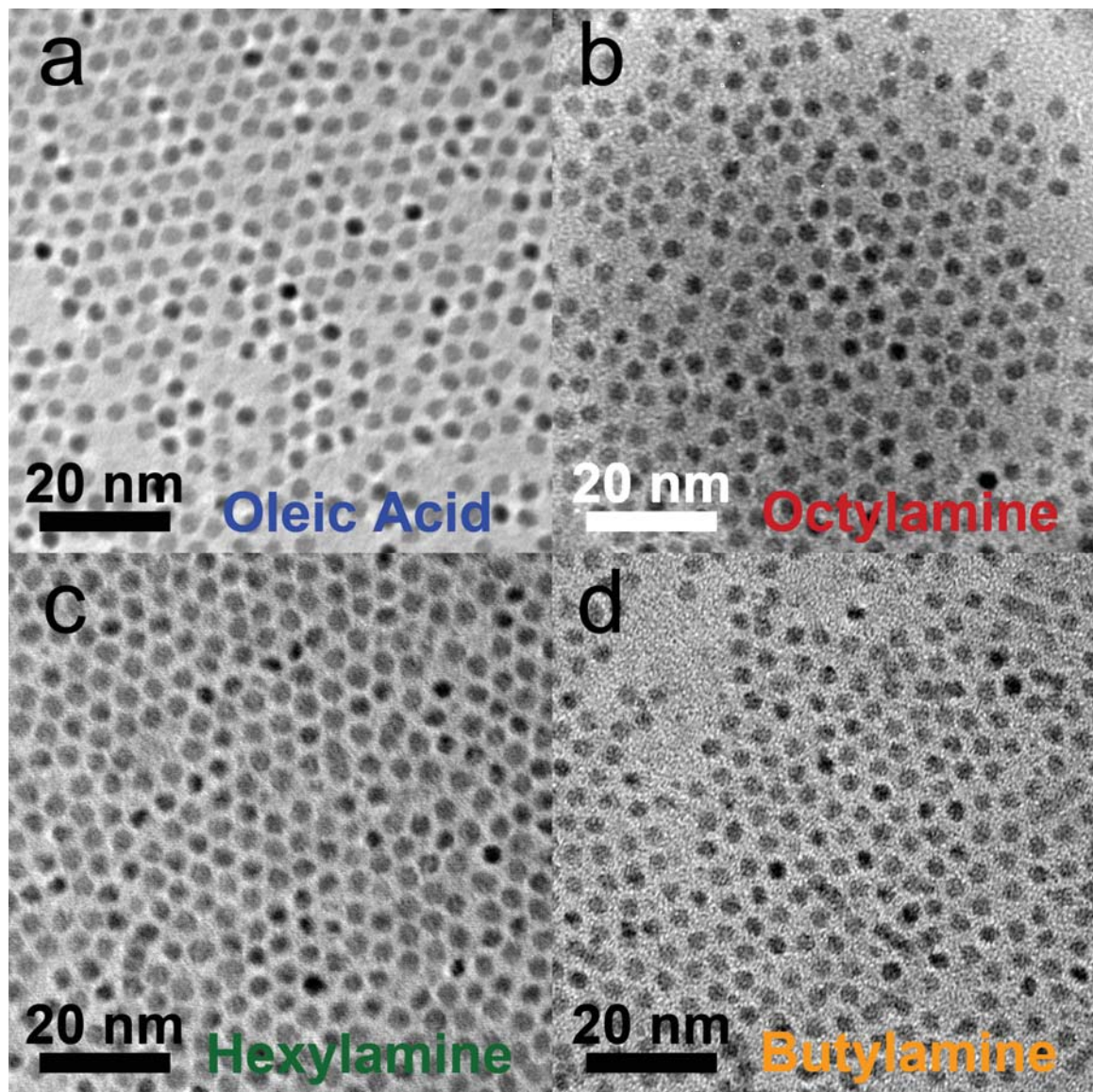


Figure 5.2: TEM images of PbSe assembly when the ligand was (a) oleic acid, (b) octylamine, (c) hexylamine, and (d) butylamine. The nanocrystals with oleic acid and hexylamine were well-assembled, and the nanocrystals with octylamine and butylamine were more poorly assembled.

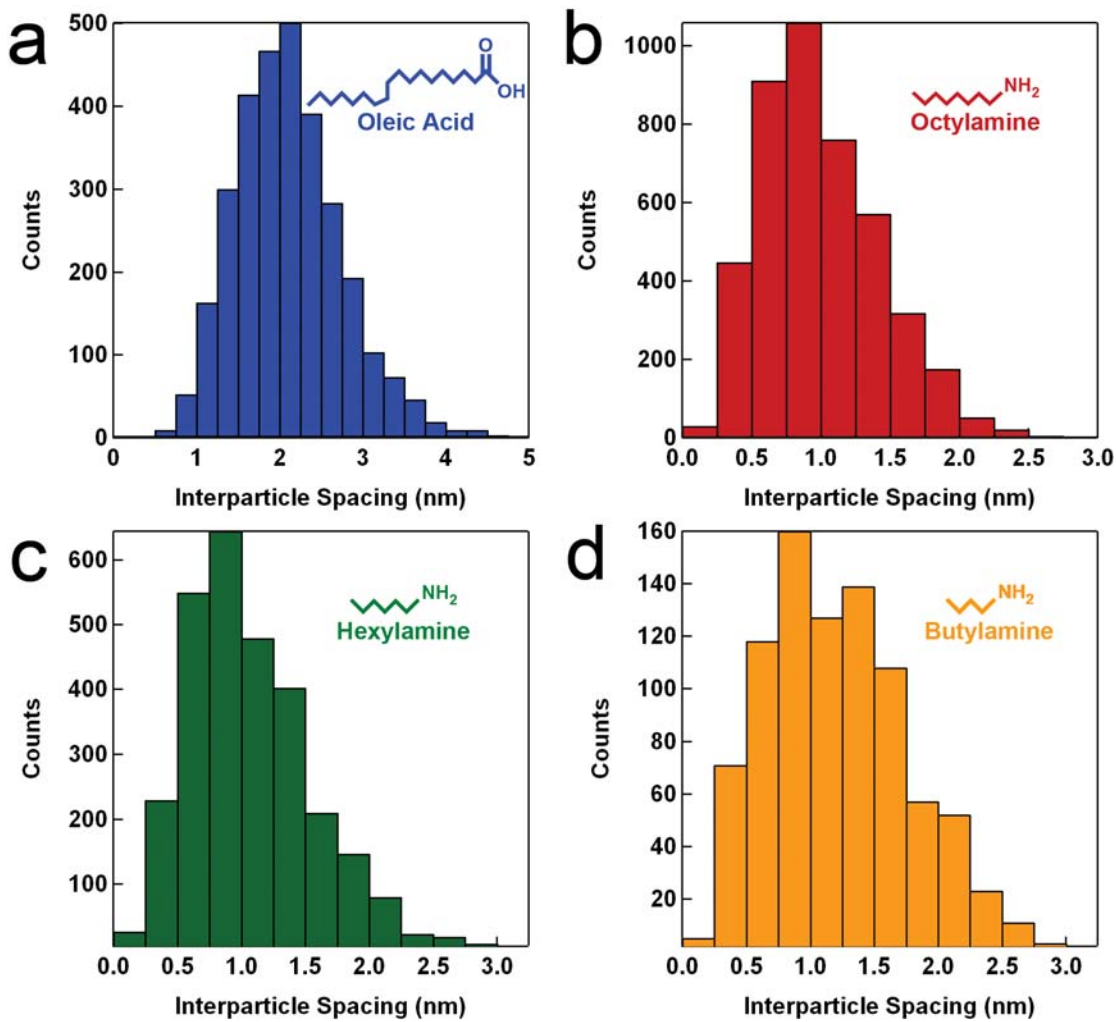


Figure 5.3: Histograms of interparticle spacing when the ligand was (a) oleic acid, (b) octylamine, (c) hexylamine, and (d) butylamine. The average spacing was 2.11 ± 0.64 nm for oleic acid, 1.00 ± 0.43 nm for octylamine, 1.07 ± 0.48 nm for hexylamine, and 1.22 ± 0.56 nm for butylamine.

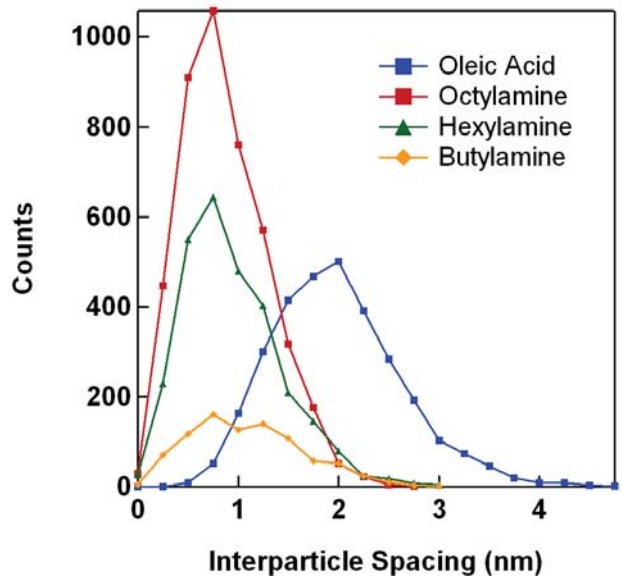


Figure 5.4: Combined histograms with the same binning of interparticle spacing when the ligand was oleic acid, octylamine, hexylamine, and butylamine.

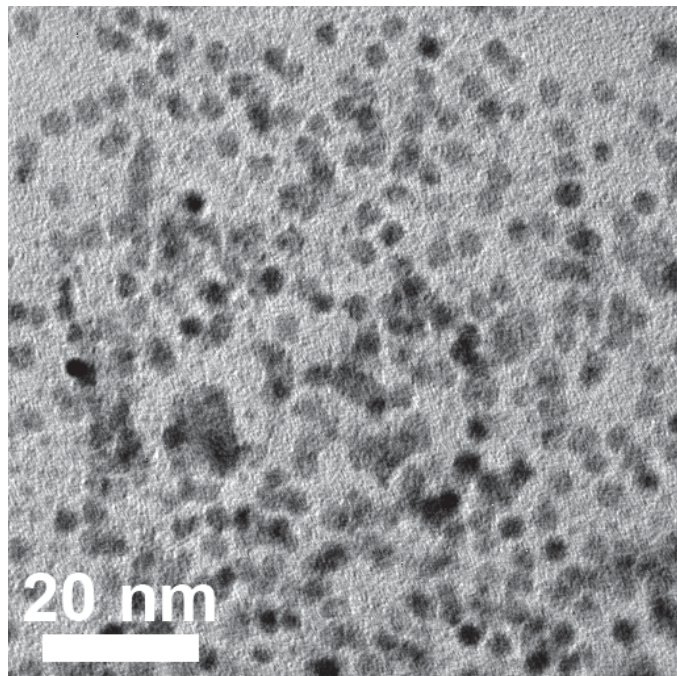


Figure 5.5: TEM of PbSe nanocrystals with a ligand exchange of diaminoheptane and octylamine. The nanocrystals became irregular and aggregated, with no ordered assembly.

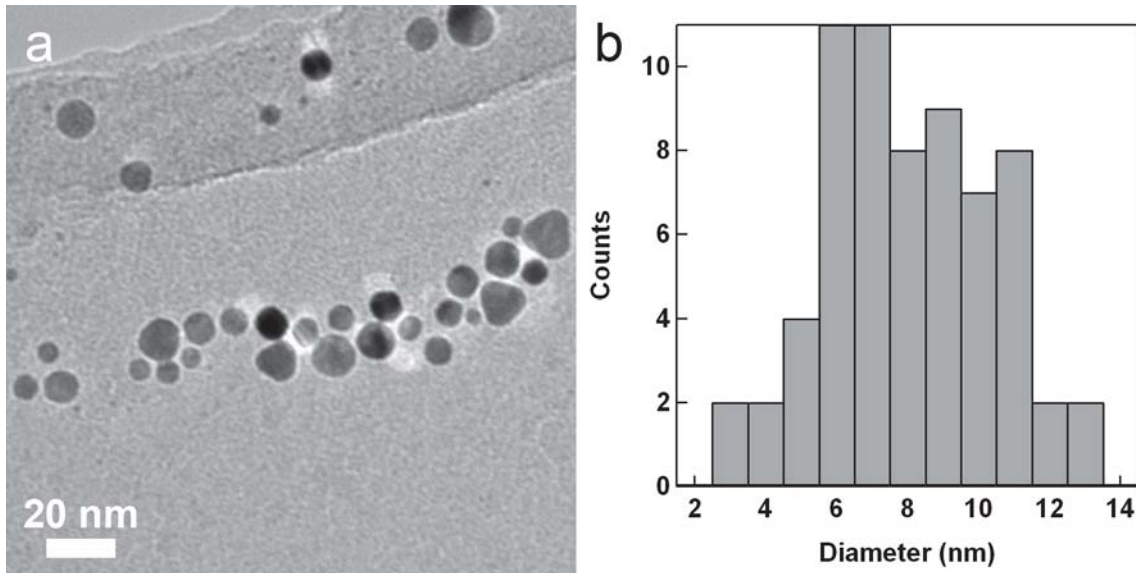


Figure 5.6: (a) TEM of synthesized gold nanocrystals. (b) Histogram of nanocrystal diameters. Each nanocrystal was measured twice, with the two measurements approximately perpendicular to each other.

was added to the flask. A solution of 0.0097 g of sodium borohydrate in 2.5 mL of water was prepared. Slowly, drop-by-drop, 1.25 mL of the sodium borohydrate (Sigma-Aldrich, 99%) solution was added, while stirring. After just a few drops, the solution turned red-black. After stirring for approximately 6 hours, the red-black organic phase was saved, and the aqueous phase was discarded. Toluene was added to the organic phase to bring its volume to 5 mL.

TEM imaging of the gold nanoparticles showed a large size distribution, including triangular and spherical particles, see Figure 5.6a. The average diameter of the particles was 8.1 nm with a standard deviation of 2.3 nm, see Figure 5.6b.

Typically, 0.06 g of lead (II) oxide (PbO, Acros, 99.999%) and 0.45 g of oleic acid (Aldrich, technical grade, 90%) was dissolved in 3.24 g of phenyl ether (Sigma-Aldrich, ≥ 99%) at 150°C for 30 minutes. The color of the solution was usually light orange. 0.0015 g of dodecylamine in 500 μL of toluene was added to the flask. A solution

Dodecylamine	Major axis (nm)	Minor axis (nm)
11×	22.99 ± 3.13 (14%)	20.34 ± 2.80 (14%)
2×	32.28 ± 7.65 (24%)	28.99 ± 7.31 (25%)
1×	22.17 ± 4.67 (21%)	18.25 ± 5.46 (30%)
20×	22.49 ± 2.39 (11%)	19.30 ± 1.93 (10%)
39×	32.27 ± 4.76 (15%)	26.81 ± 5.00 (19%)
30×	14.86 ± 3.97 (27%)	11.82 ± 2.82 (24%)

Table 5.3: Summary of interparticle spacing results for different ligands.

of 600 μL of toluene and 200 μL of gold from the synthesis is made, and 100 μL of this dilution is added to the lead precursor. A solution of 2 mL of trioctylphosphine (TOP) (Sigma-Aldrich, technical grade, 90%) and 0.0809 g of Se (Sigma-Aldrich, ~100 mesh, $\geq 99.5\%$) was freshly prepared. 0.5 mL of the TOP-Se solution was quickly injected into the lead precursor. The temperature dropped to approximately 142°C. The solution changed to a dark red after approximately one minute. The heat source was removed at four minutes. Methanol was added, and the particles were centrifuged out. Nitrogen was added to the vials to prevent oxidation.

5.3.2 Results

A sample TEM image of the synthesis showed clusters of aggregated particles, where the individual particles are still distinct, see Figure 5.7a. Sometimes two different sized clusters would appear in the same synthesis, see Figures 5.7b and c. Size analysis of the TEM images were performed by marking the outline of a cluster and then approximating it as an ellipse in ImageJ. The amount of dodecylamine was varied to see if the size of the clusters would change; however, they did not seem to correlate, see Table 5.3. One synthesis was allowed to run for thirty minutes. The clusters were made up of very pronounced ellipsoids, rather than the more randomly shaped particles that made up the clusters in the four minute syntheses, see Figure 5.8.

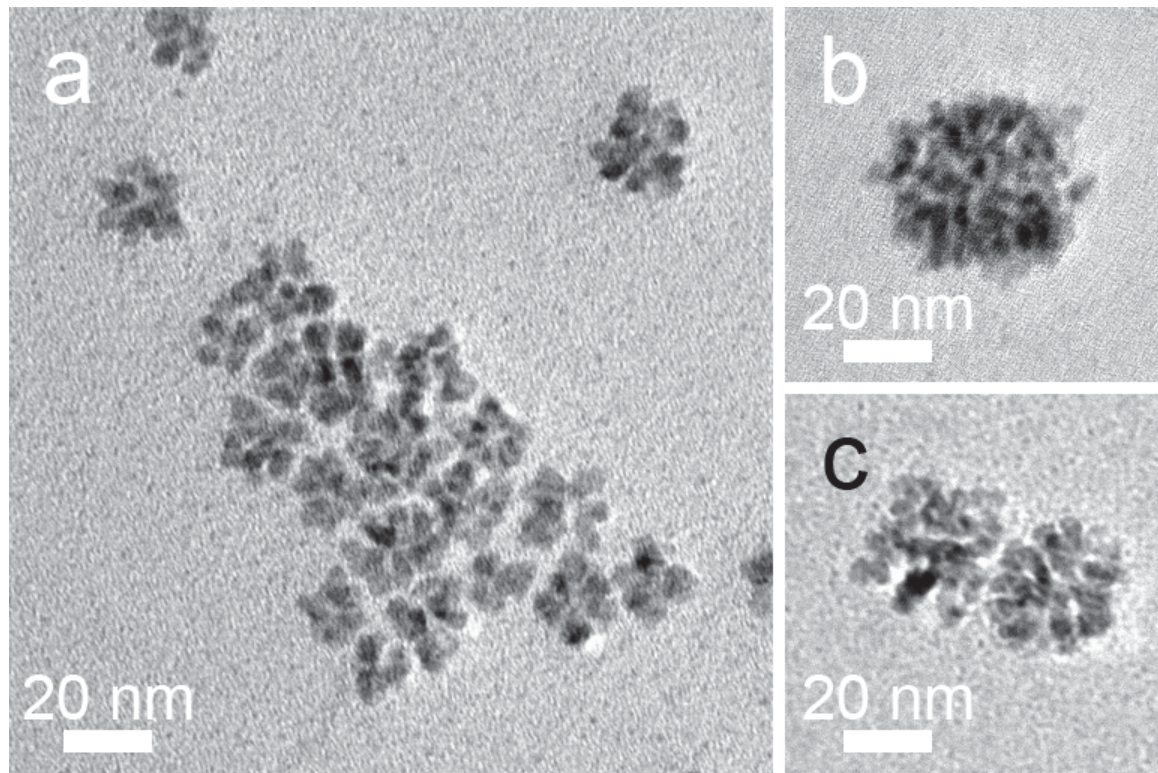


Figure 5.7: Cluster of aggregated PbSe particles.

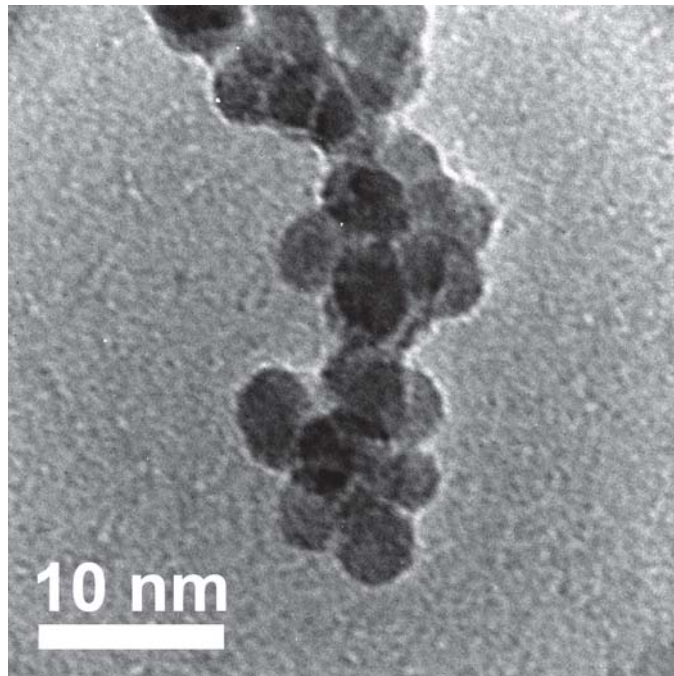


Figure 5.8: For a longer synthesis, the particles that compose the clusters are more well-defined ellipsoids.

5.4 Conclusions

The ligand exchanges from oleic acid to shorter amine chains were effective in decreasing the interparticle spacing for PbSe nanocrystals. The exchanges to octylamine, hexylamine, and butylamine gave similar interparticle spacings, and the assembly of the films may account for discrepancies in correlation between size of the chain and interparticle spacing. However, butylamine increased agglomeration, and the results from diaminoheptane were even more severe. Future work could include trying to incorporate diamines and even shorter ligands after dropcasting the nanocrystals, by soaking the sample in a solution of the new ligand. This could increase attachment without affecting the film quality.

A gold seeded PbSe synthesis yielded clusters that were agglomerations of smaller particles. They were slightly non-symmetric, and some were more rectangular than

elliptical. It was also possible that there were multiple size regimes within the same synthesis, though further size selection and more monodisperse gold seeds could eliminate this. Future work includes studying the agglomerations with TEM from aliquots taken during the synthesis, as well as testing the effects of temperature and other ligands. The spectra of the agglomerations should also be studied to see if the smaller particles within it retain any quantum effects.

CHAPTER 6

Lead Selenide Nanorod Measurements

6.1 Introduction

Nanoparticles have been a burgeoning field of interest for their broad range of optoelectronic applications including light emitters,^{131–134} photodetectors,^{19,135,136} and solar cells.^{137,138} Their tunability gives increased flexibility to study transport, though their insulating nature, as-synthesized,^{18,20} is a challenge. Many treatments have been proposed to increase their conductivity, usually by decreasing interparticle spacing or providing chemical linkers between particles in films.^{15,18–20} Little work has been done on small numbers of particles, as opposed to films.

Lead selenide (PbSe), in particular, is an attractive material to study nanoparticle transport because of its low bandgap and large Bohr radii.¹²⁴ This has made it an interesting material for a variety of optoelectronic devices, especially solar cells, due to the multiple exciton effect.^{48,139} This allows the possibility of surpassing the Shockley-Queisser limit,¹⁴⁰ because some of the previously “lost” energy can be harvested as a high energy exciton turns into multiple, lower energy excitons. However, building devices to harness this property can be challenging.

Films of quantum dots are generally highly insulating, various treatments and ligand exchanges have been reported to vastly increase its transport.^{15,18–20} Most studies have focused on spherical particles due to their well-established synthesis protocols^{125,126} and self-assembled close packing, but nanorods are also interesting due to their in-plane quantum confinement with an elongation along the c-axis to

enhance conduction. Devices for studies of small-number particle systems are now more easily fabricated with simple lithography techniques to explore properties that may be obscured by ensemble measurements.

Here we compare the charge transport of sub-monolayer networks of PbSe nanorods untreated, annealed, and with hydrazine. Annealing was of limited use for increasing conductivity of our PbSe rod networks, though it has improved other semiconducting nanoparticle films. Hydrazine greatly increased conductivity in the dark; however, photocurrent was low, suggesting that the photogenerated carriers were destroyed through recombination.

6.2 Synthesis

The synthesis of these rods is reported by Koh et al.⁵⁸ The following is a summary of a typical synthesis: 0.22 g of lead (II) oxide (PbO) was dissolved in 5 mL of squalene or 1-octadecene (ODE) and 1 mL of oleic acid (OA). The solution is dried under nitrogen atmosphere at 150°C for 30 minutes, then heated to 170°C. 3 mL of a 1M tris(diethylamino)phosphine (TDP) and selenium (Se) solution was injected into the lead precursor under vigorous stirring. To end the reaction, the solution was cooled with a water bath. Size-selective precipitation is used to increase the monodispersity.

The synthesis reported by Koh et al.⁵⁸ was an improvement on previous PbSe rod syntheses due to its simple one-pot method, free of catalysts. This is a result of the use of TDP-Se as the selenium precursor rather than the usual trioctylphosphine-(TOP-) Se precursor, which allows for the reaction to take place at lower temperatures and over longer time scales.

The length of the rods for this experiment were determined to be 49.2 nm with a standard deviation of 4.31 nm, with a diameter of 4.2 nm and a standard deviation

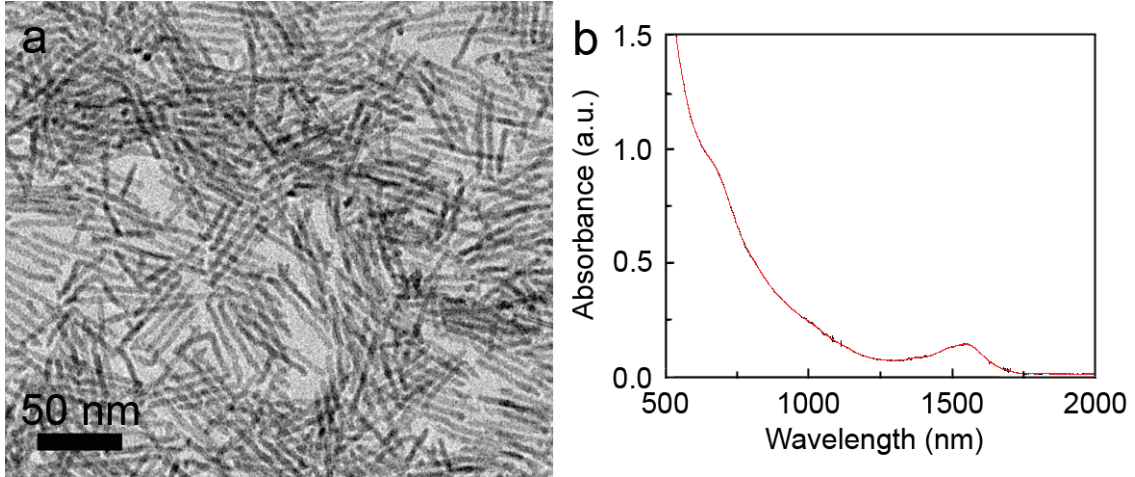


Figure 6.1: (a) TEM image of the PbSe rods. (b) Absorbance spectrum for the PbSe rods. Images courtesy of Weon-kyu Koh.

of 0.25 nm. These numbers were found by analyzing TEM images of the rods, see Figure 6.1a. Their absorbance spectrum is shown in Figure 6.1b, with the excitonic peak at approximately 1600 nm.

6.3 Device Fabrication

Figure 6.2 shows the CAD schematic of the transport device with a close-up of the gap area. Electron beam lithography (EBL) was used to pattern electrodes on a silicon nitride membrane. Thermal evaporation was used to deposit 3 nm of Ni and 30 nm of Au. Photolithography was used to pattern large wires and contact pads, followed by evaporation of 3 nm of Cr and 100 nm of Au. Lift-off for all the lithographies was done in acetone after an overnight soak.

A thin membrane is important for device fabrication due to its compatibility with high resolution TEM, as well as its reduction in backscattering during EBL. Before measurement, the gaps were inspected with TEM and some metallic debris could be seen left over from lift-off, shown in Figure 6.3a. The TEM beam can be

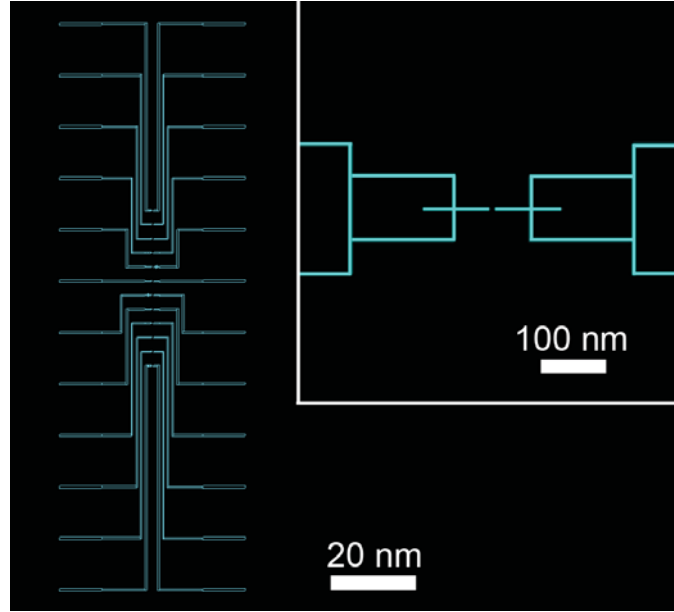


Figure 6.2: CAD schematic of the EBL electrodes. Inset: Close-up of a gap.

focused and used to ablate the metal off the substrate completely or the metal can be partially melted, causing it to migrate to the larger electrode nearby. Figure 6.3b shows the gap after the cleaning treatment has been applied. Slight changes to the electrodes both in shape and crystallinity can be seen.

6.4 Measurement Setup and Background Measurements

Electrical measurements were performed in a modified Janis ST-100H cryostat operated at $\sim 5 \times 10^{-7}$ torr. The devices were wired to a ceramic chip carrier thermally coupled to a copper cold finger and electrically addressed by silver-soldered wires. The source and drain electrodes of each pair were connected to two independent BNC breakout boxes. A Yokogawa 7651 programmable dc source was used to apply voltages. Currents were amplified and sampled at 3.33 Hz by a Keithley 428, and

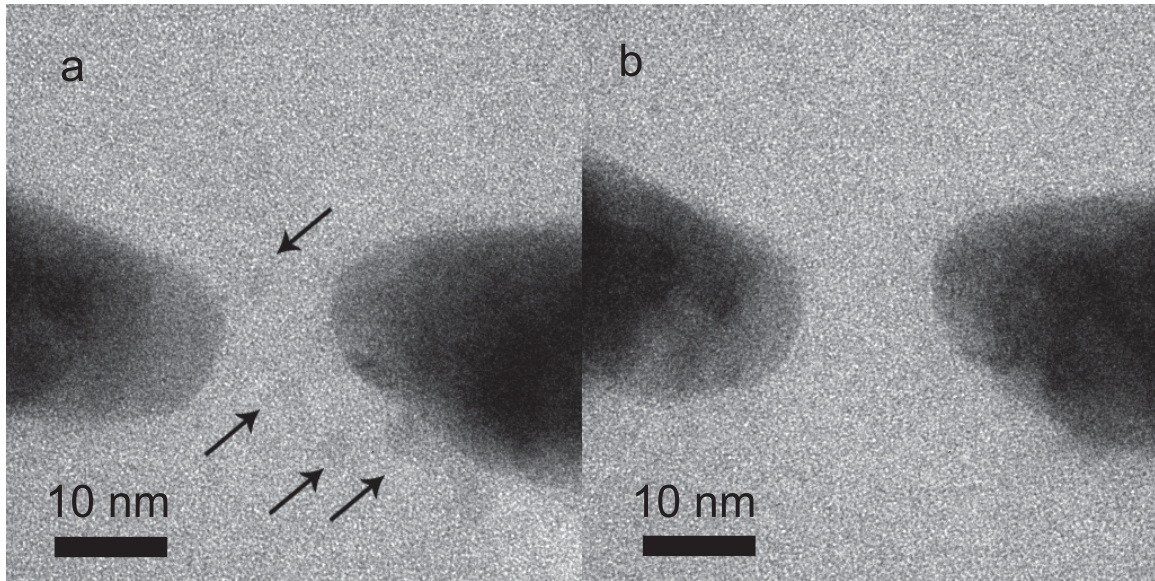


Figure 6.3: (a) TEM image of a gap before cleaning. Small metallic debris left after liftoff is indicated by arrows. (b) TEM image of the same gap after using the TEM beam to clean off the metal.

read by an Agilent 34401A digital multimeter. The IV sweeps for each device were measured by sweeping the voltage across the nanogap from 0 V to 0.5 V to -0.5 V and back to 0 V, with a typical cycle taking 200 seconds. Prior to nanocrystal deposition and after TEM inspection, the bare devices were cleaned with an O₂ plasma, then the conductance and photoresponse of the bare devices were tested. Dark measurements of devices were performed by taking an IV sweep with the nanogap in the dark, and laser measurements were performed by taking an IV sweep while the nanogap was illuminated by a continuous wave 532 nm diode laser. In each measurement set, we measured, at room temperature, the dark current of all devices on a chip, and then the photocurrent of the same devices; the device was then cooled with liquid nitrogen in a chicken feeder dewar, and both dark current and photocurrent were measured again at low temperature.

Out of the 18 gaps tested, 14 had flat, low background current. Figures 6.4a and b show a sample background measurement of such a device, which will be referred to

as Gap 1. One gap did show some background current, shown in Figures 6.4c and d, though since the current is lower than the expected signal, it was still used for measurements, and will be referred to as Gap 2. It is possible that debris in the gap from accidental electromigration could have caused this anomalous current.^{141,142}

Half of these gaps were opened to atmosphere and mercaptopropionic acid (MPA) was dropcast onto them, followed by a double rinse in acetone. The thiol in the MPA should bind well to the gold electrodes, and the carboxylic group should bind to the nanorod; this could encourage the nanorods to selectively bind to the electrode area. Measurements were taken again to ensure that the thiol did not change the background measurements. These gaps are later used in measurements with annealing and hydrazine, whereas the untreated gaps were used for measurements with only annealing.

6.5 Results

6.5.1 No Treatment

After the background measurements, nanorods were dropcast at atmospheric pressure, washed with ethanol, and then returned to vacuum after a few minutes. Figures 6.5a and b show the current for dark and laser measurements of the PbSe rods in Gap 1. The currents are comparable in magnitude to the background measurements, indicating that without treatment, these rods are highly insulating. Figures 6.5c and d show the current of the PbSe rods in the dark and with the laser in Gap 2. At room temperature, the current in the dark was less than the background measurements in the dark, which could be caused by changes to the electrodes such as electromigration or adsorption of metal debris. The current with the laser is larger than the dark current, indicating that the rods are photosensitive. At 79K, the current

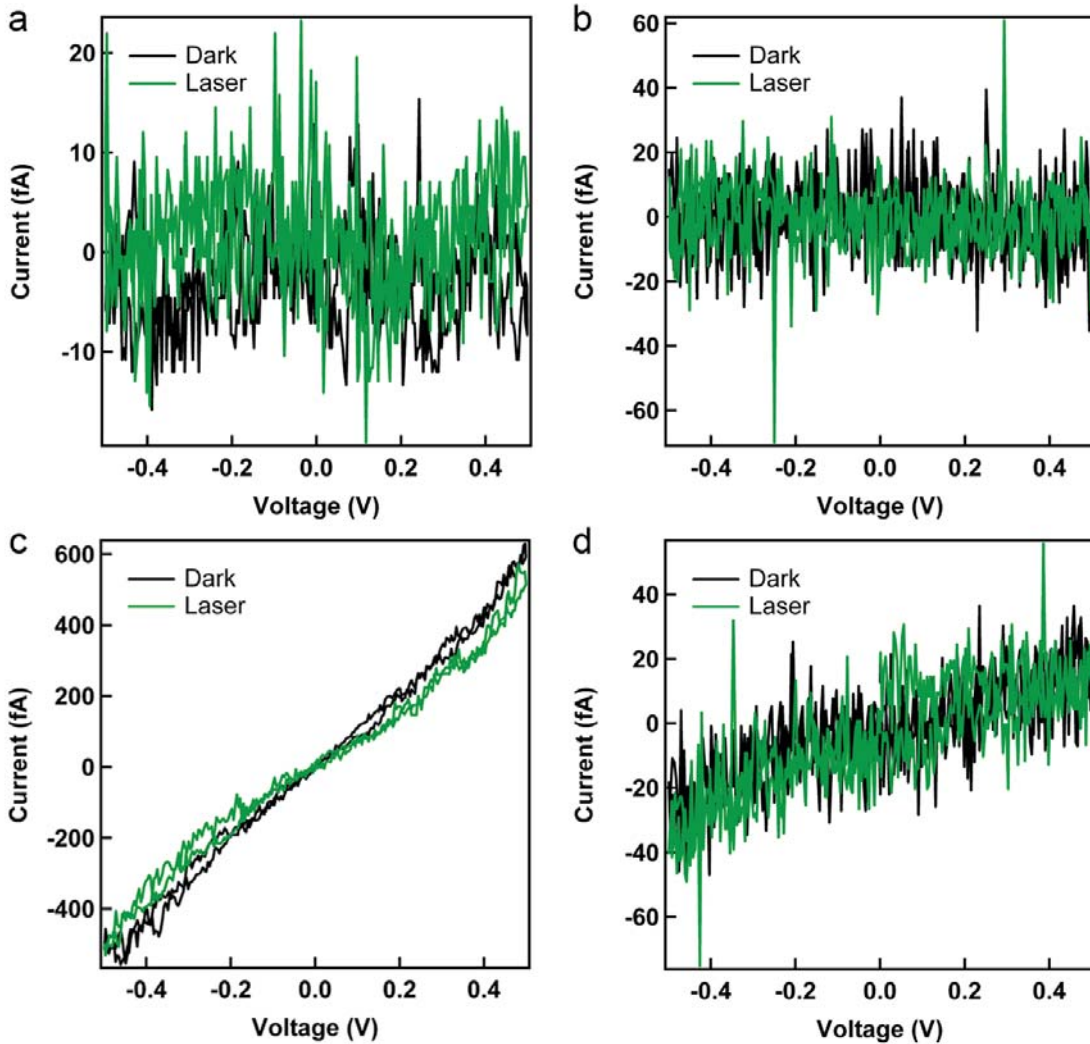


Figure 6.4: Background measurements of current in the dark and with the laser before PbSe rods were added to Gap 1 at (a) room temperature and (b) 79K. Background measurements of current in the dark and with the laser for a device with a measurable current, Gap 2, at (c) room temperature and (d) 79K.

measured is comparable to the background measurements, which is unusual due to thermal releasing of trapped charges which can recombine with charges that would have otherwise been collected by the electrodes.

6.5.2 Annealing

Devices were annealed *in situ* at 150°C for one hour and then allowed to cool. Figures 6.6a and b show the dark and laser current measurements for Gap 1. Figures 6.6c and d show the dark and laser current measurements of the annealed devices at room temperature and 79K for Gap 2. Figure 6.7 shows the calculated photocurrent for Gap 1. This was calculated by fitting a fifth order polynomial, with an R-value greater than 0.993, to the current measured in the dark and subtracting that fit from the current measured with the laser. The magnitudes of the current in the dark and with the laser were increased by annealing at room temperature. However, the amount of photocurrent did not increase with annealing, see Figure 6.8. There is no change at low temperature. The dark currents in Figure 6.8a were calculated by fitting a fifth order polynomial to the background dark current and subtracting that fit from the current measured from the rods in the dark. Similarly, the photocurrents in 6.8b were calculated by fitting a fifth order polynomial to the currents measured in the dark and subtracting that fit from the current measured with the laser. The R-values for all of the fits were greater than 0.998.

Half of the gaps measured were removed from the cryostat for TEM imaging. A close-up of the gap region before measurement is shown in Figure 6.9a. Before measurements, the gap size was approximately 14.5 nm at its narrowest point. Figure 6.9b shows the gap after PbSe rods were dropcast onto the sample and transport measurements were taken. After the measurement the gap is approximately 36.8 nm, suggesting that the gap was enlarged by electromigration. Some gaps showed no

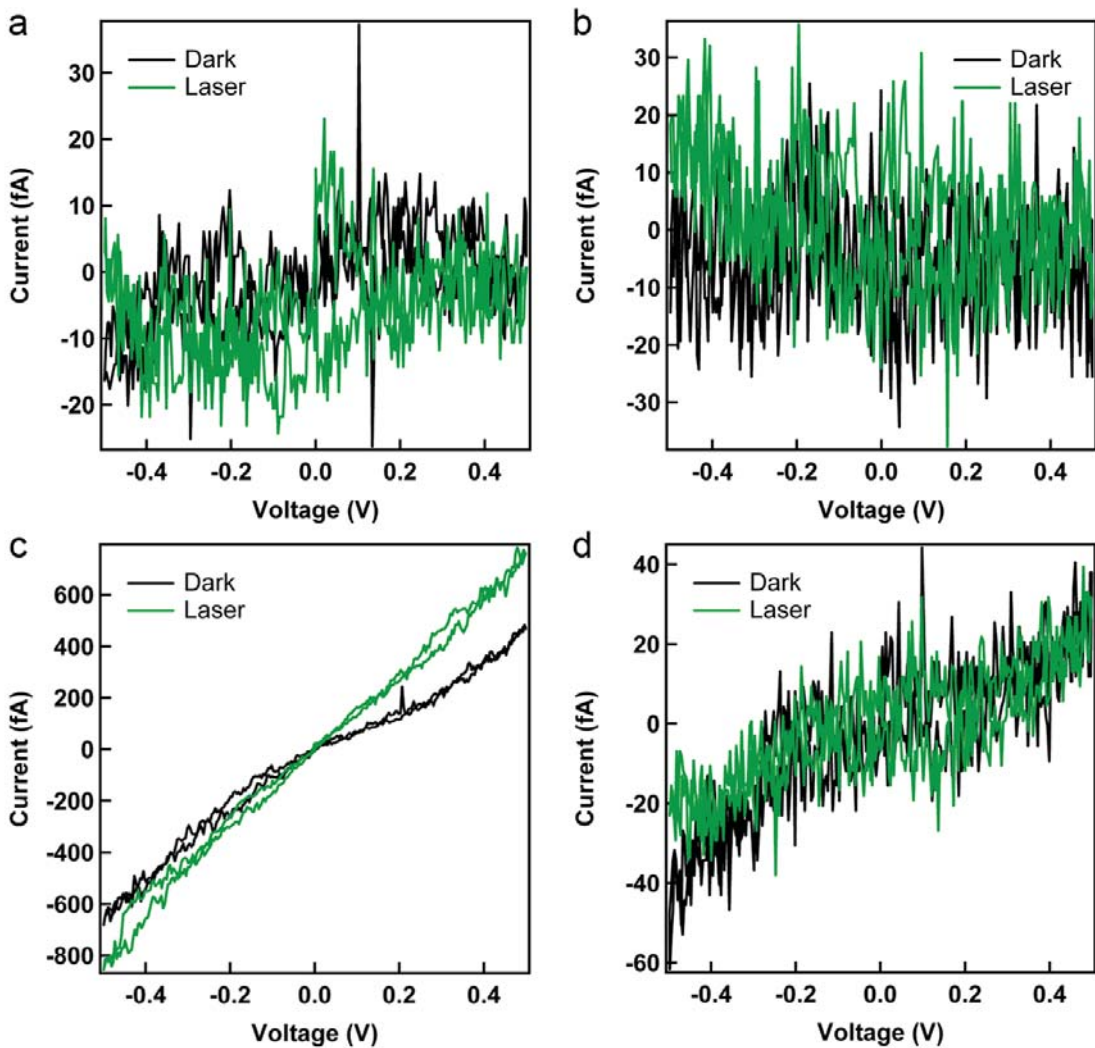


Figure 6.5: Gap 1 IV sweeps of untreated PbSe rods in the dark and with the laser at (a) room temperature and (b) 79K. Gap 2 IV sweeps of untreated PbSe rods in the dark and with the laser at (c) room temperature and (d) 79K.

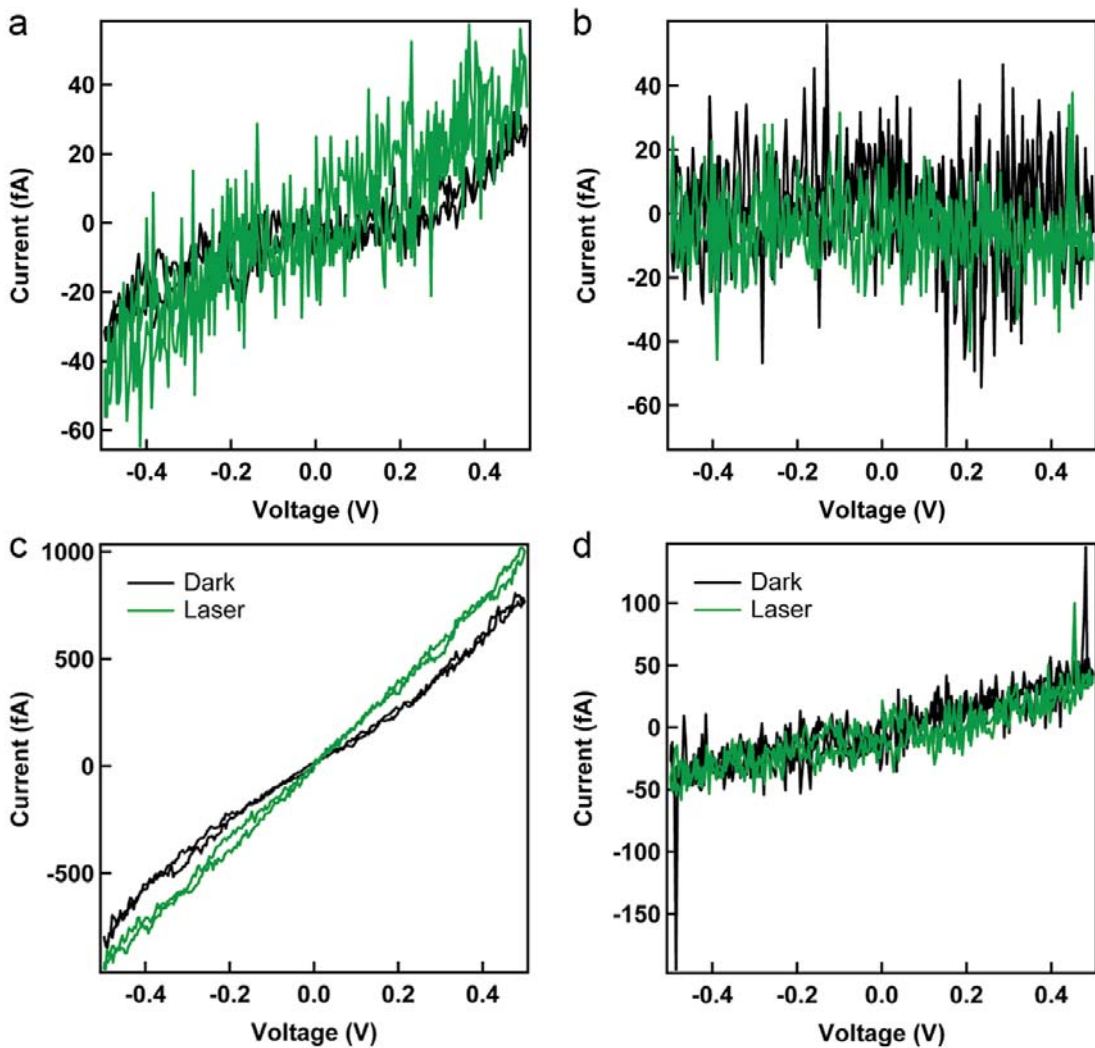


Figure 6.6: IV sweeps of Gap 1 with annealed PbSe rods in the dark and with the laser at (a) room temperature and (b) 79K. IV sweeps of Gap 2 with annealed PbSe rods in the dark and with the laser at (c) room temperature and (d) 79K.

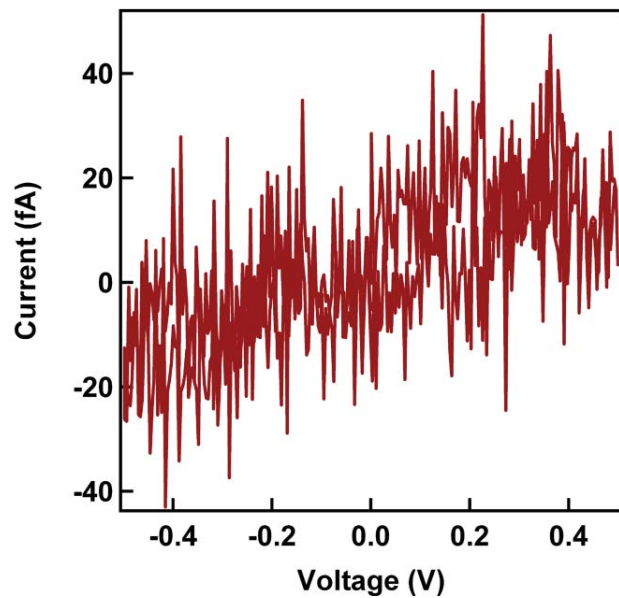


Figure 6.7: Calculated room temperature photocurrent of the annealed PbSe rods.

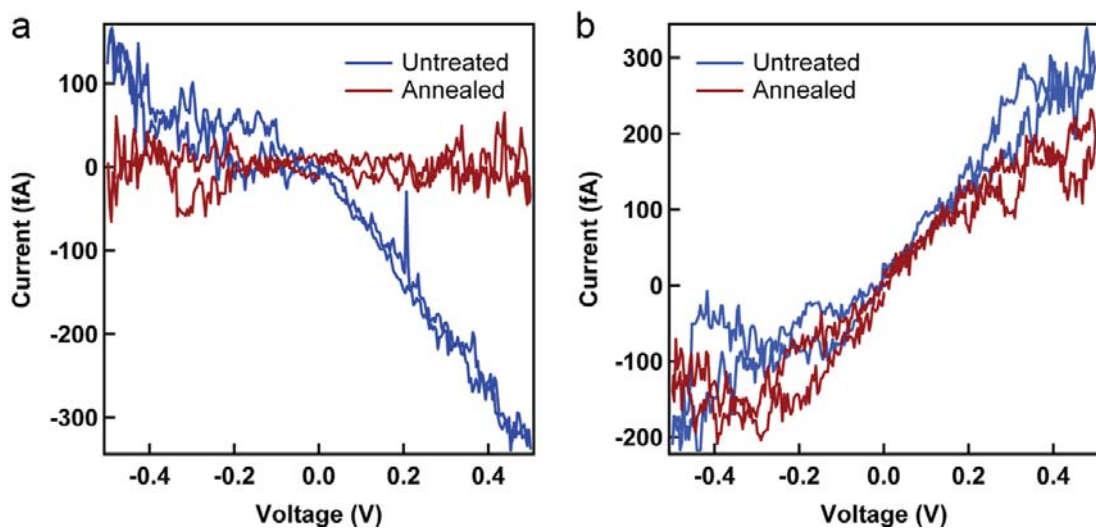


Figure 6.8: Calculated (a) dark and (b) photocurrent of the PbSe rods, both untreated and annealed at room temperature.

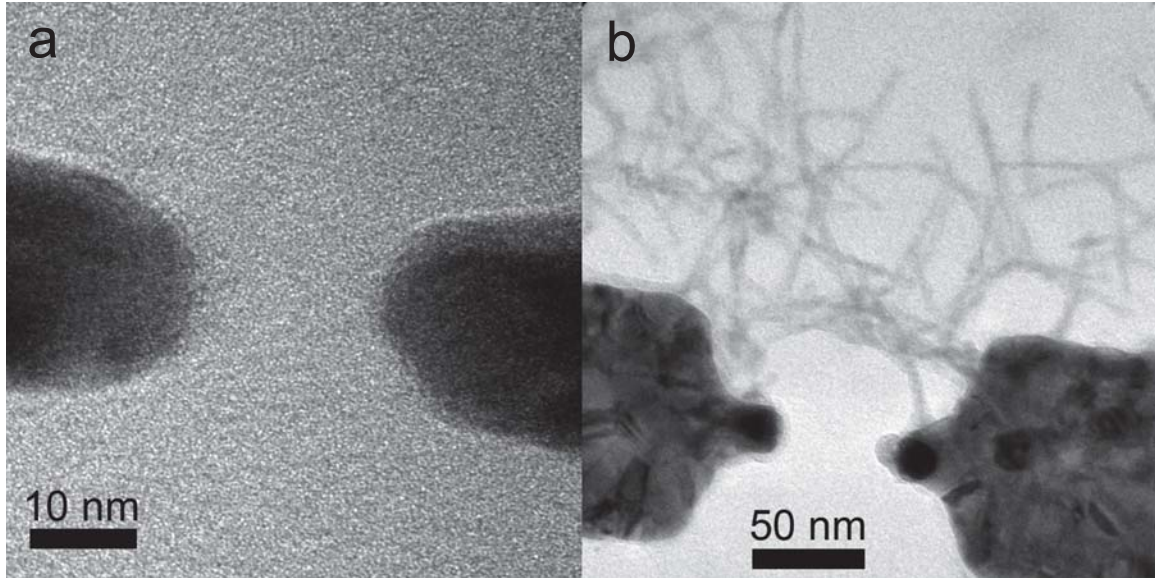


Figure 6.9: TEM images of Gap 1 (a) before measurements, zoomed in, and (b) after measurement with PbSe rods, zoomed out.

current even though they seemed to be clearly connected by the nanorods, see Figure 6.10. One explanation is that the gaps that showed current seemed to have melted or been electromigrated. The heat caused by these processes may have improved contact of the electrodes with the rods.

6.5.3 Hydrazine

Hydrazine has previously been shown to greatly increase conduction of PbSe nanocrystals.¹⁸ Even though it evaporates in vacuum and under atmospheric pressure, the increased conduction lingers. Thus, we took the remaining devices measured were taken out of the cryostat, still wirebonded to the chip carrier, and put into a nitrogen atmosphere glove box. With the nanorods already dried on the chip, 1 M hydrazine in acetonitrile was then dropcast onto the chip and allowed to dry. This was repeated two more times. The chip carrier was then put back into the cryostat and put under vacuum. The time the chip was exposed to atmosphere was not more than 20 minutes

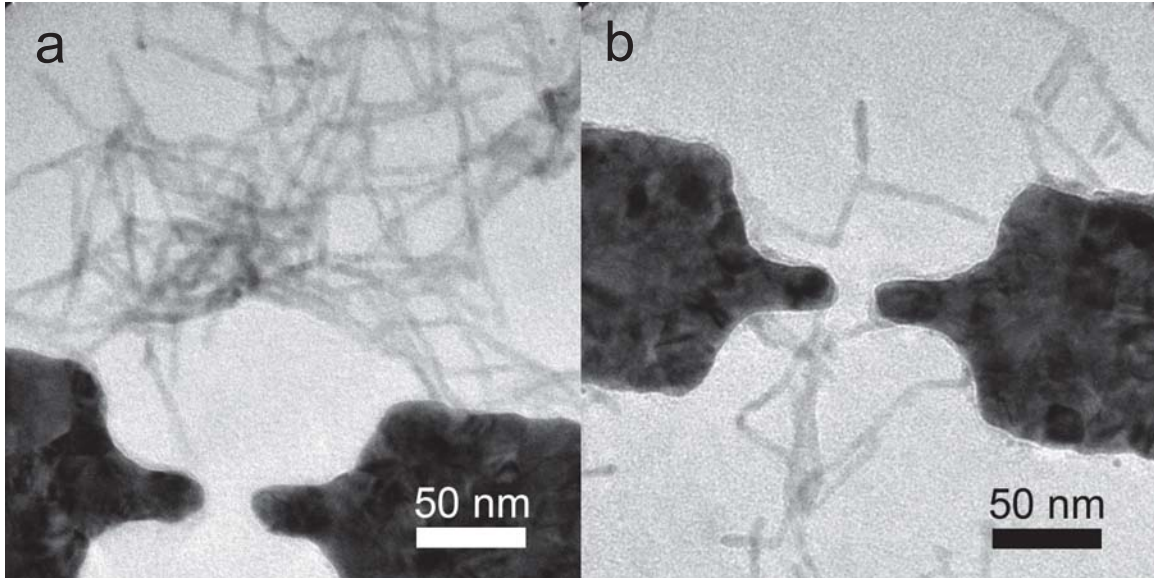


Figure 6.10: (a) Electrodes spanned by a large network of PbSe nanorods that showed no current. (b) A gap connected by two nanorods that had no measurable current.

total.

Figures 6.11a and b show the current measurements after the hydrazine treatment in the dark and with the laser for a gap that initially had very low background, which will be referred to as Gap 3. Typically, the photocurrent was lower than the dark current at room temperature. However, at 79K, the photocurrent was higher than the dark current. At room temperature, Figures 6.11b and c show the dark and photocurrent measurements for what will be referred to as Gap 4. It had a nonzero background, but the magnitude of the background signal was more than two orders of magnitude smaller; thus, it can still be neglected. At both room temperature and low temperature, the photocurrent is less than the dark current.

A TEM image of Gap 4 after measurements is shown in Figure 6.12. The gap blew up at some point, most likely due to static discharge. In Figure 6.12b, a noticeably large network of PbSe rods may have connected the electrode pair in addition to anything in the gap. Gap 3 was more significantly destroyed and could not be imaged.

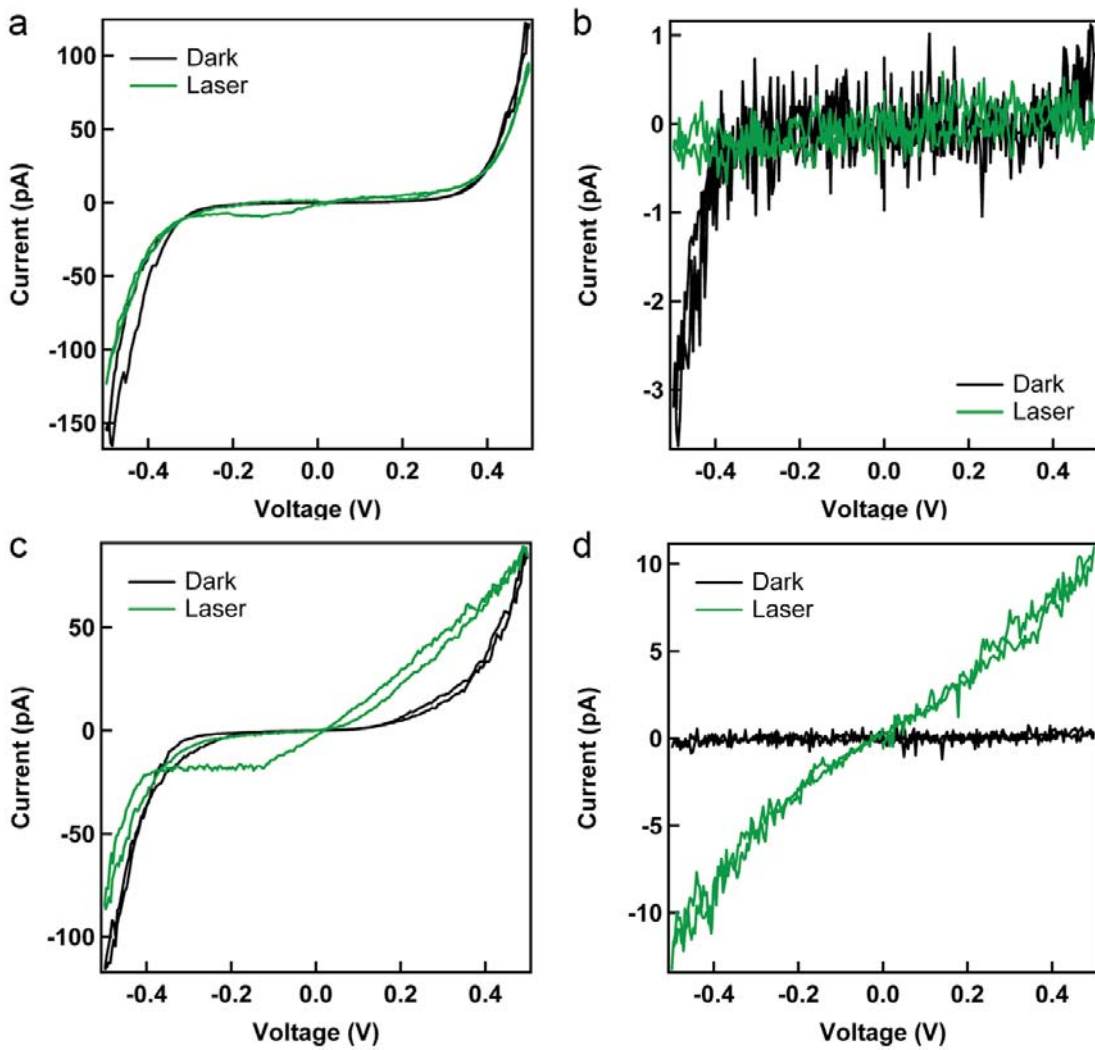


Figure 6.11: Dark and photocurrent of a flat background gap at (a) room temperature and (b) 79K after the hydrazine treatment. Dark and photocurrent of a nonzero background gap at (c) room temperature and (d) 79K after the hydrazine treatment.

6.6 Conclusions

Annealing did not increase the dark or photoconductivity of the PbSe rods. Hydrazine increases both the dark and laser currents, but the photocurrent was most often less than the dark current, possibly due to photogenerated carriers combining with voltage-induced carriers. The single case of the photocurrent being larger than the dark current was at low temperature in a gap with a nonzero room temperature. It is possible that metallic debris in the gap caused the background current, which has previously been shown to give current.¹⁴¹ This could also have increased photocurrent at 79K, since the resistance of metal should be less at 79K. There is no evidence that MPA treatment was effective in increasing nanorod attachment to the electrodes; it is likely that simple capillary forces as the solvent dries pins the nanorods between the electrodes. Future work should involve investigating whether poor contact between nanorods or between the nanorods and the electrodes is responsible for nonconducting networks. Techniques such as electrostatic force microscopy and scanning tunneling microscopy could greatly improve our understanding of how small networks of particles conduct.

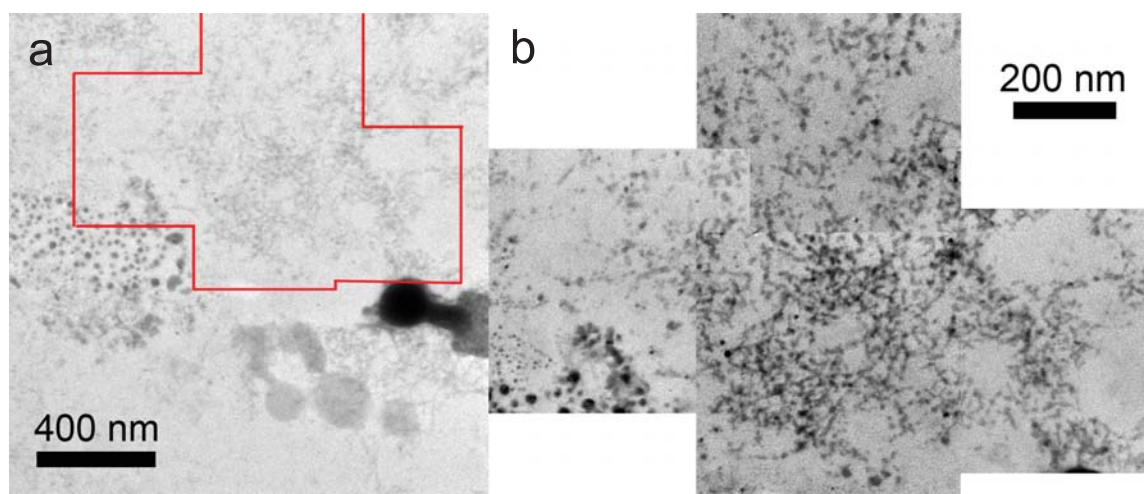


Figure 6.12: (a) TEM image of Gap 4 after it has blown up after measurement. The red lines indicate the area shown in (b) the close-up of PbSe rod network that most likely contacted the electrodes.

CHAPTER 7

Nanocrystal Traps¹

7.1 Introduction

One of the grand challenges of nanoscale systems is to control local fluctuations and disorder. As size decreases, the importance of individual defects and impurities grows, and they can cause unpredictable and undesired changes in behavior. Charge traps are ubiquitous and can affect a variety of systems: electronic states in graphene,¹⁴³ charge transport in carbon nanotubes,¹⁴⁴ photoluminescence intermittency in semiconducting nanocrystals and nanorods,^{145,146} and telegraph noise in resistance.¹⁴⁷ Local fluctuations often act as “hidden variables” that foil attempts at quantitative property measurement and interpretation. Hence, the discovery of ways to detect and control trap behavior will hasten progress in the field of nanoscience.

Here we demonstrate a robust and reproducible procedure for controlling the trap population in nanocrystal nanogap devices and show that qualitatively different photocurrent behaviors can be produced depending on how traps are initialized prior to a measurement. Electric field induced population and optically induced depopulation of traps can reverse the temperature dependence of the photoconductivity. We present a model that explains the role of traps and the importance of measurement sequence. Our method for dynamically controlling trap populations achieves optimized photodetector sensitivity at low or high temperatures for light sources, photovoltaics, electronics, and other applications. Moreover, we show that a range

¹ Adapted with permission from L. J. Willis, J. A. Fairfield, T. Dadosh, M. D. Fischbein, M. Drndić. Controlling Nanogap Quantum Dot Photoconductivity through Optoelectronic Trap Manipulation. *Nano Lett.* **2009**, 9 (12), 4191-4197. Copyright 2009 American Chemical Society.

of temperature-dependent behaviors previously attributed to material differences are reproducible in a single device and provide an explanation for contradictory reports of the temperature dependence of photoconductivity in the literature.^{16,17,34,35,43,148} These results carry implications for past and future experiments and may inspire analogous procedures for trap manipulation in other systems.

7.2 Devices

Figure 7.1a shows the schematic representation of the photodetector device, based on nanocrystals in a nanogap electrode geometry. Electrodes made of 3 nm of nickel and 30 nm of gold, separated by only 20-30 nm, approximately four nanocrystal diameters, are patterned using electron beam lithography on a silicon nitride (Si_3N_4) membrane.¹⁴⁹ The membrane is compatible with high-resolution structural characterization using transmission electron microscopy (TEM), which allows us to confirm that nanogaps did not have any metallic debris, as shown in Figure 7.1b. An optical image of lithographic features on a typical device is shown in Figure 7.1c. For more details on device fabrication, see Chapter 3. One advantage of nanoscale gaps is that the application of relatively small voltages yields high electric fields in the gap area. For a 20 nm gap with a bias voltage of 2V, the field strength experienced in the 2000 nm^2 of active area is 10^8 V/m . The active area of these photodetectors in comparison to previous literature^{16,33,34} is decreased by six orders of magnitude in area and decreased in gap size by two orders of magnitude.

7.2.1 Nanocrystal Characterization

We used Sigma-Aldrich cadmium selenide/zinc sulfide (CdSe/ZnS) core/shell nanocrystals, as shown in Figure 7.1d, which had an average diameter of 5.2 nm, and a shell

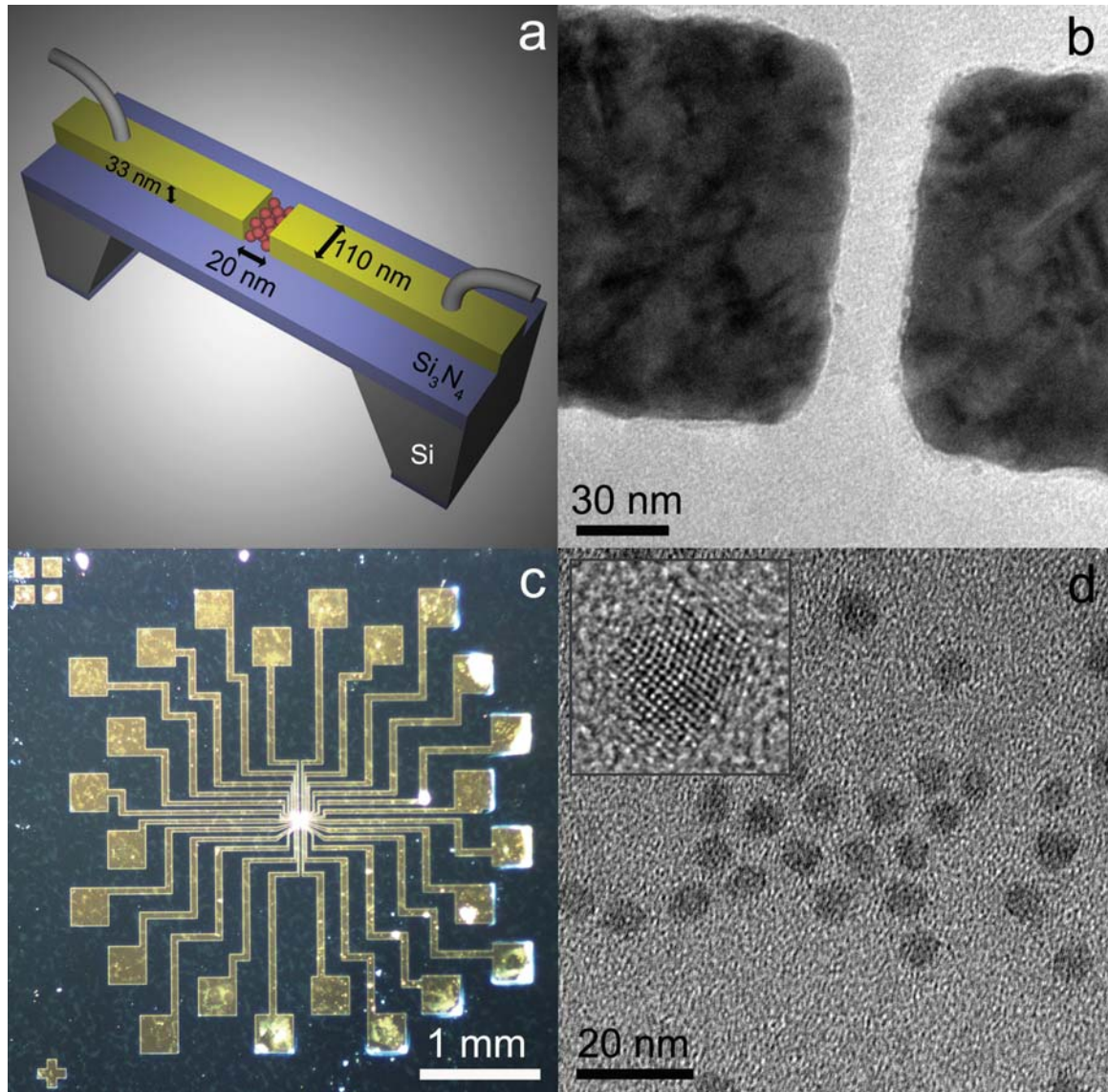


Figure 7.1: (a) Schematic of the photodetector nanogap device. Metal electrodes (3 nm of Ni and 30 nm of Au) separated by 20 to 30 nm are patterned on top of a 40 nm Si_3N_4 membrane that is supported by a Si wafer. Nanocrystals are deposited on the substrate and electrodes. (b) TEM image of the Ni/Au electrodes separated by 20 nm prior to nanocrystal deposition. (c) Optical image of the device with 12 electrode pairs. (d) TEM image of CdSe/ZnS nanocrystals with an average size of 5.2 ± 0.6 nm. Inset: Close-up TEM image of a single nanocrystal.

thickness of ~0.2 nm or ~1 monolayer, see Figure 7.2a. Nanocrystal size was determined from high-resolution TEM images as the average of 50 nanocrystals. Each nanocrystal was measured twice in ImageJ, with the measurements of the same nanocrystal roughly perpendicular to each other. These 100 measurements were averaged, giving a mean value of 5.2 nm with a standard deviation of 0.6 nm. However, there may be a slight underestimation due to the increased difficulty in discerning the ZnS shell against the carbon grid background.

Before any treatment, the nanocrystals have a primary absorption peak at 610 nm and emit at 640 nm, see Figure 7.2b. The absorption and emission spectra of nanocrystals in toluene solution were recorded using SpectraSuite from Ocean Optics. The excitation wavelength for the emission data was provided using an Ocean Optics LS-450 with a 470 nm LED and filter. The light source for the absorption spectrum was an Ocean Optics LS-1 with a tungsten halogen bulb. The reported quantum yield from Sigma-Aldrich is 30%. The nanocrystals were capped with a mixture of hexadecylamine and trioctylphosphine ligands to prevent aggregation and passivate surface traps.

Using the formula fitted by Yu et al.,¹⁵⁰

$$D = (1.6122 \times 10^{-9}) \lambda^4 - (2.6575 \times 10^{-6}) \lambda^3 + (1.6242 \times 10^{-3}) \lambda^2 - 0.4277\lambda + 41.57, \quad (7.1)$$

an absorption peak of 610 nm would correspond to a diameter of ~5.06 nm for a CdSe core nanocrystal. It has been shown that adding a ZnS shell not only broadens, but also redshifts the absorption peak, and the size of the redshift depends on the size of the nanocrystal.¹² We estimate a redshift of ~5 nm, so that the absorption peak for our CdSe core should be 605 nm. From Equation 7.1, the core diameter of our CdSe nanocrystals is ~4.81 nm. It should be noted that had we not taken into account the

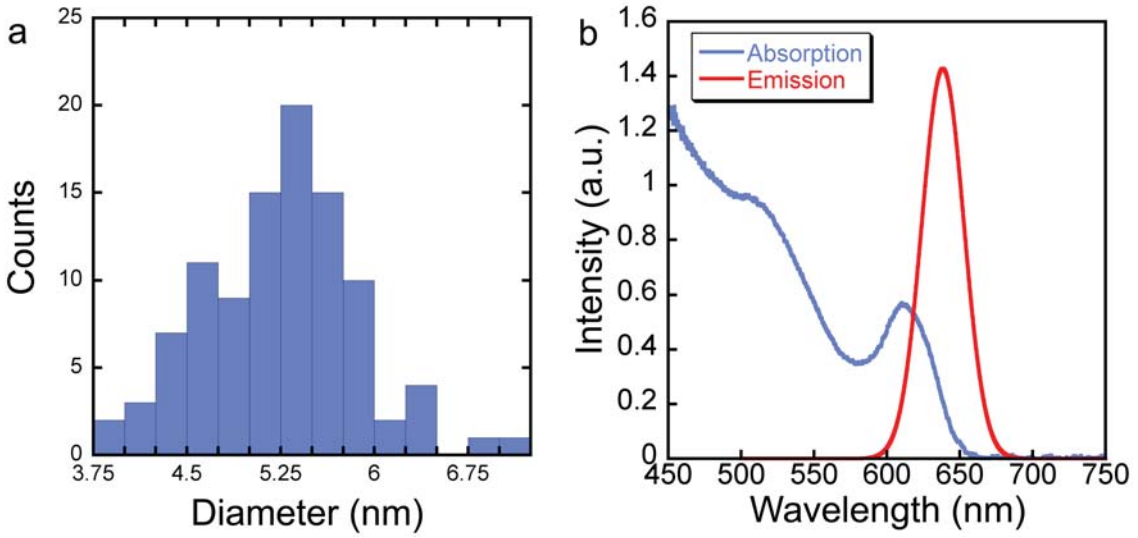


Figure 7.2: (a) Histogram of 50 nanoparticles, each measured twice from TEM images. (b) Absorption (blue) and emission (red) intensity vs. wavelength curves for the nanocrystals studied.

redshift caused by the shell, we would have overestimated the core size by ~ 0.25 nm. Knowing that the core radius is 2.4 nm and the actual nanocrystal radius, determined by TEM, is 2.6 nm, we find that the shell is ~ 0.2 nm, which is approximately one monolayer.

Five microliters of the nanocrystal solution were dropcast onto the chip and allowed to dry, forming a multilayer nanocrystal film on the surface.

7.3 Measurement Setup and Control Measurements

Electrical measurements were performed in either a modified Janis VPF-700 or ST-100H cryostat operated at $\sim 5 \times 10^{-7}$ torr. Nanogaps were wired to a ceramic chip carrier thermally coupled to a copper cold finger and electrically addressed by silver-soldered wires, which coupled the source and drain pins to two independent BNC breakout boxes. Voltages were applied with a Yokogawa 7651 programmable dc

source; current signals were amplified and filtered by a Keithley 428 current amplifier and measured with an Agilent 34401A digital multimeter. For all measurements at fixed laser intensity, the IV characteristics for each device were measured by sweeping the voltage across the nanogap from 0 V to 2 V to -2 V and back to 0 V, with a typical cycle taking 200 seconds. This gives a maximum voltage drop per nanocrystal of 0.5 V. Prior to nanocrystal deposition and after TEM inspection, the bare devices were cleaned with an O₂ plasma, then the conductance and photoresponse of the bare devices were tested. The dark current of devices was measured by performing an IV sweep with the nanogap in the dark, and photocurrent was measured by performing an IV sweep while the nanogap was illuminated by a continuous wave 532 nm diode laser. In each measurement set, we measured at room temperature the dark current of all devices on a chip, and then the photocurrent of the same devices; the device was then cooled with either liquid nitrogen or liquid helium, and both dark current and photocurrent were measured again at low temperature. Changing measurement order, e.g., performing low-temperature measurements first and room-temperature measurements second, did not affect current characteristics.

7.3.1 Annealing

The samples were annealed *in situ* because annealing has been shown to increase photocurrent in nanocrystal solids^{16,33–35} by reducing interparticle separation and lowering tunneling barriers. We detected photocurrent in 17 nanogaps, and no dark current signal above the maximum noise floor of ~0.03 pA at 295K and ~0.15 pA at 78K in 70% of devices after annealing up to 573K. From TEM imaging we confirmed that nanogaps did not have any metallic debris that could contribute to the dark current, and this was consistent with our subsequent IV characterization of the nanogaps. More importantly, all of our photocurrent is primary, with no measurable

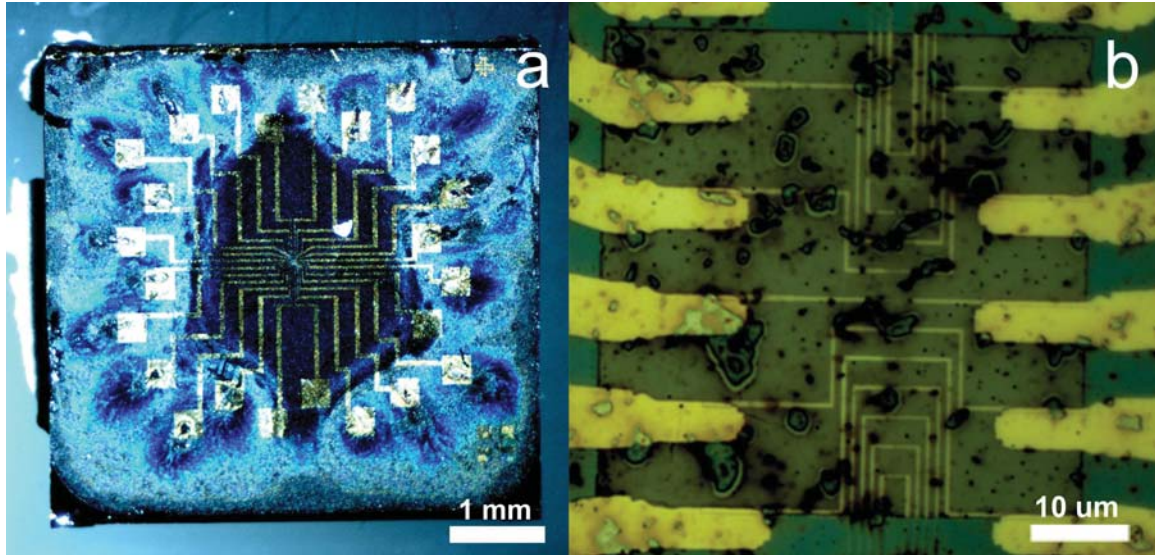


Figure 7.3: Optical images of (a) an entire chip and (b) a close-up of the window after measurements with annealed nanocrystals.

charge injection from the electrodes.¹⁷

The percentage of devices that had measurable photocurrent increased with annealing temperature T_a . For $T_a = 423K$ the yield was 44%, for $T_a = 498K$ the yield was 66%, and for $T_a = 573K$, all devices showed photocurrent response. In devices that had photocurrent above the noise floor (0.03 pA at 295K and 0.15 pA at 78K), increasing the annealing temperature from 423K to 498K increased the observed photocurrent by 20 times on average. Above 498K, there was no measurable change in photocurrent magnitude or response characteristics. All data discussed were taken from 17 active nanogaps out of 20 total that were annealed at either 498K or 573K. Sample images of devices with annealed nanocrystals are shown in Figures 7.3 and 7.4.

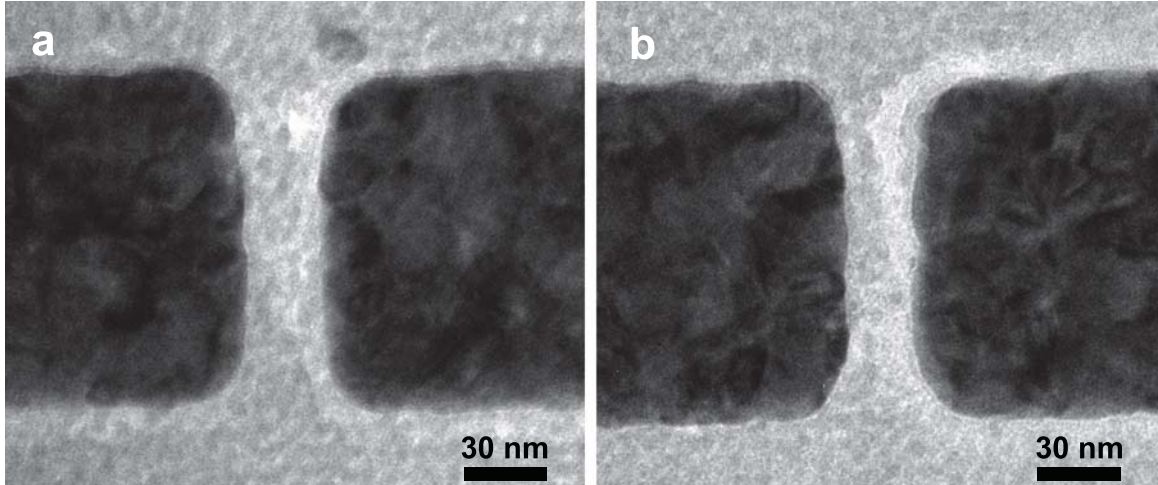


Figure 7.4: TEM images of two different nanogaps on the same chip after measurements with nanocrystals annealed at 498K.

7.3.2 Background and Dark Current Measurements

Dark current was measured on all nanogaps prior to any nanocrystal deposition, prior to any photocurrent measurements, and over the course of several months as devices were thermally cycled many times. Dark current was below the noise floor of our setup for 70% of devices measured. In Figure 7.5, we show examples of IV characteristics for a bare nanogap measured at room temperature and for nanogaps with nanocrystals that have been annealed and measured at 78K and 295K.

Less than ~30% of nanogaps, only those annealed at 573K, showed a very small dark current (~0.16 pA at 2 V), two to three orders of magnitude smaller than the corresponding photocurrent. The dark current increases exponentially with voltage and can be empirically fitted to an exponential form,

$$I_{dark} = \frac{V}{R_0} e^{\frac{V}{V_0}}, \quad (7.2)$$

where $R_0 \sim 2 \times 10^{-14} \Omega$ and $V_0 = 0.7$ V are the characteristic resistance and voltage

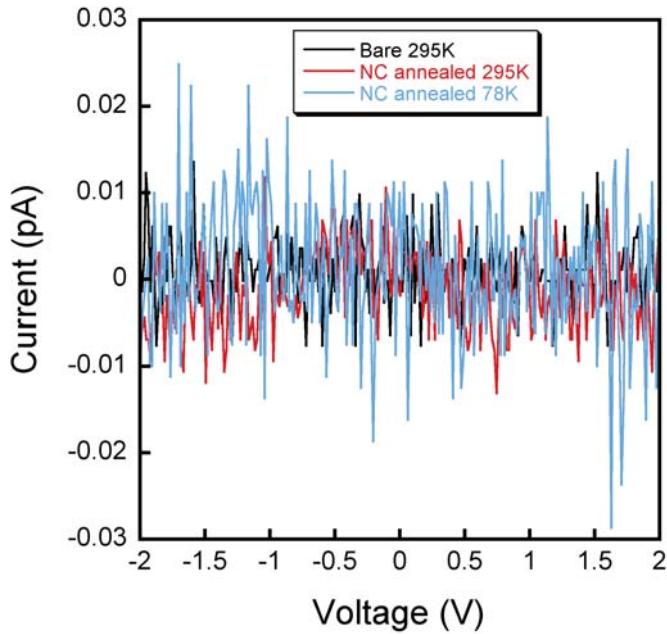


Figure 7.5: Representative IV dark current curves for a bare device and devices with nanocrystals annealed up to 573K, measured at 295K and 78K. More than 70% of devices showed no measurable dark current, making them primary photodetectors.

(Figure 7.6). This is in agreement with previously reported dark current measurements on micron-scale nanocrystal arrays.¹⁶ Consequently, because there is no clear threshold of the dark current, this also implies that there is no intrinsic difference between primary and secondary photodetectors in these systems.

Figure 7.7 shows the temperature dependence of the dark current, written as the zero-bias conductance G vs. $\frac{1}{T}$, which is representative for the few devices that exhibited measurable dark current. The dark current is thermally activated and conductance was found to scale as $G \sim e^{-\frac{E}{kT}}$. We have measured a range of activation energies from ~ 70 - 230 meV, consistent with previously published results.⁴³

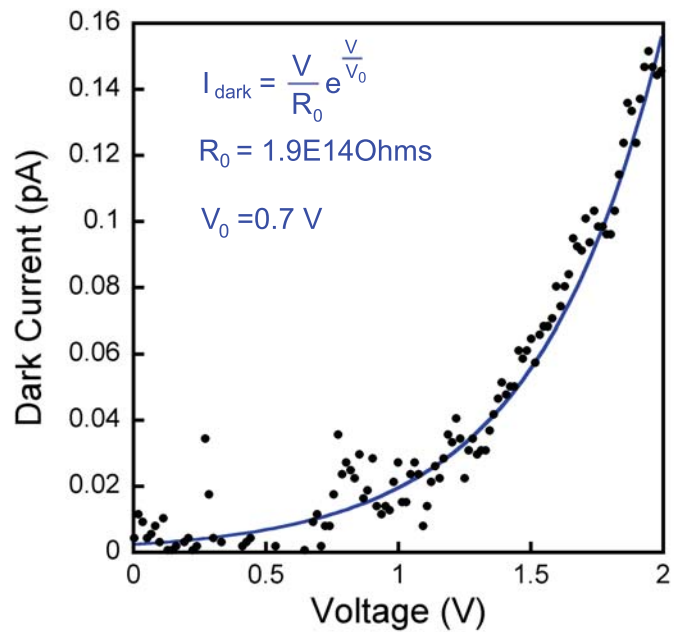


Figure 7.6: IV curve for one of the few devices with measurable dark current.

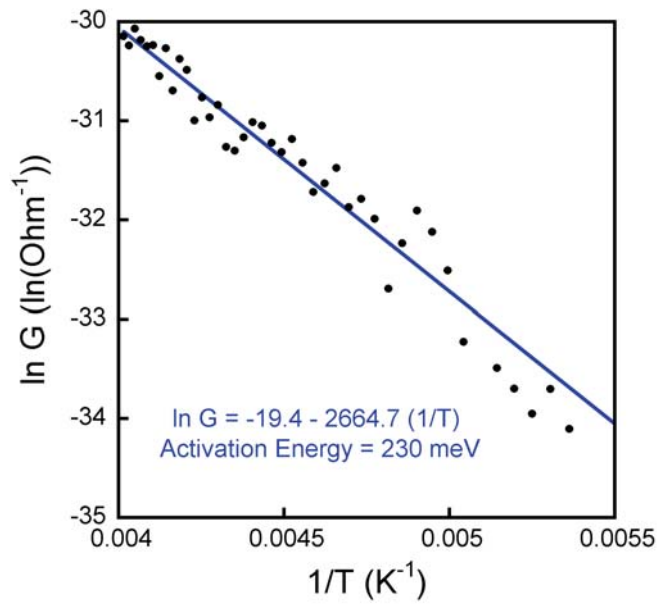


Figure 7.7: Arrhenius plot for one of the few devices with measurable dark current.

7.4 Results and Discussion

Figure 7.8 shows the IV response under 532 nm illumination at different temperatures of two different nanogaps. The photocurrent is well described by a second-order polynomial in voltage. Measurements at other wavelengths show consistent behavior once temperature-dependent absorption shifts are accounted for; see Figure 7.9 for IV characteristics obtained using different illumination wavelengths. Over all measured devices, the initial room temperature photocurrent was in the range of 0.1 to 50 pA, with a mean value of ~5 pA, and the initial low temperature photocurrent was in the range of 0.1 to 240 pA, with a mean value of ~30 pA. A histogram of photocurrent values is shown in Figure 7.10. The large variation in measured photocurrent is probably due to a small number of nanocrystals in the nanogap; thus the variations in each individual nanocrystal are not averaged out. Additionally, film thickness within the nanogap and the energy barrier at the contacts between the nanocrystals and the electrodes may vary. Transport through the nanocrystals inside the gap dominates the photocurrent, while nanocrystals outside the gap region have a negligible contribution.¹³⁶

We observed that the magnitude of the measured photocurrent depends on the recent illumination history of the device. Even more strikingly, some nanogaps showed photocurrent that was higher at 295K than at lower temperatures, while other nanogaps on the same chip and under equivalent conditions showed the opposite. Moreover, if the nanocrystals were illuminated overnight and voltage was applied (hereafter referred to as a *laser voltage treatment*), the low-temperature photocurrent was enhanced, whereas if the nanocrystals were left in darkness overnight and voltage was applied (hereafter referred to as a *dark voltage treatment*), the low-temperature photocurrent was suppressed. If voltage was not applied while the sample was left in darkness overnight, the photocurrent magnitude returned to its initial value. This

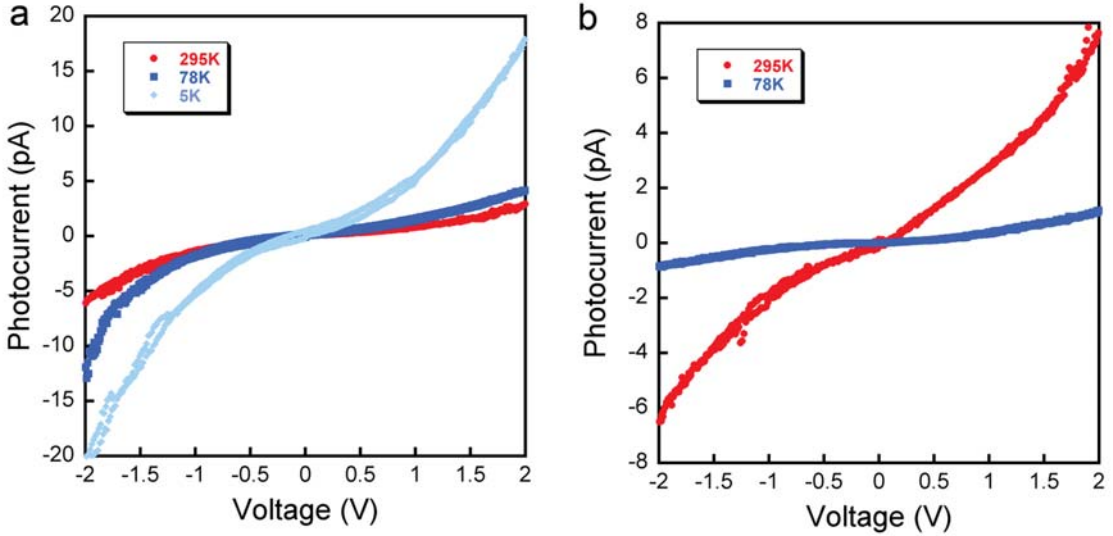


Figure 7.8: Photocurrent vs. voltage curves at 5K (light blue), 78K (dark blue), and 295K (red) for CdSe/ZnS nanocrystals in devices where the low-temperature photocurrent is higher (a) or lower (b) than the room-temperature photocurrent.

trend was repeatable over a measurement period of several months. The photocurrent at 295K followed the same trend as the low-temperature photocurrent in $\sim 75\%$ of devices, but the effect was smaller ($\sim 10\text{-}30\%$ of the photocurrent change at 78K).

To best quantify the photocurrent increase or decrease with temperature, T , it is convenient to define the *relative photocurrent ratio*,

$$R = \frac{I_{78K}}{I_{295K}}, \quad (7.3)$$

of the low-temperature photocurrent, I_{78K} , and the room-temperature photocurrent, I_{295K} . This is analogous to the relative resistance ratio between the low- and room-temperature resistance in metals, commonly used as a criterion of metal purity; if the photoconduction in nanogaps were ohmic, resistance would be well defined, and then R would be the same as that defined for metals. Each ratio, R , was calculated for one cool-down cycle of measurements taken in a single day. The relative photocurrent

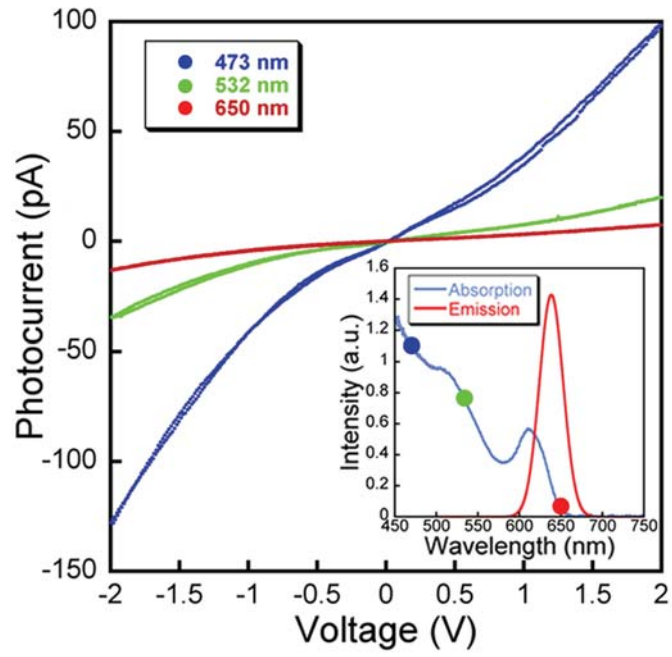


Figure 7.9: Representative photocurrent vs. voltage curves for 650 nm (red), 532 nm (green) and 473 nm (blue) laser excitations. Inset: Absorption and emission intensities vs. wavelength for CdSe/ZnS nanocrystals in solution. The blue, green, and red circles indicate the positions of the excitation wavelengths with respect to the absorption curve.

ratio has two distinguishable regimes: if $R < 1$, this means that the photocurrent increased with T , and if $R > 1$, the photocurrent decreased with T . In the discussion below, I_{78K} and I_{295K} were calculated as averages of photocurrent magnitudes for the maximum electric field applied across the nanogaps, corresponding to voltages -2 V and 2 V. The following conclusions hold qualitatively for other voltages, and also apply independently of annealing temperature. Examples of nanogaps with R smaller or greater than 1 are shown in Figure 7.8a ($R = 2.2$) and Figure 7.8b ($R = 0.1$). Out of the seventeen nanogaps, fifteen initially showed $R > 1$ and two showed $R < 1$. A histogram of R values for 532 nm illumination and a comparison of R values for both 532 and 650 nm illumination are given in Figure 7.11. As measurements progressed, illumination history was observed to affect this ratio, so that R could be increased and decreased; in a single nanogap, it was possible to switch R from less than one to greater than one, see Figure 7.12, though this was not ubiquitous. A sample table of the change in relative photocurrent ratios after laser and dark voltage treatments is given in Table 7.1.

Figure 7.13 shows a histogram of the change in R from $R_{initial}$ to R_{final} from 70 measurements over all devices after laser and dark voltage treatments. We use a logarithm transformation to write the change in R on the x-axis as $\ln\left(\frac{R_{final}}{R_{initial}}\right)$. This manner of representing the change in R is informative because $\ln\left(\frac{R_{final}}{R_{initial}}\right) = -\ln\left(\frac{R_{initial}}{R_{final}}\right)$, meaning that an increase or decrease of R by the same factor is represented on this scale symmetrically around zero; $\ln\left(\frac{R_{final}}{R_{initial}}\right) = 0$ means that R does not change. There are two distinct distributions in this histogram, showing that device behavior after a laser and dark voltage treatment is clearly separated. The laser voltage treatment increases the ratio by an average factor of 2.2, meaning that $R_{final} > R_{initial}$. The dark voltage treatment decreases the ratio by a factor of 10, meaning that $R_{final} < R_{initial}$. We have also observed this effect in a large gap with an active area of $\sim 109 \mu\text{m}^2$

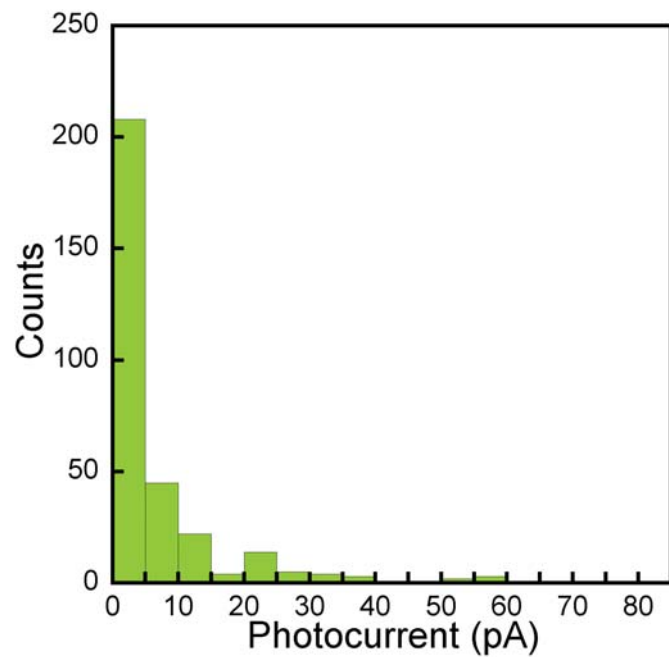


Figure 7.10: Distribution of photocurrent magnitudes for nanogap devices illuminated with 532 nm light at 295K.

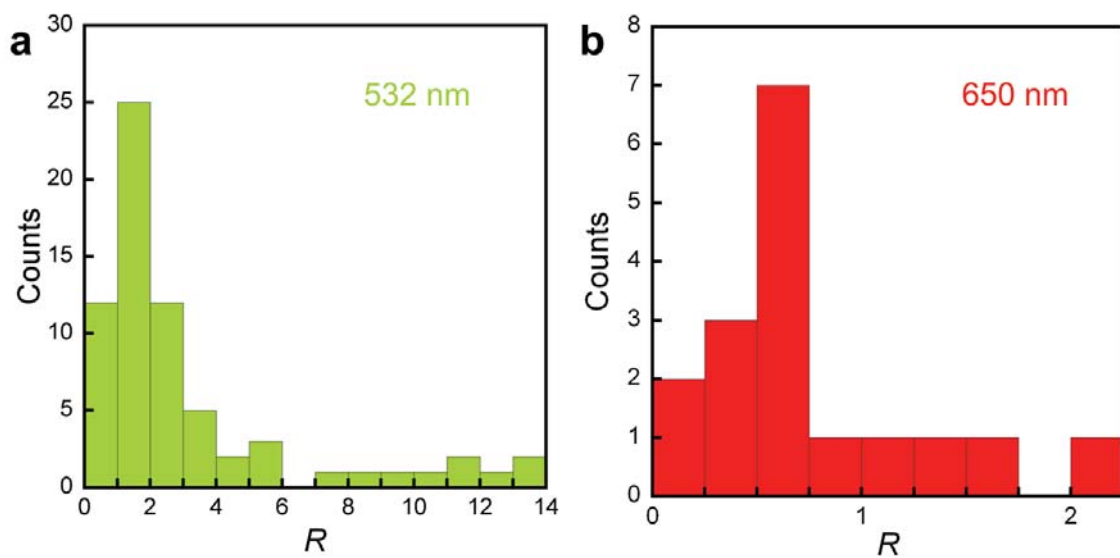


Figure 7.11: Histograms of R values for nanogap devices illuminated with (a) 532 nm and (b) 650 nm excitation.

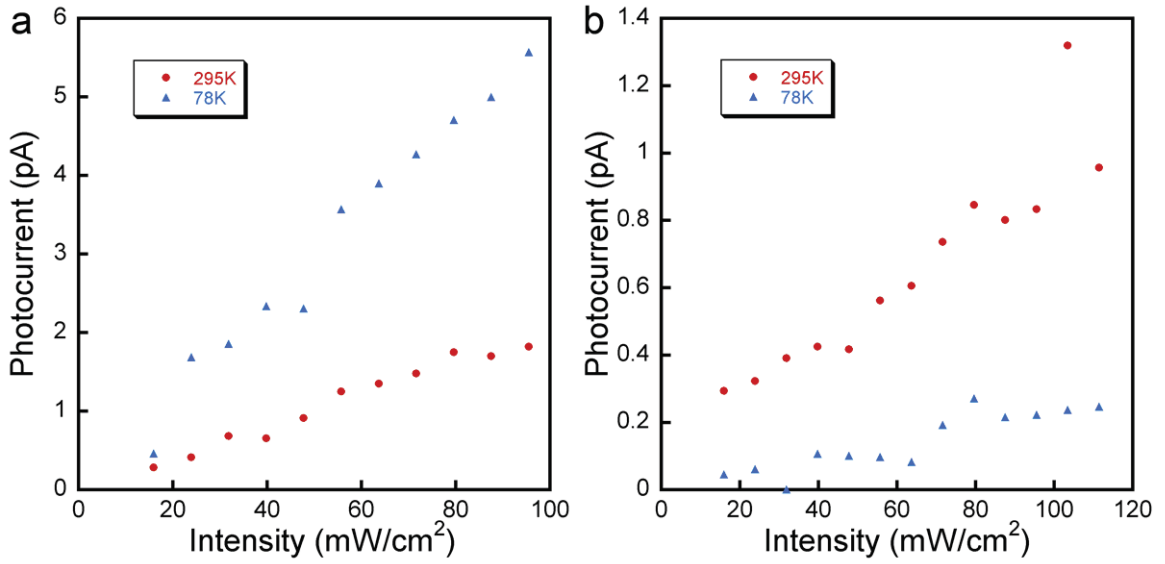


Figure 7.12: Measurements of photocurrent vs. laser intensity (a) before and (b) after a dark voltage treatment of a single nanogap that shows the ratio $R = I_{78K}/I_{295K}$ switching from (a) $R > 1$ when I_{78K} (blue) $> I_{295K}$ (red) to (b) $R < 1$ when I_{78K} (blue) $< I_{295K}$ (red) for all laser intensities used.

Gap	R after no treatment	R after laser voltage treatment	R after dark voltage treatment	R after laser voltage treatment
1	0.38	1.81	0.72	0.94
2	2.67	4.44	1.20	1.43
3	0.36	1.00	0.33	0.48
4	1.63	2.85	0.53	0.75
5	n/a	n/a	0.75	1.25
6	1.5	n/a	1.50	n/a
7	1.00	0.88	0.31	0.59
8	0.75	1.56	0.43	0.72
9	0.69	1.88	0.23	0.75
10	0.85	3.29	0.51	1.27
11	0.095	1.06	0.04	0.20

Table 7.1: Relative photocurrent ratios of the low- and room-temperature photocurrents, $R = \frac{I_{78K}}{I_{295K}}$ for several nanogap devices on a single chip, illuminated with 650 nm light, increasing or decreasing with different treatments.

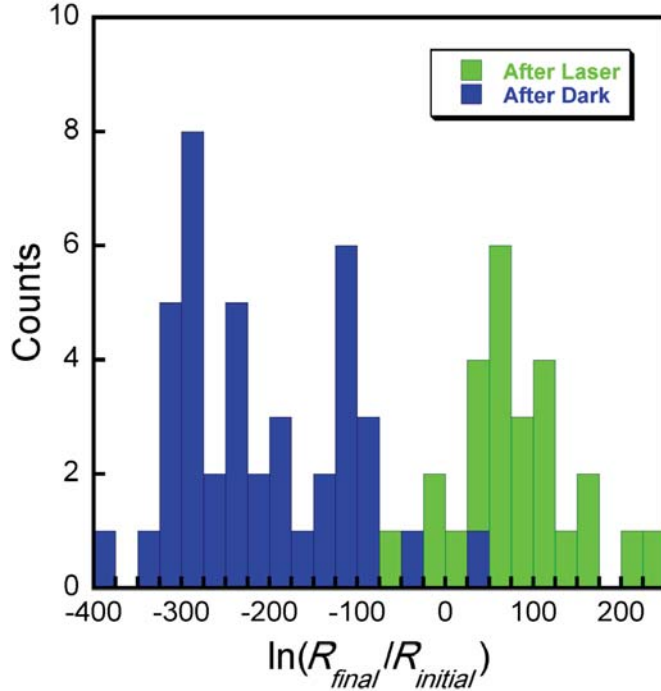


Figure 7.13: Histogram of the change in the final ratio with respect to the initial ratio, $\frac{R_{final}}{R_{initial}}$, on a logarithmic scale, with over 70 measurements including laser voltage treatments (green) and dark voltage treatments (blue). An increase or decrease of R by the same factor is represented on this logarithmic scale symmetrically around zero. Two distinct distributions clearly show that R increases after a laser voltage treatment and decreases after a dark voltage treatment on average 2.2 and 10 times, respectively.

($\sim 43.6 \times 2.5 \mu\text{m}$), implying that this effect is independent of device size.

This demonstrated change in ratio, R , with laser or dark voltage treatments shows that the temperature dependence of conductivity is controlled by the measurement protocol. Consequently, all such measurements on nanocrystal arrays must be framed in the context of the sample measurement history in order to be properly interpreted. This consideration may explain apparent discrepancies in the reported temperature dependence of observed photocurrent.^{16,17,34,35,43,148}

To understand the underlying mechanism, we must look at the energy levels through which the charge carriers travel. Figure 7.14a shows energy levels for the

electrodes with a single nanocrystal between them; the shortest charge carrier path in our devices includes four nanocrystals. The carrier tunneling between nanocrystals can be lost by recombining with other oppositely charged carriers through radiative or nonradiative recombination, which usually corresponds to free recombination or recombining with trapped carriers at recombination centers, respectively. The primary photocurrent in a semiconductor is given by

$$I(E, T) = eFG, \quad (7.4)$$

where e is the charge of an electron, F is the exciton generation rate, and G is the number of charge carriers that pass between the electrodes per second for each photon absorbed per second, which is also called the photoconductive gain.^{13,33,34} F is defined by

$$F = \Phi a \eta(E, T), \quad (7.5)$$

where Φ is the excitation flux, a is the film absorption, and $\eta(E, T)$ is the field-dependent exciton separation efficiency.³⁴ $\eta(E, T)$ is defined in terms of the relevant rates that affect exciton recombination and transport:

$$\eta(E, T) = \frac{k_E(E, T)}{k_E(E, T) + k_R(T) + k_N(T)}, \quad (7.6)$$

where $k_E(E, T)$ is the field-dependent rate of charge carriers escaping to neighboring nanocrystals or electrodes, $k_R(T)$ is the rate of charge carriers radiatively recombining, and $k_N(T)$ is the rate of charge carriers nonradiatively recombining.¹³

The tunable temperature dependence of the observed photocurrent can be explained by the relative magnitudes of the rates $k_R(T)$, $k_N(T)$, and $k_E(E, T)$ involved, shown in Figure 7.14a, and their temperature dependence. $k_R(T)$ increases

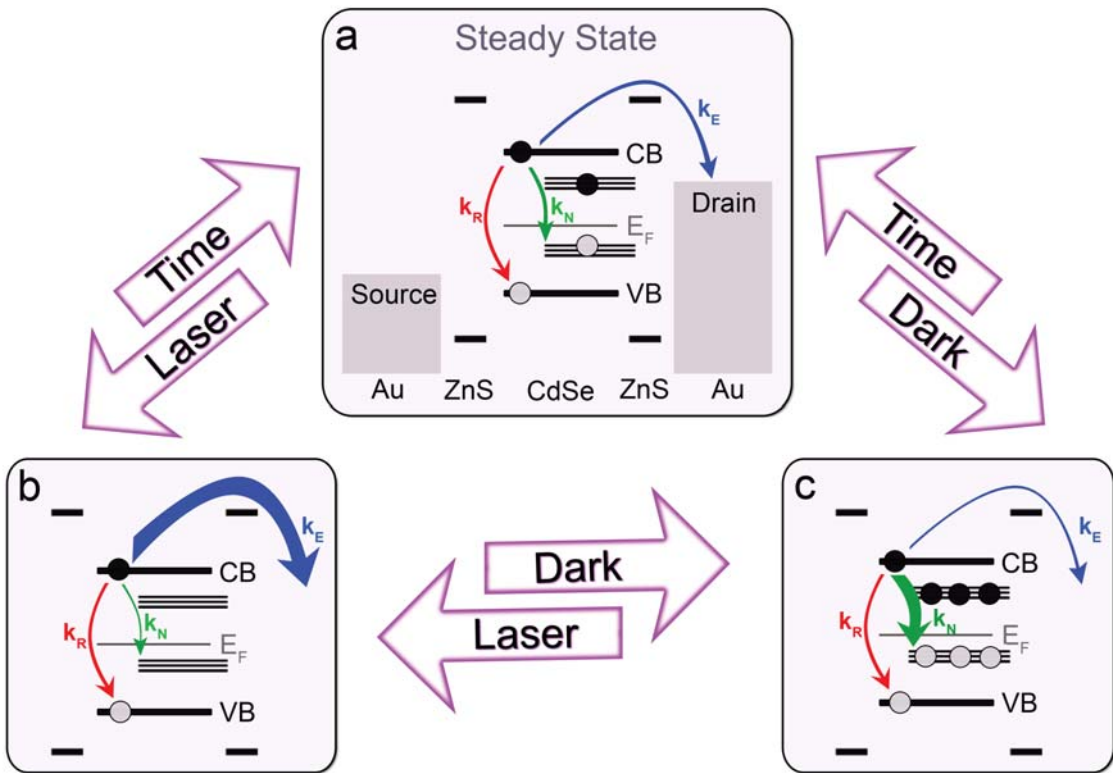


Figure 7.14: (a) The energy level diagram for a steady state CdSe/ZnS core/shell nanocrystal between two gold electrodes. Trap states above the Fermi energy, E_F , act as electron traps, whereas trap states below E_F act as hole traps. An exciton is created by illumination of the sample, and it can either recombine radiatively with rate k_R , recombine nonradiatively via the trap states with rate k_N , or tunnel away from the nanocrystal at a rate k_E related to the applied field E . (b) After applying laser voltage treatment, the traps are emptied which enhances k_E and suppresses k_N . (c) After applying dark voltage treatment, the traps are filled, which suppresses k_E and enhances k_N . Over a few days of waiting time, trap populations return to their steady state value, which also returns k_E and k_N to their steady state values. Hole processes are affected by the treatments in the same way, but are not shown.

with increasing temperature because thermal energy magnifies the probability of free charge carriers to recombine, causing photocurrent to decrease with increasing temperature.^{148,151} $k_N(T)$ decreases with increasing temperature, since nonradiative recombination occurs when charge carriers easily escape from traps with thermal energy at higher temperatures, which causes photocurrent to increase with increasing temperature.¹³ The contribution from both radiative recombination and the number of traps is constant over these measurements and fixed for a given sample, but the contribution from trap states depends on trap population, which can be adjusted by laser and dark voltage treatments.

Before any treatment, the system has a number of occupied trap states that is defined as the steady state, as in Figure 7.14a. The laser voltage treatment creates many charge carriers that recombine with carriers in trap states, causing traps that are occupied in steady state to be emptied, as in Figure 7.14b; this effect of optically stimulated trap emptying in our nanogaps is similar to an analogous phenomenon well documented in semiconductor literature.¹³ The laser voltage treatment eliminates many charge carriers, even in energetically favorable traps, and fewer charge carriers recombine with trapped charges. This increases photocurrent temporarily, but over a few days of waiting time, the trap occupancy returns to its steady state value, as energetically favorable traps are repopulated, causing photocurrent to return to a steady state value as well. Conversely, the dark voltage treatment repeatedly sweeps the voltage, increasing the population of charge carriers in the traps, as in Figure 7.14c. Thus, after dark voltage treatment even energetically unfavorable traps are populated; the populated traps capture more carriers and cause them to recombine, temporarily decreasing photocurrent. Over a few days of waiting time the trap occupancy returns to its steady state value, as charge carriers in some traps escape using thermal energy, causing photocurrent to return to a steady state value as well.

To summarize, by applying the laser and dark voltage treatments, the trap population is modified, which allows tuning of the photocurrent response; this has a greater effect at low temperature because traps can be emptied using the larger thermal energy at room temperature. Relevant processes for photogenerated electrons in the conduction band are shown in detail in Figure 7.14. The photocurrent temperature dependence can be tuned using these effects, and the resultant adjustability is robust even when other variables are changed.

Measuring photocurrent dependence on laser intensity at a fixed wavelength also supports the trap-based model in explaining the adjustable photocurrent dependence on temperature. While initial photoconductivity measurements were taken with a fixed illumination intensity of ~ 65 mW/cm², intensity was later varied between 1.6 to 120 mW/cm² at both 78K and 295K. As illumination intensity was varied, the current was measured at a constant voltage of 1 V, which corresponds to $3 \cdot 10^5$ V/cm. The laser and dark voltage treatments had little effect on the intensity dependence at 295K, but had a greater effect at 78K. The treatments can result in an inversion of the temperature dependence of the photocurrent for a wide range of intensities, see Figure 7.12.

At 295K, the intensity dependence of the photocurrent always followed a power law, $I_{photo} \propto Intensity^\alpha$, where $\alpha = 0.82 \pm 0.02$ over seven measurements, as shown in Figure 7.15a. This is consistent with previous room temperature measurements on large arrays of core/shell nanocrystals yielding the same α value.³⁴ Intensity dependence of the photocurrent at 78K gives $\alpha = 0.96 \pm 0.02$, as shown in Figure 7.15b, which is in agreement with the linear response at low temperature reported in the literature.¹⁴⁸ The specific value of α helps reveal the type of carrier dynamics present.

In order to understand the power law fit, it is instructive to examine the rate

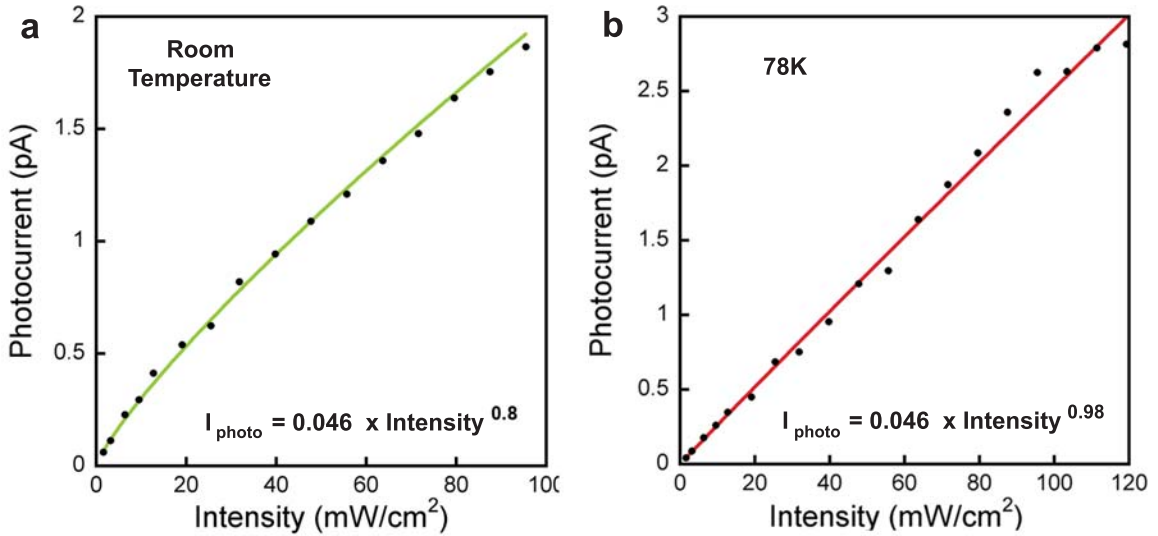


Figure 7.15: (a) Photocurrent at room temperature as a function of illumination intensity for 532 nm laser excitation measured at $3 \cdot 10^7$ V/m. The green line is a power law fit to the data with an exponent of 0.8. (b) Photocurrent at 78K as a function of illumination intensity for 532 nm laser excitation measured at $3 \cdot 10^7$ V/m. The red line is a power law fit to the data with an exponent of 0.98.

equation for n , the density of free electrons,

$$\frac{dn}{dt} = F - C(n + n_{\text{trap}})n. \quad ^{13,33} \quad (7.7)$$

Here, C is the probability of an electron to be captured, and n_{trap} is the density of trapped electrons. $n + n_{\text{trap}}$ represents the density of holes in the system which can recombine with free electrons, assuming a neutral nanocrystal. At equilibrium, $\frac{dn}{dt} = 0$, and we can rewrite F :

$$F \propto (n + n_{\text{trap}})n. \quad (7.8)$$

Substituting Equation 7.5 into Equation 7.8, we can write

$$\Phi \propto \frac{(n + n_{trap}) n}{a\eta}. \quad (7.9)$$

For $n_{trap} \gg n$, $\Phi \propto n$, but for $n_{trap} \ll n$, $\Phi \propto n^2$. Since $n \propto I_{photo}$, this means that for $n_{trap} \gg n$, $I_{photo} \propto \Phi$, but for $n_{trap} \ll n$, $I_{photo} \propto \Phi^{0.5}$. Thus, $\alpha = 1$ implies monomolecular (first-order) carrier dynamics, whereas $\alpha = 0.5$ implies bimolecular (second-order) carrier dynamics.¹³ First-order kinetics contribute more when the material has many recombination centers, such as deep hole traps, and when the material has a lower free electron concentration than in the bulk, as is the case in nanocrystals where the presence of surface traps is likely.¹⁴⁸ Contributions of surface and deep traps, which are only partially passivated by the shell and ligands, can cause a deviation of the photocurrent dependence on intensity from the expected dependence in a bulk solid, where bimolecular recombination would dominate giving $\alpha = 0.5$. Our measured exponent $\alpha = 0.8$ at room temperature implies that we observe a combination of first and second order recombination dynamics. However, at low temperature, we measured an exponent $\alpha = 1$, implying that we observe first-order recombination dynamics. The variation in the fitting exponent sheds light on the difference of recombination center density at each temperature, which supports our proposed model shown in Figure 7.14 and encompasses reported intensity dependence.^{13,34,148}

7.5 Conclusions

In conclusion, we have created nanogap devices with CdSe/ZnS core/shell nanocrystals in the gap region; after annealing, these devices can be operated as photodetectors with tunable photoconductivity. We investigated the temperature dependence of photocurrent and found that it depends on the illumination history of the device. Recent

laser illumination causes optically induced trap emptying and higher low-temperature photocurrent, while recent voltage cycling in the dark causes electric field induced trap population and lower low-temperature photocurrent. This can resolve existing discrepancies in the literature, demonstrating the difficulty in defining temperature dependence of photoconductivity for semiconducting nanocrystal systems. Additional research in this area could include investigation of trap depopulation time scales, dynamic response, dependence on nanocrystal material or size, and the optimization of treatment parameters. We find our controllable photocurrent temperature dependence to be robust over multiple wavelengths and intensities of laser excitation and suggest a route toward achieving maximal photodetector response at different temperatures. This approach of tuning the photocurrent response via trap population can be useful for nanocrystal device applications, such as sensors, solar cells, and light emitters, as well as aiding in the study of carrier dynamics and energy levels in nanoscale materials.

CHAPTER 8

Nanoelectrode Translocation Measurements¹

8.1 Introduction

Nanopores, nanometer-sized pores in thin membranes, have been studied for close to 20 years now as a potentially revolutionary DNA sequencing method,^{90,152–156} promising low-cost, high-throughput and extremely long read length. The basic concept involves placing a chamber of electrolyte solution on either side of the nanopore and applying a voltage between the chambers. This creates an ionic current through the pore, and when DNA is placed in one chamber, the voltage can also drive the DNA through the pore. The DNA then causes a decrease in the current, and this blockage can be used to interpret its physical properties, including local structure, length, and ultimately its sequence.

However, one great challenge is that the DNA moves very quickly through the nanopore so that any differences in current due the DNA sequence will be overwhelmed by noise from the amplifier electronics and the thermal motion of ions.¹⁵⁷ Three general approaches have been explored to counter this problem. The first is find ways to slow down the DNA molecule as it translocates through the pore, which has some very promising results.^{81,158} The second approach is design new electronics that would reduce noise and increase the speed of the measurement.¹⁰⁰ Our approach is to

¹ Adapted with permission from K. Healy, V. Ray, L. J. Willis, N. Peterman, J. Bartel, M. Drndić. Fabrication and characterization of nanopores with insulated transverse nanoelectrodes for DNA sensing in salt solution. *Electrophoresis*, **2012**, 33 (23), 3488-3496. Copyright 2012 WILEY-VCH Verlag GmbH & Co. KGaA, Weinheim.

add a pair of nanoelectrodes on either side of the pore, which would sense the DNA perpendicular to the molecule, see Figure 8.1a. This so called “transverse sensing” approach has yet to come close to achieving DNA sequencing, but is still of significant interest as it could enable sequencing without substantially slowing down the DNA molecule.

DNA sequencing based on tunneling current measurements was first explored in theory and simulation,^{159–165} which suggested that current differences on the order of 0.1 to 20 pA could be expected. Although tunneling current increases exponentially as the gap between the electrodes and the DNA molecule decreases,¹⁶⁶ the physical limitation is that the DNA molecule must be free to move past the electrodes. Lindsay et al.^{167–173} have studied this tunneling current in a scanning tunneling microscope (STM), using a specifically-designed molecule to mediate tunneling between the gold STM tip and the gold substrate, through the nucleotides. They have shown that each base does modulate the tunneling current in a distinct way. Kawai et al.^{174–176} have shown similar results, using bare gold nanoelectrodes without any adapter molecules. They present results with free-standing electrodes formed by break junction surrounded by solution. They also present, in a separate experiment, a nanopore configuration where the electrodes are embedded in silicon dioxide, with the gap between the nanoelectrodes being the only opening for solution to pass through.¹⁷⁷ However, they did not electrophoretically drive DNA molecules through this gap, instead depending on molecules randomly diffusing through the gap. Two other groups have also reported transverse detection of DNA molecules,^{178,179} but they showed very limited datasets and have yet to follow up on these results.

While measuring the tunneling current of DNA with nanoelectrodes has been a large focus for transverse sensing, other approaches have also been presented. One such method is to detect current modulations in current flowing through a nanowire

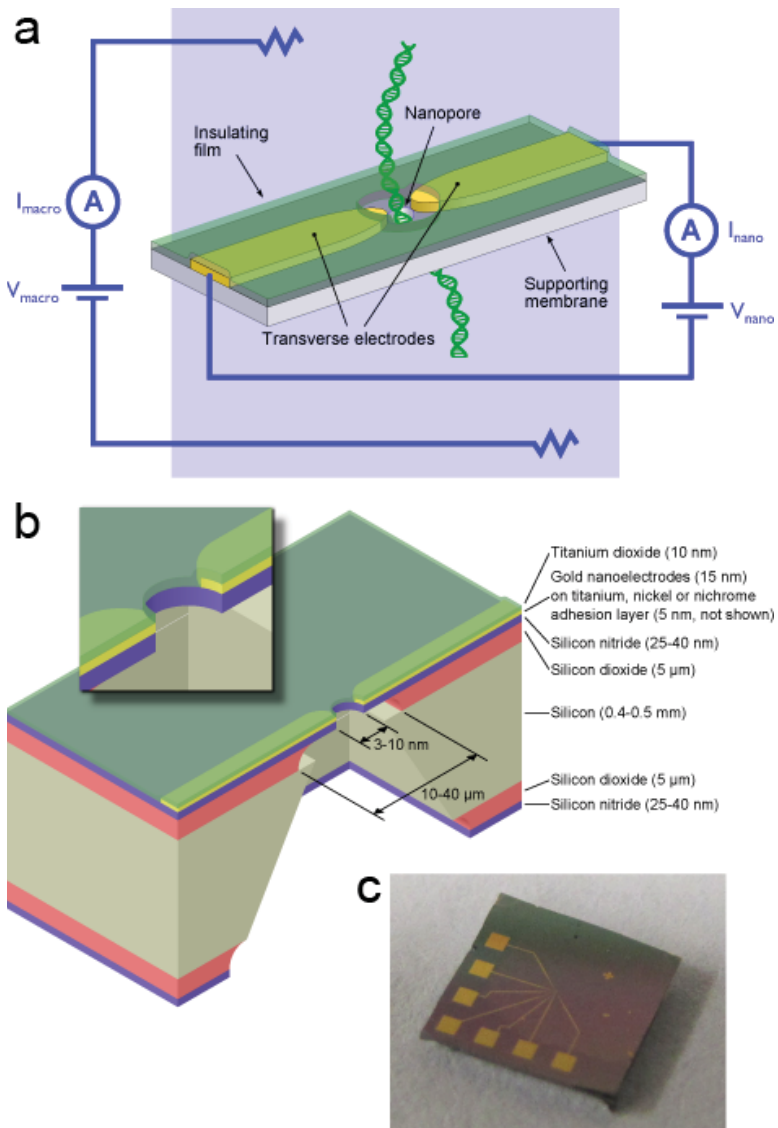


Figure 8.1: (a) Transverse sensing concept. DNA molecules are driven through the nanopore by an electric field applied via macroscopic electrodes, and the DNA bases modulate the transverse signal between the nanoelectrodes as they pass between them. (b) Diagram showing a cross-section of a silicon nitride membrane chip with a nanopore, nanoelectrodes, and insulation. The inset shows a magnified view of the nanopore area. (c) Photograph of an actual chip, where the contact pads used to interface with the nanoelectrodes can be seen. The titanium dioxide insulation layer is also faintly visible as a pinkish tinge over the connecting traces. It has been removed over the contact pads.

or graphene nanoribbon as a DNA molecule passes through or near it.^{180–182} Other geometries such as layering nanoelectrodes or graphene are also being explored.^{183–187} However, of the previous methods described, only one¹⁷⁹ is also compatible with transmission electron microscopy (TEM), which is necessary to directly measure the gap size and shape, as well as to ensure that it is free to debris.

Here we show our work on nanopores in silicon nitride membranes with aligned nanoelectrodes, for the transverse sensing of DNA across a nanopore. This has involved fabricating these devices, imaging them with TEM, and testing their electrical characteristics in salt solution. We discuss the need to insulate these nanoelectrodes, while optionally keeping their tips exposed, and describe and evaluate the process we developed to achieve this. We also explore how the presence of nanoelectrodes and insulation affects nanopore stability or DNA translocation, as observed in the ionic current signal measured using macroscopic electrodes. Finally, we summarize the failure modes of these nanopore devices during fabrication and experiments, discuss the challenges these failures pose to realizing successful and reproducible transverse measurements with nanoelectrodes, and give recommendations on how best to overcome these failures in the future.

8.2 Methods

8.2.1 Silicon Nitride Membrane Fabrication

All measurements were performed on silicon nitride membranes, which enhance electron beam lithography resolution and are compatible with TEM. Wafers begin with 500 μm silicon sandwiched between 5 μm of silicon oxide and 25-50 μm of silicon nitride. Since the oxide layer is not standard, hydrofluoric acid (HF) etches are added to the standard nitride membrane fabrication¹⁸⁸ procedure. Briefly, photolithogra-

phy is used to pattern windows and perforations onto the silicon nitride. An SF₆ etch anisotropically etches the nitride, followed by a 6:1 buffered HF etch with a few drops of Triton X-100 surfactant to reduce surface tension. A wet potassium hydroxide etch etches the silicon, followed by a second buffered HF etch. A side effect of the thick silicon dioxide layer, due to its compressive stress, is that the silicon nitride membranes are not flat, but are deformed slightly upwards. The maximum deformation occurs at the center and is approximately 1% of the membrane width.

8.2.2 Nanoelectrode Fabrication

A two-step lithography process was used to fabricate the nanoelectrodes and contacts. Nanoelectrodes and small wires that extend just off the membrane are fabricated using electron beam lithography. A 3-5 nm adhesion layer of nickel (Ni), titanium (Ti), or nichrome (NiCr) is evaporated onto the sample followed by a layer of gold, 15-30 nm thick. Next, photolithography was used to pattern contact pads, which were aligned to the small features previously fabricated. The metal for the contact pads were similar to the small features, though the layer of gold was thicker, ranging from 50-100 nm. The nanoelectrodes were insulated by 10 nm of titanium dioxide using atomic layer deposition (ALD). The ALD layer over the contact pads was removed using an SF₆ etch and a second chip to serve as a mask.

8.2.3 Nanopore Drilling and Nanoelectrode Shaping

A 5 x 5 mm chip with a fully-fabricated nanoelectrode device on a silicon nitride membrane was inserted, membrane side down, into a JEOL 2010F TEM using a modified sample holder. The gaps were inspected, and if necessary, cleared of debris or if the gap was shorted, an attempt to open the gap was made using the transmission electron beam ablation lithography (TEBAL) technique developed in our lab.¹²⁰

The ALD layer was also ablated from the nanoelectrode to allow for electrochemical conduction. A nanopore was drilled between the electrodes using the usual electron-beam drilling approach.⁹⁴ For both TEBAL and nanopore drilling, the TEM was operated at 197 kV in $\alpha 1$ mode, giving the maximum beam convergence angle. The TEM alignments were performed on a holey carbon grid prior to sample insertion, to prevent undesired damage to the nitride membrane.

To ablate more than a single spot, the condenser shifters were used to move the beam in the desired pattern. This was also the method used to account for stage drift, which could be quite significant. Gold was especially difficult to ablate, due to its high atomic weight. Sometimes, beam exposure would cause the gold to crystallize, preventing ablation. This behavior could be used to increase the yield of successful ablation by crystallizing gold adjacent to the area to be ablated. When attempting ablation, the gold would preferentially be attracted to the crystallized area, so that even if the gold was not ablated, it would retract, giving a similar effect.

8.2.4 Measurements

Devices were treated by UV/ozone to facilitate wetting, and then mounted in a custom-made poly(dimethyl siloxane) measurement (PDMS) cell. Oxygen plasma treatments gave similar results. The cell had sub-millimeter width fluidic channels to limit the area of solution in contact with the chip surface, and thus the capacitance. The laminar solution flow imposed by these channels, together with the hydrophilic nature of poly(dimethyl siloxane), make the occurrence of trapped air bubbles rare. The channels were filled with a solution of 1 M potassium chloride (KCl), 10 mM trisaminomethane-hydrochloride (Tris-HCl), 1 mM ethylenediaminetetraacetic acid (EDTA) at pH 8.5-9.0. For DNA translocation measurements, 15 kbp double-stranded DNA were also added to the solution on one side. Silver/silver chlo-

ride (Ag/AgCl) pellet electrodes made electrochemical connection to the solution, and a HEKA EPC10 triple channel patch clamp amplifier was used to apply voltage and measure and digitize current. Data was filtered using a 10 kHz 5-pole Bessel filter built into the EPC10 and digitized at 50 kHz. Custom software to record and analyze the data was written in LabVIEW. For nanoelectrode measurements, the contact pads on the silicon nitride membrane chip were bonded to a custom-designed 0.35 mm thickness printed circuit board using conductive silver paste. This enables simultaneous fluidic and electrical connection to the chip. The circuit board plugs into a flat flexible cable (FFC) connector on another circuit board, which is connected to the second channel of the EPC10 amplifier.

8.3 Results and Discussion

Figure 8.1b shows a schematic of the silicon nitride membrane chip with a nanopore and insulated nanoelectrodes. Figure 8.1c is a photograph of an actual $5 \times 5 \text{ mm}^2$ chip where the contact pads and large wires that connect to the nanoelectrodes can be seen. The titanium dioxide insulation layer is also faintly visible as a pinkish tinge over the majority of the chips; it has been removed over the contact pads.

We found that insulating the nanoelectrodes was crucial to localize sensing to the nanoelectrode gap when measuring in electrolyte solution, as well as to protect the metal from deterioration. In theory, with a perfectly pure solution and pure gold electrodes, there should be no electrochemical reaction at the voltages used, $\pm 100 \text{ mV}$. However, due to impurities in both the solution and electrodes, a large leakage current does flow, on the order of tens of nanoamps at 25 mV, relative to that expected to flow just between the electrode tips. Thus, the current flowing between areas of the electrodes away from the tips overwhelms the signal of interest. Figures

8.2a-c show finite element simulations of current density, for a potential difference of 1 V applied between the electrodes, in a solution of conductivity 1 S/m. The nanopore is 5 nm in diameter, and electrodes are 2 nm high, 5 nm wide, and 2 μ m long, with flat faces terminating at the pore edge. Where present, the insulation is 3 nm thick. These simulations were carried out using COMSOL Multiphysics. Without insulation, see Figure 8.2a and the dashed curve in Figure 8.2c, the current density decays very slowly with distance from the nanoelectrodes. In fact, the fraction of the total current that flows through a rectangle the size of the electrode cross-section, see Figure 8.2d, is negligible at less than 0.3%. With insulation, see Figure 8.2b and the solid curve in Figure 8.2c, the situation is quite different. The current density decays rapidly, and 25% of the total current flows through the same rectangle. The insulation must be thick enough to ensure uniform and complete coverage and sufficiently high resistance, but thin enough not to interfere with nanopore drilling. 10 nm of TiO₂ has been sufficient in our experience. We were not able to achieve complete coverage with thinner layers, but this could likely be addressed by optimizing our ALD process. Figure 8.2e shows a contrast-enhanced TEM image of insulated electrodes, where the titanium dioxide can be distinguished as a halo around the electrodes; this halo is not present without insulation. We test the impact of the insulation by measuring the leakage current that flows from one of the nanoelectrodes to a macroscopic electrode inserted in the solution, see the inset in Figure 8.2f. Figure 8.2f highlights that the leakage current drops by several orders of magnitude to a few pA for insulated electrodes, over the voltage range tested.

We have tested to see if the presence of nanoelectrodes and insulation affect pore stability, as observed by measuring the ionic current between macroscopic electrodes. Figure 8.3a shows the conductance of three different nanopores over a period of 60 minutes, one with insulated nanoelectrodes, one with bare nanoelectrodes, and the

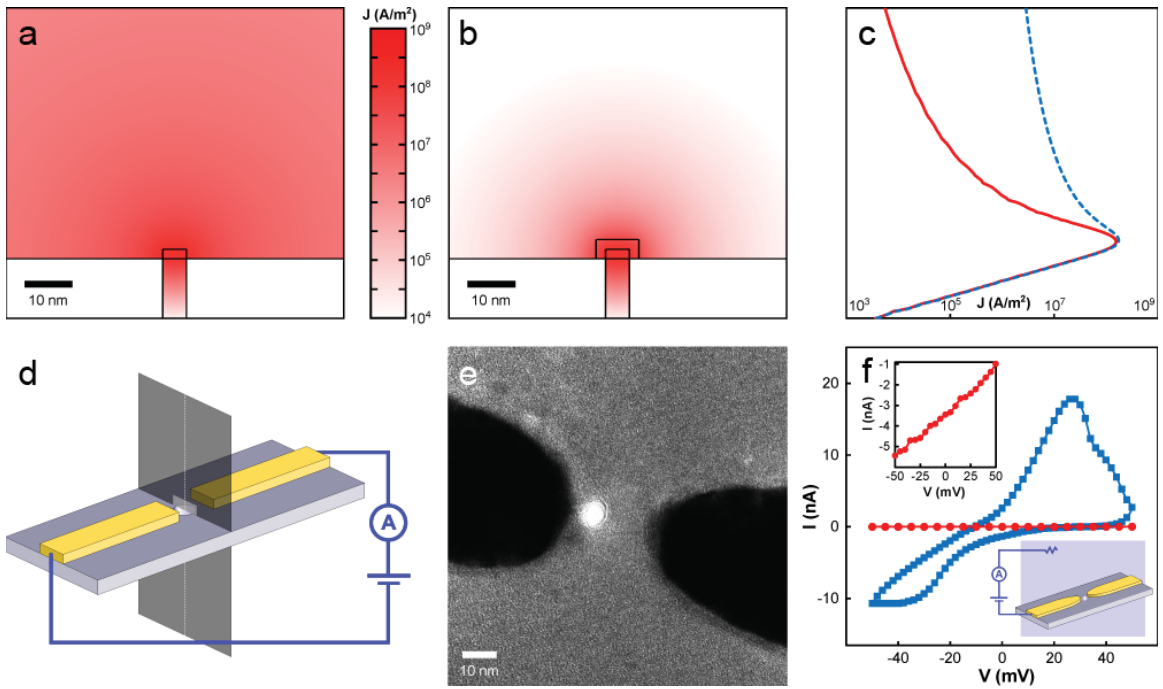


Figure 8.2: (a-c) Finite element simulations of the current density for a potential difference of 1 V between the nanoelectrodes, without (a, dashed line in c) and with (b, solid line in c) insulation. The nanopore is 5 nm in diameter, the electrodes are 2 nm high, 5 nm wide, and have flat faces terminating at the pore edge. Each nanoelectrode is 2 μm long. The insulation (if present) is 3 nm thick and covers all but the end face of the nanoelectrodes. The solution conductivity is 1 S/m. Note that the vertical axis is the same for (a-c). (d) Diagram showing how plots (a-c) are oriented. (a,b) are plots on the dark plane intersecting the membrane. The lighter rectangle on this plane is a projection of the electrode cross-section. The fraction of the total current flowing through this rectangle is quoted in the text. The curves in (c) are plots on the dashed line running along the nanopore axis. (e) TEM image of nanoelectrodes with titanium dioxide insulation. The contrast of this image is amplified to highlight the titanium dioxide layer. (f) Leakage current for uninsulated (blue squares) and insulated (red circles) electrodes, with the low leakage in the latter case highlighted in the left inset. The right inset shows the measurement configuration. This measurement was carried out in 1 M KCl, 10 mM Tris, 1 mM EDTA, pH 8.5.

other in a bare silicon nitride membrane. All nanopores were approximately 6 nm in diameter. For all cases, it can be seen that the open pore conductance remains constant around 15 nS, and there are no appreciable changes in stability over this period, which is much longer than the duration of typical nanopore sensing experiments, which are usually approximately 1-20 min. Similarly, DNA translocations are not affected. Figure 8.3b-d present ionic current recordings taken using macroscopic electrodes. These show DNA translocations through each pore, again showing that there are no significant changes with electrodes or insulation, apart from the differences that are evident in this baseline noise level. We observe that nanopores with insulated nanoelectrodes exhibit higher noise in the ionic current signal measured with macroscopic electrodes, compared to nanopores without nanoelectrodes. With bare nanoelectrodes, the noise is higher still. This is expected because the presence of nanoelectrodes increases the capacitance from one side of the membrane to the other. This capacitance scales the voltage noise of the amplifier electronics, which then contributes to the noise in the measured current. Therefore, higher capacitance means higher noise. Nanopore membranes can be reasonably approximated as parallel plate capacitors, whose capacitance is proportional to the plate area, and inversely proportional to the thickness of dielectric between the plates. The silicon support corresponds to one of the parallel plates, the silicon dioxide and silicon nitride layers are the dielectric, and the solution forms the other plate. The silicon nitride membrane with no underlying silicon dioxide in the center of the chip can be ignored in this approximation, because its area is small compared to the total area. Without nanoelectrodes, the capacitor plate area corresponds to the area of solution in contact with the SiN surface, in our case $\sim 0.7 \text{ mm}^2$. However, with uninsulated nanoelectrodes, the solution is now electrically connected to the electrodes and their associated connecting traces and contact pads, which have a significantly larger area

than that wetted by solution. Therefore, the capacitor plate area has expanded and the capacitance, and thus noise, goes up. With insulated electrodes, the additional capacitance due to the traces and contact pads outside the wetted area is in series with the capacitance from the solution through the insulation into the electrodes. As series capacitances add reciprocally, this will result in a smaller increase in capacitance and noise compared to the case of bare electrodes. The impact of this capacitance can be seen more clearly in power spectral density plots. Figure 8.3e shows power spectra of the ionic current signal measured with macroscopic electrodes for the same three nanopore devices in Figure 8.3a-d. These were control measurements without any DNA, so the ionic current was steady, without any translocation events. The capacitance-scaled amplifier voltage noise is responsible for the rise in noise power with increasing frequency on the right hand side of these plots. Higher noise in this region corresponds to higher capacitance, so, as expected, the noise is highest with uninsulated nanoelectrodes and lowest for the nanopore in a bare silicon nitride membrane. Note that the “ $1/f$ ” sloped sections on the left hand side of these plots are not related to the capacitance. High $1/f$ noise is commonly associated with poor wetting of the nanopore surface.^{189–192} Given the logarithmic nature of the plot, this $1/f$ component does not significantly influence the total noise, which was confirmed by computing the total rms noise as the integral of the spectral density with respect to frequency.

Importantly, these nanopore devices with insulated nanoelectrodes can be produced reliably. Two different shapes of electrodes were fabricated: electrodes with tips that were sharp or blunt, see Figure 8.4. Figure 8.5a-d are TEM images of a range of devices with nanoelectrodes spaced from 2.5 to 30 nm. We are aware that the distance between the nanoelectrodes in most of these devices is larger than that necessary to give a detectable tunneling current signal. We have demonstrated the

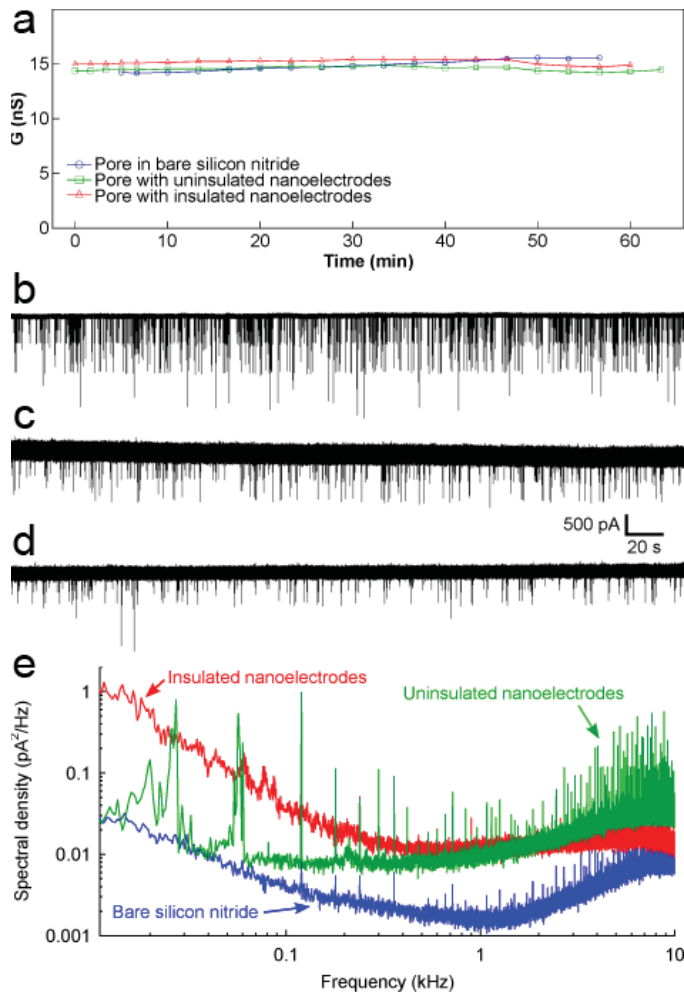


Figure 8.3: The presence of nanoelectrodes and insulation do not affect the ionic current through the nanopore (a), or the characteristics of DNA translocation (b,c,d). (b) Nanopore in a bare silicon nitride membrane without nanoelectrodes, (c) nanopore with uninsulated nanoelectrodes, (d) nanopore with insulated nanoelectrodes. (e) Noise power spectral density plots of the ionic current measured without DNA, for the same nanopore devices as in (a-d). The left-hand regions of the plots that decrease with frequency are $1/f$ noise, commonly associated with fluctuations in wetting of the nanopore surface. The right-hand regions that increase with frequency are due to the voltage noise of the amplifier scaled by the membrane capacitance. Note that the sharp spikes in these plots are all due to external interference, mainly from switching power supplies in computer equipment. These spikes are confined to very narrow frequency bands, so they do not contribute significantly to the total noise. All measurements were carried out with 120 mV bias voltage, using 1 M KCl, 10 mM Tris, 1 mM EDTA, at pH 8.5-9.0. For DNA translocation experiments, 15 kbp DNA was added to this solution.

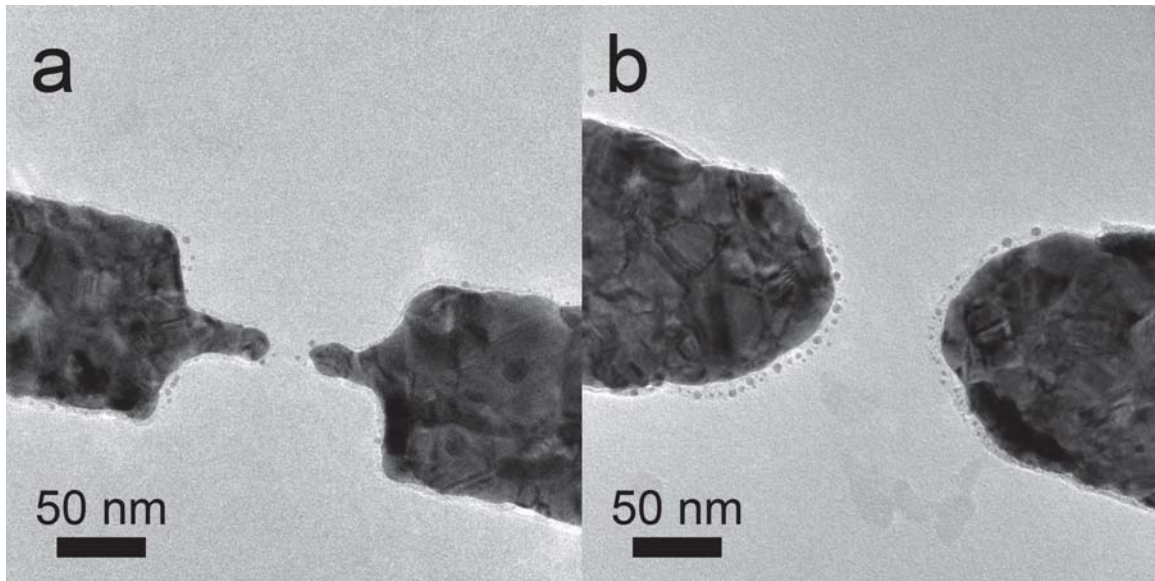


Figure 8.4: Different electrodes shapes were used: (a) electrodes with thin finger-like extensions that had a sharp tip and (b) electrodes with a blunt tip.

fabrication of small gaps to 1.5 nm,¹²⁰ but for this work on developing and refining the fabrication and experimental processes, it is simply quicker and easier to work with somewhat larger gaps as they are simpler to fabricate. In addition, we have fabricated multiple nanopores and nanoelectrodes on one silicon nitride membrane for sensing the same DNA sample in parallel, which will be necessary for eventual commercial applications. Figure 8.5e shows a device with 12 pairs of nanoelectrodes.

Fabricating nanopore-nanoelectrode devices and translocating DNA molecules through them is a complex process involving many steps. Device failure can and does occur at many points in the process and resulted in a very low yield of successful DNA translocation measurements. In addition, this low yield has prevented us to date from characterizing the transverse signal between the nanoelectrodes, or carrying out transverse measurements of DNA translocation. Over a two year period, we have fabricated over 300 of these devices. Approximately 15% of these were intact at the end of the fabrication process, as diagnosed by TEM and optical microscope

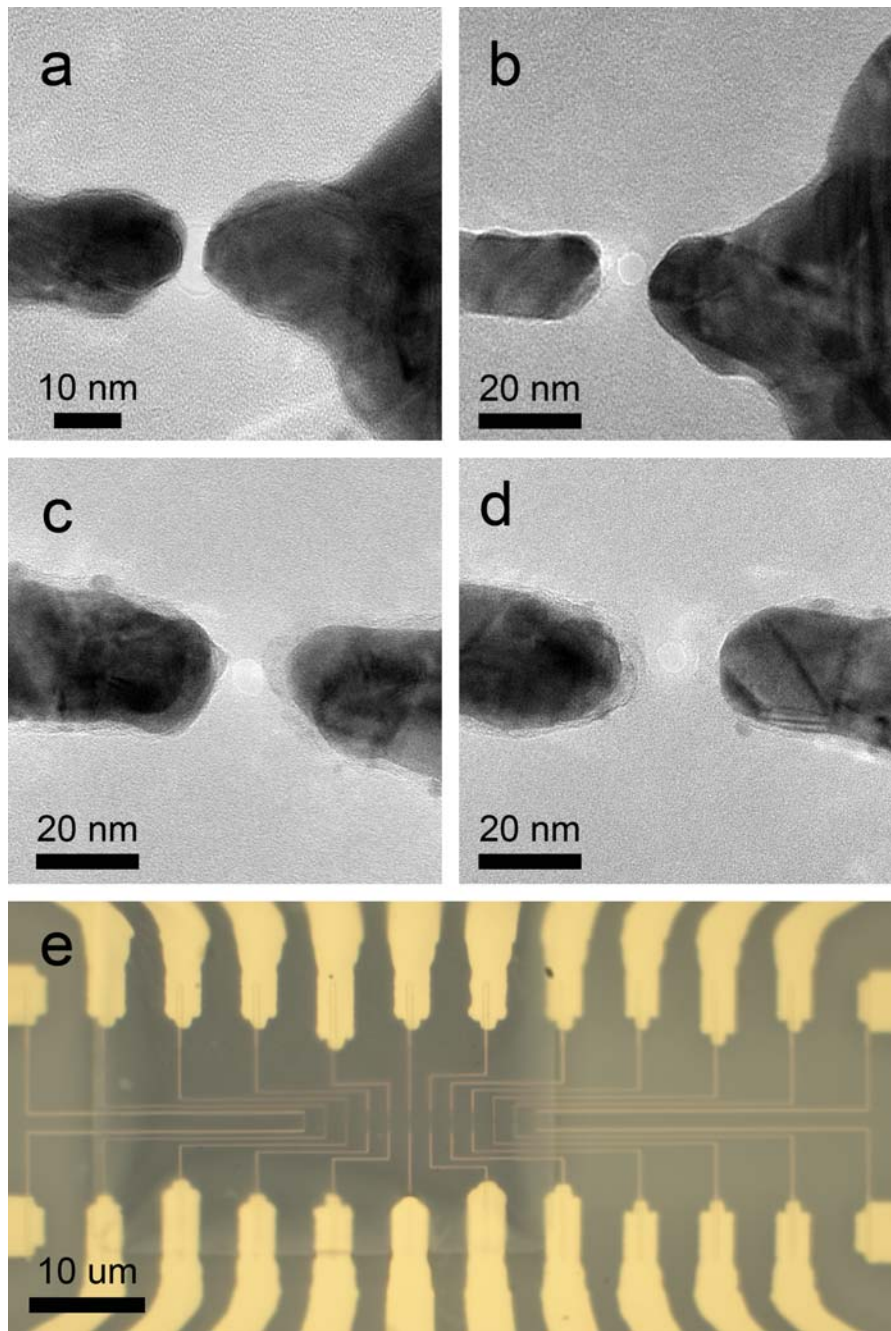


Figure 8.5: (a-d) TEM images of a range of nanopore-nanoelectrode devices. The distance between the nanoelectrodes in these devices ranges from 2.5 to 30 nm. Dark areas are gold (on a nickel, titanium or nichrome adhesion layer), lighter gray is the silicon nitride membrane, and the light circles between the gold nanoelectrodes are nanopores through the silicon nitride membrane. (e) Optical microscope image showing a silicon nitride membrane with twelve pairs of nanoelectrodes and associated connecting traces.

imaging. Of these intact devices, none yielded reliable measurements of the transverse signal between the nanoelectrodes. The devices either failed during the experiment setup or during control measurements with macroscopic electrodes, or the nanoelectrode signal was not stable. Some of these failures have not yet been encountered enough to make statistically significant conclusions, so the following can be regarded as anecdotal observations.

We see four broad classes of device failure: membrane rupture, lower (and often noisier) ionic current than would be expected for the pore's diameter and membrane thickness, devices that have expected ionic current but do not show any DNA translocation events, and devices that pass all other tests, but exhibit unstable or invalid nanoelectrode current. Membrane rupture can occur during device fabrication and during experiments. The ruptures during fabrication can be divided into two categories, the first being breakage due to mechanical shock. This is evident as jagged silicon nitride edges where the rupture occurred, much like broken glass, as shown in Figure 8.6a. The second is electrostatic discharge. This occurs centered at nanoelectrode tips and is characterized by ruptures several microns in diameter with rounded edges that could be described as melted or burned (Figure 8.6b). It is harder to analyze ruptures during experiments because removing the device from the measurement cell, cleaning it, and drying it is likely to cause further damage. However, based on the conductance, we do observe a range of rupture sizes.

Mechanical ruptures can generally be avoided by careful handling, although there are more opportunities for failure with nanoelectrodes because of the additional processing steps required to fabricate them. Electrostatic discharge is more difficult to handle. We have had success in avoiding the latter during fabrication, by connecting the nanoelectrode contact pads to each other with a narrow trace at the lithography stage. This ensures the electrodes are at the same potential, so that electrostatic

discharge will not occur from one to the other. This connecting trace is then cut just before inserting the device into the measurement cell.

The causes of lower than expected ionic current are not yet fully understood, but this has been observed previously in nanopores and is generally associated with poor wetting of the nanopore surface,^{189–192} perhaps due to organic contaminants on the surface rendering it more hydrophobic. For silicon nitride nanopores without nanoelectrodes, aggressive cleaning in hot piranha solution^{98,192} reliably resolves the issue and restores the ionic current to the expected value. Caution: piranha is a strong oxidizer that reacts violently with most organic materials. Unfortunately, piranha solution destroys our nanoelectrodes, and we have not found a similarly successful cleaning method. For devices that showed as expected ionic current, but no DNA translocation events, we do not yet have any explanation. We can only point out that this absence of DNA translocation events does not occur for nanopores without nanoelectrodes. Finally, for the few devices with which we observed DNA translocations and that did not rupture before taking a nanoelectrode measurement, the nanoelectrode signal was not reliable.

We observed cases where the signal fluctuated wildly, where the nanoelectrode current increased steadily with time, or where the current increased steadily to a plateau that was much larger than could be expected for the exposed area of gold at the electrode tips.¹⁹³ We also saw cases where the current was steady at similarly large current for the duration of the measurement. While we don't have any conclusive explanation for these results, it seems likely that either there is some remaining metal or other electrically conductive residue connecting the nanoelectrodes, or that there were gaps in the insulation layer for these particular devices. We also took post-experiment TEM images of these devices. In the majority of cases, we saw that the nanoelectrode tips had disappeared (Figure 8.6d) or peeled from the

surface of the membrane, they had been thinned significantly, or they had migrated away from the nanopore. Not enough devices survived to this point to discern any correlation between the observed nanoelectrode signals and what was observed in the post-experiment TEM images.

For those wishing to pursue this direction of research, we would emphasize that achieving a reasonable fabrication yield is crucial. Low yield makes it difficult to isolate whether experimental failures are due to fabrication issues, or more fundamental problems with the device or experiment design. Low device yield is also very time-consuming and demoralizing for those carrying out the research. For reasonable yield, it is important to minimize mechanical shock and electrostatic buildup. Mechanical shock is generally not an issue due to the robustness of silicon nitride membrane chips, but if it occurs, it can be easily identified by optical inspection, and eliminated by gentler treatment of the chips. As an aside, for silicon nitride membranes with an underlying silicon dioxide layer where the membrane is not flat due to the stress in the oxide, we would advise against depositing thick (> 100 nm) metal traces on the membrane, as the traces will distort the membrane and may cause it to rupture. To minimize the chances of membrane rupture due to electrostatic discharge, we recommend connecting the nanoelectrode contact pads to each other to keep them at the same potential, as described above. An ionizing air blower, e.g. Simco-Ion Model 5802i, may also help to prevent electrostatic buildup. In addition to fabrication yield, surface contamination is another major issue that has prevented successful nanoelectrode measurements. While we do not have absolute proof that surface contamination is the cause of lower than expected ionic current or excessive ionic current noise in nanopore devices, it is well known that these problems are eliminated by cleaning with piranha solution. While we have yet to find a cleaning method of similar effectiveness that is compatible with metal nanoelectrodes, we do note that these problems are

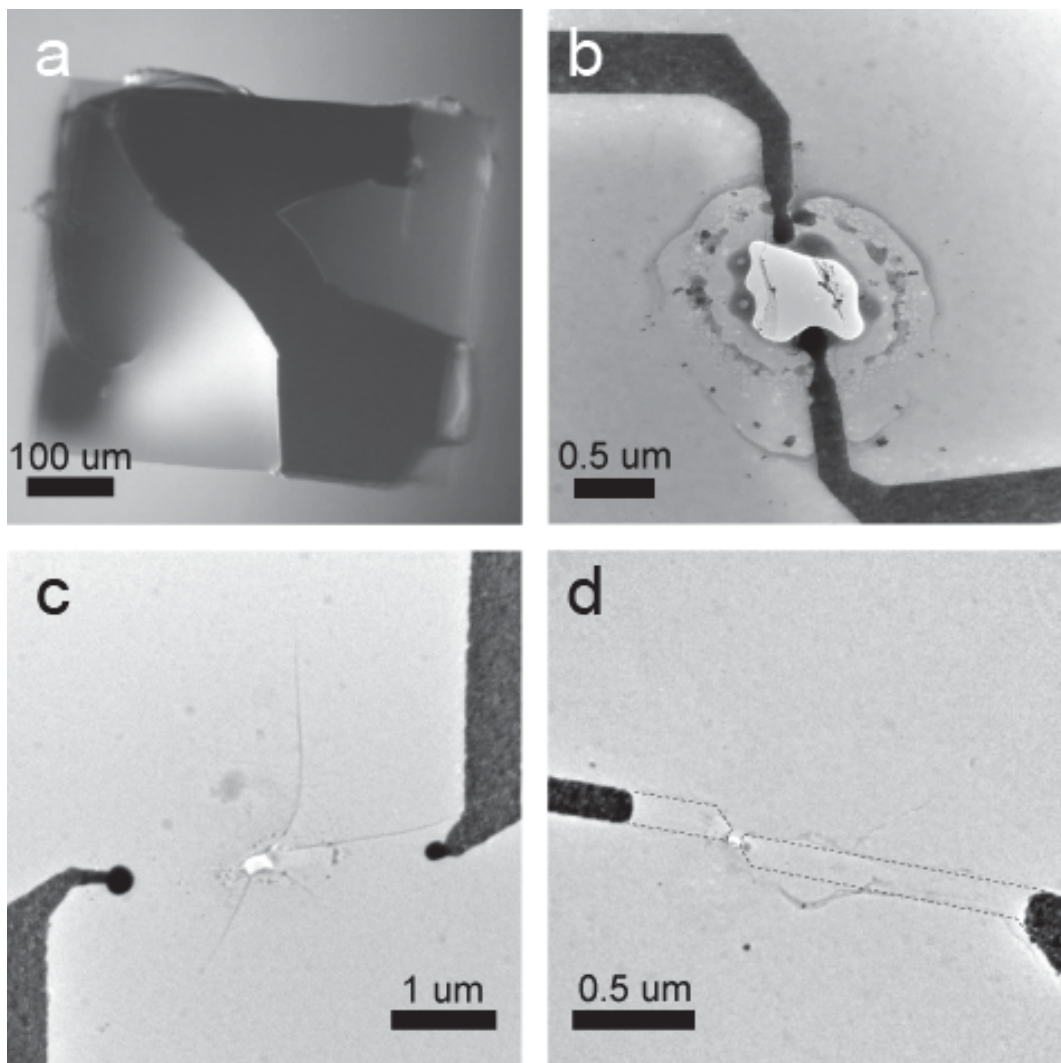


Figure 8.6: (a) Optical microscope image of a silicon nitride membrane that ruptured due to mechanical shock. This membrane is much larger than those used for nanopore experiments. It is shown here because its size illustrates the characteristics of rupture very clearly, but smaller membranes rupture in the same way. (b,c) TEM images of ruptures caused by electrostatic discharge between nanoelectrode tips. Note the difference between the smooth edge of the rupture characteristic of electrostatic discharge, compared to the jagged edge associated with mechanical shock. In the case of electrostatic discharge, the membrane may also have fractures in the radial direction, as in (c). (d) TEM image of a nanopore-nanoelectrode device after measurement in solution that did not rupture due to mechanical shock or electrostatic discharge, but where the nanoelectrode tips have disappeared. The dashed lines show the original footprints of the nanoelectrodes.

reduced when the nanopore devices are subjected to rapid thermal annealing and/or plasma cleaning directly after removal from the TEM, and then stored in 70% ethanol until they are used in an experiment.

8.4 Conclusions

We have fabricated insulated nanoelectrodes on low-capacitance silicon nitride membranes and drilled nanopores between them. Our simulations show that nanoelectrodes must be insulated, apart from their tips, to localize the sensing region, for measurements in electrolyte solution. We accomplished this insulation by atomic layer deposition and show leakage current measurements to prove that it works. By performing ionic current measurements using macroscopic electrodes, we have demonstrated that the presence of nanoelectrodes and insulation does not affect the stability of the ionic current flowing through these pores, nor does it affect the characteristics of DNA translocation. However, device failure during fabrication and experiments has been a significant issue. This has to date prevented us from reliably and reproducibly measuring current between the nanoelectrodes or studying their response to translocating DNA molecules. We have summarized the types of device failure we have encountered, discussed the causes, where known, and made recommendations on how those wishing to pursue this direction of research can minimize these failures.

CHAPTER 9

Nanowires for DNA Sensing

9.1 Introduction

DNA sequencing has the potential to revolutionize medicine. By measuring an ionic current through a nanopore in an electrolyte solution, DNA can be sensed as a current blockage. Currently, both biological and solid-state nanopores are being studied, both of which have advantages and disadvantages.^{88,90,152} While many groups have focused on measuring the ionic current, combining this data with transverse measurements shows promise.^{178–180}

Previous groups have shown that bases can be distinguished by measuring the tunneling current of different DNA bases with techniques that include using scanning tunneling microscopy (STM)^{167–173} and diffusion through electromigrated gaps^{174–176}. However, tunneling current decreases exponentially with distance from the electrode, and fabrication of solid-state nanopore tunneling devices is difficult.¹⁹⁴ Prior research has had limited success, but most devices are not compatible with transmission electron microscopy (TEM), which we believe to be crucial to ensuring that devices are clean and properly characterized.

Here we show work on nanowires integrated with TEM-compatible nanopore devices for tranverse sensing of DNA. We discuss device fabrication, electrical measurements, and DNA translocations. The DNA translocations were analyzed and shown to have three types of events: collisions, unfolded events, and folded events. We also discuss a procedure for making nanopores hydrophilic without the use of piranha.

9.2 Methods

Devices were fabricated on 50 nm thick silicon nitride membranes, see Figure 9.1a and b for an optical image of a completed chip. Wafers are 500 nm of Si sandwiched between 5 μm of silicon oxide and 25-50 μm of silicon nitride. Fabrication of the nitride membranes from a wafer with silicon oxide has been previously described.^{188,194}

Nanowires and small features were written with electron beam lithography (EBL). C4 495 PMMA was spun onto chips at 4000 RPM and baked for at least 10 minutes at 180°C. Typical writing parameters for an Elionix 7500 included a current of 20 pA and dose time of 0.1 μs with a field size of 150 μm and 240,000 dots. Samples were developed in 1:3 methyl isobutyl ketone:isopropanol (MIBK:IPA) for 60 seconds and rinsed in IPA. Chrome was evaporated onto the sample in a home-built thermal evaporator, then lifted off with acetone, see Figures 9.1b and c. Large wires and contact pads were fabricated with photolithography. Futurrex NR7 was spun at 4000 RPM and baked for three minutes at 115°C. The mask was aligned to the small features, then the sample was exposed to 365 nm light at 3.3 mW/cm² for 52 seconds. Samples were developed in Futurrex RD6 for seven seconds and rinsed in deionized water. 5 nm of titanium (Ti) and 100 nm of gold (Au) were evaporated onto the sample and lifted off with acetone. 20 nm of aluminum oxide (Al_2O_3) was deposited via atomic layer deposition (ALD) at 250°C, which is visible with TEM as a lighter grey shadow around the darker chrome, see Figure 9.1c.

The nanopores were drilled in a JEOL 2010F TEM by focusing the beam in $\alpha 1$ mode at 800,000 times magnification, see Figure 9.1. When drilling through the aluminum oxide, a volcano-like structure can often be seen, see Figure 9.2. It is caused by the beam melting the ALD layer and melted material away is pushed away from the pore. The material then reforms in a raised circle around the pore area. Imaging also becomes more difficult after drilling through the ALD layer.

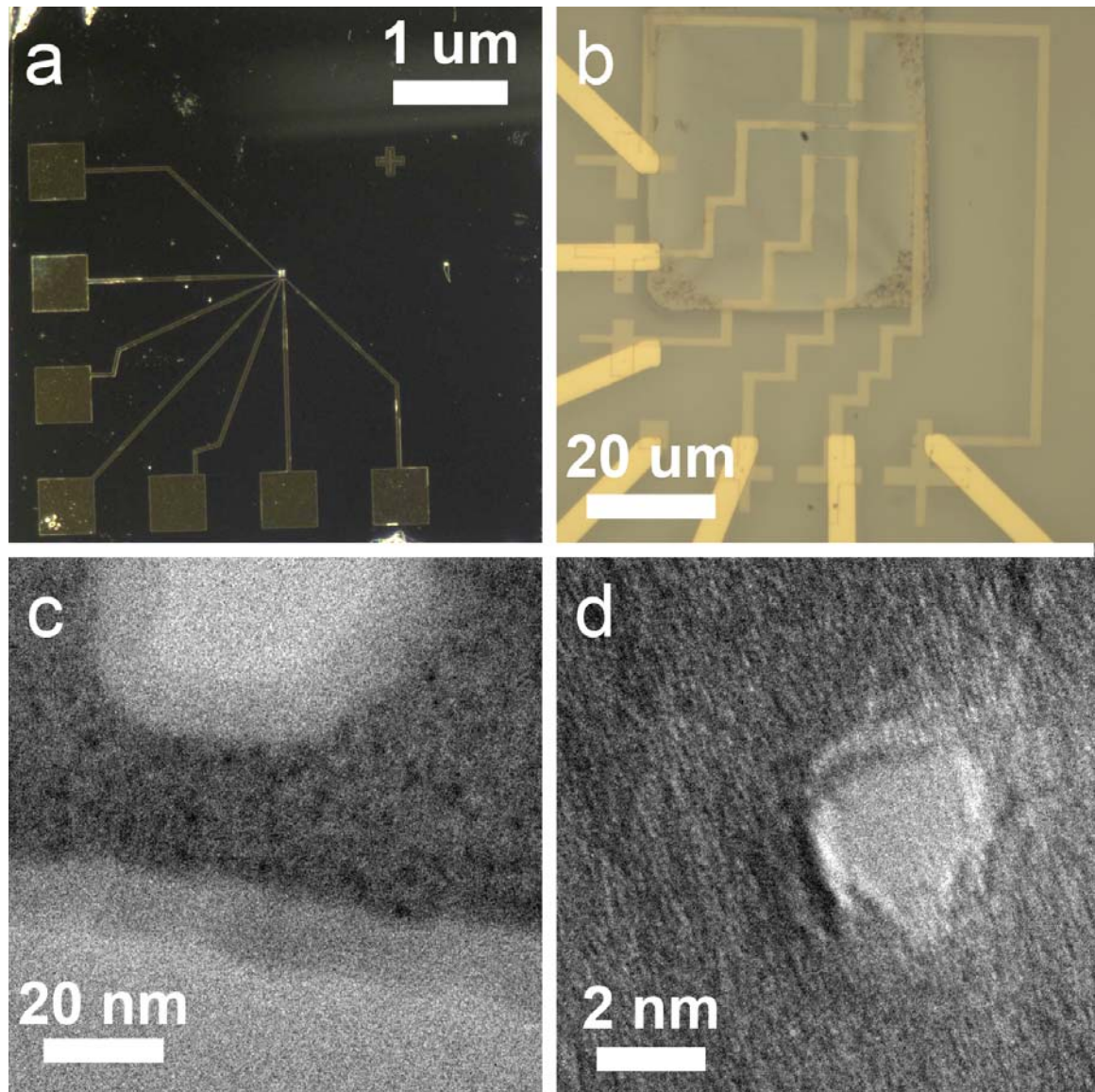


Figure 9.1: Optical images of (a) a chip with three wires and of (b) the window. The small features are chrome oxide, made with EBL, and the large features are Ti/Au, made with photolithography in a second step. (c) TEM image of a wire. The dark grey is the chrome oxide wire, and the light grey shadow around it is the aluminum oxide ALD layer. (d) TEM of a pore.

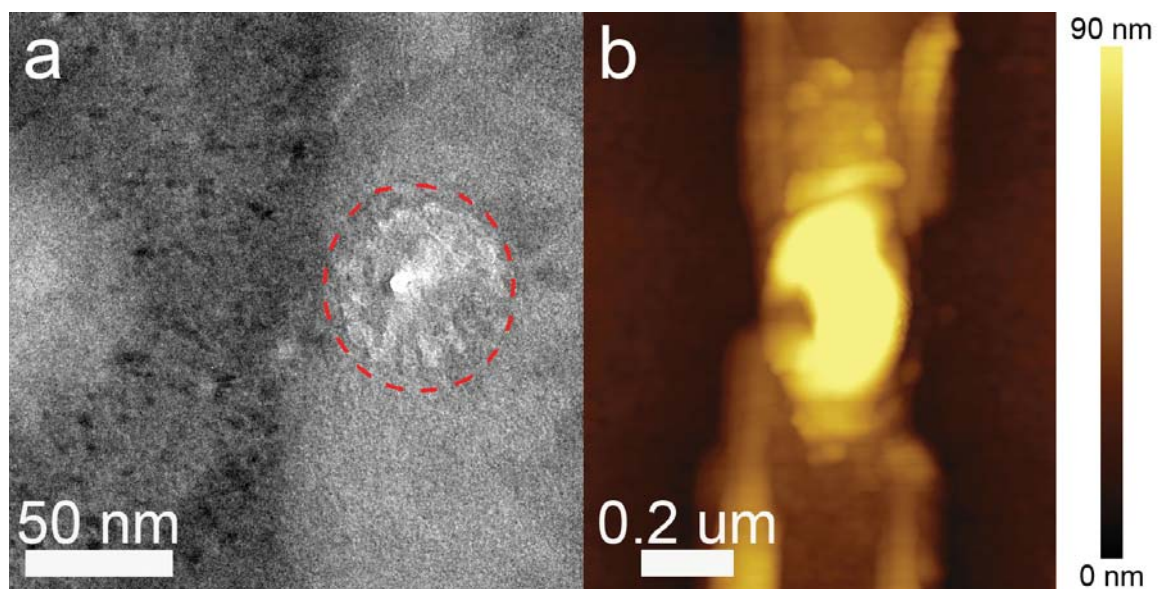


Figure 9.2: (a) TEM image of a nanowire and pore surrounded by a crystallized, circular mass of the ALD layer. The feature was caused by focusing the TEM beam and is emphasized by the red, dashed circle. (b) An atomic force micrograph of the ALD mound caused by the TEM beam. It is also possible that some height is due to carbon deposition. Image (b) courtesy of Matthew Puster.

9.3 Results and Discussion

The resistance of devices was tested after the contact pads were completed. However, most devices showed resistances in the megaohm range or even higher, see Figure 9.3a. Devices were annealed at 350°C for 10 minutes under 5% hydrogen in argon. The resistances of the wires showed improvement to the kilohm range, see Figure 9.3b. We believe that the junction between the EBL features and the photolithography features had very poor contact, without any treatments; the electrical contact was then improved with annealing.

For nanopore devices with metal features, the usual piranha cleaning cannot be used because the piranha will destroy the metal. This important cleaning step ensure the pore's hydrophilicity, and without it, pores will usually not conduct current. Yield was greatly improved with the use of heated ozone, rapid thermal annealing, and plasma cleaning. Samples are heated at 150°C in ozone for 20 minutes on each side. They are then heated in a rapid thermal annealer for one minute at 350°C under 5% hydrogen in argon. The final step is cleaning with 6.4 sccm of hydrogen and 27.5 sccm of oxygen with a forward RF power of 50W. One cycle of these cleaning steps would usually allow a pore to become hydrophilic after applying a voltage to it, including flipping the polarity several times. However, this exposed the device to high voltages in solution for a non-negligible time, and in the end not every pore would open. We found that performing the cleaning cycle twice, would regularly allow the pore to immediately give ionic current, with a low rate of failure.

The electrolyte solution used in this experiment was 3 M potassium chloride (KCl), 10 mM trisaminomethane-hydrochloride (Tris-HCl), 1 mM ethylenediaminetetraacetic acid (EDTA) at pH 10. The ionic current was filtered with a 10 kHz three-pole Bessel filter using a HEKA amplifier; data was then sampled at 50 kHz. The ionic currents were often slightly nonlinear, see Figure 9.4a. This may be due to the

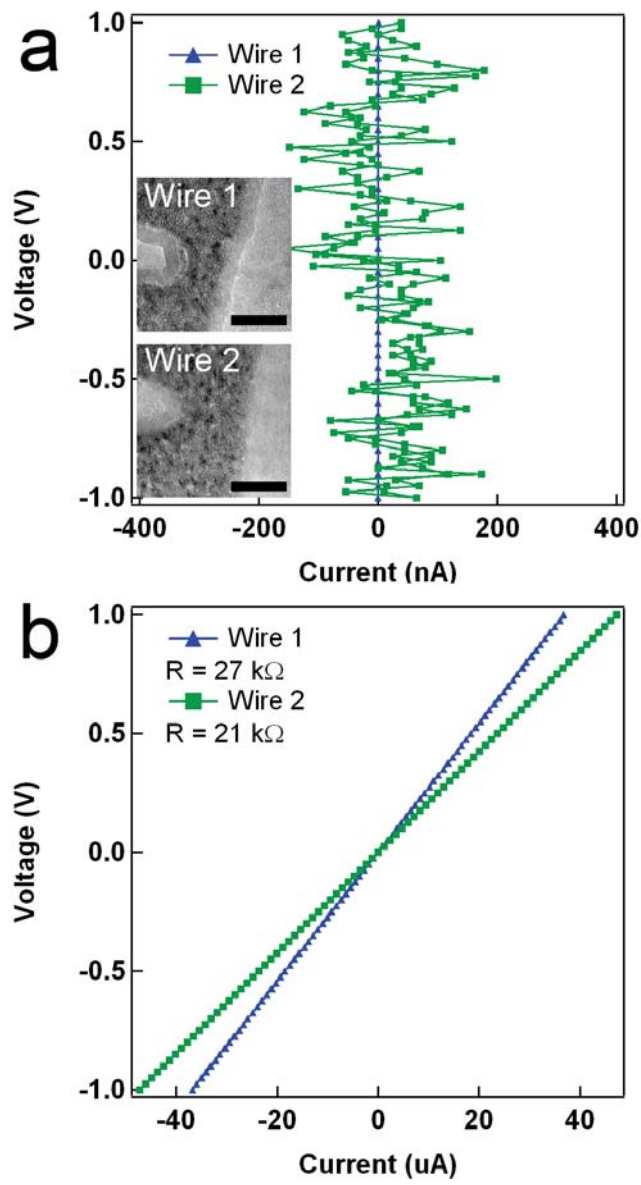


Figure 9.3: Resistance measurements of two wires (a) without treatment and (b) after rapid thermal annealing at 350°C for 10 minutes. The insets in (a) are TEM images of the wires and the scales bars are 50 nm.

ALD layer on one side: it wets differently than the silicon nitride on the back and the funnel it forms from the drilling may encourage more ion transfer than the flatter back. Translocations were not observed before adding DNA, see Figure 9.4b. Once double-stranded, 15 kilobase (kbp) pair DNA was added, translocations can be seen in the ionic current as upward spikes with a voltage of -500 mV, see Figure 9.4c.

A histogram of the blocked current, I_B with a three-gaussian fit is shown in Figure 9.5a, where

$$I_B = I - I_{open}, \quad (9.1)$$

where I is the measured current of an event and I_{open} is the mean pore current before the event. The three peaks, in order from least blocked current to most, represent collisions, unfolded events, and folded events. The mean value of these peaks were 115 pA, 236 pA, and 472 pA, respectively. In the fit, The mean value of the folded events was forced to be twice the mean value of the unfolded events. A graph of these two gaussians is shown in Figure 9.5b. A graph of the median blocked current of an event vs. the event length is shown in the inset of 9.5b. The folded and unfolded events can be seen as two different populations centered on \sim 350 pA and \sim 175 pA, respectively. No nanowire signal could be correlated with the ionic signal. Since the wire was coated with an insulator, this inhibited sensing.

The most common device failure was due to electrostatic discharge, which caused the small features to “blow up,” see Figure 9.6a. While careful grounding was generally achieved, devices often seemed to be destroyed during insertion into the TEM, even though the sample rod was grounded. It is possible that this could be mitigated by covering the sample holder, see Figure 3.11, with a conductive metal, such as gold, to ensure the sample itself is grounded to the insertion rod. Another cause of failure was the dissolution of the gold wires after being measured in solution for a significant time period, see Figure 9.6a. This dissolution occurred even though there

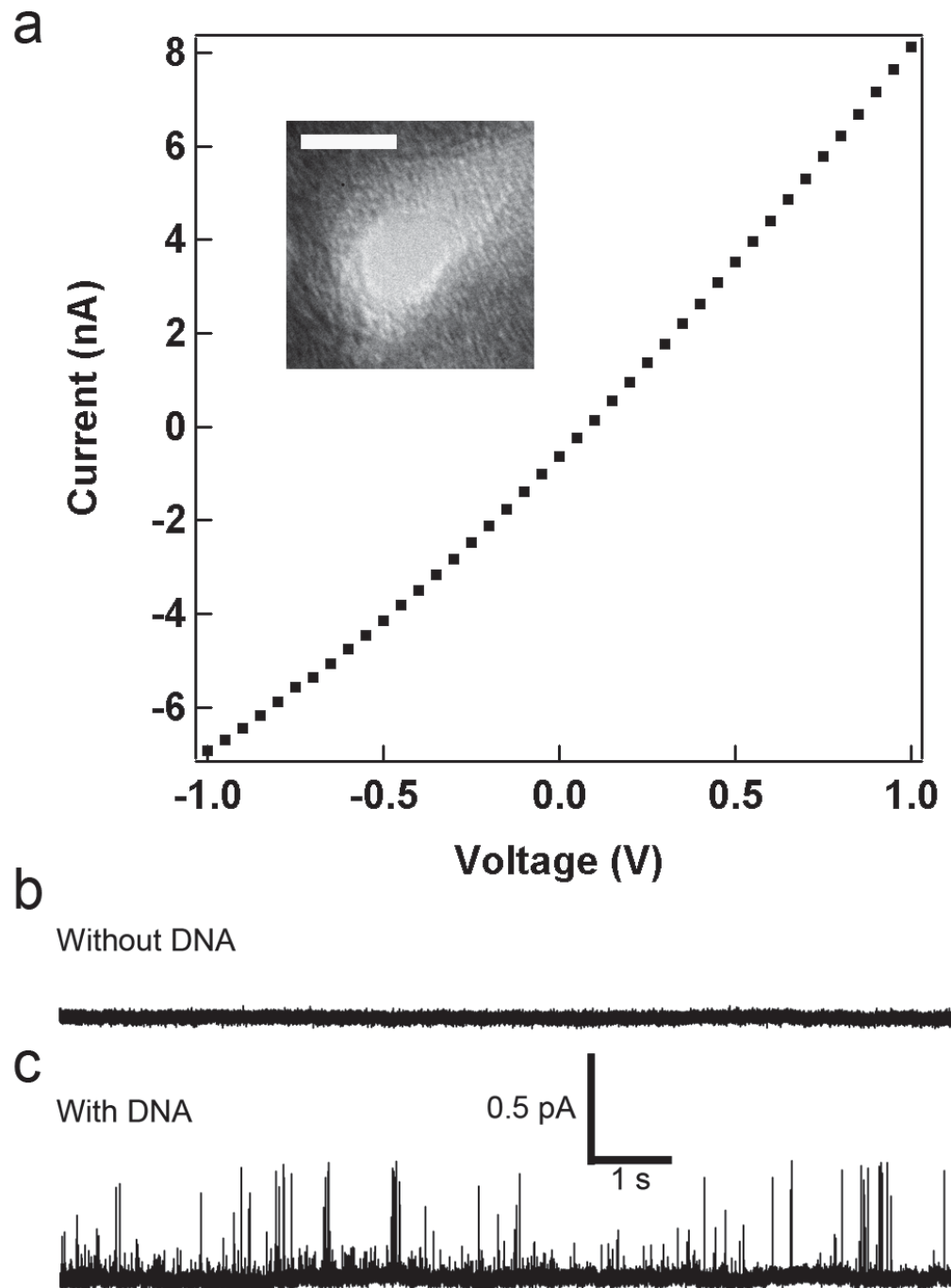


Figure 9.4: (a) IV Sweep of the same nanopore. Inset: A TEM image of the nanopore. The scale bar is 2 nm. Ionic time traces of the same nanopore (b) before DNA is added and (c) after double-stranded, 15 kbp DNA is added. These measurements were carried out in a 3M KCl, 10 mM Tris, 1 mM EDTA, pH 10 solution.

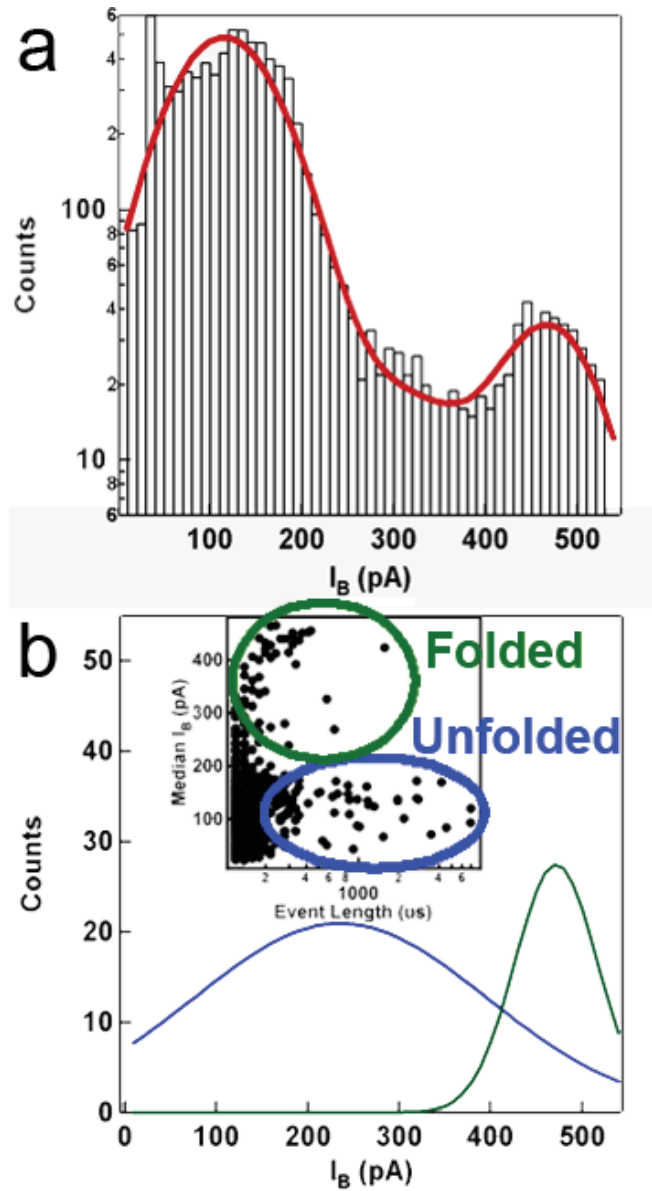


Figure 9.5: (a) Histogram of the blocked current. The data is fit with three gaussians, with mean values of 115 pA, 236 pA, and 472 pA. The first peak represents collisions, the second peak represents unfolded events, and the third peak represents folded events. For the fit, the third peak was forced to be twice the value of the second peak. (b) The fit with the collision peak removed to show just the events. Inset: Scatter plot of event length vs. the median blocked current for each event. Folded and unfolded events are highlighted with circles.

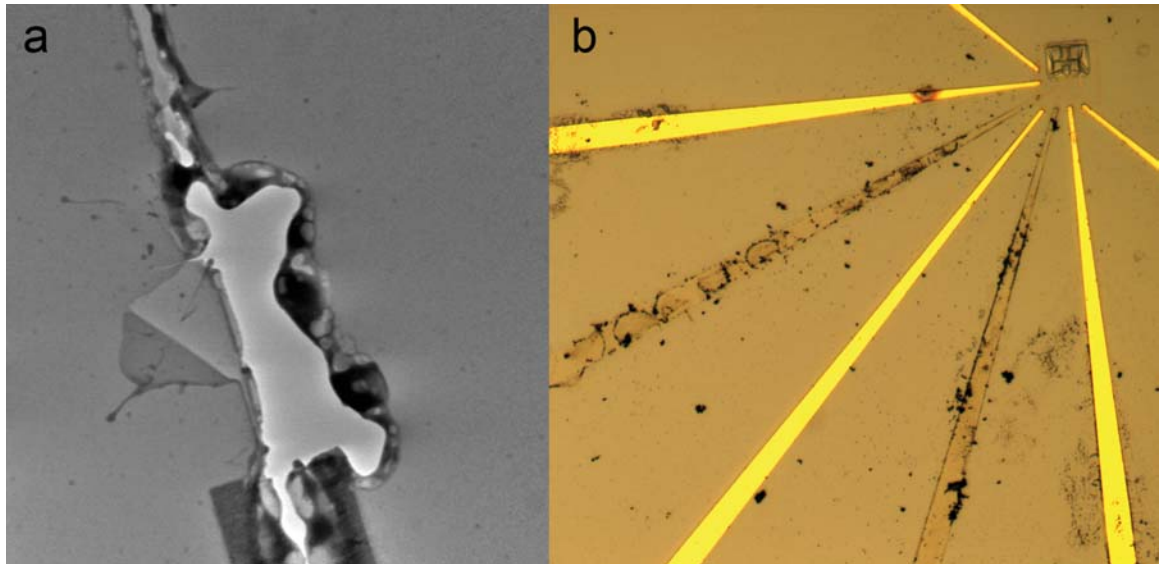


Figure 9.6: (a) When measuring in solution, the gold wires tend to react with the solution and dissolve. (b) It is very common for the nanowires to blow up before it can be measured.

was a protective ALD layer. This suggests that the ALD layer is of limited use, and due to the features it produces during the nanopore drilling, discarding it may prove beneficial to future experiments.

9.4 Conclusions

We fabricated chrome oxide wires on silicon nitride membranes, and insulated them with an ALD layer of Al_2O_3 . A nanopore was drilled near the wire for transverse sensing. Though no nanowire signal could be correlated with the ionic signal, future experiments with the pore drilled in the wire could improve correlation. While the ALD layer was for isolation of the wires from the solution, the gold still dissolved, and it may have caused the ionic signal to be nonsymmetric with voltage. It also makes drilling and imaging the nanopore more difficult, while inhibiting sensing. DNA translocations were observed ionically, and a method for making pores hydrophilic

without the use of piranha was successfully employed. Future experiments should include gating the nanowire and using different metals.

CHAPTER 10

Conclusions

Nanoelectronics have become an important method of exploring various nanoscale materials. Electron beam lithography, combined with suspended silicon nitride membranes for transmission electron microscopy, were used to push the limit of device fabrication and examination. The devices were used to measure nanocrystal transport, with the desire to learn ways to enhance their photocurrent, and to integrate DNA sensors with nanopores, with the desire to bring solid-state devices closer to fast, affordable DNA sequencing.

10.1 Nanocrystals

Semiconducting nanocrystals are an important resource for optoelectronics due to their properties being strongly size-dependent with well-studied syntheses. However, their electronic transport is limited by their interparticle spacing and insulating ligands. We have reported a gold-seeded synthesis to create lead selenide clusters of particles. While clearly joined, smaller, individual particles were still distinctly observed. We performed ligand exchanges and treatments, including annealing and hydrazine soaking, to decrease the interparticle spacing and increase interparticle conduction. We found that substituting oleic acid for shorter ligands decreased the interparticle spacing, though assembly could be affected and agglomeration was a concern. Though annealing was effective in increasing transport in large-scale films, it was shown to have a negligible effect on sub-monolayer films; for these, hydrazine was very effective. However, annealing increased photocurrent with only a negligible

increase to the dark current; hydrazine caused both to increase, and the photocurrent was often smaller than the dark current. Transport could also be increased, or decreased, through manipulation of trap states within the nanocrystals by sweeping the voltage while illuminating them with a laser or while keeping them in the dark. This effect was most pronounced in the photocurrent at liquid nitrogen temperatures. These studies have increased our understanding of nanocrystal transport, and may lead to improved nanocrystal-based optoelectronics.

10.2 Nanopores

Current DNA sequencing methods are expensive and time-consuming, and as personalized medicine becomes a reality, new methods are quickly being created. We have shown techniques to fabricate nanoelectrodes and nanowire sensors near solid-state nanopores using electron beam lithography and transmission electron microscopy. While direct sensing with the transverse electronics was not realized, DNA translocations were measured ionically. We also describe methods to make the pore hydrophilic without the use of piranha were developed. These methods include heating in a rapid thermal annealer, exposure to heated ozone, and exposure to oxygen/hydrogen plasma. We discussed common device failures with recommendations to mitigate future failures, including grounding every instrument and tool, as well as cleaning samples at every stage. We expect that these findings will bring us one step closer to sequencing DNA with fast, robust, reusable, and affordable solid-state nanopore devices.

APPENDIX A

Recipes

A.1 Lithography

A.1.1 Electron Beam Lithography

For the following recipes, the resist is dripped onto the sample with a pipette while spinning at a low speed, such as 500 RPM. For small features on the order of hundreds of nanometers or less, C2 950 PMMA was spun onto a chip at 5000 RPM for approximately 45 seconds. The chip was then baked at 180°C for at least ten minutes. For larger features, C4 495 PMMA was spun on at 3000 RPM for 45 seconds and baked at 180°C for at least ten minutes. For better liftoff of larger features, a double layer of PMMA may be used: C4 495 was spun on first, followed by C2 950, with both using a spin speed of 3000 RPM for 45 seconds and a baking time of ten minutes at 180°C.

After writing a pattern, the chip was developed in 1:3 methyl isobutyl ketone:isopropanol (MIBK:IPA) for 60 seconds with no swishing. It is then put in IPA for another minute and then gunned dry. Previously, the chip was swished in the developer for 60 seconds, and after evaporation of an adhesion layer and gold, the all of the gold lifted off, leaving only the adhesion layer.

Elionix

For obtaining very small gaps on silicon nitride membranes without an oxide layer, C2 950 PMMA was dripped onto the sample with a pipette while spinning at a low

Resist	Field Size (μm)	Dots	Dose Time (μs)	Current (pA)
C2 950 PMMA	300	240,000	0.56	20
C4 495 PMMA	150	240,000	0.1	20
HSQ	150	240,000	1.2	20

Table A.1: Writing parameters for the Elionix.

speed, such as 500 RPM. It was then spun at 5000 RPM for 50 seconds and baked at 180°C for at least ten minutes. For a field size of 300 μm and 240,000 dots, the dose time was 0.56 $\mu\text{s}/\text{dot}$. For the gaps used in the DNA project, C4 495 PMMA was dripped onto the sample with a pipette while spinning at a low speed, such as 500 RPM. It was then spun at 4000 RPM for 50 seconds and baked at 180°C for at least ten minutes. For a field size of 150 μm and 240,000 dots, the dose time was 0.1 $\mu\text{s}/\text{dot}$.

To make ribbons using HSQ resist, the HSQ was dripped onto the sample using a plastic pipette, since a glass pipette causes the resist to solidify and precipitate. The resist is added while the sample was slowly spinning, and then the speed was increased to 4000 RPM for 50 seconds. There was no baking before exposure. For a field size of 150 μm and 240,000 dots, the dose time was 1.2 $\mu\text{s}/\text{dot}$. For the HSQ developer, see Section A.3

For a summary of these recipes, see Table A.1.

Johnson Lab SEM

The magnification and field size must multiply to 80000. The most commonly used were 2000X and 40 μm for fine features, 850X and 92 μm for medium-sized features (note that this does not multiply to 80,000, but was still used for historical reasons), and 25X and 3200 μm for large features, including contact pads. For the 40 μm field, typically a dose of 700 $\mu\text{C}/\text{cm}^2$, a current of 10 pA, and a pixel size of 0.0012 μm

Magnification	Field Size (μm)	Dose ($\mu\text{C}/\text{cm}^2$)	Current (pA)	Pixel Size (μm)
2000X	40	700	10	0.0012
850X	92	750	30	0.0042
25X	3200	600	20,000	0.9766

Table A.2: Writing parameters for PMMA the Johnson lab SEM.

was used. For the $92 \mu\text{m}$ field, typically a dose of $750 \mu\text{C}/\text{cm}^2$, a current of 30 pA, and a pixel size of $0.0042 \mu\text{m}$ was used. The increase in dose was to ensure that even if pixels were skipped if the beam moves too quickly, the proximity effect will ensure that the features are properly connected. Generally, it was not recommended for the beam to travel faster than 1 mm/s for medium-sized features that include diagonal features. For the $3200 \mu\text{m}$ field, typically a dose of $600 \mu\text{C}/\text{cm}^2$, a current of 20 nA, and a pixel size of $0.9766 \mu\text{m}$ was used. See Table A.2 for a summary.

A.1.2 Photolithography

Two recipes were used to make the 24 contact pad pattern. AZ5214E was dripped onto the sample while stationary until it covered the sample surface. The sample was then spun at 4000 RPM on a Headway spinner for 45 seconds. It was prebaked at 100°C for two minutes, and then exposed to 365 nm light at $5 \text{ mW}/\text{cm}^2$ for four seconds. The sample was postbaked at 120°C for two minutes, followed by a flood exposure for four minutes with the same light source as the exposure. It was developed in AZ 726 for 30 seconds with gentle swishing; then it was rinsed in DI water for 60 seconds. A nitrogen gun was used to dry the sample. The second recipe used Futurrex NR7, a negative resist. The resist was dripped onto the sample while stationary until it covered the sample suface. It was spun at 4000 RPM on a Headway spinner for 45 seconds and baked for three minutes at 115°C . The sample was exposed to 365 nm light at $5 \text{ mW}/\text{cm}^2$ for one minute and then baked at 115°C for three minutes.

Development was seven seconds in RD6 while gently swishing. The sample was then rinsed in DI water and gunned dry. This recipe actually slightly underexposed the resist because it makes the points of the wire sharper without sacrificing liftoff.

For the seven contact pad pattern, NR7 was also used. The procedure is the same as previously described except the exposure time was 34 seconds. For the NX2600, the exposure time for NR7 was 11 s.

A.2 Wafer Processing

For the wafers with silicon oxide, the wafer was vacuum vapor primed with HMDS for five minutes. It was baked at 115°C for three to five minutes. If the wafer does not have silicon oxide, HMDS may not be necessary. For either type of wafer, S1818 was spun at 4000 RPM for 45 seconds on the cleanest side of the four inch wafer. This was the side onto which devices are fabricated. The wafer was then baked at 115°C for three minutes. The opposite side was coated with NR7 spun at 4000 RPM for 45 seconds and baked at 115°C for three minutes. In the past, there had been some difficulty getting a smooth, even coat of NR7, so AZ5412E could be used. This was spun at 4000 PRM for 45 seconds and baked at 100°C for two minutes. If NR7 was used, the wafer was exposed for 34 seconds with a 365 nm light at a power of 5 mW/cm², then baked at 115°C for three minutes. If AZ5412E is used, the wafer is exposed for four seconds with a 365 nm light at a power of 5 mW/cm², then baked at 120°C for two minutes, followed by a flood exposure for four minutes. The wafer was developed for seven seconds in Futurrex RD6 for NR7 or 30 seconds in AZ 726 for AZ5412E. The wafer was then rinsed in water and gunned dry.

The wafer was put in the WNF Technics etcher and descummed with oxygen plasma for one minute at 100 mTorr above vacuum at 50 W. SF₆ is used to etch the

silicon nitride exposed by the photolithography for 10 minutes with a pressure of 300 mTorr above the vacuum at 50 W. Glass slides on either side of the wafer are used to prevent sideways motion. The wafer was then rotated 180° and etched again for 10 minutes with a pressure of 300 mTorr above the vacuum at 50 W. Previously, the paramters for the Johnson lab Technics were two or three minutes with a pressure of 400 mTorr at 50 W.

For the wafers with silicon oxide, the next was an HF etch. The HMDS vacuum vapor prime was necessary to prevent the resist from coming off during this etch. The HF bath in the Wolf Nanofabrication Facility, or a teflon beaker of 6:1 buffered hydrofluoric acid with a few drops of Triton X-100 surfactant, could be used. The wafer must be carefully dipped in and out to remove bubbles that form in the exposed areas. A small teflon rod can also be used to pop any bubbles. The wafer was etched for 70 minutes.

For either type of wafer, the resist was removed using a stripper such as Shipley Microposit Remover 1165 or 1-methyl-2-pyrrolidone. A 40%, by weight, KOH in water wet etch is prepared and heated to 62°C, while stirring. Typically, 1 liter of water and 667 grams of KOH was used. The wafer was placed window side down so that etched materials can easily fall from the wafer, and the stirring was set to a very slow speed. The top of the beaker was covered with parafilm to reduce evaporation, which would cause the concentration to change. The etch took approximately 22.5 hours, though it should be checked starting at approximately 21 hours. With the lights off, a flashlight was put behind the wafer facing the window side. If red windows could be seen, the wafer was not ready yet, and the etch should continue until the light from the windows turned white. Once white windows could be seen, the etch was allowed to continue for 30 minutes, and then the wafer was placed in deionized water for ten minutes. The wafer should be transferred to another beaker of deionized water for

ten minutes, then gunned dry.

If the wafer has silicon oxide, the wafer was HDMS vacuum vapor primed for five minutes, then baked at 115°C for three to five minutes. S1818 was spun onto the clean side of the wafer at 4000 RPM and baked at 115°C for three minutes. Note that due to the previous etches, the spinner may not hold vacuum at high speeds. In this case, the wafer may be spun at a slower speed, and then baked for a longer time. Next, the wafer was submerged in either the WNF HF bath or a teflon beaker of 6:1 buffered hydrofluoric acid with a few drops of Triton X-100 surfactant for 100 minutes, taking care to get rid of as many bubbles as possible. The resist was removed using a stripper such as Shipley Microposit Remover 1165 or 1-methyl-2-pyrrolidone.

For either type of wafer, the last step was to soak the wafer in Cyantek Nano-strip at 85°C or pirhana at 200°C for 10 minutes. It was then rinsed and gunned dry with nitrogen.

A.3 Solutions for DNA Project

To make 500 mL of 1 M potassium chloride (KCl) buffer with 10 mM trisaminomethane-hydrochloride (Tris-HCl) and 1 mM ethylenediaminetetraacetic acid (EDTA), 37.28 g of KCl, 605 mg of Tris-HCl, and 186 mL of EDTA were used. To change the pH, KOH or HCl were added. While other bases or acids can be used, these will not introduce new ions. Tris-HCl was used in buffer to maintain the pH, and EDTA was used to maintain low reactivity.

The HSQ developer was 1% NaOH and 4% NaCl, by weight, in water. For example, for 96 mL of water, 1 g of NaOH and 4 g of NaCl were added.

BIBLIOGRAPHY

- [1] L. Manna, E. C. Scher, and A. P. Alivisatos. Synthesis of Soluble and Processable Rod-, Arrow-, Teardrop-, and Tetrapod-Shaped CdSe Nanocrystals. *J. Am. Chem. Soc.*, 122(51):12700–12706, 2000.
- [2] X. Peng. Mechanisms for the Shape-Control and Shape-Evolution of Colloidal Semiconductor Nanocrystals. *Adv. Mater.*, 15(5):459–463, 2003.
- [3] K.-S. Cho, D. V. Talapin, W. Gaschler, and C. B. Murray. Designing PbSe Nanowires and Nanorings through Oriented Attachment of Nanoparticles. *J. Am. Chem. Soc.*, 127(19):7140–7147, 2005.
- [4] A. J. Houtepen, R. Koole, D. Vanmaekelbergh, J. Meeldijk, and S. G. Hickey. The Hidden Role of Acetate in the PbSe Nanocrystal Synthesis. *J. Am. Chem. Soc.*, 128(21):6792–6793, 2006.
- [5] K.-T. Yong, Y. Sahoo, M. T. Swihart, and P. N. Prasad. Shape Control of CdS Nanocrystals in One-Pot Synthesis. *J. Phys. Chem. C*, 111(6):2447–2458, 2007.
- [6] A. R. Kortan, R. Hull, R. L. Opila, M. G. Bawendi, M. L. Steigerwald, P. J. Carroll, and L. E. Brus. Nucleation and growth of cadmium selendie on zinc sulfide quantum crystallite seeds, and vice versa, in inverse micelle media. *J. Am. Chem. Soc.*, 112(4):1327–1332, 1990.
- [7] C. F. Hoener, K. A. Allan, A. J. Bard, A. Campion, M. A. Fox, T. E. Mallouk, S. E. Webber, and J. M. White. Demonstration of a shell-core structure in

- layered cadmium selenide-zinc selenide small particles by x-ray photoelectron and Auger spectroscopies. *J. Phys. Chem.*, 96(9):3812–3817, 1992.
- [8] M. A. Hines and P. Guyot-Sionnest. Synthesis and Characterization of Strongly Luminescing ZnS-Capped CdSe Nanocrystals. *J. Phys. Chem.*, 100(2):468–471, 1996.
- [9] C. B. Murray, D. J. Norris, and M. G. Bawendi. Synthesis and characterization of nearly monodisperse CdE (E = sulfur, selenium, tellurium) semiconductor nanocrystallites. *J. Am. Chem. Soc.*, 115(19):8706–8715, 1993.
- [10] Z. A. Peng and X. Peng. Formation of High-Quality CdTe, CdSe, and CdS Nanocrystals Using CdO as Precursor. *J. Am. Chem. Soc.*, 123(1):183–184, 2001.
- [11] X. Peng, J. Wickham, and A. P. Alivisatos. Kinetics of II-VI and III-V colloidal Semiconductor Nanocrystal Growth: “Focusing” of Size Distributions. *J. Am. Chem. Soc.*, 120(21):5343–5344, 1998.
- [12] B. O. Dabbousi, J. Rodriguez-Viejo, F. V. Mikulec, J. R. Heine, H. Mattoussi, R. Ober, K. F. Jensen, and M. G. Bawendi. (CdSe)ZnS Core-Shell Quantum Dots: Synthesis and Characterization of a Size Series of Highly Luminescent Nanocrystallites. *J. Phys. Chem. B*, 101(46):9463–9475, 1997.
- [13] Richard H. Bube. *Photoconductivity of Solids*. John Wiley and Sons, 1960.
- [14] Y. Yin and P. Alivisatos. Colloidal nanocrystal synthesis and the organic-inorganic interface. *Nature*, 437(7059):664–670, 2005.
- [15] D. Yu, C. Wang, and P. Guyot-Sionnest. n-Type Conducting CdSe Nanocrystal Solids. *Science*, 300(5623):1277–1280, 2003.

- [16] M. Drndic, M. V. Jarosz, N. Y. Morgan, M. A. Kastner, and M. G. Bawendi. Transport properties of annealed CdSe colloidal nanocrystal solids. *J. of Appl. Phys.*, 92(12):7498–7503, 2002.
- [17] M. V. Jarosz, V. J. Porter, B. R. Fisher, M. A. Kastner, and M. G. Bawendi. Photoconductivity studies of treated CdSe quantum dot films exhibiting increased exciton ionization efficiency. *Phys. Rev. B*, 70(19):195327, 2004.
- [18] D. V. Talapin and C. B. Murray. PbSe Nanocrystal Solids for n- and p-Channel Thin Film Field-Effect Transistors. *Science*, 310(5745):86–89, 2005.
- [19] G. Konstantatos, I. Howard, A. Fischer, S. Hoogland, J. Clifford, E. Klem, L. Levina, and E. H. Sargent. Ultrasensitive solution-cast quantum dot photodetectors. *Nature*, 442(7099):180–183, 2006.
- [20] M. Law, J. M. Luther, Q. Song, B. K. Hughes, C. L. Perkins, and A. J. Nozik. Structural, Optical, and Electrical Properties of PbSe Nanocrystal Solids Treated Thermally or with Simple Amines. *J. Am. Chem. Soc.*, 130(18):5974–5985, 2008.
- [21] R. Rossetti, S. Nakahara, and L. E. Brus. Quantum size effects in the redox potentials, resonance Raman spectra, and electronic spectra of CdS crystallites in aqueous solution. *J. Chem. Phys.*, 79(2):1086–1088, 1983.
- [22] D. J. Norris and M. G. Bawendi. Measurement and assignment of the size-dependent optical spectrum in CdSe quantum dots. *Phys. Rev. B*, 53:16338–16346, 1996.
- [23] M. A. Kastner. Artificial Atoms. *Phys. Today*, 46(1):24–31, 1993.

- [24] A. P. Alivisatos. Semiconductor Clusters, Nanocrystals, and Quantum Dots. *Science*, 271(5251):pp. 933–937, 1996.
- [25] Ramamurti Shankar. *Principles of Quantum Mechanics*. Plenum Press, 2nd edition, 1994.
- [26] Jun John Sakurai. *Modern Quantum Mechanics*. Addison-Wesley Publishing Company, 1994.
- [27] David J. Norris. Electronic Structure in Semiconductor Nanocrystals. In Victor I. Klimov, editor, *Semiconductor and Metal Nanocrystals*, chapter 2. Marcel Dekker, Inc., 2004.
- [28] Michael P. Marder. *Condensed Matter Physics*. John Wiley and Sons, Inc., corrected printing edition, 2000.
- [29] Fausto Rossi. *Theory of Semiconductor Quantum Devices, Microscopic Modeling and Simulation Strategies*. Springer, 2011.
- [30] Neil W. Ashcroft and N. David Mermin. *Solid State Physics*. Brooks/Cole, Cengage Learning, 1976.
- [31] A. M. Smith and S. Nie. Semiconductor Nanocrystals: Structure, Properties, and Band Gap Engineering. *Acc. Chem. Res.*, 43(2):190–200, 2010.
- [32] F. W. Wise. Lead Salt Quantum Dots: the Limit of Strong Quantum Confinement. *Acc. Chem. Res.*, 33(11):773–780, 2000.
- [33] M. V. Jarosz, N. E. Stott, M. Drndic, N. Y. Morgan, M. A. Kastner, and M. G. Bawendi. Observation of Bimolecular Carrier Recombination Dynamics in Close-Packed Films of Colloidal CdSe Nanocrystals. *J. Phys. Chem. B*, 107(46):12585–12588, 2003.

- [34] V. J. Porter, S. Geyer, J. E. Halpert, M. A. Kastner, and M. G. Bawendi. Photoconduction in Annealed and Chemically Treated CdSe/ZnS Inorganic Nanocrystal Films. *J. Phys. Chem. C*, 112(7):2308–2316, 2008.
- [35] M. D. Fischbein and M. Drndic. CdSe nanocrystal quantum-dot memory. *Appl. Phys. Lett.*, 86(19):193106, 2005.
- [36] J. E. B. Katari, V. L. Colvin, and A. P. Alivisatos. X-ray Photoelectron Spectroscopy of CdSe Nanocrystals with Applications to Studies of the Nanocrystal Surface. *J. Phys. Chem.*, 98(15):4109–4117, 1994.
- [37] M. Brust, D. Bethell, C. J. Kiely, and D. J. Schiffrin. Self-Assembled Gold Nanoparticle Thin Films with Nonmetallic Optical and Electronic Properties. *Langmuir*, 14(19):5425–5429, 1998.
- [38] David S. Ginger and Neil C. Greenham. Electrical Properties of Semiconductor Nanocrystals. In Victor I. Klimov, editor, *Semiconductor and Metal Nanocrystals*, chapter 7. Marcel Dekker, Inc., 2004.
- [39] A. A. Middleton and N. S. Wingreen. Collective transport in arrays of small metallic dots. *Phys. Rev. Lett.*, 71:3198–3201, 1993.
- [40] R. Parthasarathy, X.-M. Lin, K. Elteto, T. F. Rosenbaum, and H. M. Jaeger. Percolating through Networks of Random Thresholds: Finite Temperature Electron Tunneling in Metal Nanocrystal Arrays. *Phys. Rev. Lett.*, 92:076801, 2004.
- [41] C. A. Neugebauer and M. B. Webb. Electrical Conduction Mechanism in Ultrathin, Evaporated Metal Films. *J. Appl. Phys.*, 33(1):74–82, 1962.
- [42] C. T. Black, C. B. Murray, R. L. Sandstrom, and S. Sun. Spin-Dependent

- Tunneling in Self-Assembled Cobalt-Nanocrystal Superlattices. *Science*, 290(5494):1131–1134, 2000.
- [43] D. S. Ginger and N.C. Greenham. Charge injection and transport in films of CdSe nanocrystals. *J. Appl. Phys.*, 87(3):13611368, 2000.
- [44] B. Abeles, P. Sheng, M. D. Coutts, and Y. Arie. Structural and electrical properties of granular metal films. *Adv. Phys.*, 24(3):407–461, 1975.
- [45] N. F. Mott. Conduction in non-crystalline materials. *Philos. Mag.*, 19:835–852, 1969.
- [46] A. L. Efros and B. I. Shklovskii. Coulomb gap and low temperature conductivity of disordered systems. *J. Phys. C Solid State*, 8(4):L49, 1975.
- [47] D. Yu, C. Wang, B. L. Wehrenberg, and P. Guyot-Sionnest. Variable Range Hopping Conduction in Semiconductor Nanocrystal Solids. *Phys. Rev. Lett.*, 92:216802, 2004.
- [48] R. D. Schaller and V. I. Klimov. High Efficiency Carrier Multiplication in PbSe Nanocrystals: Implications for Solar Energy Conversion. *Phys. Rev. Lett.*, 92:186601, 2004.
- [49] R. J. Ellingson, M. C. Beard, J. C. Johnson, P. Yu, O. I. Micic, A. J. Nozik, A. Shabaev, and A. L. Efros. Highly Efficient Multiple Exciton Generation in Colloidal PbSe and PbS Quantum Dots. *Nano Lett.*, 5(5):865–871, 2005.
- [50] R. D. Schaller, M. A. Petruska, and V. I. Klimov. Effect of electronic structure on carrier multiplication efficiency: Comparative study of PbSe and CdSe nanocrystals. *Appl. Phys. Lett.*, 87(25):253102, 2005.

- [51] J. E. Murphy, M. C. Beard, A. G. Norman, S. P. Ahrenkiel, J. C. Johnson, P. Yu, O. I. Mićić, R. J. Ellingson, and A. J. Nozik. Pbte colloidal nanocrystals: synthesis, characterization, and multiple exciton generation. *J. Am. Chem. Soc.*, 128(10):3241–3247, 2006.
- [52] J. J. H. Pijpers, E. Hendry, M. T. W. Milder, R. Fanciulli, J. Savolainen, J. L. Herek, D. Vanmaekelbergh, S. Ruhman, D. Mocatta, D. Oron, A. Aharoni, U. Banin, and M. Bonn. Carrier Multiplication and Its Reduction by Photodoping in Colloidal InAs Quantum Dots. *J. Phys. Chem. C*, 111(11):4146–4152, 2007.
- [53] M. C. Beard, K. P. Knutsen, P. Yu, J. M. Luther, Q. Song, W. K. Metzger, R. J. Ellingson, and A. J. Nozik. Multiple Exciton Generation in Colloidal Silicon Nanocrystals. *Nano Lett.*, 7(8):2506–2512, 2007.
- [54] Y. Kobayashi, T. Udagawa, and N. Tamai. Carrier Multiplication in CdTe Quantum Dots by Single-photon Timing Spectroscopy. *Chem. Lett.*, 38(8):830–831, 2009.
- [55] S. K. Stubbs, S. J. O. Hardman, D. M. Graham, B. F. Spencer, W. R. Flavell, P. Glarvey, O. Masala, N. L. Pickett, and D. J. Binks. Efficient carrier multiplication in InP nanoparticles. *Phys. Rev. B*, 81:081303, 2010.
- [56] S. M. Sze and Kwok K. Ng. *Physics of Semiconductor Devices*. John Wiley and Sons, Inc., 3rd edition, 2007.
- [57] A. Goetzberger and E. H. Nicollian. TRANSIENT VOLTAGE BREAKDOWN DUE TO AVALANCHE IN MIS CAPACITORS. *Appl. Phys. Lett.*, 9(12):444–446, 1966.

- [58] W.-K. Koh, A. C. Bartnik, F. W. Wise, and C. B. Murray. Synthesis of Monodisperse PbSe Nanorods: A Case for Oriented Attachment. *J. Am. Chem. Soc.*, 132(11):3909–3913, 2010.
- [59] F. Valle, M. Favre, P. De Los Rios, A. Rosa, and G. Dietler. Scaling Exponents and Probability Distributions of DNA End-to-End Distance. *Phys. Rev. Lett.*, 95:158105, 2005.
- [60] F. Sanger, S. Nicklen, and A. R. Coulson. DNA sequencing with chain-terminatin inhibitors. *Proc. Natl. Acad. Sci. USA*, 74(12):5463–5467, 1977.
- [61] L. M. Smith, J. Z. Sanders, R. J. Kaiser, P. Hughes, C. Dodd, C. R. Connell, C. Heiner, S. B. H. Kent, and L. E. Hood. Fluorescence detection in automated DNA sequence analysis. *Nature*, 321:674–679, 1986.
- [62] H. Swerdlow and R. Gesteland. Capillary gel electrophoresis for rapid, high resolution DNA sequencing. *Nucleic Acid Res.*, 18(6):1415–1419, 1990.
- [63] R. D. Mitra and G. M. Church. In situ localized amplification and contact replication of many individual DNA molecules. *Nucleic Acid Res.*, 27(24):e34–e39, 1999.
- [64] D. Dressman, H. Yan, G. Traverso, K. W. Kinzler, and B. Vogelstein. Transforming single DNA molecules into fluorescent magnetic particles for detection and enumeration of genetic variations. *Proc. Natl. Acad. Sci. USA*, 100(15):8817–8822, 2003.
- [65] Michal Janitz, editor. *Next-Generation Genome Sequencing: Towards Personalized Medicine*. Wiley-VCG, 2008.

- [66] R. D. Mitra, J. Shendure, J. Olejnik, E.-K. Olejnik, and G. M. Church. Fluorescent in situ sequencing on polymerase colonies. *Anal. Biochem.*, 320(1):55–65, 2003.
- [67] S. Brenner, M. Johnson, J. Bridgham, G. Golda, D. H. Lloyd, D. Johnson, S. Luo, S. McCurdy, M. Foy, M. Ewan, R. Roth, D. George, S. Eletr, G. Albrecht, E. Vermaas, S. R. Williams, K. Moon, T. Burcham, M. Pallas, R. B. DuBridge, J. Kirchner, K. Fearon, J. Mao, and K. Corcoran. Gene expression analysis by massively parallel signature sequencing (MPSS) on microbead arrays. *Nat. Biotechnol.*, 18:630–634, 2000.
- [68] J. Luo, D. E. Bergstrom, and F. Barany. Improving the fidelity of *Thermus thermophilus* DNA ligase. *Nucleic Acids Res.*, 24(14):3071–3078, 1996.
- [69] A. S. Bhagwat, R. J. Sanderson, and T. Lindahl. Delayed DNA joining at 3' mismatches by human DNA ligases. *Nucleic Acids Res.*, 27(20):4028–4033, 1999.
- [70] P. Liu, A. Burdzy, and L. C. Sowers. DNA ligase ensure fidelity by interrogating minor groove contacts. *Nucleic Acids Res.*, 32(15):4503–4511, 2004.
- [71] D. R. Bentley. Whole-genome re-sequencing. *Curr. Opin. Genet. Dev.*, 16(6):545–552, 2006.
- [72] D. R. Bentley, S. Balasubramanian, H. P. Swerdlow, G. P. Smith, J. Milton, C. G. Brown, K. P. Hall, D. J. Evers, C. L. Barnes, H. R. Bignell, J. M. Boutell, J. Bryant, R. J. Carter, R. Keira Cheetham, A. J. Cox, D. J. Ellis, M. R. Flatbush, N. A. Gormley, S. J. Humphray, L. J. Irving, M. S. Karbelashvili, S. M. Kirk, H. Li, X. Liu, K. S. Maisinger, L. J. Murray, B. Obradovic, T. Ost, M. L. Parkinson, M. R. Pratt, I. M. Rasolonjatovo, M. T. Reed, R. Rigatti,

C. Rodighiero, M. T. Ross, A. Sabot, S. V. Sankar, A. Scally, G. P. Schroth, M. E. Smith, V. P. Smith, A. Spiridou, P. E. Torrance, S. S. Tzonev, E. H. Vermaas, K. Walter, X. Wu, L. Zhang, M. D. Alam, C. Anastasi, I. C. Aniebo, D. M. Bailey, I. R. Bancarz, S. Banerjee and S. G. Barbour, P. A. Baybayan, V. A. Benoit, K. F. Benson, C. Bevis, P. J. Black, A. Boodhun, J. S. Brennan, J. A. Bridgham, R. C. Brown, A. A. Brown, D. H. Buermann, A. A. Bundu, J. C. Burrows, N. P. Carter, N. Castillo, M. Chiara E. Catenazzi, S. Chang, R. Neil Cooley, N. R. Crake, O. O. Dada, K. D. Diakoumakos, B. Dominguez-Fernandez, D. J. Earnshaw, U. C. Egbujor, D. W. Elmore, S. S. Etchin, M. R. Ewan, M. Fedurco, L. J. Fraser, K. V. Fuentes Fajardo, W. Scott Furey, D. George, K. J. Gietzen, C. P. Goddard, G. S. Golda, P. A. Granieri, D. E. Green, D. L. Gustafson, N. F. Hansen, K. Harnish, C. D. Haudenschild, N. I. Heyer, M. M. Hims, J. T. Ho, A. M. Horgan, K. Hoschler, S. Hurwitz, D. V. Ivanov, M. Q. Johnson, T. James, T. A. Huw Jones, G.-D. Kang, T. H. Kerelska, A. D. Kersey, I. Khrebtukova, A. P. Kindwall and Z. Kingsbury, P. I. Kokko-Gonzales, A. Kumar, M. A. Laurent, C. T. Lawley, S. E. Lee, X. Lee and A. K. Liao, J. A. Loch, M. Lok, S. Luo, R. M. Mammen, J. W. Martin, P. G. McCauley, P. McNitt, P. Mehta, K. W. Moon, J. W. Mullens, T. Newington, Z. Ning, B. Ling Ng, S. M. Novo, M. J. O'Neill, M. A. Osborne, A. Osnowski and O. Ostadan, L. L. Paraschos, L. Pickering, A. C. Pike, A. C. Pike, D. Chris Pinkard, D. P. Pliskin, J. Podhasky, V. J. Quijano, C. Raczy, V. H. Rae, S. R. Rawlings, A. Chiva Rodriguez, P. M. Roe, J. Rogers, M. C. Rogert Bacigalupo, N. Romanov, A. Romieu, R. K. Roth, N. J. Rourke, S. T. Ruediger, E. Russman, R. M. Sanches-Kuiper, M. R. Schenker, J. M. Seoane, R. J. Shaw, M. K. Shiver, S. W. Short, N. L. Sizto, J. P. Sluis, M. A. Smith, J. Ernest Sohma, Sohma, E. J. Spence, K. Stevens, N. Sutton, L. Szajkowski, C. L. Tregidgo,

- G. Turcatti, S. vandeVondele, Y. Verhovsky, S. M. Virk, S. Wakelin, G. C. Walcott, J. Wang, G. J. Worsley, J. Yan, L. Yau, M. Zuerlein, J. Rogers, J. C. Mullikin, M. E. Hurles, N. J. McCooke, J. S. West, F. L. Oaks, P. L. Lundberg, D. Klenerman, R. Durbin, and A. J. Smith. Accurate whole human genome sequencing using reversible terminator chemistry. *Nature*, 456:53–59, 2008.
- [73] M. Margulies, M. Egholm, W. E. Altman, S. Attiya, J. S. Bader, L. A. Bemben, J. Berka, M. S. Braverman, Y.-J. Chen, Z. Chen, S. B. Dewell, L. Du, J. M. Fierro, X. V. Gomes, B. C. Godwin, S. Helgesen W. He, C. H. Ho, G. P. Irzyk, S. C. Jando, M. L. I. Alenquer, T. P. Jarvie, K. B. Jirage, J.-B. Kim, J. R. Knight, J. R. Lanza, J. H. Leamon, S. M. Lefkowitz, M. Lei, J. Li, K. L. Lohman, H. Lu, V. B. Makhijani, K. E. McDade, M. P. McKenna, E. W. Myers, E. Nickerson, J. R. Nobile, R. Plant, B. P. Puc, M. T. Ronan, G. T. Roth, G. J. Sarkis, J. F. Simons, J. W. Simpson, M. Srinivasan, K. R. Tartaro, A. Tomasz, K. A. Vogt, G. A. Volkmer, S. H. Wang, Y. Wang, M. P. Weiner, P. Yu, R. F. Begley, and J. M. Rothberg. Genome sequencing in microfabricated high-density picolitre reactors. *Nature*, 437(7057):376–380, 2005.
- [74] J. Eid, A. Fehr, J. Gray, K. Luong, J. Lyle, G. Otto, P. Peluso, D. Rank, P. Baybayan, B. Bettman, A. Bibillo, K. Bjornson, B. Chaudhuri, F. Christians, R. Cicero, S. Clark, R. Dalal, A. deWinter, J. Dixon, M. Foquet, A. Gaertner, P. Hardenbol, C. Heiner, K. Hester, D. Holden, G. Kearns, X. Kong, R. Kuse, Y. Lacroix, S. Lin, P. Lundquist, C. Ma, P. Marks, M. Maxham, D. Murphy, I. Park, T. Pham, M. Phillips, J. Roy, R. Sebra, G. Shen, J. Sorenson, A. Tomaney, K. Travers, M. Trulson, J. Vieceli, J. Wegener, D. Wu, A. Yang, D. Zaccarin, P. Zhao, F. Zhong, J. Korlach, and S. Turner. Real-Time DNA Sequencing from Single Polymerase Molecules. *Science*, 323(5910):133–138, 2009.

- [75] A. Valouev, J. Ichikawa, T. Tonthat, J. Stuart, S. Ranade, H. Peckham, K. Zeng, J. A. Malek, G. Costa, K. McKernan, A. Sidow, A. Fire, and S. M. Johnson. A high-resolution, nucleosome position map of *C. elegans* reveals a lack of universal sequence-dictated positioning. *Genome Res.*, 18(7):1051–1063, 2008.
- [76] A. M. Smith, L. E. Heisler, R. P. St.Onge, E. Farias-Hesson, I. M. Wallace, J. Bodeau, A. N. Harris, K. M. Perry, G. Giaever, N. Pourmand, and C. Nislow. Highly-multiplexed barcode sequencing: an efficient method for parallel analysis of pooled samples. *Nucleic Acids Res.*, 38(13), 2010.
- [77] R. Drmanac, A. B. Sparks, M. J. Callow, A. L. Halpern, N. L. Burns, B. G. Kermani, P. Carnevali, I. Nazarenko, G. B. Nilsen, G. Yeung, F. Dahl, A. Fernandez, B. Staker, K. P. Pant, J. Baccash, A. P. Borcherding, A. Brownley, R. Cedeno, L. Chen, D. Chernikoff, A. Cheung, R.n Chirita, B. Curson, J. C. Ebert, C. R. Hacker, R. Hartlage, B. Hauser, S. Huang, Y. Jiang, V. Karpinchyk, M. Koenig, C. Kong, T. Landers, C. Le, J. Liu, C. E. McBride, M. Morenzoni, R. E. Morey, K. Mutch, H. Perazich, K. Perry, B. A. Peters, J. Peterson, C. L. Pethiyagoda, K. Pothuraju, C. Richter, A. M. Rosenbaum, S. Roy, J. Shafto, U. Sharanhovich, K. W. Shannon, C. G. Sheppy, M. Sun, J. V. Thakuria, A. Tran, D. Vu, A. W. Zarnek, X. Wu, S. Drmanac, A. R. Oliphant, W. C. Banyai, B. Martin, D. G. Ballinger, G. M. Church, and C. A. Reid. Human Genome Sequencing Using Unchained Base Reads on Self-Assembling DNA Nanoarrays. *Science*, 327(5961):78–81, 2010.
- [78] G. Church, D. Deamer, D. Branton, R. Baldarelli, and J. Kasianowicz. Characterization of individual polymer molecules based on monomer-interface interactions. *US Patent*, 5795782, 1995.
- [79] J. J. Kasianowicz, E. Brandin, D. Branton, and David W. Deamer. Characteri-

- zation of individual polynucleotide molecules using a membrane channel. *Proc. Natl. Acad. Sci. USA*, 93(24):13770–13773, 1996.
- [80] I. M. Derrington, T. Z. Butler, M. D. Collins, E. Manrao, M. Pavlenok, M.l Niederweis, and J. H. Gundlach. Nanopore DNA sequencing with MspA. *Proc. Natl. Acad. Sci. USA*, 107(37):16060–16065, 2010.
- [81] E. A. Manrao, I. M. Derrington, A. H. Laszlo, K. W. Langford, M. K. Hopper, N. Gillgren, M. Pavlenok, M. Niederweis, and J. H. Gundlach. Reading DNA at single-nucleotide resolution with a mutant mspa nanopore and phi29 dna polymerase. *Nat. Biotechnol.*, 30(3):349–354, 2012.
- [82] L. Song, M. R. Hobaugh, C. Shustak, S. Cheley, H. Bayley, and J. E. Gouaux. Structure of Staphylococcal α -Hemolysin, a Heptameric Transmembrane Pore. *Science*, 274(5294):1859–1865, 1996.
- [83] M. Akeson, D. Branton, J. J. Kasianowicz, E. Brandin, and D. W. Deamer. Microsecond Time-Scale Discrimination Among Polycytidylic Acid, Polyadenylic Acid, and Polyuridylic Acid as Homopolymers or as Segments Within Single RNA Molecules. *Biophys. J.*, 77(6):3227–3233, 1999.
- [84] A. Meller, L. Nivon, E. Brandin, J. Golovchenko, and D. Branton. Rapid nanopore discrimination between single polynucleotide molecules. *Proc. Natl. Acad. Sci. USA*, 97(3):1079–1084, 2000.
- [85] Y. Astier, O. Braha, and H. Bayley. Toward Single Molecule DNA Sequencing: Direct Identification of Ribonucleoside and Deoxyribonucleoside 5'-Monophosphates by Using an Engineered Protein Nanopore Equipped with a Molecular Adapter. *J. Am. Chem. Soc.*, 128(5):1705–1710, 2006.

- [86] S. E. Henrickson, M. Misakian, B. Robertson, and J. J. Kasianowicz. Driven DNA Transport into an Asymmetric Nanometer-Scale Pore. *Phys. Rev. Lett.*, 85:3057–3060, 2000.
- [87] S. L. Cockroft, J. Chu, M. Amorin, and M. R. Ghadiri. A Single-Molecule Nanopore Device Detects DNA Polymerase Activity with Single-Nucleotide Resolution. *J. Am. Chem. Soc.*, 130(3):818–820, 2008.
- [88] U. F. Keyser. Controlling molecular transport through nanopores. *J. R. Soc. Interface*, 8(63):1369–1378, 2011.
- [89] Z. McDougall. Oxford Nanopore introduces DNA ‘strand sequencing’ on the high-throughput GridION platform and presents MinION, a sequencer the size of a USB memory stick. <http://www.nanoporetech.com/news/press-releases/view/39>, 2012.
- [90] K. Healy. Nanopore-based single-molecule DNA analysis. *Nanomedicine*, 2(5):459–481, 2007.
- [91] C. A. Merchant, K. Healy, M. Wanunu, V. Ray, N. Peterman, J. Bartel, M. D. Fischbein, K. Venta, Z. Luo, A. T. Johnson, and M. Drndic. DNA Translocation through Graphene Nanopores. *Nano Lett.*, 10(8):2915–2921, 2010.
- [92] G. F. Schneider, S. W. Kowalczyk, V. E. Calado, G. Pandraud, H. W. Zandbergen, L. M. K. Vandersypen, and C. Dekker. DNA Translocation through Graphene Nanopores. *Nano Lett.*, 10(8):3163–3167, 2010.
- [93] S. Garaj, A. Reina, J. Kong, D. Branton, and J. A. Golovchenko. Graphene as a subnanometre trans-electrode membrane. *Nature*, 467:190–193, 2010.

- [94] A. J. Storm, J. H. Chen, X. S. Ling, H. W. Zandbergen, and C. Dekker. Fabrication of solid-state nanopores with single-nanometre precision. *Nat. Mater.*, 2(8):537–540, 2003.
- [95] D. Fologea, J. Uplinger, B. Thomas, D. S. McNabb, and J. Li. Slowing DNA Translocation in a Solid-State Nanopore. *Nano Lett.*, 5(9):1734–1737, 2005.
- [96] U. F. Keyser, J. van der Does, C. Dekker, and N. H. Dekker. Optical tweezers for force measurements on DNA in nanopores. *Rev. Sci. Instrum.*, 77(10):105105, 2006.
- [97] U. F. Keyser, B. N. Koeleman, S. van Dorp, D. Krapf, R. M. M. Smeets, S. G. Lemay, N. H. Dekker, and C. Dekker. Direct force measurements on DNA in a solid-state nanopore. *Nature Phys.*, 2:473–477, 2006.
- [98] M. Wanunu and A. Meller. Chemically Modified Solid-State Nanopores. *Nano Lett.*, 7(6):1580–1585, 2007.
- [99] B. Yameen, M. Ali, R. Neumann, W. Ensinger, W. Knoll, and O. Azzaroni. Ionic Transport Through Single Solid-State Nanopores Controlled with Thermally Nanoactuated Macromolecular Gates. *Small*, 5(11):1287–1291, 2009.
- [100] J. K. Rosenstein, M. Wanunu, C. A. Merchant, M. Drndic, and K. I. Shepard. Integrated nanopore sensing platform with sub-microsecond temporal resolution. *Nat. Methods*, 9(5):487–492, 2012.
- [101] D. C. Bell, W. K. Thomas, K. M. Murtagh, C. A. Dionne, A. C. Graham, J. E. Anderson, and W. R. Glover. DNA Base Identification by Electron Microscopy. *Microsc. Microanal.*, 18:1049–1053, 2012.

- [102] W. B. Russell, D. A. Saville, and W. R. Schowalter. *Colloidal Dispersions*. Cambridge University Press, 1992.
- [103] A. Y. Grosberg and Y. Rabin. DNA capture into a nanopore: Interplay of diffusion and electrohydrodynamics. *J. Chem. Phys.*, 133(16):165102, 2010.
- [104] D. Long, J.-L. Viovy, and A. Ajdari. Simultaneous Action of Electric Fields and Nonelectric Forces on a Polyelectrolyte: Motion and Deformation. *Phys. Rev. Lett.*, 76:3858–3861, 1996.
- [105] John Moore and Ralph Pearson. *Kinetics and Mechanism*. John Wiley and Sons, 3rd edition, 1981.
- [106] M. Wanunu, W. Morrison, Y. Rabin, A. Grosberg, and A. Meller. Electrostatic focusing of unlabelled DNA into nanoscale pores using a salt gradient. *Nat. Nanotechnol.*, 5:160–165, 2010.
- [107] Bertil Hille. *Ion Channels of Excitable Membranes*. Sinauer Associates, Inc., 2001.
- [108] G. Maglia, M. R. Restrepo, E. Mikhailova, and H. Bayley. Enhanced translocation of single DNA molecules through α -hemolysin nanopores by manipulation of internal charge. *Proc. Natl. Acad. Sci. USA*, 105(50):19720–19725, 2008.
- [109] T. P. Ma. Making silicon nitride film a viable gate dielectric. *IEEE T. Electron Dev.*, 45(3):680 –690, 1998.
- [110] K. M. Eisele. SF₆, a Preferable Etchant for Plasma Etching Silicon. *J. Electrochem. Soc.*, 128:123–126, 1981.
- [111] Mark A. McCord and Michael J. Rooks. Electron beam lithography. In P. Rai-Choudhury, editor, *Handbook of Microlithography, Micromachining, and Micro-*

- fabrication. Volume 1: Microlithography*, chapter 2. Society of Photo-Optical Instrumentation Engineers, 1997.
- [112] T. H. P. Chang. Proximity effect in electron-beam lithography. *J. Vac. Sci. Technol.*, 12(6):1271–1275, 1975.
- [113] S. Mackie and S. P. Beaumont. Materials and processes for nanometer lithography. *Solid State Technol.*, 28(8):117–122, 1985.
- [114] Harry J. Levinson. *Principles of Lithography*. SPIE Publications, 2nd edition, 2005.
- [115] M. Rothschild, M. W. Horn, C. L Keast, R. R. Kunz, V. Liberman, S. C. Palmateer, S. P. Doran, A. R. Forte, R. B Goodman, J. H. C. Sedlacek, R. S. Uttaro, D. Corliss, and A. Grenville. Photolithography at 193 nm. *Linc. Lab. J.*, 10(1), 1997.
- [116] R. H. French and H. V. Tran. Immersion Lithography: Photomask and Wafer-Level Materials. *Annu. Rev. of Mater. Res.*, 39(1):93–126, 2009.
- [117] C. Fonseca, M. Somervell, S. Scheer, W. Printz, K. Nafus, S. Hatakeyama, Y. Kuwahara, T. Niwa, S. Bernard, and R. Gronheid. Advances and Challenges in Dual-Tone Development Process Optimization. *Proc. SPIE*, 7274:72740I, 2009.
- [118] S. Lee, J. rey Byers, P. Zimmerman, B. Rice, N. J. Turro, and C. G. Willson. An analysis of double exposure lithography options. *Proc. SPIE*, 6924:69242A, 2008.
- [119] F. Reif. *Fundamentals of statistical and thermal physics*. McGraw-Hill, Inc., 1965.

- [120] M. D. Fischbein and M. Drndic. Sub-10 nm Device Fabrication in a Transmission Electron Microscope. *Nano Lett.*, 7(5):1329–1337, 2007.
- [121] H.-M. Kim, M.-H. Lee, and K.-B. Kim. Theoretical and experimental study of nanopore drilling by a focused electron beam in transmission electron microscopy. *Nanotechnology*, 22(27):275303, 2011.
- [122] M. D. Fischbein and M. Drndic. Electron beam nanosculpting of suspended graphene sheets. *Appl. Phys. Lett.*, 93(11):113107, 2008.
- [123] H. Du, C. Chen, R. Krishnan, T. D. Krauss, J. M. Harbold, F. W. Wise, M. G. Thomas, and J. Silcox. Optical Properties of Colloidal PbSe Nanocrystals. *Nano Lett.*, 2(11):1321–1324, 2002.
- [124] A. L Efros and A. L Efros. Interband absorption of light in a semiconductor sphere. *Sov. Phys. Semicond.*, 16:772–775, 1982.
- [125] W. W. Yu, J. C. Falkner, B. S. Shih, and V. L. Colvin. Preparation and Characterization of Monodisperse PbSe Semiconductor Nanocrystals in a Non-coordinating Solvent. *Chem. Mater.*, 16(17):3318–3322, 2004.
- [126] J. S. Steckel, B. K. H. Yen, D. C. Oertel, and M. G. Bawendi. On the Mechanism of Lead Chalcogenide Nanocrystal Formation. *J. Am. Chem. Soc.*, 128(40):13032–13033, 2006.
- [127] M. D. Fischbein, M. Puster, and M. Drndic. Monolayer Suppression of Transport Imaged in Annealed PbSe Nanocrystal Arrays. *Nano Lett.*, 10(6):2155–2161, 2010.
- [128] K.-T. Yong, Y. Sahoo, K. R. Choudhury, M. T. Swihart, J. R. Minter, and

- P. N. Prasad. Shape Control of PbSe Nanocrystals Using Noble Metal Seed Particles. *Nano Lett.*, 6(4):709–714, 2006.
- [129] C. Gautier, M. Cambon-Muller, and M. Averous. Study of PbSe layer oxidation and oxide dissolution. *Appl. Surf. Sci.*, 141(1-2):157–163, 1999.
- [130] M. Brust, M. Walker, D. Bethell, D. J. Schiffrin, and R. Whyman. Synthesis of thiol-derivatised gold nanoparticles in a two-phase Liquid-Liquid system. *J. Chem. Soc., Chem. Commun.*, pages 801–802, 1994.
- [131] V. I. Klimov, A. A. Mikhailovsky, Su Xu, A. Malko, J. A. Hollingsworth, C. A. Leatherdale, H.-J. Eisler, and M. G. Bawendi. Optical Gain and Stimulated Emission in Nanocrystal Quantum Dots. *Science*, 290(5490):314–317, 2000.
- [132] Z. Zhong, F. Qian, D. Wang, and C. M. Lieber. Synthesis of p-Type Gallium Nitride Nanowires for Electronic and Photonic Nanodevices. *Nano Lett.*, 3(3):343–346, 2003.
- [133] B. Butun, J. Cesario, S. Enoch, R. Quidant, and E. Ozbay. InGaN green light emitting diodes with deposited nanoparticles. *Photon. Nanostruct. Fundam. Appl.*, 5(2-3):86–90, 2007.
- [134] X.-M. Zhang, M.-Y. Lu, Y. Zhang, L.-J. Chen, and Z. L. Wang. Fabrication of a High-Brightness Blue-Light-Emitting Diode Using a ZnO-Nanowire Array Grown on p-GaN Thin Film. *Adv. Mater.*, 21(27):2767–2770, 2009.
- [135] D. C. Oertel, M. G. Bawendi, A. C. Arango, and V. Bulovic. Photodetectors based on treated CdSe quantum-dot films. *Appl. Phys. Lett.*, 87(21):213505, 2005.

- [136] M. Hegg and L. Y. Lin. Near-field photodetection with high spatial resolution by nanocrystal quantum dots. *Opt. Express*, 15(25):17163–17170, 2007.
- [137] X. Jiang, R. D. Schaller, S. B. Lee, J. M. Pietryga, V. I. Klimov, and A. A. Zakhidov. PbSe nanocrystal/conducting polymer solar cells with an infrared response to 2 micron. *J. Mater. Res.*, 22:2204–2210, 2007.
- [138] J. J. Choi, Y.-F. Lim, M. B. Santiago-Berrios, M. Oh, B.-R. Hyun, L. Sun, A. C. Bartnik, A. Goedhart, G. G. Malliaras, H. D. Abrunña, F. W. Wise, and T. Hanrath. PbSe Nanocrystal Excitonic Solar Cells. *Nano Lett.*, 9(11):3749–3755, 2009.
- [139] O. E. Semonin, J. M. Luther, and M. C. Beard. Quantum dots for next-generation photovoltaics. *Mater. Today*, 15(11):508–515, 2012.
- [140] W. Shockley and H. J. Queisser. Detailed Balance Limit of Efficiency of p-n Junction solar Cells. *J. Appl. Phys.*, 32(3):510–519, 1961.
- [141] A. A. Houck, J. Labaziewicz, E. K. Chan, J. A. Folk, and I. L. Chuang. Kondo Effect in Electromigrated Gold Break Junctions. *Nano Lett.*, 5(9):1685–1688, 2005.
- [142] R. Sordan, K. Balasubramanian, M. Burghard, and K. Kern. Coulomb blockade phenomena in electromigration break junctions. *Appl. Phys. Lett.*, 87(1):013106, 2005.
- [143] H. Tachikawa, Y. Nagoya, and H. Kawabata. A Density Functional Theory Study of Ground and Low-Lying Excited Electronic States in Defective Graphenes. *J. Chem. Theory Comput.*, 5(8):2101–2107, 2009.

- [144] J. Tersoff. Low-Frequency Noise in Nanoscale Ballistic Transistors. *Nano Lett.*, 7(1):194–198, 2007.
- [145] F. Cichos, C. von Borczyskowski, and M. Orrit. Power-law intermittency of single emitters. *Curr. Opin. Colloid Interface Sci.*, 12(6):272–284, 2007.
- [146] C. Querner, S. Wang, K. Healy, J. A. Fairfield, M. D. Fischbein, and M. Drndic. Fluorescence Dynamics of Smiconductor Nanorod Clusters Studied by Correlated Atomic Force, Transmission Electron, and Fluorescence Microscopy. *J. Phys. Chem. C*, 112(50):19945–19956, 2008.
- [147] K. S. Ralls, W. J. Skocpol, L. D. Jackel, R. E. Howard, L. A. Fetter, R. W. Epworth, and D. M. Tennant. Discrete Resistance Switching in Submicrometer Silicon Inversion Layers: Individual Interface Traps and Low-Frequency ($\frac{1}{f}$?) Noise. *Phys. Rev. Lett.*, 52:228–231, 1984.
- [148] C. A. Leatherdale, C. R. Kagan, N. Y. Morgan, S. A. Empedocles, M. A. Kastner, and M. G. Bawendi. Photoconductivity in CdSe quantum dot solids. *Phys. Rev. B*, 62(4):2669–2680, 2000.
- [149] M. D. Fischbein and M. Drndic. Nanogaps by direct lithography for high-resolution imaging and electronic characterization of nanostructures. *Appl. Phys. Lett.*, 88(6):063116, 2006.
- [150] W. W. Yu, L. Qu, W. Guo, and X. Peng. Experimental Determination of the Extinction Coefficient of CdTe, CdSe, and CdS Nanocrystals. *Chem. Mater.*, 15(14):2854–2860, 2003.
- [151] S. A. Crooker, T. Barrick, J. A. Hollingsworth, and V. I. Klimov. Multiple temperature regimes of radiative decay in CdSe nanocrystal quantum dots:

- Intrinsic limits to the dark-exciton lifetime. *Appl. Phys. Lett.*, 82(17):2793–2795, 2003.
- [152] K. Healy, B. Schiedt, and A. P. Morrison. Solid-state nanopore technologies for nanopore-based DNA analysis. *Nanomedicine*, 2(6):875–897, 2007.
- [153] C. Dekker. Solid-state nanopores. *Nat. Nanotechnol.*, 3(4):209–215, 2007.
- [154] D. Branton, D. W. Deamer, A. Marziali, H. Bayley, S. A. Benner, T. Butler, M. Di Ventra, S. Garaj, A. Hibbs, X. Huang, S. B. Jovanovich, P. S. Krstic, S. Lindsay, X. S. Ling, C. H. Mastrangelo, A. Meller, J. S. Oliver, Y. V. Pershin, J. M. Ramsey, R. Riehn, G. V. Soni, V. Tabard-Cossa, M. Wanunu, M. Wiggin, and J. A. Schloss. The potential and challenges of nanopore sequencing. *Nat. Biotechnol.*, 26(10):1146–1153, 2008.
- [155] B. M. Venkatesan and R. Bashir. Nanopore sensors for nucleic acid analysis. *Nat. Nanotechnol.*, 6(10):615–624, 2011.
- [156] M. Wanunu. Nanopores: A journey towards DNA sequencing. *Phys. Life Rev.*, 9(2):125–218, 2012.
- [157] David W Deamer and Mark Akeson. Nanopores and nucleic acids: prospects for ultrarapid sequencing. *Trends Biotechnol.*, 18(4):147 – 151, 2000.
- [158] G. M. Cherf, K. R. Liberman, H. Rashid, C. E. Lam, K. Karplus, and M. Akeson. Automated forward and reverse ratcheting of DNA in a nanopore at 5-Å precision. *Nat. Biotechnol.*, 30(3):344–348, 2012.
- [159] M. Zwolak and M. Di Ventra. Electronic Signature of DNA Nucleotides via Transverse Transport. *Nano Lett.*, 5(3):421–424, 2005.

- [160] J. Lagerqvist, M. Zwolak, and M. Di Ventra. Fast DNA Sequencing via Transverse Electronic Transport. *Nano Lett.*, 6(4):779–782, 2006.
- [161] X.-G. Zhang, P. S. Krstić, R. Zikić, J. C. Wells, and M. Fuentes-Cabrera. First-Principles Transveral DNA Conductance Deconstructed. *Biophys. J.*, 91(1):L04–L06, 2006.
- [162] J. Lagerqvist, M. Zwolak, and M. Di Ventra. Influence of the Environment and Probes on Rapid DNA Sequencing via Transverse Electronic Transport. *Biophys. J.*, 93(7):2384–2390, 2007.
- [163] V. Meunier and P. S. Krstić. Enhancement of the transverse conductance in DNA nucleotides. *J. Chem. Phys.*, 128(4):041103, 2008.
- [164] M. Krems, M. Zwolak, Y. V. Pershin, and M. Di Ventra. Effect of Noise on DNA Sequencing via Transverse Electronic Transport. *Biophys. J.*, 97(7):1990–1996, 2009.
- [165] X. Chen, I. Rungger, C. D. Pemmaraju, U. Schwingenschlögl, and S. Sanvito. First-principles study of high-conductance DNA sequencing with carbon nanotube electrodes. *Phys. Rev. B*, 85:115436, 2012.
- [166] H. W. Ch. Postma. Rapid Sequencing of Individual DNA Molecules in Graphene Nanogaps. *Nano Lett.*, 10(2):420–425, 2010.
- [167] J. He, L. Lin, P. Zhang, and S. Lindsay. Identification of DNA Basepairing via Tunnel-Current Decay. *Nano Lett.*, 7(12):3854–3858, 2007.
- [168] J. He, L. Lin, P. Zhang, Q. Spadola, Z. Xi, Q. Fu, and S. Lindsay. Transverse Tunneling through DNA Hydrogen Bonded to an Electrode. *Nano Lett.*, 8(8):2530–2534, 2008.

- [169] S. Chang, J. He, A. Kibel, M. Lee, O. Sankey, P. Zhang, and S. Lindsay. Tunnelling readout of hydrogen-bonding-based recognition. *Nat. Nanotechnol.*, 4(5):297–301, 2009.
- [170] S. Chang, J. He, L. Lin, P. Zhang, F. Liang, M. Young, S. Huang, and S. Lindsay. Tunnel conductance of watson-crick nucleoside-base pairs from telegraph noise. *Nanotechnology*, 20(18):185102, 2009.
- [171] S. Chang, S. Huang, J. He, F. Liang, P. Zhang, S. Li, X. Chen, O. Sankey, and S. Lindsay. Electronic Signatures of all Four DNA Nucleosides in a Tunneling Gap. *Nano Lett.*, 10(3):1070–1075, 2010.
- [172] S. Huang, J. He, S. Chang, P. Zhang, F. Liang, S. Li, M. Tuchband, A. Fuhrmann, R. Ros, and S. Lindsay. Identifying single bases in a DNA oligomer with electron tunneling. *Nat. Nanotechnol.*, 5(12):868–873, 2010.
- [173] S. Huang, S. Chang, J. He, P. Zhang, F. Liang, M. Tuchband, S. Li, and S. Lindsay. Recognition Tunneling Measurement of the Conductance of DNA Bases Embedded in Self-Assembled Monolayers. *J. Phys. Chem. C*, 114(48):20443–20448, 2010.
- [174] T. Tanaka and T. Kawai. Partical sequencing of a single DNA molecule with a scanning tunnelling microscope. *Nat. Nanotechnol.*, 4(8):518–522, 2008.
- [175] M. Tsutsui, M. Taniguchi, K. Yokota, and T. Kawai. Identifying single nucleotides by tunnelling current. *Nat. Nanotechnol.*, 5(4):286–290, 2010.
- [176] M. Tsutsui, K. Matsubara, T. Ohshiro, M. Furuhashi, M. Taniguchi, and T. Kawai. Electrical Detection of Single Methylcytosines in a DNA Oligomer. *J. Am. Chem. Soc.*, 133(23):9124–9128, 2011.

- [177] M. Tsutsui, S. Rahong, Y. Iizumi, T. Okazaki, M. Taniguchi, and T. Kawai. Single-molecule sensing electrode embedded in-plane nanopore. *Sci. Rep.*, 1:46, 2011.
- [178] X. Liang and S. Y. Chou. Nanogap Detector Inside Nanofluidic Channel for Fast Real-Time Label-Free DNA Analysis. *Nano Lett.*, 8(5):1472–1476, 2008.
- [179] A. P. Ivanov, E. Instuli, C. M. McGilvery, G. Baldwin, D. W. McComb, T. Albrecht, and J. B. Edel. DNA Tunneling Detector Embedded in a Nanopore. *Nano Lett.*, 11(1):279–285, 2011.
- [180] P. Xie, Q. Xiong, Y. Fang, Q. Qing, and C. M. Lieber. Local electrical potential detection of DNA by nanowire-nanopore sensors. *Nat. Nanotechnol.*, 7(2):119–125, 2012.
- [181] T. Nelson, B. Zhang, and O. V. Prezhdo. Detection of Nucleic Acids with Graphene Nanopores: Ab Initio Characterization of a Novel Sequencing Device. *Nano Lett.*, 10(9):3237–3242, 2010.
- [182] K. K. Saha, M. Drndic, and B. K. Nikolic. DNA Base-Specific Modulation of Microampere Transverse Edge Currents through a Metallic Graphene Nanoribbon with a Nanopore. *Nano Lett.*, 12(1):50–55, 2012.
- [183] S. Polonsky, S. Rossnagel, and G. Stolovitzky. Nanopore in metal-dielectric sandwich for DNA position control. *Appl. Phys. Lett.*, 91(15):153103, 2007.
- [184] S. Harrer, S. Ahmed, A. Afzali-Ardakani, B. Luan, P. S. Waggoner, X. Shao, H. Peng, D. L. Goldfarb, G. J. Martyna, S. M. Rossnagel, L. Deligianni, and G. A. Stolovitzky. Electrochemical Characterization of Thin Film Electrodes Toward Developing a DNA Transistor. *Langmuir*, 26(24):19191–19198, 2010.

- [185] S. Harrer, P. S. Waggoner, B. Luan, A. Afzali-Ardakani, D. L. Goldfarb, H. Peng, G. Martyna, S. M. Rossnagel, and G. A. Stolovitzky. Electrochemical protection of thin film electrodes in solid state nanopores. *Nanotechnology*, 22(27):275304, 2011.
- [186] Z. Jiang, M. Mihovilovic, J. Chan, and D. Stein. Fabrication of nanopores with embedded annular electrodes and transverse carbon nanotube electrodes. *J. Phys.: Condens. Matter*, 22(45):454114, 2010.
- [187] B. M. Venkatesan, D. Estrada, S. Banerjee, X. Jin, V. E. Dorgan, M.-H. Bae, N. R. Aluru, E. Pop, and R. Bashir. Stacked Graphene-Al₂O₃ Nanopore Sensors for Sensitive Detection of DNA and DNA-Protein Complexes. *ACS Nano*, 6(1):441–450, 2012.
- [188] A. W. Grant, Q.-H. Hu, and B. Kasemo. Transmission electron microscopy ‘windows’ for nanofabricated structures. *Nanotechnology*, 15(9):1175, 2004.
- [189] P. Chen, T. Mitsui, D. B. Farmer, J. Golovchenko, R. G. Gordon, and D. Branton. Atomic Layer Deposition to Fine-Tune the Surface Properties and Diameters of Fabricated Nanopores. *Nano Lett.*, 4(7):1333–1337, 2004.
- [190] R. M. M. Smeets, U. F. Keyser, M. Y. Wu, N. H. Dekker, and C. Dekker. Nanobubbles in Solid-State Nanopores. *Phys. Rev. Lett.*, 97:088101, 2006.
- [191] C. Danelon, C.n Santschi, J. Brugger, and H. Vogel. Fabrication and Functionalization of Nanochannels by Electron-Beam-Induced Silicon Oxide Deposition. *Langmuir*, 22(25):10711–10715, 2006.
- [192] V. Tabard-Cossa, D. Trivedi, M. Wiggin, N. N. Jetha, and A. Marziali. Noise analysis and reduction in solid-state nanopores. *Nanotechnology*, 18(30):305505, 2007.

- [193] M. Tuchband, J. He, S. Huang, and S. Lindsay. Insulated gold scanning tunneling microscopy probes for recognition tunneling in an aqueous environment. *Rev. Sci. Instrum.*, 83(1):015102, 2012.
- [194] K. Healy, V. Ray, L. J. Willis, N. Peterman, J. Bartel, and Marija Drndić. Fabrication and characterization of nanopores with insulated transverse nanoelectrodes for DNA sensing in salt solution. *Electrophoresis*, 33(23):3488–3496, 2012.